WASM: Minerals, Energy, and Chemical engineering

The Optimization of Perovskite Solar Cells from Power Conversion Efficiency and Operational Stability

Pengyun Liu

0000-0003-2114-8103

This thesis is presented for the Degree of
Doctor of Philosophy
of
Curtin University

October 2020

Declaration

To the best of my knowledge and belief this thesis contains no material previously published by any other person except where due acknowledgment has been made.

This thesis contains no material which has been accepted for the award of any other degree or diploma in any university.

Signature: … [redacted]…………

Date: …2020/10/28…………………..

Acknowledgements

Time flies and three and half years passed in a flash. This period has given me source of the most precious experiences in my life. I not only learned how to make research but also understanded that I should use a positive and optimistic attitude to face life no matter what difficulties I met in life. I am so blessed to be a member of such a great group and make so many friends here. I would like to acknowledge a number of people who were accompanying me through the whole journey here.

First of all, I want to express my deepest and sincerest gratitude to my supervisor Professor Zongping Shao for his continuous support of my PhD study. He is very patient, so supportive and understanding to me. He not only offered me valuable suggestions in the academic studies but also taught me how to deal with life, welcome challenges and overcome difficulties. He is the best advisor and mentor for my PhD study. His guidance will benefit me for a lifetime. I would also like to gratefully thank my co-supervisor Professor Moses Tade for his guidance and help.

Furthermore, I would like to give my hearty thanks to all members in my group. Thanks to Dr. Chao Su for her endless encouragement, collaboration and help. Thanks to Mr. Yijun Zhong, Mr. Xiaomin Xu, Ms. Yangli Pan and Mr. Paulo Sérgio Barros Julião for their help, comments and suggestions for some problems. In addition, I also want to thank my friends Ning Han, Zhengxin Yao, Ruofei Chen for their support, accompany and help. When I am confronted with some difficulties, they are always giving me some suggestions and encouraging me.

Due to the fact that some necessary experimental equipment for my PhD thesis is unavailable in Curtin, I had to do many experiments in Nanjing Tech university. I gratefully thank the members in this group for their collaboration and help. I would like to wholeheartedly thank Professor Wei Wang, Professor Wei Zhou and Guangming Yang for their help and guidance. I also want to thank Yonghui Chen, Xiaoqing Yang, Huimin Xiang, Hongbo Xiao, Amin Xie, Xiao Han, Jingsheng He and other students in this group for their collaborations and help. I also express my sincere thanks to Jie Miao, Jie Dai, Chuan Zhou, Qian Lu, Xixi Wang and other students in this group for their help and encouragement.

Last but not least, I am grateful to my beloved family, my parents and my sister for their continuous love and support which are my source of strength. They have provided me through moral and emotional support in my life. I love them forever.

Abstract

The development of society and the rise of global population have rapidly increased the global energy demand, which traditional fossil fuel cannot meet. In addition, the increasing consumption rate of traditional fossil fuel has caused severe environmental problems such as global warming. Thus, developing renewable energy sources has become an inevitable trend. Among various new energy sources, solar energy has gained wide public attention due to its easy accessibility and diverse pathways of utilization. Solar energy can be utilized via the pathways of photocatalysis and photovoltaic. Solar cells are one of important energy conversion devices, which convert solar energy to electronic energy. In recent years, organic-inorganic hybrid halide perovskites have been extensively researched as light-absorbing materials in solar cells because of their long charge carrier diffusion length, adjustable bandgap, and strong capacity of light absorption. The emerging perovskite solar cells (PSCs) have become a rising star in the photovoltaic field owing to their high efficiency and simple fabrication process. In spite of the significantly boosted efficiency during the past decade, PSCs suffer from poor stability which restricts their commercialization process.

In this thesis, some strategies were employed to improve the power conversion efficiency (PCE) and stability of PSCs. $CH_3NH_3PbI_3$ ($MAPbI_3$) and $CsPbIBr_2$-based PSCs were fabricated as the research subjects via the solution-processed spin-coating method. Photovoltaic performance was obtained via testing *J-V* curves under AM 1.5G illumination at 100 mW cm^{-2}. To investigate the change of the properties of perovskite films and the corresponding devices, a variety of characterization techniques were utilized. X-ray diffraction (XRD) was used to analyze the crystallinity and crystal structure. X-ray photoelectron spectroscopy (XPS) was employed to study the change of chemical environment. Scanning electron microscopy (SEM) was measured to observe morphology. Additionally, a series of electrochemical testing such as electrochemical impedance spectroscopy (EIS), Mott-Schottky (MS) curves et al. were carried out to investigate some properties of PSCs. The specific contents of this thesis were introduced as follows:

Firstly, considering the negative influence of defects on the photovoltaic performance of

PSCs, a bilateral cyano molecule was utilized as an effective additive to reduce defects. Succinonitrile (SN) was selected to modify $MAPbI_3(Cl)$) perovskite film. SN has two cyano groups (-C≡N) at both ends of the carbon chain, which offer two cross-linking points to allow perovskite grains to gather together via forming hydrogen bond with $-NH_2$ in perovskite and interacting with uncoordinated Pb^{2+}. The incorporation of SN into perovskite film can reduce the appearance of pinholes and microcracks on the perovskite film surface and increase the crystallinity of perovskite, thereby enhancing light absorption and decreasing defects. Benefiting from these merits brought by SN additive, the PCE of $MAPbI_3$ (Cl)-based devices improved from 18.4% to 20.3%. Meanwhile, the stability of devices in N_2 and humid air atmosphere was significantly improved. In the second research work, a metal acetate salt (antimony acetate ($Sb(Ac)_3$)) was selected to modify $MAPbI_3$. As for this metal acetate salt, both the cation and anion have positive impact on the device performance. The introduction of $Sb(Ac)_3$ increased the crystallinity of perovskites, optimized surface morphology of perovskite films, enhanced light absorption, optimized the energy level of perovskite and suppressed charge carrier recombination. Through in-depth analysis, it was discovered that the anion (Ac^-) and cation (Sb^{3+}) play different roles, in which Ac^- serves more as a film growth relator to optimize the file morphology while Sb^{3+} is more involved in tuning the electronic property to improve the energy level of perovskite. The synergistic effect of Ac^- and Sb^{3+} endowed $MAPbI_3$-based PSCs with a high PCE above 21% and an enhanced stability against humid air and heat.

Although $MAPbI_3$-based solar cells have achieved high efficiency and good stability against water with the assistance of SN and $Sb(Ac)_3$, they still suffered from poor thermal stability. To fabricate thermally stable PSCs, the research attention in this thesis was transferred to all-inorganic halide perovskites-based PSCs. $CsPbIBr_2$-based PSCs were selected as a research subject. The biggest problem of $CsPbIBr_2$-based PSCs is their relatively low PCE, which is still far from their organic-inorganic hybrid halide counterparts. The difficulty in fabricating high-quality $CsPbIBr_2$ perovskite films limits the achievement of high efficiency of devices. Thus, a strategy of functional Cu^{2+} doping was adopted to optimize the film quality and tune optoelectronic properties. It was found that appropriate amount of Cu^{2+} doping was

capable of improving $CsPbIBr_2$ film quality, increasing the perovskite crystallinity, expanding grain size, improving energy level alignment and effectively inhabiting charge recombination. All these merits improved the PCE of $CsPbIBr_2$-based PSCs from 7.81% to 10.4%, enhanced the moisture and thermal stability, and also relieved hysteresis.

List of Publications

1. **Pengyun Liu**, Wei Wang, Shaomin Liu, Huagui Yang, Zongping Shao, Fundamental Understanding of Photocurrent Hysteresis in Perovskite Solar Cells, Adv. Energy Mater. 2019, 1803017.
2. **Pengyun Liu**, Xiaoqing Yang, Yonghui Chen, Huimin Xiang, Wei Wang, Ran Ran, Wei Zhou, Zongping Shao *, Promoting the Efficiency and Stability of $CsPbIBr_2$-Based All-Inorganic Perovskite Solar Cells through a Functional Cu^{2+} Doping Strategy, ACS Appl. Mater. Interfaces 2020, 12, 23984-23994.
3. **Pengyun Liu**, Ning Han, Wei Wang, Ran Ran, Wei Zhou, Zongping Shao, High-Quality Ruddlesden-Popper Perovskite Film Formation for High-Performance Perovskite Solar Cells, Adv. Mater. 2021, 33, 2002582.
4. **Pengyun Liu**, Huimin Xiang, Wei Wang, Ran Ran, Wei Zhou, Zongping Shao, A Bilateral Cyano Molecule Serving as an Effective Additive Enables High-Efficiency and Stable Perovskite Solar Cells, J. Energy Chem. 2021, DOI: 10.1016/j.jechem.2021.03.024.
5. Huimin Xiang, **Pengyun Liu**, Wei Wang, Ran Ran, Wei Zhou, Zongping Shao, Towards Highly Stable and Efficient Planar Perovskite Solar Cells: Materials Development, Defect Control and Interfacial Engineering, Chem. Eng. J. 2020, DOI: doi.org/10.1016/j.cej.2020.127599.
6. Xiaoqing Yang, Yonghui Chen, **Pengyun Liu**, Huimin Xiang, Wei Wang, Ran Ran, Wei Zhou, Zongping Shao, Simultaneous Power Conversion Efficiency and Stability Enhancement of $Cs_2AgBiBr_6$ Lead-Free Inorganic Perovskite Solar Cell through Adopting a Multifunctional Dye Interlayer, Adv. Funct. Mater. 2020, 2001557.
7. **Pengyun Liu**, Yonghui Chen, Huimin Xiang, Xiaoqing Yang, Zongping Shao, Benefitting from Synergistic Effect of Anion and Cation in Antimony Acetate for Stable $CH_3NH_3PbI_3$-Based Perovskite Solar Cell with Efficiency Beyond 21% (Submitted).

Contents

Chapter 1 Introduction

1.1 Background

The traditional energy structure cannot meet the demands of the development of society and the rise of global population which have rapidly increased the global energy demand. The massive consumption of fossil fuel has caused growing concerns about the greenhouse emission and environmental pollution. Thus, it is imperative to develop clean and renewable energy sources to settle these issues. Various new energy resources such as wind energy, ocean energy, tidal energy and biomass energy have been widely explored and developed in order to overcome the energy crisis. Among them, solar energy has been considered as one of the most abundant clean and inexhaustible energies and the conversion of solar energy to electric energy or chemical energy has become a core part of the sustainable energy research.

In the photovoltaic field, solar cells have experienced more than a hundred years of development history from the first generation of single crystalline silicon solar cells to various novel up-to-date solar cells. In terms of the crystalline silicon solar cells as the first generation of solar cells, they have been commercialized and took over the market. Worldwide installed capacity of crystalline silicon solar cell has exceeded 400 GW. The second generation of solar cells is thin film solar cells with shorter energy payback time. However, these thin film solar cells did not replace first-generation silicon solar cells due to their relatively low efficiency, poor stability as well as the utilization of rare materials.[1-4] Thus, it is necessary to develop new photovoltaic devices to further promote the development of photovoltaic technology. Since 2009, a novel light-absorbing material has attracted extensive attention. At that time, organic-inorganic hybrid halide perovskites $CH_3NH_3PbI_3$ ($CH_3NH_3^+$, MA^+) and $CH_3NH_3PbBr_3$ were utilized as dyes to absorb sunlight in dye-sensitized solar cells (DSSCs), and the corresponding DSSCs achieved efficiency of 3.81% and 3.13%, respectively.[5] However, the utilization of liquid electrolytes caused severer leakage problem and instability of devices, hindering their development. Until 2012, this tricky problem was resolved by using a solid-state hole transporting material to substitute the liquid electrolyte. The utilization of spiro-

OMeTAD not only enhanced the device stability but also improved the efficiency to 9.7%.[6] After that, perovskite solar cells (PSCs) have developed as an independent branch in the photovoltaic field and various other halide perovskites have also been employed as light-absorbing materials in PSCs.[7]

During the past several years, the efficiency of PSCs has been boosted to 25.5%, which is almost comparable with that of mature silicon solar cells and can be further improved.[8] However, there is still plenty of room for the achievement of the commercialization of PSCs because stability has become a biggest hurdle that restricts their commercialization process. In terms of halide perovskites, many of them are vulnerable to environmental factors. The typical organic-inorganic hybrid halide perovskite $MAPbI_3$ can easily decompose at high temperatures and humid environment as the A-site organic cation is extremely unstable and will escape from the perovskite structure under these conditions.[9-11] For another organic-inorganic hybrid halide perovskite $NH_2CHNH_2PbI_3$ ($NH_2CH{=}NH_2^+$, FA^+), although it shows better thermal stability than $MAPbI_3$, this halide perovskite suffers from the instability of phase structure. The photoactive α-perovskite phase is apt to convert to undesired hexagonal δ-perovskite phase at room temperature which is less-photoactive. Particularly, the presence of moisture will accelerate this conversion process.[12, 13] This problem about the phase instability also troubles all-inorganic halide perovskites like $CsPbI_3$ with superior heat resistance.[14, 15] Due to the sensitivity of halide perovskites, perovskite films were fabricated in nitrogen-filled or argon-filled glove box in most cases.

Therefore, it is of great importance to take measurements to further enhance the performance of PSCs, including further improving the efficiency and enhancing the long-term stability. In pursuit of high-performance PSCs, various strategies have been adopted, including optimizing the device structure, developing new materials and improving the fabrication technique.[16-19] PSCs are composed of different functional layers including perovskite layer, charge extracting and transporting layers and electrodes. Seeing from the current research situations, some researchers paid attention to the improvement of perovskite layers and others mainly focused on the optimization and development of charge transporting materials.[20-23]

1.2 Research objectives

In this thesis, the research work is mainly focused on the improvement of the properties of halide perovskite materials and aims to enhance the efficiency and operational stability of PSCs. After adopting strategies to improve the perovskite layer, the internal mechanism of how these utilized strategies give rise to the improved performance of PSCs is expected to be clarified via a variety of characterization techniques and a series of optoelectronic property analysis. The specific goals of this thesis are listed as below.

- Gaining a good understanding of the origin and working mechanism of PSCs, defining the existing problems and challenges of PSCs and summarizing the current research status of various halide perovskites utilized in PSCs, transporting materials and the effective strategies employed to improve the photovoltaic performance of PSCs.
- Investigating the influence of defects on the photovoltaic performance of PSCs and the reasons for the appearance of defects in PSCs. Selecting a bilateral cyano molecule as an additive to reduce the defects and studying how this additive participate in the film formation process and optimize the perovskite film properties to reduced defects.
- Searching a metal salt whose cation and anion are both beneficial for the perovskite layer. Introducing this metal salt into perovskite precursor solution to serve as a layer modifier. Investigating the influence of the incorporation of this metal salt on the properties and morphology of perovskite films. Studying the individual role of the cation and anion in determining the final photovoltaic performance of PSCs.
- Employing composition engineering to adjust the properties of all-inorganic halide perovskites. Incorporating Cu^{2+} into $CsPbIBr_2$ for the purpose of improving the efficiency and stability of $CsPbIBr_2$-based all-inorganic PSCs. Analyzing the impact of Cu^{2+} incorporation on the optoelectronic properties of devices.

1.3 Thesis organization

This thesis includes six chapters. The first chapter is about introduction and the thesis organization. The second chapter is literature review. Following by this is three research work.

The last chapter is conclusions and future perspectives. The thesis structure and organization are shown in **Figure 1.1**.

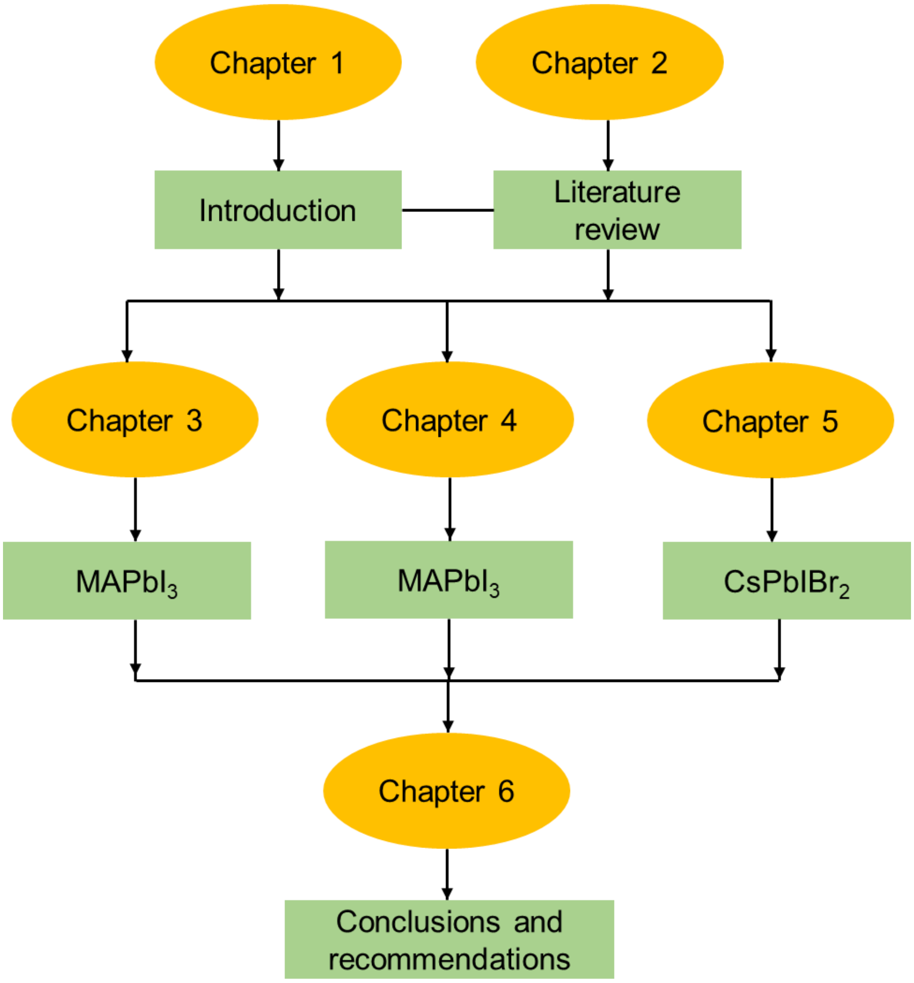

Figure 1.1 Schematic of thesis structure and organization.

Chapter 1: Introduction

This chapter briefly presents the background of PSCs, including the origin and the current research status, and also gives the reasons for doing this research. Research objectives and the thesis structure and organization are also presented in this chapter.

Chapter 2: Literature Review

This chapter first introduces some basic knowledge of PSCs, including devices structures and working mechanism, photovoltaic performance parameters as well as some influential factors of PSC photovoltaic performance. Then, according to different halide perovskites, various types of PSCs are introduced. Then, the challenges that PSCs are faced with are elucidated. Followed by this, the strategies utilized to overcome these challenges are proposed.

Finally, the development direction of PSCs is stated.

Chapter 3: A Bilateral Cyano Molecule Serving as an Effective Additive Enables High-Efficiency and Stable Perovskite Solar Cells

This chapter aims to improve the photovoltaic performance of $MAPbI_3(Cl)$-based PSCs via introducing a bilateral cyano molecule (succinonitrile, SN) into perovskite precursor solution. The addition of SN reduced defects and thus effectively suppressed charge trap-assisted recombination. In addition, suitable amount of SN addition also enhanced the crystallinity of perovskites and light absorption of perovskite films. As a consequence, the efficiency and stability of $MAPbI_3(Cl)$-based devices were significantly improved.

Chapter 4: Benefitting from Synergistic Effect of Anion and Cation in Antimony Acetate for Stable $CH_3NH_3PbI_3$-Based Perovskite Solar Cell with Efficiency Beyond 21%

This thesis also aims to further enhance the photovoltaic performance of $MAPbI_3$-based PSCs via carefully selecting an appropriate metal salt to modify perovskite films. Both the cation and anion of this metal salt are expected to be beneficial for $MAPbI_3$ perovskite film. On this basis, antimony acetate ($Sb(Ac)_3$) was utilized, in which both Sb^{3+} and Ac^- can exert positive effect on the $MAPbI_3$ perovskite film, giving rise to improve photovoltaic performance of $MAPbI_3$-based PSCs. The individual role of Sb^{3+} and Ac^- was also explored in this work via using lead acetate ($Pb(Ac)_2$) and antimony iodide (SbI_3) as comparison. Benefiting from the synergetic effect of Sb^{3+} and Ac^-, $Sb(Ac)_3$-modified PSCs achieved high photovoltaic performance.

Chapter 5: Promoting the Efficiency and Stability of $CsPbIBr_2$-Based All-Inorganic Perovskite Solar Cells through a Functional Cu^{2+} Doping Strategy

In this chapter, the subject of this research is all inorganic $CsPbIBr_2$-based PSCs. Composition engineering was adopted to improve the photovoltaic performance of all inorganic $CsPbIBr_2$-based PSCs. Via a strategy of Cu^{2+} doping, the properties of $CsPbIBr_2$ perovskite films were optimized, thereby giving rise to a high-performance PSC with enhanced stability against water and heat.

Chapter 6: Conclusions and Recommendations

In this chapter, important research outcomes in each chapter are sum up and some constructive suggestions are also elucidated here.

1.4 Reference

[1] K. L. Chopra, P. D. Paulson, V. Dutta, *Prog. Photovolt. Res. Appl.* **2004**, *12*, 69-92.

[2] C. Battaglia, A. Cuevas, S. De Wolf, *Energy Environ. Sci.* **2016**, *9*, 1552-1576.

[3] T. Saga, *NPG Asia Mater.* **2010**, *2*, 96-102.

[4] T. D. Lee, A. U. Ebong, *Renew. Sust. Energ. Rev.* **2017**, *70*, 1286-1297.

[5] A. Kojima, K. Teshima, Y. Shirai, T. Miyasaka, *J. Am. Chem. Soc.* **2009**, *131*, 6050-6051

[6] H.-S. Kim, C.-R. Lee, J.-H. Im, K.-B. Lee, T. Moehl, A. Marchioro, S.-J. Moon, R. Humphry-Baker, J.-H. Yum, J. E. Moser, M. Grätzel and N.-G. Park, *Sci. Rep.* **2012**, *2*, 591.

[7] M. A. Green, A. Ho-Baillie, H. J. Snaith, *Nat. Photonics* **2014**, *8*, 506-514.

[8] N.-G. Park, *Adv. Energy. Mater.* **2020**, *10*, 1903106.

[9] Y. Han, S. Meyer, Y. Dkhissi, K. Weber, J. M. Pringle, U. Bach, L. Spiccia, Y.-B. Cheng, *J. Mater. Chem. A* **2015**, *3*, 8139-8147.

[10] Y.-B. Lu, W.-Y. Cong, C. Guan, H. Sun, Y. Xin, K. Wang, S. Song, *J. Mater. Chem. A* **2019**, *7*, 27469-27474.

[11] Z. Ahmad, A. S. Shikoh, S. Paek, M. K. Nazeeruddin, S. A. Al-Muhtaseb, F. Touati, J. Bhadra, N. J. Al-Thani, *J. Mater. Sci-Mater. El.* **2019**, *30*, 1354-1359.

[12] T. M. Koh, K. Fu, Y. Fang, S. Chen, T. C. Sum, N. Mathews, S. G. Mhaisalkar, P. P. Boix, T. Baikie, *J. Phys. Chem. C* **2014**, *118,* 16458-16462.

[13] F. Ma, J. Li, W. Li, N. Lin, L. Wang, J. Qiao, *Chem. Sci.* **2017**, *8*, 800-805.

[14] G. E. Eperon, G. M. Paternò, R. J. Sutton, A. Zampetti, A. A. Haghighirad, F. Cacialli, H. J. Snaith, *J. Mater. Chem. A* **2015**, 3, 19688-19695.

[15] W. Ahmad, J. Khan, G. Niu, J. Tang, *Sol. RRL* **2017**, *1*, 1700048.

[16] J. Seo, J. H. Noh, S. I. Seok, *Acc. Chem. Res.* **2016**, *49,* 562-572.

[17] F. Wang, Y. Cao, C. Chen, Q. Chen, X. Wu, X. Li, T. Qin, W. Huang, *Adv. Funct. Mater.* **2018**, *28*, 1803753.

[18] A. Dubey, N. Adhikari, S. Mabrouk, F. Wu, K. Chen, S. Yang, Q. Qiao, *J. Mater. Chem.*

A **2018**, *6*, 2406-2431.

[19] F. Li, M. Liu, *J. Mater. Chem. A* **2017**, *5*, 15447-15459.

[20] E. H. Jung, N. J. Jeon, E. Y. Park, C. S. Moon, T. J. Shin, T.-Y. Yang, J. H. Noh, J. Seo, *Nature* **2019**, *567*, 511-515.

[21] D. Liu, T. L. Kelly, *Nat. Photonics* **2014**, *8,* 133-138.

[22] Z. Yu. L. Sun, *Adv. Energy Mater.* **2015**, *5*, 1500213.

[23] J. Urieta-Mora, I. García-Benito, A. Molina-Ontoria, N. Martín, *Chem. Soc. Rev.* **2018**, *47*, 8541-8571.

Chapter 2 Literature Review

2.1 Introduction

The rapidly increasing global energy demand, fossil fuel consumption rate and growing concerns about the greenhouse emission and environmental pollution have attracted more and more intention and research interests in the development of clean and renewable energy sources and relevant energy conversion and storage devices/systems. Various new energy resources such as wind energy, ocean energy, tidal energy and biomass energy have been widely explored and developed in order to overcome the energy crisis. Among them, solar energy has been considered as the most abundant clean energies, which can be utilized via diverse pathways. Converting solar energy to electric energy has become one of core parts of utilizing solar energy.

Solar cells are a perpetually hot topic attracting continuous enthusiasm for research and development, as they can directly convert clean and inexhaustible solar energy into usable electricity. Solar cells have experienced more than a hundred years of development history from single crystalline silicon solar cells to various novel up-to-date solar cells.[1, 2] To be specific, the first generation of solar cells are single crystalline silicon solar cells and polycrystalline silicon solar cells. Then, a variety of thin film solar cells including CdTe, GsAs, CuInSe and so on solar cells appeared and developed, becoming the second generation of solar cells. At present, solar cells have entered the third generation in which solar cells are expected to be more efficient, stable and eco-friendly. The third generation of solar cells are mainly composed of dye-sensitized solar cells (DSSCs) and emerging perovskite solar cells (PSCs). [3-7]

Even though solar cells continued to advance and develop during the past century, the current solar or photovoltaic cell market is still dominated by crystalline silicon panels, which display excellent stability and a high-power conversion efficiency (PCE) of up to 25.6%.[8] However, the cost of these silicon solar cells is very high as they require the preparation of ultrahigh-purity silicon via energy intensive crystal growth and vapor deposition methods. In the current market, even with government subsidies, people still feel reluctant to adopt this technology for electricity generation.[9] To advance applications, the manufacturing cost of solar cells must be reduced. Fortunately, the encouraging results from PSCs bring new hope to the field and gained increasing attention and recognition because of their high efficiency, tunable bandgap and simple fabrication process. Despite the short-term development of 12 years, the highest PCE of PSCs has exceeded 25%, which is comparable with that of silicon solar cells, making PSCs become one of the most promising candidates of new-generation solar cells.[10, 11]

In this literature review, I systematically reviewed PSCs starting from introducing the fundamental knowledge of PSCs, including the device structure, working mechanism, important photovoltaic parameters as well as influential factors of device performance. Then various types of PSCs were summarized according to different perovskites as photo-active layers. Although PSCs have witnessed great boost in terms of PCE during the past decade, there are also some tricky problems which hurdle the commercialization process of PSCs. Thus, I elucidated these typical challenges that PSCs are confronted with and need to be overcome. Followed by this section, I proposed strategies which have been widely implemented to settle the above-mentioned issues. Last but not least, I outlooked the future development direction of PSCs. This literature review would provide a comprehensive understanding of PSCs and offer valuable guidance to promote the further development of PSCs.

2.2 Basic knowledge of perovskite solar cells

2.2.1 Device structure and working mechanism

For most complete PSC devices, they are composed of F-doped SnO_2 (FTO)/In-doped SnO_2 (ITO) conducting glass, electron transporting layers (ETLs), hole transporting layers (HTLs), perovskite layers as well as electrodes. The perovskite layer is normally sandwiched by an ETL and a HTL. Based on this configuration structure, the perovskite layer functions as light-absorbing layers to generate electrons and holes, which will diffuse to the interface of perovskite/ETLs and perovskite/HTLs. ETLs and HTLs serve as charge transporting layers to extract and transport photo-generated electrons and holes, respectively. Then, electrons will inject into the external circuit via FTO substrates and holes will enter into electrodes to achieve the collection of current. This is the mechanism of the conversion of light to electricity via PSCs.[12, 13]

Figure 2.1 shows the crystal structure of perovskite ABX_3, where the A cation is located at the eight corners of the cubic unit cell and B cation is at the center surrounded by six X anions in an octahedral $[BX_6]^{4-}$ arrangement. To be specific, the A site could be occupied by organic cations, such as $CH_3NH_3^+$ (MA+) and $NH_2CH{=}NH_2^+$ (FA^+), or even inorganic cations, including cesium (Cs^+), while the B site could contain Pb^{2+} or Sn^{2+}, and the X site is for halide anions: I^-, Br^- and Cl^-.[14-19] Among these, $MAPbX_3$ are widely used for PSCs because of their favorable optical properties, including a high sunlight absorption coefficient, tunable bandgap energy, long carrier diffusion length, and the ambipolar property. These $MAPbX_3$-based halide perovskites not only work as the light harvesting material but can also effectively suppress the recombination of excited charge carriers.[20-23]

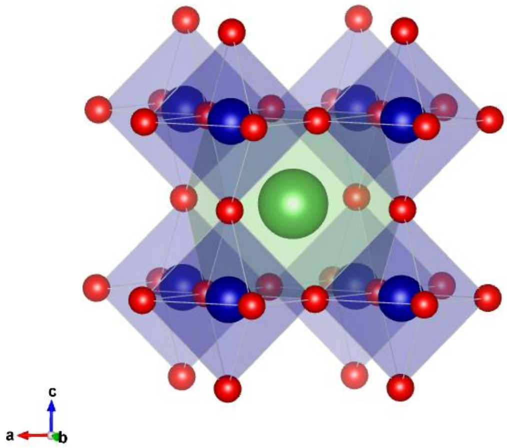

Figure 2.1 The schematic of crystal structure of ABX_3. (The green, blue and red spheres represent A-site, B-site and X-site ions, respectively).

As for ETLs, in addition to separating and transporting electrons, they also act as a blocking layer to block holes entering into the electron side which will lead to severe charge carrier recombination. To function as efficient ETLs, the materials should meet three basic requirements. Firstly, the n-type semiconductors can easily form compact films via simple fabrication method. Secondly, the conduction band minimum (CBM) (or the lowest unoccupied molecular orbital (LUMO) of the ETL should not be higher than that of the perovskite layer. Thirdly, the ETL materials should process good electron conductivity and mobility. Similar to ETLs, the main function of HTLs is to extract and transport holes and block electrons to reduce charge carrier recombination. To fully exercise these roles, HTL materials should not only show high hole conductivity and mobility but also appropriate valence band maximum (VBM). To be specific, the highest occupied molecular orbital (HOMO) (or VBM) of the HTL should not be lower than that of the perovskite layer.[24]

The structure of PSCs can be classified into two types: mesoporous structure and planar heterojunction. The mesoporous structure prepared from metal oxides such as TiO_2, ZnO_2, Al_2O_3, and ZrO_2 which function as the scaffold to support the perovskite and as the isolator to prevent holes from undesirably migrating to the electron-transporting side. Due to their CBM energy levels being lower than those of the organic perovskites, some oxides including TiO_2 and ZnO_2 can facilitate the electron transport and extraction processes. In contrast, oxides such as Al_2O_3 and ZrO_2 have higher CBM energies and can only serve as the porous substrate to support the perovskite photo active materials.[25] The PSCs based on mesoporous Al_2O_3 and ZrO_2 are also referred to as meso-superstructured PSCs, in which the electron transport is completed via the perovskite only.16 Planar heterojunction PSCs possess the n-i-p (regular) structure or the p-i-n (inverted) structure according to the different positions of the ETL and HTL. The four main structures of PSCs are presented in **Figure 2.2**.[26]

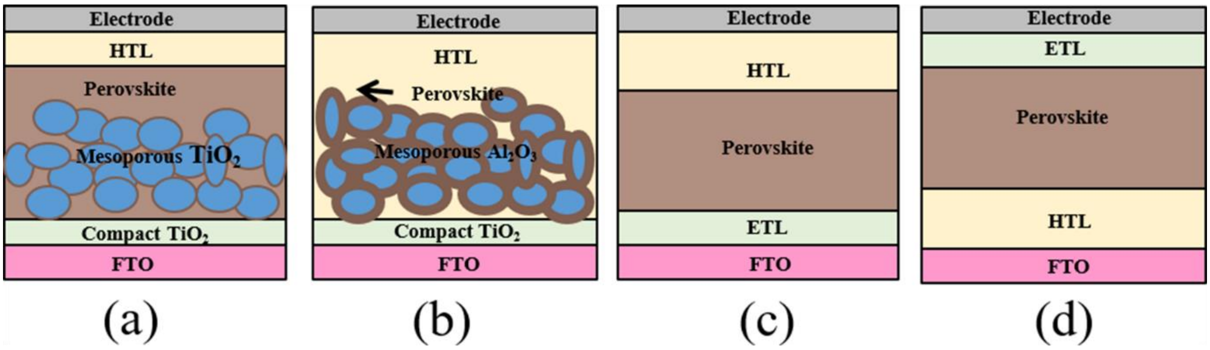

Figure 2.2 Device structures of PSCs: (a) mesoporous structure, (b) meso-superstructure, (c) planar n-i-p (regular) structure, and (d) planar p-i-n (inverted) structure.[26] (Reproduced with permission. Copyright 2019, John Wiley and Sons)

These four PSC structures exhibit individual advantages per their different aspects. The normal mesoporous structure in **Figure 2.2a** is derived from DSSCs. This conventional mesoporous structure has been the most widely applied in the current exploration to further improve PSC efficiency. In 2012, Snaith's group first introduced the concept of a meso-superstructure (**Figure 2.2b**) to replace mesoporous TiO_2 (mp-TiO_2) with Al_2O_3 in the PSC design;[16] this configuration not only improved the operational stability under UV light but also facilitated electron transport via the perovskite absorber.[27] In addition to the typical mesoporous structure, the planar heterojunction structure (**Figure 2.2c** and **d**) has also captured abundant attention due to the simplified and low-temperature fabrication processes of the ETL and HTL. The effectiveness of the planar structure has also been confirmed by Snaith's group via a vapor deposition method. This simplified procedure enables PSC production over large areas on flexible substrates.[28]

2.2.2 Important photovoltaic performance parameters

In terms of solar cells, PCE is the most important evaluation index to access the device performance. Higher PCE value means more effective conversion capability from solar energy to electric energy. Noteworthy that PCE is eventually determined by three important photovoltaic parameters, namely, short-circuit current density (J_{sc}), open-circuit voltage (V_{oc}) as well as fill factor (FF), which are correlated and interinhibitive. These photovoltaic parameters can be gained from J-V) curves.

In J-V curves, the intercept on the vertical coordinate represents J_{sc}, meaning the biggest current density that solar cells can produce. The intercept on the horizontal coordinate represents V_{oc}, meaning the highest voltage that solar cells can generate. FF means the ratio between the maximum power that solar cells can output and the theoretical power that solar cell can output, which can be donated via the ratio of the corresponding area in J-V curves. PCE can be calculated via **Equation 2.1**.

$$\mathrm{PCE} = \frac{V_{oc} J_{sc} FF}{P_{in}} \tag{2.1}$$

2.2.3 Influential factors of PSC photovoltaic performance

The photovoltaic performance of solar cells is affected by multiple factors. In this section, I summarized some important influential factors and discussed how these factors influence photovoltaic parameters and finally determine the photovoltaic performance.

Film quality plays a vital role in device performance. In terms of ETLs and HTLs, compact and homogenous films are necessary to reduce current loss as the cracks or pinholes in perovskite films. Poor ETL and HTL films will cause severe charge carrier recombination. More importantly, the perovskite film quality should attract sufficient attention considering that it greatly affects the optoelectrical properties of perovskite films. Different from single-crystal perovskites-based PSCs, perovskite films are polycrystalline films in most PSCs so grain boundaries unavoidably exist, where the defect density is usually high and the charge carrier recombination hence easily occur, consequently limiting the further increase in the PCEs of PSCs. Moreover, grain boundaries in halide perovskite films have been found to have much faster ion migration than bulk crystals, which has been considered to have a detrimental influence on the device performance. Enhancing the film surface coverage, improving the crystallinity of the grains and enlarging the grain size have been widely considered as effective routes to reduce the overall bulk defect density and mitigate the hysteresis since improved film surface coverage can suppress charge carrier trapping, which may be the culprit of performance degradation and hysteretic phenomenon of PSCs. In addition to increasing grain size for reduced grain boundaries, grain boundaries can be decreased via passivation through simple material filling or complicated chemical interaction between introduced molecules and halide perovskites. For the simple material filling, excessive PbI_2 in $MAPbI_3$ perovskite film has been reported to passivate grain boundaries for the efficiency enhancement. For the complicated chemical interaction, previous studies have indicated that under-coordinated Pb atoms and Pb-I antisite defects at grain boundaries have been recognized as the main sources of the trap states and these defects can be reduced through introducing some semiconducting molecules with Lewis-acid or Lewis-base functional groups. From the perspective of device stability, grain boundaries are more likely to be invaded by water and have been considered as the degradation source of perovskites due to the fast ion migration and the presence of a large number of defects.

Thus, it is very important to optimize the perovskite film quality to gain compact, smooth films with full coverage, large grain sizes and reduced grain boundaries for the purpose of fabricating highly efficient and stable PSCs.

Energy level alignment among different layer is another significant factor influencing device photovoltaic performance.[29,30] Due to the layer structure of PSCs, there are many interfaces in PSC devices, including HTL/anode, perovskite layer/HTL, ETL/perovskite layer and cathode/ETL. These interfaces play an important role in PSC devices as the charge extraction is mainly determined by the energy offsets at the interfaces. The lower CBM of ETLs than that of perovskite layers allows electrons freely transfer into ETLs, while the higher VBM of HTLs than that of perovskite layers make holes inject from perovskite layers into HTLs, achieving the efficient separation and extraction of charges. Furthermore, the relative energy level location of ETL and perovskite layer as well as HTL and perovskite layer has a great influence on J_{sc} and V_{oc}. In general, larger energy level difference between CBM of perovskite layers and ETLs or VBM of HTLs provides larger driving force for electrons and holes to be extracted, which can reduce charge recombination and is beneficial for J_{sc} enhancement. However, the larger energy level difference unfortunately leads to greater energy loss, causing the decrease in V_{oc}. In order to improve V_{oc}, the smaller energy level difference between CBM of perovskite layers and ETLs or VBM of HTLs is expected.[31]

Noteworthy that the energy level of functional layers can be affected by many aspects. On one hand, it is closely related to the film composition, which has been confirmed via many UPS results. It is important to note that perovskites may possess different semiconductor types and therefore have different energy levels with respect to the Fermi level (E_f), which can be controlled via managing the film composition. For instance, the removal of MAI from the MAI-PbI_2 system converted the semiconductor type of perovskite from p-type to n-type.[32] In another case, it has been found that the VBM of $MAPbI_3$ can be varied with the concentration of MAI changing.[33] In addition, different halides in perovskite have a significant influence on the energy level, which indicates that the energy level of perovskite films can be managed via selecting different halides. On the other hand, the energy level of perovskite rests in the underlying layer type. For mesoporous-structure and planar n-i-p PSCs in which perovskite layers lie on top of n-type ETLs, E_f pinned into the CBM of perovskite, indicative of the p-type of perovskites. By contrast, the p-type underlying substrates in inverted PSCs made the perovskite more n-type.[29, 34, 35] Furthermore, the energy level of perovskite films is governed by the surface states, particularly steaming from Pb^0. Thus, the surface states can be controlled to optimize the energy level match between perovskite layers and other neighboring layers.[36]

In addition to film quality and energy level alignment, charge recombination should be paid great attention considering its adverse effect on photovoltaic performance of PSCs. Charge recombination is inevitable in PSCs during the charge transfer process due to the existence of defects, which will degrade device performance. Charge recombination has been regarded as a governing factor that determines V_{oc} and FF in a solar cell. Herein, it is imperative to retard charge recombination as possible for the production of better PSCs.[37-39] In term of perovskite layers, their surface morphology has some influences on charge recombination as mentioned above. Besides, the thickness of perovskite layers has been found to influence charge recombination. From the perspective of light absorption, in order to absorb enough sunlight, thicker perovskite layers are needed. But if the perovskite layer is too thick, particularly beyond the charge diffusion length, charge cannot arrive at the interface of perovskite layers/ charge transporting layers and cannot be extracted by their corresponding transport layers timely, causing severer charge recombination at the interfaces and thus weakening the photovoltaic performance. Besides, ETLs and HTLs also play a crucial role in the charge recombination process. For both of them, high electron mobility and hole mobility are expected for them, respectively. Under the condition of high electron and hole mobility, it is very vital to keep the balance between charge transport and hole transport as unbalanced charge transport would lead to charge recombination, which has been considered as one of possible reasons for hysteretic behavior occurring in PSCs.[26] For typical organic-inorganic hybrid halide perovskites like $MAPbI_3$, they can transport electrons and holes by themselves due to the ambipolar property, but the electrons and holes are transported imbalancedly in perovskite films owing to the difference of diffusion lengths between holes and electrons.[16, 40, 41] Specifically speaking, holes can be more efficiently transported than electrons by perovskites themselves. So to compensate for the inefficient transport of electrons in perovskites, ETL is often added in PSCs to help electron extraction from the perovskite layer. However, the typical TiO_2 ETL possesses an electron mobility ($\approx 10^{-4}$ cm^2 V^{-1} s^{-1}) lower than the hole mobility ($\approx 10^{-3}$ cm^2 V^{-1} s^{-1}) of some commonly used HTL materials, such as spiro-OMeTAD and poly[bis(4-phenyl) (2,4,6-trimethylphenyl)amine] (PTAA).[42] Therefore, the unbalanced charge transport phenomenon still exists in PSCs, which could be alleviated by improving the electron mobility of the ETL materials.

As discussed above, the photovoltaic performance is jointly affected by many aspects including film quality, energy level alignment and charge recombination. To fabricate high-performance of PSCs with high efficiency and excellent durability, a large number of efforts have been devoted from optimizing the film quality, adjusting the energy level match among different functional layers and suppressing charge recombination. I will elucidate detailly these efforts in section 2.5.

2.3 Various types of PSCs

2.3.1 Three-dimensional (3D) organic-inorganic hybrid halide PSCs

As aforementioned, the chemical formula of 3D halide perovskites is ABX_3, in which A-site cations are organic cations such as MA^+ and FA^+ or inorganic cations like Cs^+ and Rb^+, B-site cations are Pb^{2+} or Sn^{2+} while X-site ions refer to halide ions including I^-, Br^- and Cl^-. 3D organic-inorganic hybrid halide PSCs are solar cells using organic-inorganic hybrid halide perovskites whose A-site cations include organic cations as light absorbers.

The typical 3D organic-inorganic hybrid halide perovskite is $MAPbI_3$, which has been widely researched. The bandgap of $MAPbI_3$ is about 1.59 eV with special sensitivity of up to 800 nm, which is a suitable bandgap in terms of light absorbing in solar cells.[43] The bandgap can be increased to 2.3 and 3.1 eV via substituting the X-site anions to Br^- and Cl^-, respectively. Due to the unique optical and exitonic properties and good electricity conductivity of $MAPbI_3$, it was selected as a dye self-organized in TiO_2 in DSSCs, delivering 3.8% of PCE in the year of 2009.[44] In 2011, the PCE of $MAPbI_3$-based DSSCs was improved to 6.5% via applying TiO_2 surface treatment.[45] In these liquid electrolyte-based DSSC, the liquid electrolyte reacted with the perovskite dyes, resulting in the degradation of device performance. After that in 2012, the appearance of spiro-OMeTAD as solid-state hole transporting material to replace traditional liquid electrolytes settled this issue. More surprisingly, the PCE of solar cells was improved to 9.7% with 17 mA cm^{-2} of J_{sc}, 0.888 V of V_{oc} and 0.62 of FF and the device stability was also dramatically enhanced.[14] Since then, PSCs using $MAPbI_3$ and other similar halide perovskites as light absorbers, as a novel solar cell category, have gradually captured the attention of an increasing number of researchers in the photovoltaic field.

Almost simultaneously (mid-2012), Snaith and co-workers reported a series of additional developments of $MAPbI_3$-based PSCs using spiro-OMeTAD as HTL materials. One report was that using mixed halide ($MAPbI_{1-x}Cl_x$)-based perovskites as light absorbing materials outperformed its pure iodide counterparts in terms of stability and carrier transport. The second development was forming extremely thin absorber, outperforming nanoporous TiO_2-based counterparts. The third work was published in science and the PCE of $MAPbI_3$-based solar cells was boosted to 10.9% deriving from the significantly improved V_{oc} via substituting mesoporous TiO_2 with non-conducting Al_2O_3. This work also demonstrated that perovskites not only served as light absorbers but also were able to transport electrons and holes between device terminals.[16] Until 2013, the PCE of $MAPbI_3$-based PSCs exceeded 15% via constantly optimizing the preparation process.[28, 46] At the end of 2013, PSCs achieved a PCE of 16.2% via using the mixed-halide $MAPbI_{3-x}Br_x$ as light-absorbing material and a poly-triarylamine as HTL material. All these findings laid a good foundation for the development of PSC technology.

During the development process of $MAPbI_3$-based PSCs, researchers started to design and research some other organic cation-based halide perovskites and apply them to replace $MAPbI_3$ as light absorbers for different requirements. Among them, $FAPbI_3$ has attracted the most attention. In comparison with MA^+, FA^+ has larger ionic radius, which leads to the nearly cubic structure of $FAPbI_3$, while $MAPbI_3$ shows a tetragonal rather than a cubic structure due to the smaller size of MA^+. And $FAPbI_3$ displays narrower band gap (~ 1.43 eV) compared with $MAPbI_3$. Such a narrowed bandgap means that $FAPbI_3$ can absorb light of up to 870 nm.[15, 47] FA^+ was first employed to substitute MA^+ to synthesize pure $FAPbI_3$ perovskite used as light absorber by Pang et al. in 2014. Compared with one-step spin-coating method, the two-step dipping technology was more suitable to produce a relatively high PCE (7.5%).[48] At the same year, Snaith's group reported $FAPbI_3$-based planar heterojunction PSCs, achieving the PCE of up to 14.2%.[49] And Lee et al. reported more efficient $FAPbI_3$-based solar cells with the PCE over 16% via optimizing the $FAPbI_3$ film fabrication technique. In this work, a pure black polymorph single phase of $FAPbI_3$ was synthesized by reacting PbI_2 with impurity-free FAI.[50] In 2015, the PCE of $FAPbI_3$-based solar cells exceeded 20%. In this study, the high performance of $FAPbI_3$-based PSCs was mainly attributed to the formation of high-quality $FAPbI_3$ perovskite films deposited via the direct intramolecular exchange process in which DMSO molecules inserted into PbI_2 with FAI. By this fabrication technique, the produced $FAPbI_3$ films exhibited (111)-preferential crystallographic orientation, large-size grains, compact and smooth surface without radical PbI_2.[51]

In addition to the replacement of A-site cations, X-site anions have been adjusted to obtain other perovskites such as $MAPbBr_3$. Compared with $MAPbI_3$, $MAPbBr_3$ possesses larger bandgap, limiting the light absorption and thus leading to relatively low J_{sc} but relatively high V_{oc} in the corresponding PSCs. Actually, before $MAPbI_3$ was applied into DSSCs as dyes, $MAPbBr_3$ had been tried to use in DSSCs in 2006, achieving 2.2% of PCE. In 2013, the utilization of a new p-type polymer HTL material (PCBTDPP) helped to improve the PCE of $MAPbBr_3$ based solar cells to 3.04% with high V_{oc} of 1.15 V.[52] In another work, selecting a HTL material with a deeper HOMO resulted in a higher V_{oc} of up to 1.40 eV and a high FF of 0.79 as well as a PCE of 6.7%.^{31} After that, Liang et al. fabricated highly-efficient HTL-free $MAPbBr_3$-based PSCs with carbon electrodes. It was found that the carbon electrode was able to effectively extract holes which is produced in $MAPbBr_3$. Importantly, the voltage (energy) loss across the $MAPbBr_3$/carbon interface is very small, giving rise to a V_{oc} of up to 1.57 eV and a high PCE of 8.70%.[53] In another case, Shengzhong Frank Liu's group made efforts to optimize the morphology and crystallinity of $MAPbBr_3$ films via using anti-solvent treatment, achieving a PCE of 9.54%.[54] Overall, the research on $MAPbBr_3$-based PSCs is less than that on $MAPbI_3$ and $FAPbI_3$-based PSCs because of the low PCE of $MAPbBr_3$-based PSCs in comparison with its counterparts, which limits its further development in the photovoltaic field.

Apart from these pure $MAPbI_3$, $FAPbI_3$ and $MAPbBr_3$ perovskites, mixed MA^+ and FA^+

and mixed halide anions-based perovskites have drawn increasing attention because of the decent properties brought by the cooperation among different ions. Michael Grätzel's group first applied this concept into the PSC field and observed that the combination of MA^+ and FA^+ in the A position of the $APbI_3$ perovskite was capable of red-shifting the light absorption onset, thus contributing to significantly enhanced J_{sc} and superior devices to only MA^+-based counterparts.[55] In 2015, Sang Il Seok's group significantly enhanced the PSC photovoltaic performance via composition engineering, in which $FAPbI_3$ combined with $MAPbBr_3$ to form mixed MA^+ and FA^+ and mixed I^- and Br^--based perovskites as light absorbers. The incorporation $MAPbBr_3$ into $FAPbI_3$ not only stabilized the phase structure of $FAPbI_3$ but also improved the morphology of perovskite layers.[56] Since then, mixed organic cations and halide anions-based perovskites have become a popular research object for further boosting the performance of PSCs.

2.3.2 All-inorganic PSCs.

In the perovskite structure of ABX_3, if the A-site organic cations are completely replaced by an inorganic cation Cs^+, the formed perovskite is all-inorganic perovskites and the PSCs using these inorganic halide perovskites as light absorbing materials are all-inorganic PSCs. For B-site Pb-based inorganic halide perovskites ($CsPbX_3$), there are four main materials according to the X-site anions, namely, $CsPbI_3$, $CsPbI_2Br$, $CsPbIBr_2$ and $CsPbBr_3$.These four inorganic halide perovskites as photoactive materials in PSCs display their individual advantages and disadvantages.

$CsPbI_3$ with pure I^- occupying the X site shows the relatively narrow bandgap (1.73 eV) which is beneficial for light absorption. $CsPbI_3$-based PSCs hold the champion PCE among the above-mentioned four inorganic halide perovskites-based solar cells. Additionally, this bandgap enables $CsPbI_3$ with great potential to function as top cells in silicon solar cells -based tandem devices. However, $CsPbI_3$ suffers from severer stability in its phase structure because the small size of Cs^+ conduces the unideal tolerance factor, which destabilizes the phase structure. To be specific, the α-$CsPbI_3$ perovskite structure which is valid for light absorbers in solar cells easily converts to a non-photoactive phase (δ-$CsPbI_3$) with large bandgap of 2.82

eV at room temperature and the α-$CsPbI_3$ perovskite structure is only stable at high temperatures over 330 °C.[57, 58] The problem of phase structure instability hurdles the development of $CsPbI_3$-based PSCs, so it is imperative to resolve this issue.

$CsPbI_3$-based PSCs was first reported by Snaith's group in 2015. They fabricated planar junction devices using $CsPbI_3$ as light absorbers, achieving 2.9% PCE and finding that this all-inorganic material shows long-range electron and hole transport. It was also confirmed that organic cations are not essential and all-inorganic lead triiodide perovskites have great potential for photovoltaic applications. In spite of low PCE achieved in this work, it paved the way for the development of thermally stable all-inorganic PSCs.[18] To improve the PCE of $CsPbI_3$-based PSCs, Luo et al. fabricated more efficient $CsPbI_3$-based PSCs via employing sequential solvent engineering to fabricate stable and high-quality $CsPbI_3$ films. Through a new phase-transition route processing at low temperature, the newly formed intermediate Cs_4PbI_6 played a vital role in producing stable α-$CsPbI_3$ at room temperature, which afforded the PSCs a PCE of 4.13%.[59] After that, phase-stable and efficient $CsPbI_3$ quantum dots (QD)-based solar cells with a PCE of 10.77% were fabricated, in which $CsPbI_3$ QD films displayed excellent phase stability for months in ambient air.[60] In another work, stable two-dimensional (2D) ethylenediamine cations (EDA^{2+})-based halide perovskite material ($EDAPbI_4$) was introduced into $CsPbI_3$ films with the purpose of stabilizing the phase structure of α-$CsPbI_3$ at room temperature. The terminal NH_3^+ groups in EDA^{2+} was capable of cross-linking the $CsPbI_3$ perovskite crystal units, thus inhabiting then to transform to unwanted phase structure. In addition to the obviously enhanced stability, the modification of $EDAPbI_4$ improved the PCE of $CsPbI_3$-based PSCs to 11.8% with high reproducibility.[61]

Inspired by all these previous works, more and more researchers have paid great attention to $CsPbI_3$-based PSCs and devoted themselves to fabricating highly efficient all-inorganic PSCs with superior stability against water, heat and light. Until the year of 2019, $CsPbI_3$-based PSCs achieved the PCE of up to 18%. Noteworthy that such a high PCE was not yielded by the commonly researched α-$CsPbI_3$-based solar cells but β-$CsPbI_3$-based solar cells. Different from α-$CsPbI_3$ with cubic crystal structure, β-$CsPbI_3$ with tetragonal crystal structure has been theoretically predicted to have a more stable perovskite structure at lower temperatures.

However, experiments have demonstrated that it is hard to obtain high-quality and stable β-$CsPbI_3$ perovskite films for PSCs. Yixin Zhao's group first fabricated high-quality β-$CsPbI_3$ films with the assistance of dimethylammonium iodide and achieved 15.5% of PCE in the planar PSC. The low V_{oc} of 1.05 V and FF of 0.72 limited the improvement of PCE. To further enhance the PCE of β-$CsPbI_3$-based PSCs, this group passivated the perovskite film surface via choline iodine (CHI), which had been also utilized for hybrid perovskite film passivation. As a consequence, the corresponding PCE was boosted to 18.4% with dramatically improved V_{oc} to 1.11 V and FF to 0.82.[62] This significant scientific achievement actually opens a new window for the application of $CsPbI_3$ in solar cells and encouraged researchers to explore more possibilities for the development of PSC technology.

In terms of $CsPbI_2Br$, its bandgap (~ 1.91 eV) is a little bit larger than that of $CsPbI_3$ due to the appearance of Br^- in the X site. But the phase stability of $CsPbI_2Br$ is better than that of $CsPbI_3$, thus attracting ever-increasing attention to develop high-performance all-inorganic $CsPbIBr_2$-based PSCs. Nicholas et al. found that $CsPbI_2Br$ can keep stable photoactive cubic phase structure even in low temperatures.[63] The first reported of $CsPbI_2Br$-based PSCs was in 2016, in which Snaith's group found the great potential of $CsPbI_2Br$ to function as a valid light-absorbing material in solar cells. 9.8% PCE with over 5% stabilized PCE was achieved in this report.[64] Then, the PCE of solution-processing based $CsPbI_2Br$ PSCs reached 10% via potassium incorporation.[65] And the co-evaporation technique was used to fabricate high-quality $CsPbI_2Br$ films, leading to 11.8% PCE in the corresponding PSCs.[66] All the reported $CsPbI_2Br$ needed to be annealed in a high temperature ((>250 °C), which limited their utilization in some tandem solar cells with sensitive underlying layers to heat and in flexible solar cells with the low tolerance of substrates to high temperatures. In pursuit of more widespread application of $CsPbI_2Br$ in various devices, it is very important to prepare high-quality $CsPbIBr_2$ films at relatively low temperatures. Lau et al. compared low-temperature-annealed $CsPbI_2Br$ (at 100 °C) and high-temperature-annealed $CsPbI_2Br$ films and their corresponding PSCs, finding that both temperatures formed well orientated cubic perovskite crystals along (100) direction. But low-temperature annealed $CsPbI_2Br$ films displayed smaller grain size (200-500 nm) than high-temperature annealed $CsPbI_2Br$ films (1-2 um). And the low-temperature-annealed $CsPbI_2Br$-based PSCs yielded higher PCE than the high-temperature-annealed counterparts. Further through doping strontium, the low-temperature-annealed $CsPbI_2Br$-based PSCs obtained 10.7% PCE.[67] Afterwards, the PCE of $CsPbI_2Br$-based PSCs was further improved via a series of strategies including controlling crystal morphology, passivating grain boundaries, optimizing device structure and implementing interface engineering.[68-71 72]

In addition to $CsPbI_2Br$, another mixed halide all-inorganic perovskite that has gained some attention and been applied in solar cells is Br-rich $CsPbIBr_2$. In comparison with $CsPbI_3$ and $CsPbI_2Br$, $CsPbIBr_2$ possesses a larger bandgap (~ 2.05 eV) and better phase-structure stability as well as the higher resistance to heat and water. Similar to the above-mentioned materials, $CsPbIBr_2$ with a particular bright-red color is also suitable for tandem solar cells. The first report of $CsPbIBr_2$ was a HTL-free PSC with $CsPbIBr_2$ fabricated via dual source thermal evaporation, but only 4.7% PCE was achieved.[73] In another work at the same time, a $CsPbIBr_2$ film was prepared via a spray-assisted solution-processed method in which the $PbBr_2$ film was first deposited via spin-coating the solution, followed by spraying CsI on the $PbBr_2$ substrate in air. With optimizing the annealing temperature and time, $CsPbIBr_2$ annealed at 300 °C for 10 min-based PSCs produced the highest PCE of 6.3% with negligible hysteresis and highly thermal stability.[74] In spite of the relatively low PCE obtained in the initial study on $CsPbIBr_2$-based PSCs, these studies bring researchers hope that this type of all-inorganic can become alternatives to organic metal halide perovskites for PSC applications. After that, inverted-structure $CsPbIBr_2$-based PSCs with the configuration of FTO/NiO_x/$CsPbIBr_2$/MoO_x/Au was fabricated, yielding only 1.3% PCE. This low PCE was improved to 5.52% via inserting an ultra-thin MoO_x layer between $CsPbIBr_2$ film and Au electrodes. The enhanced PCE was mainly ascribed to the reduced Schottky barrier, the defects and the contact resistance by the insertion of MoO_x layer.[75] The main reason for the low PCE of $CsPbIBr_2$-based PSCs is the poor perovskite film quality because of the trouble of preparing high-quality $CsPbIBr_2$ films. In terms of the commonly used solution-based spin-coating method to prepare $CsPbIBr_2$ films, there are always a large number of pinholes appearing on the surface of the film, which would generate a risk on shutting paths. In addition, by this way, the grain size is small with a lot of grains, which would hinder charge carrier diffusion and cause severer charge recombination. To improve the quality of $CsPbIBr_2$ films, a facile intermolecular exchange strategy was proposed, in which an optimized methanol solution of CsI was utilized to post-treat the $CsPbIBr_2$ film fabricated via one-step spin-coating technique. Benefiting from this method, the pure-phase $CsPbIBr_2$ films with full coverage, large grain size (≈0.65 μm), fewer grain boundaries were produced, contributing to a PCE of 9.15% and decent stability against heat and humidity in PSCs.[76] Some other optimization of the fabrication process, such as the light processing technology, aging the precursor solution, using antisolvent treatment as well as preheating the substrates have also been performed for high-quality $CsPbIBr_2$ films and highly-efficient $CsPbIBr_2$-based PSCs.[77-80]

In addition to optimizing the fabrication technique, the $CsPbIBr_2$ film quality has been improved via introducing extraneous ions such as Mn^{2+}, Li^{+} and Cu^{2+}. A small amount of Mn^{2+}, Li^{+} and Cu^{2+} incorporation not only helped to reduce voids appearing in the pristine $CsPbIBr_2$ films but also obviously increased the grain size, increased crystallinity and reduced surface roughness, which reduced defects and thus suppressed charge recombination and enhanced device performance.[81-83] Furthermore, modifying the underlying surface also provided possibilities for the improvement of $CsPbIBr_2$ film quality. For example, NH_4Cl introduced into ZnO assisted in tuning the surface morphology of $CsPbIBr_2$ films.[84] In another case, modifying the TiO_2 surface via $SmBr_3$ improved the crystallinity and morphology of $CsPbIbr_2$ perovskite films.85 Recently, the pure $CsPbIBr_2$-based PSCs have achieved 11.04% PCE via utilizing an ultra-thin MgO layer to modify the interface between SnO_2 ETL and $CsPbIBr_2$ perovskite layer. The modification of ultrathin MgO layer not only accelerated the electron transport and blocked holes because of the optimized energy level alignment but also optimized the perovskite growth, reduced defects and suppressed the appearance of undesirable δ-phase.[86] Despite that a lot of endeavors have been devoted to improving the PCE of $CsPbIBr_2$-based PSCs, it still lags behind the PCE of $MAPbI_3$, $CsPbI_3$ and $CsPbI_2Br$-based PSCs. Therefore, it is necessary to further improve the performance of $CsPbI_2Br$-based PSCs for the achievement of further development of them in photovoltaic field.

If the X-site of $CsPbX_3$ is completely occupied by Br^-, this all-inorganic halide perovskite is $CsPbBr_3$. Among all the four mentioned all-inorganic perovskites, $CsPbBr_3$ shows the best phase stability and best tolerance to temperature and humidity. Particularly, due to its high stability, $CsPbBr_3$ films can be fabricated in ambient atmosphere, avoiding the usage of glove box. However, the biggest disadvantage of $CsPbBr_3$ serving as light absorber in solar cells is its too wide bandgap (~ 2.3 eV), which greatly limits the light absorption, thereby generating low photocurrent density in solar cells. In 2015, Kulbak et al. studied $CsPbBr_3$-based PSCs and compared with $MAPbBr_3$, confirming that the organic cation is not necessary for photovoltaic applications as the all-inorganic version $CsPbBr_3$ works equally well as the organic one, especially in terms of generating large V_{oc}. In this work, mesoporous-structured $CsPbBr_3$-based devices achieved a PCE of 5.95% with 1.28 V of V_{oc}, 6.24 mA cm^{-2} of J_{sc} and 0.74 of FF.[87] In the following work, they further investigated the long-term stability of $CsPbBr_3$-based PSCs. Compared with $MAPbBr_3$-based PSCs, all-inorganic perovskite $CsPbBr_3$-based PSCs were as efficient as but more stable than the $MAPbBr_3$-based counterparts.[88] The high thermal stability of $CsPbBr_3$-based PSCs was further evidenced via fabricating HTL-free PSCs and comparing with $MAPbI_3$-based ones. It was found that $CsPbBr_3$-based HTL-free PSCs remained over 85% of initial PCE while $MAPbI_3$-based HTL-free counterparts lost above 60% of initial PCE after storing for 250 h at 80 °C.[89] Numerous efforts have been made to improve the PCE of $CsPbIBr_2$-based PSCs. For example, incorporating of alkali metal cations for A site and lanthanide cation for the replacement of Pb^{2+} have been carried out to further enhance the performance of $CsPbIBr_2$-based PSCs.[90-92] Sm-doped $CsPbBr_3$ serving as light absorber contributed to a high PCE of 10.1% PCE.[91] Overall, the superior stability of $CsPbBr_3$ enabled this material to become a promising light-absorbing material for PSCs, but the PCE achieved by the corresponding PSCs is not comparable with that of organic-inorganic hybrid perovskites and $CsPbI_3$-based solar cells. Therefore, the PCE of $CsPbBr_3$-based PSCs should continue to be improved for their further development in the photovoltaic fields.

2.3.3 Ruddlesden-Popper (RP) PSCs

Another type of PSCs is RP PSCs which use RP-type halide perovskites with the chemical formula of $L_2A_{n-1}B_nX_{3n+1}$ as light-absorbing materials. Structurally, L represents a large aliphatic or aromatic alkylammonium cation such as 2-phenylethylammonium (PEA^+) and n-butylammonium ($n\text{-}BA^+$) as space cations. The 2D perovskite crystal is natural multiple-quantum-well structures in which n layers of $[BX_6]^{4-}$ octahedral inorganic sheets are sandwiched by two layers of large organic spacer cations. To be specific, the inorganic slabs function as the potential "wells", while the large organic spacers act as the "barriers" due to their hydrophobic nature, which protects the perovskite from being damaged by water and some other environmental factors.[93] The hydrophobicity of RP halide perovskites is mainly derived from its unique layered structure, especially the hydrophobic space organic cations. Furthermore, the large aliphatic or aromatic alkylammonium spacer cation can also protect the vulnerable B-site cations like Sn^{2+} from being oxidized to Sn^{4+}, providing a feasible avenue to fabricate efficient and stable Sn-based PSCs. From another perspective, RP halide perovskites possess high formation energy since the hydrophobic organic space cations connect with their adjacent layers via strong van der Waals forces, leading to superior ambient stability of RP halide perovskites.[94] Additionally, ion migration that easily occurs in 3D counterparts and has been considered to accelerate the disintegration of 3D organic-inorganic halide perovskites can be suppressed in RP perovskites, blocking the occurrence of instability and the hysteretic behavior.26 What's more, the formed RP perovskites via introducing large space cations into the unstable perovskites also can stabilize the phase structure. Benefiting from these merits, RP halide perovskites are suitable for PSC applications and hopefully resolve the problem of stability that 3D PSCs are faced with.

In spite of the increased stability benefitting from the existence of the large space cations, the large space cations impose restrictions on charge carrier transportation if these introduced large organic cations in crystals do not align appropriately. In most cases, it has been demonstrated that RP perovskite crystals growing parallel to the substrates will hinder the charge transport in perpendicular direction, causing severer charge recombination. Therefore, it is important to carefully manage the crystal growth orientation which is a governing factor influencing charge transport capability.[95]

In addition, it is very important to take the phase alignment into consideration for RP perovskite films as the synthesized RP perovskite films finally exist in the form of multiple phases in most situations rather than a phase-pure RP perovskite film. Generally speaking, there are four types of phase alignment in RP perovskite films. If those phases with different n values distribute irregularly and unevenly, this is random phase alignment, which is undesired as it has an adverse effect on the optoelectronic properties of RP perovskite films. According to the distribution location of small and large n phases, the phase distribution contains two types.[95] The normal-graded phase distribution refers to that large n phases are located at the surface while small n phases distribute at the bottom. The opposite order with small n phases at the surface and large n phases at the bottom is the reverse-graded phase distribution. Both graded phase distributions endow the type-II band alignment, which is beneficial to the self-driven charge carrier separation.[96, 97] Generally, both the CBM and VBM of RP perovskites increase with a decrease in the n value.[98] Accordingly, electrons generated from small n phases can spontaneously inject into large n phases and holes generated from large n phases can spontaneously hop into small n phases. This property makes these two-distribution type suitable for different device configurations. The normal-graded phase distribution is more appropriate for inverted (p-i-n) planar PSCs while the reverse-graded phase distribution is applicable to n-i-p planar PSCs. Furthermore, the reverse-graded phase distribution confers the RP perovskite films better moisture stability as the smaller n phases at the surface can function as a stable barrier to protect vulnerable large n phases at the bottom from water.[96, 97, 99] Although graded-vertical phase distribution models are approved of being able to promote the charge carrier transport by many researchers, there are some controversial views. The graded distribution of quasi-2D RP phases with the small n phases at the bottom of the film has been considered to obstruct the charge transport in the interlayer and have a negative effect on the device performance. Thus, the homogenous phase distribution in the whole RP perovskite film is expected. In this model, the prominent large n-based RP phase homogeneously distributes rather than concentrating the distribution in the top or bottom.[100]

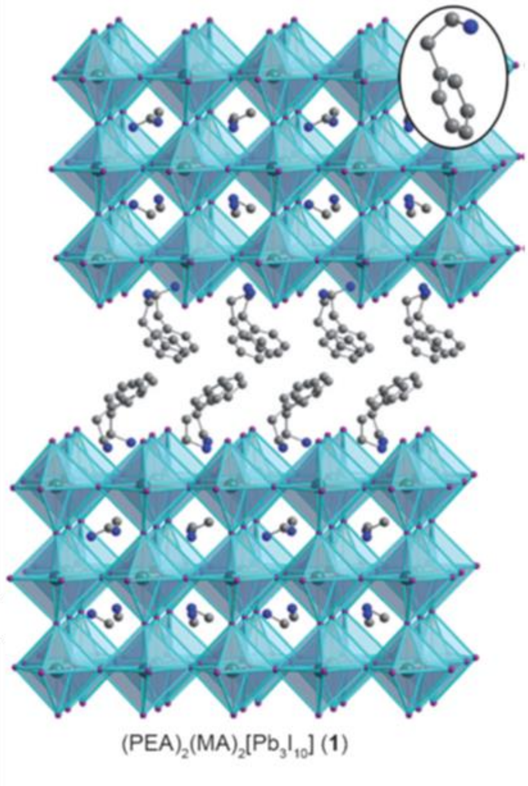

Figure 2.3 Crystal structure of $(PEA)_2(MA)_2Pb_3I_{10}$ RP perovskite. (Reproduced with permission. Copyright 2014, John Wiley and Sons)

As for RP PSCs, one type is to utilize RP halide perovskites directly as light absorbing materials in solar cells. n-BA and PEA RP perovskites-based solar cells have gained the most attention. RP PSC was first reported in 2014 by Smith et al. who employed layered perovskite $(PEA)_2(MA)_2Pb_3I_{10}$ (**Figure 2.3**) as an absorber in a solar cell and achieved 4.73% PCE. It was surprisingly to find that this layered perovskite as light absorber exhibited better resistance to moisture than 3D $MAPbI_3$ perovskites.[101] Motivated by this work, 2D RP perovskite n-$BA_2(MA)_{n-1}Pb_nI_{3n+1}$ was systematically studied in 2015 and discovered to be able to act as the light absorbers to fabricate solar cells. n-$BA_2(MA)_2Pb_3I_{10}$ based solar cells yielded 4.02% PCE [98]. In the initial stage of development of low-dimensional RP PSCs, the obtained PCE was relatively low and unsatisfactory due to the unoptimized preparation technique which normally did not produce high-quality RP perovskite film quality with preferential crystal growth orientation. Until 2016, the PCE of RP PSCs was boosted to 12.51% by adopting hot-casting method to fabricate $(BA)_2(MA)_3Pb_4I_{13}$ (n = 4) films. Through this way,

$(BA)_2(MA)_3Pb_4I_{13}$ thin films of near-single-crystalline quality with preferentially perpendicular inorganic perovskite component, which significantly promoted the charges transport and reduced recombination and giving rise to high-performance photovoltaic devices.[102]

In addition to BA and PEA-based RP perovskites utilized in solar cells, many new large organic ammonium ions have been synthesized and tried to be inserted into $MAPbI_3$ perovskites as space cations to form novel low-dimensional RP halide perovskite and be applied in solar cells. Note that when selecting the organic space cations in RP halide perovskites, the functional groups in these cations should be taken into consideration as these functional groups can usually exert a profound influence on the photoelectrical properties control and the film quality management of RP halide perovskites. For example, the fluorine-substituted PEA^+, 4-fluorophenylethylammonium ($4FPEA^+$),[103] pentafluorophenylethylammonium (FEA^+),[104] S-bearing thiophene-2-ethylamine (TEA),[105] 2-thiophenemethylammonium (ThMA),[106] 2-(methylthio)ethylamine (MTEA)]107] and N-involving 4-(aminoethyl)pyridine (4-AEP),[108] cyclohexane-based cyclohexane methylamine (CMA)[109] as well as multiple-ring-based 1-naphthalenemethylammonium (NpMA) and 9-anthracenemethylammonium (AnMA)[110] have been reported as novel space cations to produce new RP halide perovskites for high-performance solar cells.

Besides, there is another research field of RP PSCs-mixed 2D-3D PSCs, in which the large organic ammonium halides are introduced into the 3D halide perovskite system and then the formed perovskite films are composed of both 3D perovskites and 2D perovskites. From the perspective of structure, mixed 2D-3D PSCs can fall into three categories, namely, bulk heterojunction, planar heterojunction and graded heterojunction. Bulk heterojunction 2D-3D PSCs mainly refer to that 2D perovskites is embed between 3D perovskite grains to form hybrid 2D and 3D perovskites as photo absorbers. As aforementioned, when synthesizing $L_2A_{n-1}B_nX_{3n+1}$ RP-type perovskites, different n value-based phases including 3D phase co-exist. If these phases align randomly, this can be considered as the bulk heterojunction 2D-3D structure. In this section, we mainly focus on rationally designed bulk heterojunction 2D-3D PSCs, in which 3D perovskites play a dominant role in absorbing sunlight while 2D perovskites modify grain boundaries of 3D perovskites. In terms of planar heterojunction, a 2D perovskite layer forms on the top or bottom of the 3D perovskite layer. In comparison, there is a transition area between 2D perovskite layer and 3D perovskite layer in the graded heterojunction structure. In the transition area, 2D and 3D perovskites co-exist. No matter which structure, the 3D perovskites function as the main light absorbing material while the 2D perovskite play an important role in protecting the sensitive 3D perovskites from water and some other environment factors.

The representative of the bulk heterojunction 2D-3D PSCs is 2D-3D hetero-structured BA-Cs-FA lead halide perovskites obtained via incorporating BA^+ into $FA_{0.83}Cs_{0.17}Pb(I_yBr_{1-y})_3$ 3D perovskite. The formed RP-type 2D perovskite platelets intersperse between highly orientated 3D perovskite grains, which not only enhances crystallinity but also reduces defects via passivating grain boundaries. This contributes to improved efficiency and reduced hysteresis as well as enhanced moisture stability. The final performance is dependent on the amount of the introduced BA^+.[111] Leonardo R. V. Buizza et. al have systematically studied the impact of BA^+ on the properties of $BA_x(FA_{0.83}Cs_{0.17})_{1-x}Pb(I_{0.6}Br_{0.4})_3$. It was concluded that small amounts of BA^+ introduction can enhance charge-carrier mobilities and reduce trap-mediated charge-carrier recombination, which contributes to longer charge-carrier diffusion lengths, while excessive BA^+ introduction amount induced poor crystallization and inhomogeneous film formation.[112] This example enlightens that the relative amount of 2D and perovskites should be elaborately controlled and regulated for better device performance.

In the planar heterojunction 2D-3D PSC field, this design philosophy originates from 2006 when Hu et. al fabricated a perovskite/perovskite heterojunction solar cell. The method is similar to that of fabricating the bulk heterojunction structure via solution-based large alkylammonium cation infiltration process. What different is that the formed 2D perovskites tend to cap on the top of 3D perovskites in the form of a thin layer rather than local modification like passivating grain boundaries of 3D perovskite crystals. This 2D-3D planar heterojunction structure-based PSCs produced a PCE of 16.84% with increased V_{oc}. However, J_{sc} slightly decreased, which is attributed to the organic interlayer alignment orientation (perpendicular to the charge transport orientation) and the increased thickness of perovskite layer.[113] Generally speaking, the RP perovskites with hydrophobic property on top of 3D perovskites can function as a water-proofer to protect 3D perovskites from water invasion. And if the introduced organic ammonium halides contains some special functional groups, such as n-propylammonium iodide which possesses carboxyl groups, it is also possible to obstruct oxygen penetration and significantly enhance device stability.[114] As regards the fabrication method, in addition to this direct way of introducing alkylammonium salts into 3D perovskite precursor, a 2D perovskite capping layer can in-situ grow on top of 3D perovskite films via spin-coating large organic halides, immersing 3D perovskites in organic halide solutions and space organic halide vapor treatment.[104, 115, 116] For example, spin-coating a PEAI solution upon the 3D perovskite film can form a PEA_2PbI_4 layer covering on the top of this 3D perovskite film. PEAI reacts with the excess PbI_2 in the 3D perovskite film, leading to the formation of PEA_2PbI_4. This rationally designed 2D-3D structure in n-i-p devices gives rise to high efficiency (18.51%), decent humid stability (remaining 90% of its initial PCE after 1000 h under humid environment).[115] Noteworthy that the PEAI treatment do not always create a 2D perovskite protective layer as sometimes an amorphous PEA-PbI_2 covering layer may form rather than PEAI slat state itself or 2D perovskites. Fortunately, such an amorphous layer also passivated the perovskite surface, reducing trap density and suppressing non-radiative recombination.[117] Compared with the post-treatment of alkylammonium halides, a more effective way is the post-treatment of large organic molecules. The former way is more likely to form various n value RP-perovskites with different thickness, while the later way can create pure n=1 RP-type perovskite on top of 3D perovskites. When using BA and BAI to treat $MAPbI_3$ film, they react with $MAPbI_3$ according to $2BA + MAI + MAPbI_3 \rightarrow (BA)_2PbI_4 + 2MA\uparrow$ and $2BAI + nMAPbI_3 \leftrightarrow (BA)_2(MA)_{n+1}PbnI_{3n+1} + MAI$, respectively. The pure $(BA)_2PbI_4$ phase brings about better surface and grain boundary modification, thus leading to a higher efficiency in solar cells.[118]

As for the 2D-3D graded heterojunction structure, an ultra-stable PSC has been fabricated via this dimensional engineering. In the ultra-stable 2D-3D $(HOOC(CH_2)_4NH_3)_2PbI_4$-$MAPbI_3$ junction perovskite solar cell, a graded heterojunction interface forms, where the individual 2D and 3D phases are retained. This 2D/3D interface also serves as a template to control the growth of 3D $MAPbI_3$ phases and stabilize a novel oriented $MAPbI_3$ at this interface. Applying this junction structure in a large-scale printable HTL-free solar cell, 11.2% efficiency with > 10000 h stability was delivered.[119] Afterwards, a more efficient PSC via the graded 2D-3D halide perovskite interface appeared. Different from the last example in which alkylammonium salts are directly introduced into the pristine perovskite precursor, the alkylammonium salt is introduced via the anti-solvent. Through this route, a 3D-2D graded interface is obtained, which not only improves the interface energy level to reduce charge recombination but also passivates grain boundaries to suppress ion migration. In the NiO_x based p-i-n device, this in-situ-formed graded 3D-2D interface achieved not only the high efficiency (19.89%), good moisture stability but also the improved thermal stability.[120]

2.3.4 Dion–Jacobson (DJ) PSCs

Dion–Jacobson (DJ) type halide perovskites with the chemical formula of $L'A_{n-1}B_nX_{3n+1}$ is another type of low-dimensional perovskite and have also attracted intensive attention due to their decent optoelectronic properties. In contrast to RP halide perovskites with two sheets of univalent space cations between layers, L' represents a divalent organic space cation and there is only one sheet of this divalent space cation between layers in DJ halide perovskites.[121, 122] The crystal structure of DJ and RP perovskites is shown in **Figure 2.4**. Structurally, DJ perovskites are more stable but less flexible than RP perovskites because replacing two univalent cations by one divalent cation results in the disappearance of the van der Waals gap, making the adjacent inorganic layers linked closer. In addition, two hydrogen bonds formed at both ends of the divalent cation strengthen the layered structure, further improving the stability of DJ perovskites.[95, 123-125]

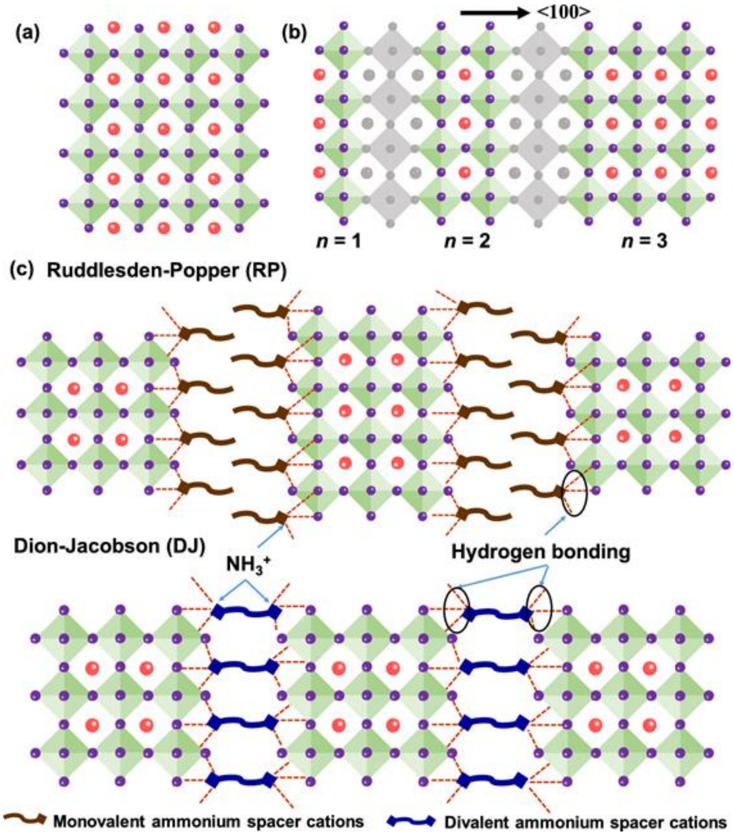

Figure 2.4 (a) Crystal structure of a 3D perovskite, (b) structure diagram showing the position of space cations and (c) crystal structures of RP and DJ layered perovskites (n = 3).[126] (Reproduced with permission. Copyright 2019, American Chemical Society)

DJ phases are a new type of halide perovskites with few studies. The application of DJ halide perovskites in solar cells started from 2016. But at that time only n=1-based DJ halide perovskites were utilized as light absorbers and the efficiency of devices was very low (< 2%).[127,128] Afterwards, a variety of 3-(aminomethyl)piperidinium (3AMP) or 4-(aminomethyl)piperidinium (4AMP)-based $A'MA_{n-1}Pb_nI_{3n+1}$ DJ perovskites were synthesized and their optical properties were studied. PSCs using $(3AMP)(MA)_3Pb_4I_{13}$ as light absorbers delivered a PCE of 7.32%.[124] In addition to MA-based DJ halide perovskites, researchers also paid attention to FA-based halide perovskites. Using 1,4-phenylenedimethanammonium (PDMA) as a space cation-based, $(PDMA)\text{-}FA_2Pb_3I_{10}$ was first studied and the corresponding solar cell achieved a PCE exceeding 7% with excellent moisture stability, which opens a new avenue to develop highly stable PSCs.[123]

Similar to RP halide perovskites, the photoelectronic properties of DJ halide perovskites are closely related to the type of the space cation and the n value. Based on this, various novel space cation-based DJ halide perovskites have been tried to be used as light absorbers and their photovoltaic performance can be further improved via changing the n value.[125, 129-133] For example, $(PDA)(MA)_3Pb_4I_{13}$-based device produced a PCE of 13.3%, which was higher than n = 2 (9.10%) and n = 1 (1.27%) based counterparts.[125] In another study, a n=10 1,4-benzenedimethanamonium iodide (BzDA)-based DJ halide perovskite $(BzDA)A_9Pb_{10}(I_{0.93}Br_{0.07})_{31}$) was reported. Such a PSC delivered a high PCE of 15.6%.[130] Additionally, some other commonly adopted strategies as the A-site cation-based composition engineering, additive engineering and combining with typical 3D halide perovskite to build mixed 2D-3D PSCs are also implemental for improving the photovoltaic performance of DJ PSCs.[134-137]

2.3.5 Charge dynamics of lead halide perovskites

Many reports have presented that lead halide perovskites show low exciton binding energy which is normally lower than the thermal activation energy. The kinetics of the carrier concentration photo-generated in perovskite films is determined by various charge recombination process, including the first-order trap state mediated charge recombination, the second-order non-geminate free carrier recombination, and the three body Auger recombination.[138] In case of low exciton densities (($<10^{15}$ cm^{-3})), monomolecular trap-mediated and first-order geminate recombination is the main charge dynamic process, in which monomolecular trap-mediated recombination is dominant.[139] The second-order non-geminate recombination and the third-order Auger recombination will become major when the exciton densities are higher than $>10^{15}$ cm^{-3}.[138] In addition to the charge dynamics at the low excited states near the band edge, it is meaningful to pay attention to hot charge dynamics because it provides a feasible way for PSCs to break Shockley–Queisser limit on efficiency of ~30% via effectively harvesting charge carriers. Carriers can substantially reabsorb optical photons, which is called hot-phonon bottleneck.[140] The hot-phonon bottleneck will decelerate the cooling rate of hot charges in lead halide perovskites, which is more obvious in organic-inorganic hybrid halide perovskites than all-inorganic halide perovskites. Hot charges also have long diffusion length in perovskites, which can reach ~230 nm.[141]

In spite of the large tolerance of trap states that lead halide perovskites exhibit, the existence of shallow traps has an adverse effect on charge transport, which will impede the charge mobility and weaken the photovoltaic performance of PSCs.[138] Noteworthy that polycrystalline perovskite films show higher trap state than sing-crystal perovskite films. Thus, single-crystal perovskite films have better charge transport properties than polycrystalline counterparts.[142] For working PSCs, many factors affect the trap states and charge transport properties. It has been found that the trap states in perovskite films are dynamically changing. The continuous light illumination process can help to fill trap states, explaining why the PCE of PSCs can be improved under light soaking.[143] In addition, the phase transition also influences the charge dynamics. The mobilities of holes and electrons vary with the perovskite ($MAPbI_3$) phase changing from tetragonal to cubic crystalline structures.[143] In another case, α-phase $FAPbI_3$ was found to show larger charge mobility yet fewer defect densities than δ-phase $FAPbI_3$. That's why δ-phase $FAPbI_3$ PSCs delivered higher photovoltaic performance.[144]

Compared with 3D lead halide perovskites, the charge dynamics of low-dimensional RP halide perovskites show some differences. In terms of the exciton binding energy, it is higher (above 150 meV) for RP halide perovskites than 3D analogs (only 13-16 meV).[145, 146] The charge carrier can achieve intrinsic separation in RP perovskite, which can promote the carrier extraction. The existence of middle gap energy states at the surface of RP perovskite can help to dissociate the strongly bound excitons to free carriers.[147] On the other hand, these edge states will trap free charges but this process is believed to be beneficial for the performance of RP PSCs because the trapped charges will be protected from losing their energy via nonradiative processes.[146]

2.3.6 Crystallization dynamics for lead halide perovskites

No matter which types of halide perovskites serve as light absorbers, the film morphology and microstructure have significant influence on the photoelectronic properties of perovskite films and play a vital role in determining the eventual photovoltaic performance of PSCs. Thus, it is important to pay attention to the crystallization dynamics and gain a better understanding of the formation process of perovskite films.

The crystallization dynamics of perovskite films is closely related to the fabrication methods. Solution-based one-step spin-coating method is commonly utilized to fabricate perovskite films. As for this method, when dropping perovskite precursor solution on the substrate, the spin-coating process makes excess precursor solution leave from the substrate and the solvents will evaporate from the precursor left on the substrates to a solid or intermediate film. Subsequently, a thermal annealing process is often needed to completely crystallize perovskite films.[148] During the spin-coating process, the rapid and uneven crystallization process will occur because of the ununiform evaporation rate of solvents at different positions, which will result in heterogenous nucleation and unfavorable film quality.[54] Many factors including the solvent types, precursor chemical composition, the surface properties of underlying layer, the post-annealing conditions and general spin coating parameters will affect the crystallization process. To obtain perovskite films of high quality with large grains size and full coverage, it is significant to manage the interaction among these factors.[149]

Apart from one-step spin-coating technique, two-step sequential deposition method has been also employed to prepare halide perovskite films. As for the typical two-step sequential deposition method, a PbI_2 film is first fabricated via spin-coating method or thermal evaporation method. Then, the substrate with PbI_2 film is dipped into the MAI or FAI solution for some time to get perovskite films.[150, 151] Afterwards, the typical solid-liquid reaction was changed to solid-solid and solid-vapor reaction. For the solid-solid one, a MAI/FAI layer was deposited on top of PbI_2 layer via spin-coating the corresponding solution. Then, the perovskite film is formed via the reaction between PbI_2 layer and MA/FAI layer after thermal annealing.[152] When using this method to fabricate $FAPbI_3$ perovskite film, it was found that the crystallization of $FAPbI_3$ initiates during the process of spin-coating of the FAI precursor by an inter-diffusion manner. For the solid-vapor two-step one, MAI/FAI vapor is utilized to treat the formed PbI_2 layer at an elevated temperature to form the solid perovskite film.[153] It is critical to control the reaction kinetics between PbI_2 and MAI/FAI as well as manage the perovskite crystallization process in order to produce high-quality perovskite films via two-step sequential deposition method.[149] It has been presented that the final film quality of perovskites is closely related to the morphology of the deposited PbI_2 layer which can control the number of nuclei of perovskite. Generally, the nucleation rate is required to be inhibited and the growth rate is needed to be promoted to get larger size of crystals.[150]

For all-inorganic halide perovskite ($CsPbX_3$), the above-mentioned techniques are also applicative. Noteworthy that one-step spin-coating method cannot be directly utilized to fabricate $CsPbBr_3$ films due to the poor solubility of CsBr. Under this circumstance, two-step sequential deposition method and even multistep solution-processing method show a greater advantage. Using the typical two-step sequential deposition method to prepare $CsPbBr_3$ will cause the decomposition of the formed $CsPbBr_3$ film when directly dipping $PbBr_2$ into CsBr solution, thereby leading to poor film morphology.[154] To inhibit the decomposition of $CsPbBr_3$ in CsBr solution and better manage the crystallization process of $CsPbBr_3$, CsBr solution can be spin-coated onto $PbBr_2$ layer. The deposition cycle (n) of CsBr solution can determine the phase conversion process. $n \leq 3$ and $n \geq 5$ result in the formation of $CsPb_2Br_5$ and Cs_4PbBr_6, respectively. And $n = 4$ gives rise to the generation of desired $CsPbBr_3$.[155]

As for low-dimensional RP halide perovskites, the crystallization dynamics is more complicated compared with 3D counterparts. This is because it is difficult to obtain pure-phase RP halide perovskites with the formula of $L_2A_{n-1}B_nX_{3n+1}$. In most cases, the formed RP halide perovskite films are composed of many different n values-based phases. Both the phase composition and distribution significantly affect the optoelectronic properties of RP halide perovskite film and photovoltaic performance of devices. In this regard, I have written a review paper to discuss the crystallization dynamics of RP halide perovskite.[95]

2.4 The challenges of PSCs

2.4.1 Stability

In spite of the high efficiency that PSCs have achieved, the stability is the biggest obstacle that hurdles their commercialization process. The main reasons for instability of PSCs are that halide perovskites are sensitive to many environmental factors during the fabrication and testing processes, including water, O_2, temperature and light. Additionally, although all inorganic halide perovskites exhibit superior heat stability, some of them suffer from severer phase stability and environmental factors can even accelerate the phase transformation. Furthermore, other functional layers such as ETLs, HTLs and even electrodes in PSCs may be instable in some conditions, jointly leading to the degradation of the complete devices. Thus, it is important to analyse the decomposition process of halide perovskites as well as the function of other functional layers during the degradation process, which can provide some routes about how to improve the stability of PSCs.

As for $MAPbI_3$, when exposed to water and oxygen atmosphere, it has been proposed to decompose according to the following series of reaction:[156, 157]

$MAPbI_3\ (s) \leftrightarrow PbI_2\ (s) + MAI\ (aq)$

$MAI\ (aq) \leftrightarrow MA\ (aq) + HI$

$4HI\ (aq) + O_2\ (g) \leftrightarrow 2I_2\ (s) + 2H_2O\ (l)$

$2HI\ (aq) \leftrightarrow H_2\ (g) + I_2\ (s)$

Due to the induced degradation of organic-inorganic hybrid perovskites by water and O_2, they often need to be fabricated in a N_2 or Ar glove box in most cases to avoid detrimental influence of these factors. Water has been considered as the catalyst to lead to the irreversible degradation of the perovskite material. $MAPbI_3$ has been found to start to decompose at a humidity of 55%, under which dark brown of perovskites will change to yellow.[158] Generally, the $MAPbI_3$ with perovskite structure exhibits dark brown. If the color changes to light brown, that means the production of I_2. If the film color changes to light yellow, PbI_2 is produced.

In addition to the above decomposition mechanism, another decomposition pathway for $MAPbI_3$ under the exposure of water was also put forward. A water molecule as a Lewis acid could remove one proton from ammonium via combining with $MAPbI_3$. Then, an intermediate of $[(MA^+)_{n-1}(MA)PbI_3][H_3O^+]$ formed, which decomposed into HI, MA, and finally into PbI_2 by phase changes of hydrogen iodide (soluble in water) and MA. According to this decomposition mechanism, introducing aprotic organic ions, like tetramethylammonium,

$(CH_3)_4N^+$, has been considered as an effective way to stabilize the perovskite under the humid environment.[159] In another study, Christians et al. held the view that the formed $MA_4PbI_6.2H_2O$ in $MAPbI_3$ in the presence of water reduced the light absorption but did not have an influence on the charge carrier dynamics on a short time scale. In this case, the formation of the hydrate compound was regarded to be closely related to the relative strength of the hydrogen bonding interaction between either the MA^+ or H_2O with PbI_6. Based on this, the moisture stability of $MAPbI_3$ can be improved via strengthening the bound between the cation can lead halide.[160]

The instability of PSCs under the UV light is closely related to the TiO_2 ETLs because TiO_2 is a typical catalyst can catalyze for oxidizing water and some organic materials. Thus, when used in solar cells as electron transporting materials, it may catalyze the occurrence of some reactions under the light illumination.[161] Hitoshi and co-workers observed that the original $MAPbI_3$ layer decomposed into PbI_2 after light exposure for 12h. The related decomposition pathway under exposure of UV light is shown as below:

$2I^- \leftrightarrow I_2 + 2e^-$ [at the interface between TiO_2 and $MAPbI_3$]

$3MA^+ \leftrightarrow 3MA + 3H^+$

$I^- + I_2 + 3H^+ + 2e^- \leftrightarrow 3HI$

Accordingly, TiO_2 first extracted electrons from I^- and the structure of $MAPbI_3$ started to be deconstructed, resulting in the generation of I_2. In the second step, the continuous elimination of H^+ lead to the reaction forward. Finally, the extracted electrons at the interface between TiO_2 and perovskite layer could reduce the formed I_2, leading to the formation of HI. On this basis, the insertion of some other thin layer such as Sb_2S_3 which can deactivate the reaction of I^-/I_2 at the surface of TiO_2 can be implemented to improve the device stability under exposure of UV light.[162] Snaith and co-workers attributed to the poor UV-light stability of PSCs with TiO_2 as ETL to the existence of a large number of oxygen vacancies. Under UV light illumination, these empty vacancies will trap electrons from perovskite materials. These trapped immobile electrons will recombine with holes, leading to sever charge recombination and the degradation of PCE efficiency. Based on this view, it has been believed that the appearance of oxygen is beneficial for the improvement of UV-light stability as oxygen is able to occupy these empty vacancies appearing on TiO_2 surface. To avoid the appearance of oxygen vacancies, Al_2O_3 has been utilized to replace TiO_2 as a scaffold to support light absorbers, exhibiting a stable performance for a period of over 1000 h.[27] Alternatively, UV filters can be inserted in front of TiO_2 layer to prevent the TiO_2 from absorbing UV light so as to get rid of the bed influence of UV light on the PSC photovoltaic performance.[163] For example, a down-shifting Eu^{3+} doped YVO_4 can absorb UV light and emit visible light. By inserting this layer in front of TiO_2 layer, the devices showed significantly enhance stability under long-term illumination.[163] Besides, some materials like Sb_2S_3 can be inserted into the TiO_2/perovskite interface to protect the decomposition of perovskite via blocking the occurrence of TiO_2-based photocatalysis under UV light illumination.[162]

Apart from the above-mentioned moisture, O_2 and UV light induced instability of PSCs, heat is also an important aspect affecting the device stability, particularly for organic-inorganic PSCs. To some extent, thermal stability of PSCs should be paid more attention as thermal annealing is almost a necessary step during the process of fabricating a complete PSC device. In general, solution-processed perovskite films need to be annealed at a temperature in order to obtain the better film quality with increased crystallinity, reduced pinholes and full coverage. Thus, the annealing parameters including the temperatures and time should be carefully manipulated via researching the thermal stability behavior of perovskites. From the perspective of practical application of PSCs, continuous sunlight exposure will cause the elevated temperature during operation. Therefore, the thermal stability of PSCs is expected to be improved for the practical application.

On one hand, thermal stability of perovskite is closely related to the measurement conditions. The appearance of water and O_2 normally would reduce the resistance of perovskites to heat. In one case, it has been observed that $MAPbI_3$ even started to decompose at 85 ^{o}C at the ambient atmosphere. Under vacuum conditions, $MAPbI_3$ start to decompose at a higher temperature. For example, Philippe et al. found that $MAPbI_3$ started to decompose at 100 ^{o}C under ultra-high vacuum of $\sim10^{-8}$ mbar.[164] In another study, $MAPbI_3$ was found to show greater thermal stability at a pressure of $\sim10^{-5}$ mbar. Surprisingly, annealing at 200 ^{o}C caused the rapid decomposition of $MAPbI_3$ to PbI_2, while annealing at 150 ^{o}C induced recrystallization of $MAPbI_3$ which improved the perovskite film quality and reduced the structural defects. On the other hand, the thermal stability of perovskite layers is influenced by their underlying charge transporting layers. It has been reported that the ZnO as ETL materials accelerated the thermal decomposition of $MAPbI_3$ perovskite layer, which has been attributed to the deprotonation of the methylammonium cation caused by the surface hydroxyl groups appearing in ZnO films.[165]

In a complete PSC device, ETLs and HTLs may be also sensitive to high temperatures. Particularly, organic materials used in devices are more vulnerable to high temperatures compared with inorganic charge transporting materials. Taking the commonly used organic HTL material spiro-OMeTAD as an example, heating can improve the crystallization and oxidation of spiro-OMeTAD, which is beneficial for the improvement of current density via promoting the hole transfer and transport. However, heating will lead to the migration of doped Li-TFSI to and the evaporation of 4-tert-butylpyridine (tBP), which has an adverse effect on V_{oc} and FF and finally causes the degradation of device performance. Although the transition temperature of spiro-OMeTAD is around 150 °C, the PSC devices using it as a HTL material witnessed a great degradation of photovoltaic performance at relatively low 85 °C.[156, 166] To improve the thermal stability of PSCs, it is also necessary to seek for and utilize stable charge transporting materials showing high tolerance to high temperatures, except for enhancing the thermal stability of perovskite layers.

2.4.2 Hysteresis

Hysteresis a well-observed phenomenon of the different shapes of J-V curves varying with scan direction, range, and rate during the characterizations of PSCs. The biggest problem caused by the presence of hysteresis is that it makes it difficult to evaluate, characterize and reproduce PSCs in a repeatable manner. This is a tricky problem that urgently needs to be solved as the photovoltaic performance of PSCs should be accurately evaluated prior to developing into the next application step.

I have written a review to discuss about this issue in detail. In this review, the hysteresis issue was addressed by discussing its origin and influential factors, providing strategies of elimination and advice for future works. Although PSCs originated from DSSCs, the hysteretic behavior does not appear in DSSCs and it is a unique phenomenon for PSCs. Thus, a brief introduction of the structure and mechanism difference between PSCs and DSSCs was made before the survey of the main issue of hysteresis, which will serve to facilitate a better understanding for newcomers in the field.

To clarify the culprit of hysteresis in PSCs, it is very important to find out which factors can affect this phenomenon. In this review, a series of influential factors of the hysteresis phenomenon were explored. It has been found that the device structure, the materials utilized in PSCs including various functional layer materials, and the testing conditions all have an influence of the hysteresis phenomenon in PSCs.

The degree of hysteresis has been found to vary with the cell architecture in PSCs. In general, mesoporous PSCs exhibit a smaller hysteresis than do normal planar heterojunction ones when TiO_2 is applied as the ETL material. This observation can be attributed to the larger contact area between the mp-TiO_2 and perovskite material, leading to more efficient electron transfer and separation. The significance of the mesoporous ETL in relieving hysteresis is also reflected in SnO_2-based PSCs.[167] The more serious hysteresis occurring with the n-i-p structure of PSCs can be alleviated by just inverting the structure. For instance, the inverted planar PSCs, typically using PCBM or C60 as the ETL material and PEDOT:PSS or nickel oxide as the HTL material, showed reduced hysteresis compared with that of the TiO_2-based regular planar heterojunction structures.[168] Compared with m-TiO_2 PSCs, Al_2O_3-based meso-superstructured PSCs exhibited more serious hysteresis,[169] which proves again the importance of effective electron separation and transport as determined by m-TiO_2. Furthermore, in Al_2O_3-based meso-superstructured PSCs, the absence of the TiO_2 compact layer can magnify the hysteresis phenomenon.[168] All these findings suggest that the cell architecture should be carefully selected to eliminate hysteresis.

A complete PSC is composed of different functional materials that show different influences on the hysteresis in various ways. First, the light-absorbing perovskite material in PSCs can impact the hysteretic behavior. Both MA and FA at the A site of $APbX_3$ perovskites, as the photoactive material, seem to create lower hysteresis than $MAPbX_3$ in PSCs. Not only is the severity of the hysteresis different but the hysteresis type also shows a discrepancy. [170] Furthermore, for a specific perovskite, the crystal size of the perovskite has some influence on the hysteresis. The measured HI values for PSCs based on 440, 170, and 130 nm perovskite crystals are 0.087, 0.080, and 0.212, respectively, indicating a reduced hysteresis with increased perovskite crystal size.[15] As seen, the hysteresis of PSCs can be relieved by the application of the appropriate composition and perovskite crystal size. As for electron-transporting materials, the thickness of the mp-TiO_2 ETL layer influences the severity of the hysteresis. [15, 169]

In addition to the influence of mp-TiO_2, the hysteresis is also sensitive to the thickness of the prepared compact TiO_2 (c-TiO_2) layer. One typical example is that the variation of c-TiO_2 thickness alters the hysteresis from the inverted type to the normal type.[171] The interfaces of the perovskite/ETL, perovskite/HTL, and even the HTL/electrode are another critical factor that affects the hysteresis because the response to charge separation and accumulation at an interface can be remarkably influenced by the nature of the contact.[172-175] The role of interface contact in hysteretic behavior may reflect the importance of energy alignment between the perovskite and the extraction layers in PSCs.[176] Four types of PSCs with different selective contact layers have been investigated in the planar structure.[42] The normal planar structure with the TiO_2/$MAPbI_3$/spiro-OMeTAD configuration displays the largest J–V hysteresis, which could be reduced when PCBM replaces TiO_2 and this structure is inverted via displacing spiro-OMeTAD with NiO_x and PEDOT:PSS as HTL materials. Moreover, the modification of spiro-OMeTAD and different hole-transporting materials as well as the selection of electrodes can also lead to different hysteresis behaviors.[174, 176-178]

In addition to the effects of some internal factors, the external test conditions should also be taken into consideration when analyzing the hysteresis in PSCs, as the test conditions not only influence the degree of hysteresis but also determine the hysteresis type in some cases. Researchers have found that the hysteresis behavior in PSCs varies with the scan rate of the J–V test and the illumination intensity. In planar heterojunction PSCs, a lower scan rate increases the hysteresis in the range of 0.3–0.011 V s^{-1}.[169] On the other hand, the typical mp-TiO_2-based PSCs show the opposite trend, where the hysteresis becomes more pronounced at high scan rates but could vanish at sufficiently slow scan rates.[179] Moreover, the starting scan bias and the bias range have an impact on the hysteresis behavior.[42, 180] It seems that the photovoltaic efficiency undergoes a more dramatic decrease when the scan starts from a more negative bias voltage resulting in a pronounced hysteresis.[42] For the bias range, it has been verified that the hysteresis decreases with a slow sweep rate in a small scan range; however, this trend varies in a large scan range.[180] The hysteresis type is also sensitive to scan rates and the prepoling bias. Higher scan rates and a negative prepoling bias are prone to the inverted hysteresis and vice versa.[181, 182[

The voltage settling time can also change the hysteresis. It has been found that the hysteresis loops of mp-TiO_2-based PSCs measured with a 3000 ms settling time are smaller than those measured after a 200 ms settling time, while the opposite observation has been made for TiO_2-based planar heterojunction PSCs.[15] These results indicate that the photovoltaic current intensity of PSCs is relevant along with the voltage settling time and the cell structure. In addition, the hysteresis of PSCs also changes with the scan time. The inverted hysteresis of the mixed perovskite-based solar cells is not very evident with the initial scan but becomes more apparent with the scan time.[170] The change in hysteresis with these external test conditions might be related to multiple factors such as the electric field, electron diffusion, and cell structure, which are further interlinked to increase the complexity of the origin of hysteresis.

The precise origin of hysteresis behavior occurring in PSCs actually remain unclear but has been confirmed to be correlated with ion migration, the ferroelectric effect, and unbalanced charge carrier transport as well as trap-assisted charge recombination.

2.4.3 Lead toxicity

In addition to the abovementioned problems about stability and hysteresis, the utilization of Pb-based materials in highly promising PSCs has caused concerns about environmental pollution and human health. The potential hazard of lead toxicity on human health made the public reluctant to accept this new technology of PSCs, which impedes the commercialization of PSCs.

The content of lead in PSCs is low, only a few hundred milligrams per square meter of a solar device, which is below the content of lead that is produced by the coal industry for the generation of equal amount of electricity. However, noteworthy that the solubility of lead in water is very high, making it readily move through the biogeochemical cycle. Compared with cadmium telluride (CdTe) solar cells, the toxicity of Cd and Te also has potential threat to human health, which has stirred up extensive discussions at the beginning of this technology. However, CdTe is a chemically and thermally stable compound with a very low solubility, which reduced the harm of the toxicity of Cd and Te to an extremely low level. Thus, CdTe solar cells have been industrialized since the 1990s. Differently, Pb-containing perovskite materials widely used as light absorbers can easily decompose to Pb-based compounds and some environmental factors even can accelerate the decomposition process of perovskites as mentioned in last section. The intake of Pb-containing chemical can be achieved via three routes including gastrointestinal, respiratory and dermal uptake. The long-term and continuous Pb exposure will lead to the accumulation of lead in the body, which is a huge heath risk.[183,184]

Therefore, it is very imperative to replace Pb with other nontoxic elements to develop lead-free PSCs. It may be also optional to utilize effective additives to convert soluble lead-based compounds to insoluble ones upon destruction of a large perovskite solar power plant.185 Alternatively, it is very important to find ways to recycle PSCs to reduce lead waste and limit the release of lead into environment. Binek et al. have reported an environmentally-friendly and low-cost recycling technology for $MAPbI_3$-based PSCs, in which PSCs can be peeled off via a layer-by-layer method. The collected materials of every layers can be reused for PSC fabrication. And the re-fabricated devices did not lose too much of their initial PCE. This approach provides PSCs with one step closer to their commercialization.[186]

2.5 Strategies to promote the development of PSCs

2.5.1 Composition engineering

Some properties of 3D halide perovskites with the formula of ABX_3 can be flexibly tuned and improved via introducing some foreign ions into the structure, which has become a facile and effective way to resolve the tricky problems restricting the development of PSCs.[187-189] To select appropriate cation to dope into ABX_3 perovskite crystal lattice, tolerance factor (t) is an important parameter that should be taken into consideration, which can be defined according to the following equation:[190]

$$t = \frac{r_A + r_X}{\sqrt{2}(r_{B+}r_{X)}}$$

r_A, r_B and r_X represent the ionic radius of A-site, B-site cations and X-site anions, respectively. In general, to guarantee the formation of 3D ABX_3 perovskites, the value of t should be between 0.81 to 1.11.[191] For the perovskite with cubic structure, t should be close to 1. Too large the ionic radius of A-site cation will make the value of t exceed 1.11, precluding the formation of ABX_3 perovskites. Too small ionic radius of the A-site cation will result in the formation of compounds with other structures rather than perovskite structure.

As for the A-site cations, organic cations including MA^+ and FA^+ and inorganic cation Cs^+ have been often used to synthesize $MAPbI_3$, $FAPbI_3$ and $CsPbI_3$ which are commonly called as single-cation perovskites. It has been found that mixing two ions at the A site to form double-cation perovskites can improve the properties of perovskite light absorbers, which is beneficial for the enhancement of PSC performance and stability. For example, both $MAPbI_3$ and $FAPbI_3$ suffer from instability in ambient conditions, especially the phase instability. This problem can be improved via mixing MA^+ and FA^+ at the A site which can help to stabilize the crystal structure. The formed double-cation perovskite $(MA)_x(FA)_{x-1}PbI_3$ also exhibited more suitable bandgap than $MAPbI_3$, thereby extending light absorption range.[62] Although the incorporation MA^+ into $FAPbI_3$ contributed to the stabilization of black $FAPbI_3$ along with enhanced PCE, the PSCs still suffered from the problem of the photo and thermal stability. Luckily, combining Cs^+ with FA^+ in the A site of $FAPbI_3$ provided an alternative way to resolve this issue. Partial substitution of Cs cation for FA cation endowed $Cs_{0.1}FA_{0.9}PbI_3$ perovskite with significantly reduced trap densities, thereby improving PCE of $FAPbI_3$ based PSCs from 14.9% to 16.5% Furthermore, the stability of the corresponding devices was enhanced under continuous light illumination.[192] The stabilized black perovskite phase via mixing Cs^+ and FA^+ has been attributed to the entropic gains and the small internal energy input required to form their solid solution.[193]

Composition engineering has been also applied for X-site cations. To tune the optoelectronic properties, I^- is often combined with Br^- to occupy the X site in the structure of halide perovskites. In most cases, mixed A-site cations and mixed X-site halide anions were simultaneously adopted to optimize the properties of halide perovskites. Jeon et al. first found that incorporating $MAPbBr_3$ into $FAPbI_3$ can stabilize the phase structure of $FAPbI_3$ and optimize the perovskite film morphology, finally improving the PCE of PSCs to over 18%.[56] In another study, introducing Cs^+ into $MA_{0.17}FA_{0.83}Pb(I_{0.83}Br_{0.17})_3$ as light absorbers in PSCs resulted in higher photovoltaic performance. The small amount of Cs^+ addition was capable of suppressing the phase impurities, improving the thermal stability, and reducing the sensitivity to various environmental conditions. As a result, the formed triple cation perovskite $Cs_{0.05}(MA_{0.17}FA_{0.83})_{0.95}Pb(I_{0.83}Br_{0.17})_3$-based PSCs exhibited a stabilized power output of 21.1% and a PCE of 18% after 150 h under operational conditions.[194] In addition to Cs^+, other alkali metal ions including Rb^+ and K^+ have also reported to dope into $Cs_{0.05}(MA_{0.17}FA_{0.83})_{0.95}Pb(I_{0.83}Br_{0.17})_3$ for further improved device stability. In spite of not being suitable as a pure $RbPbI_3$ compound because of the small ionic radii of Rb^+, the small incorporation Rb^+ into FA-based halide perovskites could help stabilize the black phase of FA-based perovskites. Thereby, $Rb_{0.05}(Cs_{0.05}MA_{0.17}FA_{0.83})_{0.95}Pb(I_{0.83}Br_{0.17})_3$-based PSCs achieved the stabilized PCE up to 21.6% and exhibited excellent thermal stability.[195] In another study, the incorporation of K^+ into $Cs_{0.05}(FA_{0.85}MA_{0.15})_{0.95}Pb(I_{0.85}Br_{0.15})_3$ perovskites eliminated the hysteresis in PSCs, which has been attributed to the increased grain size, lowered defect density, prolonged charge carrier lifetime and promoted charge transportation.[196]

As for A-site organic cations, guanidinium ($C(NH_2)_3^+$, GA^+) has also been paid attention. In consideration of too large ionic radius of GA^+, it seems impossible to incorporate it into the A site of 3D perovskite crystal structure. However, it has been verified that suitable amount of GA^+ can be incorporated into $MAPbI_3$ perovskite crystal lattice. The formed $GA_xMA_{1-x}PbI_3$ showed longer carrier life time, improved thermal and environmental stability compared with pristine $MAPbI_3$ perovskites, thereby improving the performance of the related devices.[197-199] GA^+ doped into $FA_{0.83}Cs_{0.17}PbI_3$ can tune the crystal structure of perovskites and tailor the hysteresis phenomenon of PSC devices.[200] GA^+-based quadruple-cation perovskite $Cs_{0.05}(FA_{0.83}(MA_{1-x}GA_x)_{0.17})_{0.95}Pb(I_{0.83}Br_{0.17})_3$ has been investigated. It was found that the introduction of GA^+ into CsMAFA-based triple perovskites conduced to a phase separation. In addition to 3D perovskite, 2D $FAGAPbI_4$ and 1D δ-$FAPbI_3$ formed. Such a 1D/3D structure of perovskites endowed the corresponding PSCs with higher PCE, enhanced stability and negligible hysteresis.[201] In another case, $GA_{0.05}Cs_{0.15}FA_{0.8}Pb(I_{0.85}Br_{0.15})_3$-based PSCs achieved significantly enhanced photothermal stability and delivered a high PCE of 21.3%.[202]

Ethylammonium ($CH_3CH_3NH_3^+$, EA^+) is another alternative A-site cation. The ionic of EA^+ (2.3 Å) is larger than that of MA^+ (1.8 Å) but smaller than that of FA^+ (2.6 Å). The t value of $MA_{1-x}EA_xPbI_3$ changes from 0.83 to 0.94. This indicates that EA^+ can be successfully doped into ABX_3 perovskites for the optimization of optoelectronic properties.[203] It has been found that the properties of $MA_{1-x}EA_xPbI_3$ are different from the MA–FA mixed-cation perovskites. Unfortunately, not like FA^+ doping into $MAPbI_3$ which can improve photovoltaic performance of PSCs, the incorporation of EA^+ into $MAPbI_3$ had a negative effect on device performance.[204] Although doping EA^+ into perovskites did not improve performance, EA^+-based halides have been utilized as effective additives to fabricate higher-quality perovskite films and as a retarding agent to inhibit and decelerate the decomposition of perovskites, thus enhancing the device performance and stability.[205, 206]

X-site composition engineering is also very essential as X-site anions play an important role in determining the structure and photoelectronic properties of perovskites via occupying the six vertices of the octahedral BX_6 structure. Different radius of X-site anions may lead to the structural distortions, which will further influence the band gap, crystal structure, and charge transport of the perovskite. For example, with changing the X-site halide anions from I^- to Cl^- of $MAPbX_3$ perovskite, the formed perovskites $MAPbI_3$, $MAPbBr_3$ and $MAPbCl_3$ exhibited increased bandgaps and greatly enhanced stability.[207] The too large bandgap of $MAPbBr_3$ and $MAPbCl_3$ limits their device performance. However, introducing small amount of Br^- and Cl^- into X site to cooperate with I^- is favorable for performance enhancement.[208-210] For example, the incorporation of Cl^- into $MAPbI_3$ via the sequential fabrication method optimized optical, electrical, structural and morphological properties of perovskites, giving rise to improved device performance.[211] It has also been found that the small amount of Cl^- introduced into $MAPbI_3$ transformed the perovskite crystal structure of $MAPbI_3$ from tetragonal structure to cubic structure.[212]

In addition to the common halide X-site cations, pseudohalide such as thiocyanate anion (SCN^-), tetrafluoroborate (BF_4^-) and hexafluorophosphate (PF_6^-) are also good choice of X-site anions. SCN^- is a typical pseudohalide anion which has ionic radius similar to I^-, making it an alternative X-site anion for ABX_3 perovskites. Moreover, the long-pair electrons around N and S atoms of SCN^- allow it to strongly interact with Pb^{2+}, thereby generating stronger electrostatic force.[213] $MAPb(SCN)_2I$ and $MAPb(SCN_xI_{1-x})_3$ -based PSCs have been reported and both of them exhibited improved photovoltaic performance and enhanced stability in comparison with $MAPbI_3$-based counterparts.[214, 215] BF_4^- and PF_6^- which also have similar ionic radius to I^- could partially substitute I^- in perovskite. Hongwei Han's group incorporated BF_4^- into $MAPbI_3$ and used the formed mixed-anion perovskite $MAPbI_{3-x}(BF_4)_x$ to fabricate hole-conductor-free PSCs. The introduction of BF_4^- facilitated charge recombination and suppressed charge recombination, thereby conferring the devices with a PCE of 13.24%.[216] The detailed mechanism of performance enhancement with BF_4^- doping was further explored by Alex K.-Y. Jen's group. Adding small amount of BF_4^- into $(FAPbI_3)_{0.83}(MAPbBr_3)_{0.17}$ ((with molar ratio between 0.5% and 2%)) not only inhibited non-radiative recombination but also reduced the charge transport loss. Benefiting from these merits, 1% BF_4^- doped perovskites-based PSCs yielded 20.16% with significantly improved V_{oc} and FF.[217] In terms of PF_6^--doped perovskites in PSCs, Chen et al. utilized molecular ion PF_6^- to post-treat the fabricated $FA_{0.88}Cs_{0.12}PbI_3$ film, finding that a thin $FA_{0.88}Cs_{0.12}PbI_{3-x}(PF_6)_x$ layer was formed via ion exchange reaction. The introduction of such a PF_6^--based interlayer increased carrier lifetime and reduced defects, finally increasing V_{oc}, FF and relieving hysteresis as well as enhancing stability.[218]

As for B-site composition engineering, even though lead-free PSCs are expected, the photovoltaic performance of lead-free PSCs is unsatisfying, which will be discussed in detail in the next section. Thus, partial replacement of Pb^{2+} via introducing other appropriate divalent metal cations has been adopted to reduce the utilization amount of Pb as possible and tune the properties of perovskites for the improvement of PSC performance. Numerous divalent and trivalent metal cations including Sn (II), Ge (II), Co (II), Mn (II), Cu (II), In (III), Al (III), and Sb (III) have been used to partially replace Pb to form binary metal perovskites as light absorbers in PSCs.[219-222] Among them, Sn-Pb allying halide perovskites have been extensively studied.[223-226] Tavakoli et al. prepared large-grain Sn-rich perovskite films via employing a chemical vapor deposition process. The fabricated devices delivered 14.04% PCE, which was very close to that achieved by pure Pb-based devices and significantly higher than pure Sn-based devices.[227] In a recent work, an impressive PCE of 20.7% has been achieved by the $(FASnI_3)_{0.6}(MAPbI_3)_{0.4}$-based devices via adding excess Sn powder into the $FASnI_3$ precursor solution which can reduce the content of Sn^{4+}.[228] Apart from binary metal perovskites-based PSCs, Pb-Sn-Cu ternary PSCs have been reported to deliver 21.08% of PCE via replacing Pb^{2+} with both Sn^{2+} and Cu^{2+}. To be specific, Sn^{2+} plays an essential role in tunning the absorption onset, while Cu^{2+} serves more in improving the perovskite film quality and crystallinity of Sn-containing alloyed perovskites.[229]

Noteworthy that what I discussed here is mainly attributed to the composition engineering of perovskites, especially organic-inorganic hybrid halide perovskites. However, the strategy of composition engineering has been widely applied in all-inorganic halide perovskites, RP type halide perovskites and other functional materials, including ETL materials and HTL materials. Taking TiO_2-based ETL as an example, many elements such as Al, Co, Er, Yb, Mn, W, Sr and so forth have been doped into TiO_2 ETL with the purpose of improving the properties of ETLs and tuning the energy alignment between ETL and perovskite layers.[230-234]

2.5.2 Additive engineering

In terms of solution-processed perovskite films, the film quality is strongly dependent on the precursor composition and processing conditions. Note that defects inevitably exist in the perovskite films, especially distributing at grain boundaries and even bulk perovskites, which greatly affected the device photovoltaic performance. In pursuit of high-quality perovskite films with reduced defects and improved surface morphology, a variety of substances have been added into the perovskite precursor solution as additives to tune crystallization and growth of perovskite crystals.[235, 236]

There are many electron-rich defects which can be regarded as Lewis bases. On this basis, the addition of Lewis acids into the perovskite films can passivate these electron-rich defects as Lewis acids can accept a pair of non-bonding electrons. Many metal halides and derivatives have been used as Lewis acid-based additives to passivate agents via ionic bonding and other electrostatic interactions with the electron-rich defects in perovskites. For example, PbI_2 as a typical Lewis acid has been presented to locally passivate grain boundaries via releasing the organic species during annealing.[237] In addition, incorporating a small amount of excess PbI_2 into perovskite phase could effectively suppress ion migration and relieve hysteresis, thereby improving the overall performance of PSCs.[238] In addition, alkali metal iodides including KI and NaI also have the ability to passivate grain boundaries and reduce defects.[239, 240] With the assistance of KI, $Cs_{0.06}FA_{0.79}MA_{0.15}Pb(I_{0.85}Br_{0.15})_3$-based PSCs delivered a high PCE of 21.5%, in which K^+ could ionically bond with undercoordinated halides or reduce negatively charged trap states at the grain surface and I^- could fill I^- vacancies. [241] The influences of some monovalent cation halide additives including CuBr, CuI, NaI, AgI on the structural and optoelectronic properties of $MAPbI_3$ perovskites and the solar cell performance have been studied. It was found that these additives not only could tune the bandgap, optimize the film surface morphology but also conduce a passivation of trap states at the crystallite surfaces, thereby improving device performance.[242] Besides, various other metal halides such as $CaCl_2$, $CuBr_2$, $InCl_2$ have also been utilized as additives to improve the film properties of halide perovskites. It is important to mention that these metal halides serve as effective additives to tailor the growth of perovskite grains and the film quality for the achievement of larger grain size and smooth film surface via two ways. On one hand, some metal ions with suitable ionic radius may partially replace A-site cations like MA^+ or B-site cations like Pb^{2+} to adjust some internal properties of perovskites. On the other hand, they played a critical in modulating the crystallization kinetics and film formation process.[243]

Fullerene-based materials are ETL materials in PSCs. In addition to acting as ETL materials, they are also good additives for perovskite layers as adding moderate amount of them into perovskite precursor solution not only can promote the electron transportation in perovskites but also passivate grain boundaries to reduce defects. C60 and its derivatives as well as PC61BM have been introduced into perovskite films, which can form the bulk heterojunctions of perovskite-fullerene. Such a formed bulk heterojunction can help to suppress charge recombination, lower trap density, and even hinder the drift of ions and facilitate charge separation efficiency.[244-246] Benefitting from these merits, the PCE and stability of PSCs can be enhanced and the hysteresis can be relieved. For example, Chiang et al. added an appropriate amount of PC61BM into PbI_2 solution and fabricated perovskite films via two-step spin-coating method. The introduction of PC61BM into perovskite films improved the film quality via filling pinholes and vacancies, thereby producing larger perovskite grains with fewer grain boundaries.[247] As for one-step spin-coating method, the incorporated PC61BM was also implemental for reducing defects. PC61BM distributing at perovskite grain boundaries could fill halide-rich antistites and also interact with uncoordinated halides.[248] In addition to directly adding them into perovskite precursor solution, these fullerene additives can be dragged into perovskite films via the antisolvents, which can served as a template to optimize the perovskite growth and passivate the film surface.[249-251]

In terms of positively charged uncoordinated Pb^{2+}, Lewis base additives which can donate electrons are useful and can bond with these uncoordinated PbI_2 to passivate defects. Substances containing O, S, N atoms with lone-pair electrons have been utilized as Lewis base additives in many cases, which play an important role in passivating defects and improving the charge transfer and collection process. Some organics and polymers like urea, ethyl cellulose (EC) and poly(methyl methacrylate) (PMMA) containing O atoms have been reported to act as effective Lewis base additives to improve film quality and enhance device performance.[252, 253] The S-containing Lewis base additives mainly include thiourea, thiophene and their derivatives and the commonly used N-containing Lewis base additives are pyridine and its derivatives as well as some $-NH_2$ derivatives.[254-256] In some cases, substances simultaneously containing two or three atoms can generate cross-linking effect among perovskite grains, inhibiting the migration of ions and passivating the trap states at the grain boundaries.[257, 258]

In addition to above-mentioned additives, inorganic acids such as hydriodic acid, and hydrochloric acid have been used as additives to improve the film formation process.[259-261] These inorganic acids can increase the solubility of perovskite precursors. On this basis, the nucleation process can be improved, which finally resulted in a full-coverage perovskite film with large grain size. In addition, these inorganic acids can adjust the growth rate and crystallization process of the perovskite via interacting with PbI_2 to form a pre-crystallized intermediate state. Moreover, the addition of inorganic acids can enhance the perovskite film stability because the oxidation process of I^- to I_2 can be suppressed in the acid environment.[243] Besides, some nanoparticles such as PbS nanoparticles and Au@SiO_2 nanoparticles[262], metal-organic frameworks,[263] carbon materials[264, 265] have been added into perovskite films to tune the film formation process and passivate defects for the purpose of improving the performance and stability of PSCs.

2.5.3 Solvent engineering

As mentioned above, the choice of solvent affects the crystallization dynamics and partially determines the perovskite film morphology. Thus, solvent engineering is another effective approach for adjusting the perovskite film morphology, which is particularly important for solution-processed one-step spin-coating method and planar-structured PSCs. Solvent engineering mainly includes two aspects. One is the choice of solvents to dissolve various precursor substances. The other is the choice of antisolvents. In general, solvent engineering are faced with two main challenges. One challenge is the difficulty to produce high-quality dense perovskite films via using a single solvent. In addition, the intermediate phase will inevitably form during the process of solvent treatment, which is of great significance to the growth of perovskite crystals. But the accurate crystal structure of the intermediate phase is still uncertain, which needs to be further explored.

Polar aprotic solvent N, N-Dimethylformamide (DMF) is the commonly used solvent to dissolve various halides due to its decent solubility and lower boiling temperature which allows the crystal nucleus to reach substantial in size steadily.[266] However, the utilization of single DMF solvent cannot obtain high-quality perovskite films due to the imperfect crystallization process in most cases. In order to better optimize the crystallization dynamics of perovskites, DMF often cooperated with dimethyl sulfoxide (DMSO) to prepare perovskite films. DMSO had stronger coordination ability with PbI_2 than DMF, which has been proven to be able to retard the crystallization of PbI_2 when using sequential two-step method to fabricate $MAPbI_3$ perovskite film.[267] Rong at al. have found that the formation of the intermediate phase $MA_2Pb_3I_8 \cdot 2DSMO$ is favorable for creating high-quality perovskite films. The mixed DMF and DMSO solvent engineering are also employed to fabricate all-inorganic halide perovskites and RP halide perovskites. The introduction of DMSO into DMF assisted in forming high-quality $CsPbI_2Br$ perovskite film via enhancing the mass transport.[268] In another case, high-quality $(BA)_2(MA)_3Pb_4I_{13}$ perovskite film was obtained by the dual solvent engineering of DMF and DMSO. The fast volatilization of single DMF solvent promotes the homogenous nucleation, thereby leading to the random crystallization orientation of perovskite grains. By contrast, the addition of DMSO can slow the crystallization process via forming intermediate phase and induce the perovskite crystals to crystallize perpendicular to the substrate.[269]

In addition to DMF and DMSO, γ-butyrolactone (GBL) and N-methyl-2-pyrrolidone (NMP) are also widely utilized solvents to prepare perovskite films. Compared with DMF and DMSO, the solubility of GBL and NMP is inferior, which often leads to poor film morphology and thinner film thickness. To improve the film quality, they need to mix with other solvents like DMF and DMSO when fabricating perovskite films.[270] For example, the mixed solvent of GBL and DMSO was utilized to prepare uniform and dense $MAPb(I_{1-x}Br_x)_3$ ($x = 0.1$-0.15) films, where MAI(MABr)-PbI_2-DMSO intermediate phase was formed to help improve the crystallization process.[271] Compared with DMF, DMSO and NMP possess relatively high boiling point. Apart from DMF, dimethylacetamide (DMAc) is another low boiling pint solvent. Combing NMP with DMAc has been reported to fabricate high-quality $MAPbI_3$ perovskite film without the post-annealing process, which overperformed DMF/DMSO and DMAc/DMSO-based counterparts. The formation of high-quality $MAPbI_3$ perovskite film at room temperature was attributed to the instant crystallization process induced by the existence of NMP when the antisolvent was dropped.[272] In a word, it is important to take full consideration of the dissolving copiability, boiling point, coordination ability with PbI_2 as well as the interaction with antisolvent when selecting solvents to fabricate perovskite films as all these factors play a vital role in determining the perovskite film quality.

Besides, it is also significant to pay close attention to the choice of antisolvents because antisolvent also influences the crystallization dynamics of perovskites and the eventual perovskite film quality. The basic requirement for antisolvent to fabricate halide perovskite films for PSC application is that it should be inter-miscible with solvents and cannot dissolve any precursor substance of perovskite and perovskite itself. In addition, antisolvent is believed to possess lower boiling point than solvents, which can facilitate the evaporation of solvents from the perovskite film. Thanks to the good miscibility with solvent and low boiling point, chlorobenzene (CB) and toluene (Tol) are widely used antisolvent when employing one-step sin-coating method to fabricate perovskite films.[56, 273-275] However, Paek et. al revealed that lower boiling point is not a necessary condition for antisolvent. By comparing various antisolvents (trifluorotoluene (TFT), p-xylene (Xyl), diethyl ether, and dichloromethane (DCM), Tol, CB with different physicochemical properties to prepare perovskite films, they found that dielectric constants are a more important factor. Only antisolvents which are miscible with solvents and have higher dielectric constants than 5 can promote the formation of perovskite crystal and confer the devices with high photovoltaic performance. In this work, TFT with high boiling point as a novel antisolvent surpassed typical CB and Tol antisolvents, endowing PSCs with a higher PCE of 20.3%.[276] In another case, the strong interaction between antisolvent and solvent was reported to play a crucial role in favoring the crystalline quality of perovskite. In this work, diphenylether (DPE) as antisolvent afforded better film quality of $MAPbBr_3$ layer than other antisolvent including CB, TFT, DPE, di-isopropyl ether (DIP) and Xyl as antisolvent.[54] In addition, anisole with high boiling point has been presented to be a superior antisolvent to fabricate large-area perovskite film owing to its high viscosity and the strong intermolecular interaction with DMF/DMSO.[277]

Despite that various antisolvent can help optimize the crystallization and growth process of perovskites, it is worth mentioning that most of these antisolvents are toxic and harmful to health. Based on this, it is imperative to find some green antisolvents to fabricate perovskite films. For example, low-toxicity methoxybenzene (PhOMe), ethyl acetate (EA), and methylamine bromide (MABr) in ethanol have been utilized to replace toxic CB and Tol to prepare high-quality perovskite films.[278-282] More importantly, antisolvent-free deposition method is more recommended and expected to fabricate perovskite films, which not only avoids the use of toxic antisolvent but also simplifies the fabrication process.[283]

2.5.4 Interface engineering

Interface engineering is also crucial for the device performance improvement, particularly for devices with planar structures. Interface engineering mainly refers to the insertion of a new layer between two functional layers or the post treatment of the formed layers to tune the film surface properties. Generally, interface engineering aims to improve the charge transfer process, passivate defects and tune energy level alignment. These optimized properties in devices is favorable for the improvement of device photovoltaic performance.

Some efforts have been made to optimize the surface properties of perovskite films via introducing a new thin layer on top of perovskite layer. For example, 2-aminoterephthalic acid with an ammonium group and two carboxyl groups could easily assemble at the grain boundaries and form a hydrophobic passivating layer via the post treatment process, which not only reduced defects at grain boundaries but also protected the perovskite films from water invasion.[257] In terms of polymers, directly introducing them into precursor solutions may have an adverse effect on the crystallinity of perovskite, although some polymers can passivate defects via interacting with perovskites. Taking this into consideration, it is a better way to use these polymers to modify the surface of perovskite films via spin-coating the polymer solution on top of perovskite layers.[284, 285] Note that the solvent of the post-treatment solution should be carefully selected. The solvents should not dissolve and damage the formed perovskites. Based on this consideration, the commonly used solvents for the post-treatment solution are CB and IPA. It is also important to optimize the concentration of post-treatment solution as too high concentration makes the modifying layer too thick, which may exert a negative influence on the charge transportation and separation process.

In addition, many researches were focused on the interface of ETL/perovskite layers and HTL/perovskites as the properties at the interface is governing factor determining the charge separation and extraction. At the side of FTO/ETL/perovskite layer or perovskite layer/ETL/electrode, some materials have been selected as interlayer to be inserted between ETL and perovskite layers. The insertion of such an interlayer can optimize the energy level match or passivate defects, thereby promoting electron separation and reducing charge recombination.[286-289] For example, a thin insulating layer of polystyrene (PS) has been added between perovskite layer and ETL, which can allow electrons to transport from perovskite layer to C60 ETL through tunneling and block holes.[290] Similar to this, at the side of FTO/HTL/perovskite layer or perovskite layer/HTL/electrode, the thin interlayer can be inserted between HTL and perovskite layers to optimize the interface properties at the HTL/perovskite interface.[291-293]

2.6 Future development direction of PSCs

2.6.1 Lead-free PSCs

In consideration of the potential harm of lead-containing perovskites, an increasing number of researchers have shown great interest in designing and developing lead-free PSCs via seeking for nontoxic elements to substitute Pb or synthesizing novel perovskite materials to be used as light absorbers in solar cells.

Sn from Group IV has been considered as the most suitable candidate to replace Pb in halide perovskites. And Sn-based halide perovskites have received wide attention thanks to their potential optoelectronic properties such as suitable optical bandgap, super charge carrier mobility and small exciton binding energy. As for the typical Sn-based organic-inorganic halide perovskite ($MASnI_3$), it has a bandgap of 1.33 eV which is smaller than that of $MAPbI_3$ (1.5 eV). In the first report on $MASnI_3$-based PSCs, it has been demonstrated that the fabricated $MASnI_3$ films possess approximately 1.6 $cm^2V^{-1}s^{-1}$ of charge carrier mobility and approximately 30 nm of the carrier diffusion length, which yielded a PCE of over 6%.[19] In another study, via implementing the bandgap engineering, $MASnIBr_2$-based PSCs delivered a PCE of 5.73%.[294]

Another commonly researched Sn-based organic-inorganic halide perovskite is $FASnI_3$ with a single stable phase over a broad temperature range up to 200 °C, which has been reported to be more stable than $MASnI_3$. $FASnI_3$ shows a bandgap of 1.41 eV, approaching the optimum band gap for single-junction solar cells. Such a bandgap affords it the ability to harvest photons almost up to 900 nm. Applying it into solar cells with the device structure of FTO/c-TiO_2/m-TiO_2/$FASnI_3$/spiro-OMeTAD/Au produced only 2.10% of PCE via introducing SnF_2 as an additive.[295] Afterwards, the PCE of $FASnI_3$-based PSCs was improved to 4.8% via introducing pyrazine which could interact with SnF_2 to form pyrazine-SnF_2 complex as additives. The introduction of pyrazine inhibited the phase separation caused by the excess of SnF_2, contributing to optimized surface morphology. In addition, combining SnF_2 additive with diethyl ether dripping, high-quality and uniform $FASnI_3$ perovskite films with full coverage were obtained. When used in an inverted planar device, the devices achieved a PCE up to 6.22%.[296]

In addition to Sn-based organic-inorganic halide perovskites serving as promising lead-free photovoltaic materials, Sn-based all inorganic perovskites like $CsSnI_3$ also show great potential for solar cell applications due to their suitable bandgap (1.27 eV) and large optical absorption coefficient (10^4 cm $^{-1}$). In terms of $CsSnI_{3-x}Br_x$, the bandgap changes from 1.27 eV for $CsPbI_3$ to 1.37, 1.65, 1.75 eV for $CsSnI_2Br$, $CsSnIBr_2$, and $CsSnBr_3$ respectively.[297] $CsSnI_3$-based PSCs can extend the spectral response to 950 nm, thus being capable of generating high photocurrent densities of more than 22 mA cm $^{-2}$. The first reported $CsSnI_3$-based PSCs yielded 2.02% PCE via introducing suitable amount of SnF_2 to reduce defects in $CSsSnI_3$.[298] In 2016, Marshall et al. fabricated simplified $CsSnI_3$-based PSCs without electron blocking layer, which delivered a PCE of 3.56% via introducing $SnCl_2$ which can form n-type doping of fullerene electron-transport layer. More importantly, such $CsSnI_3$-based devices exhibited significantly enhance stability compared with $MAPbI_3$-based devices with the same structure.[299]

Sn-based halide perovskites are faced with many challenges when applying them in solar cells as light-absorbing materials. These challenges are mainly derived from two aspects. One is that different from Pb whose divalent ion (Pb^{2+}) is very stable, Sn^{2+} is extremely unstable and can be easily oxidized to Sn^{4+}. Thus, self-oxidation of Sn^{2+} can readily occur for Sn-based halide perovskites, which can lead to the existence of numerous Sn vacancies in these Sn-based halide perovskites, the formation of a high level of p-doping and the large loss of device voltage. To mitigate the oxidation of Sn^{2+}, SnF_2 is often used as an additive. The other is the difficulty in fabricating high-quality films. Without the assistance of additives, the fabricated Sn-based halide perovskite films exhibited poor film quality with discontinuous coverage and a large number of pinholes via the solution-processed spin-coating method in most cases.[296] To further advance the photovoltaic performance of Sn-based lead-free PSCs, it is of significance to find out effective strategies to overcome these obstacles. By now, a variety of strategies have been adopted from the aspect of optimizing the device structure and fabrication technique, introducing co-additives in addition to SnF_2, and building a hybrid 2D/3D perovskite crystal structure.[300] For example, various reducing agents such as hypophosphorous acid[301] phenylhydrazine hydrochloride[302], hydrazinium iodide[303] have been employed as additives to fabricate Sn-based halide perovskite films. Adding these reducing agents into perovskite precursor solution can not only protect Sn^{2+} from being oxidized into Sn^{4+} but also help to optimize the crystallization process of perovskites films, thereby improving the perovskite film quality and enhancing the photovoltaic performance of the corresponding devices. By far, $FASnI_3$-based PSCs have achieved over 11% PCE, which is still behind the PCE obtained by their Pb-based counterparts and needs to be further improved.

In addition to Sn, Ge is another Group IV element and can become possible substitute for Pb. In terms of 3D $AGeI_3$ perovskites, all-inorganic perovskite $CsGeI_3$ shows a bandgap of around 1.6 eV, while Ge-based organic-inorganic perovskites $MAGeI_3$ and $FAGeI_3$ show bigger bandgap of around 1.9 eV and 2.2 eV, respectively. In view of bandgap, it seems that only $CsGeI_3$ is appropriate as light absorbers in solar cells. And many theoretical studies have demonstrated that some Ge-based perovskites like $CsGe_{2/3}Si_{1/3}I_3$ have the potential to become the light absorption layer in solar cells.[304, 305] Unfortunately, the experimental results in Ge-based lead-free PSCs are disappointing. $CsGeI_3$-based PSCs did not deliver good photovoltaic performance and the obtained PCE by $CsGeI_3$-based PSCs is more inferior than that achieved by Sn-based PSCs. $AGeI_3$-based PSCs were first reported in 2015 and $CsGeI_3$ and $MAGeI_3$-based PSCs yielded only 0.11% and 0.20% PCE, respectively. The more suitable bandgap of $CsGeI_3$ confers $CsGeI_3$-based solar cells higher current density but lower PCE than $MAGeI_3$. The limited PCE of $CsGeI_3$-based PSCs was ascribed to the poor film forming ability and the oxidizing tendencies.[306] Even though Kopacic et al. tried to improve the PCE of $MAGeI_3$-based solar cells via tunning the composition of X-site ions, the PCE was only enhance to 0.57%, which is far from Sn-based and Pb-based PSCs.[307] However, it is interesting to find that mixed Sn-Ge based all-inorganic perovskite ($CsSn_{0.5}Ge_{0.5}I_3$)-based devices achieved a remarkable PCE of 7.11% with high stability thanks to the formation of a uniform and full-coverage stable native-oxide layer, which encapsulated and passivated the perovskite film surface. The proposed native-oxide passivation strategy in this study provided an alternative avenue for enhancing the photovoltaic performance and stability of lead-free PSCs.[308]

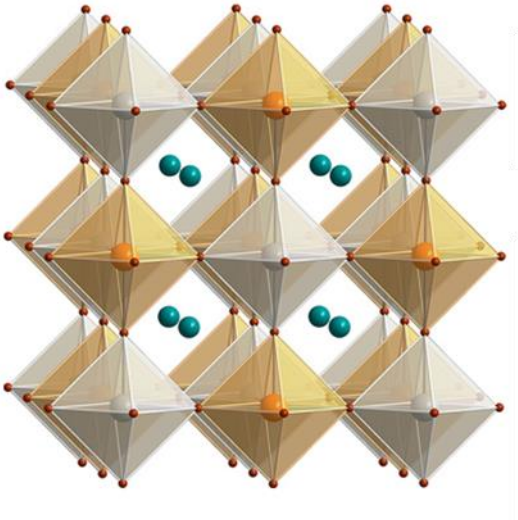

Figure 2.5 Crystal structure of the double perovskite $Cs_2AgBiBr_6$ (Orange, gray, turquoise, and brown spheres mean Bi, Ag, Cs, and Br atoms, respectively)[309] (Reproduced with permission. Copyright 2016, American Chemical Society).

Apart from replacing Pb with Sn and Ge for ABX_3 perovskites, an alternative way is to form double perovskites with the chemical formula of $A_2M^{+}M^{3+}X_6$ via replacing one divalent Pb^{2+} with one monovalent M^{+} ion and one trivalent M^{3+} ion. Thus, trivalent Bi^{3+} and Sb^{3+} can collaborate with monovalent Ag^{+} to form various double perovskites, some of which have been reported to display photovoltaic properties. The most studied halide double perovskite utilized as light-absorbing materials in solar cells is $Cs_2AgBiBr_6$ which exhibits an indirect bandgap of 1.95 eV and a long room-temperature fundamental PL lifetime of ca. 660 ns.[309] **Figure 2.5** shows the crystal structure of the double perovskite $Cs_2AgBiBr_6$. $Cs_2AgBiBr_6$-based PSCs was first reported in 2018 and achieved 1.44% of PCE.[310] During the past two years, although some efforts have been devoted to improving the performance of $Cs_2AgBiBr_6$-based PSCs, the highest PCE obtained is still below 3%.[311, 312] The short electron diffusion length that

$Cs_2AgBiBr_6$ suffers from has been considered as one of the major factors limiting the performance of $Cs_2AgBiBr_6$-based PSCs. The existence of energetic disorder and a high density of electron traps may be the main reason for the short electron diffusion length.[309] Therefore, there is a long way to go for completely replacing Pb-containing perovskites-based PSCs with $Cs_2AgBiBr_6$-based PSCs for the realization of commercialization.

2.6.2 Large-area PSCs

For the realization of the commercialization of PSCs, large-scale production of PSCs is an inevitable developing direction. However, the commonly utilized solution-processing spin-coating method can hardly satisfy the needs of large-scale industrial production. The efficiency of PSCs will greatly decline when using solution-based spin-coating method to fabricate large-area perovskite films because the film quality will be negatively influenced by expanding the area of spin-coating. From the perspective of environmental and safety grounds, the use of many organic solvents and the waste of the toxic Pb-containing materials during the solution-processed spin-coating process also limit the large-scale production. Therefore, it is vital to seek for more effective fabrication methods with the ability to prepare large-area perovskite films with high quality for large-scale deployment of PSCs.

The vacuum deposition technique is suitable for large-area fabrication of perovskite films. The vacuum deposition technique used to fabricate halide perovskite films for solar cell applications was first reported by Henry J. Snaith's group. They employed dual-source (including organic source and inorganic source) vapor deposition method to prepare homogenous $MAPbI_3$ perovskites films with full coverage. [28] In fact, the way was not been widely employed in the later studies, which may be because of the difficulty in controlling the MAI deposition rate due to its small molecular weight. After that, Chen et al. employed the sequential vacuum deposition technique to fabricate $MAPbI_3$, in which the $PbCl_2$ film was first deposited, followed by the MAI deposition during the annealing process of $PbCl_2$ and then $PbCl_2$ can be transformed to uniform and high-coverage $MAPbI_{3-x}Cl_x$ perovskite films.[313]

In addition to vapor deposition technique, CH_3NH_2 gas-induced film formation process has been reported. By pressing CH_3NH_2 gas into MAI and PbI_2, $MAI.3CH_3NH_2$ and $PbI_2.CH_3NH_2$

solutions were formed and the perovskite precursor solution was obtained via mixing them with ultrasonicating. The precursor solution was dropped on a large-area substrate and then then the precursor was covered by the polyimide (PI) films. A 120-bar pressure was put to make the liquid precursor solution spread under the PI film, followed by annealing at 50 °C for 2 min. After peeling off the PI film, a dense and uniform perovskite film was formed. By using this technique to fabricate perovskite films, the obtained PSCs with an aperture area of 36 cm^2 achieved a PCE of 12.1%.[314]

Some other solution-based techniques are also appropriate for the large-area fabrication of perovskite films. Michael Grätzel's group utilized a vacuum flash-assisted solution processing (VASP) to prepare large-area perovskite films. As for this method, after spin-coating the perovskite precursor solution, the films were put in a vacuum chamber for several seconds, which can help to remove most of the residual solvents, thereby promoting the rapid crystallization of the perovskite intermediate phase. By this way, large-area $FA_{0.81}MA_{0.15}PbI_{2.51}Br_{0.45}$ PSCs with over 1 cm^2 of square aperture areas delivered a high PCE of 19.6%.[315] Spray coating method has also been utilized to prepare large-area perovskite films.[316, 317] $MAPbI_3$-based PSCs with the area of (1 cm × 1 cm) fabricated via two-step ultrasonic spray deposition generated a PCE of 13.09%.[318] And ink-jet printing, black coating, and slot-diet coating also suit the fabrication of large-area PSCs.[319-324] For example, Li et al. incorporated monoammonium zinc porphyrin (ZnP) into $MAPbI_3$ and fabricated the perovskite film via blade-coating method. The devices with the area of 1.96 cm^2 achieved a high PCE of 18.3%.[324]

Although many strategies have been implemented to improve the performance of large-area PSCs, the efficiency of single large-area PSCs over 10 cm^2 is still below 10%. Most of current research are focused on 10-100 cm^2 minimodules. The research on large-area PSCs with the area of over 200 cm^2 is very limited. In addition to the limitation of fabrication techniques, some effective strategies used to enhance performance of small-area PSCs have not been fully upscaled, which also limited the large-scale production of PSCs.[325] Furthermore, the costs of components materials of PSCs, particularly HTL materials should be taken into consideration. The commonly used spiro-OMeTAD as HTL materials is very expensive and requires additional chemical doping for efficient hole separation ability, which increased the production costs for large-scale fabrication of PSCs. Therefore, it is very imperative to design and develop low-cost materials used in PSCs for large-scale production.[326]

2.6.3 Flexible PSCs

PSCs also develop towards the direction of flexible devices to adapt the development need for portable electronics, shaped display devices and wearable electronic textiles. Compared with rigid PSCs, flexible PSCs have the advantage in storage and transportation because of flexibility, light weight, portability, and compatibility with curved surfaces. Flexible PSCs are fabricated on the flexible polymer substrates with low heat resistance. As this point, it is of great importance to fabricate the functional layer of devices at low temperatures. Additionally, the fabricated devices show exhibit decent anti-bending ability.[327]

As for most of organic-inorganic hybrid halide perovskites, especially $MAPbI_3$, they can be obtained at the temperature around 100 ºC, making then suitable for flexible PSCs. In terms of all-inorganic halide perovskites such as $CsPbI_3$, $CsPbI_2Br$ and $CsPbBr_3$, relatively high annealing temperatures (> 180 ºC) are needed to obtain high-quality all-inorganic perovskite films with high crystallinity and large grain size. Thus, to fabricate all-inorganic halide perovskites-based flexible PSCs, it is imperative to find ways to prepare high-quality all-inorganic perovskite films at decreased temperatures.[328, 329] One report of RT solution-processed $CsPbX_3$-based PSCs with the device configuration of ITO/NiO_x/$CsPbI_2Br$/C60/ BCP/Ag yielded a PCE of 6.4%, which was furthered improved to 10.4% by post-annealing the fabricated perovskite films at 120 ºC.[330] In another work, α-$CsPbI_2Br$ perovskite film was fabricated via a one-step method with a low-temperature (100-130 °C) annealing process and the devices achieved a PCE of 10.56%.[331] In comparison with organic-inorganic hybrid halide perovskites, all-inorganic halide perovskites are faced with more difficulties for utilizing in flexible PSCs and more research work are needed to resolve these problems.[332]

Charge transporting layers (ETLs and HTLs) should also be fabricated at a low temperature for the application of flexible PSCs. Fullerenes and their derivatives-based films used as ETLs and some organic HTLs can be easily fabricated at room temperature or low temperatures. However, many deposited metals oxides-based charge transporting layers such as TiO_2 and NiO_x layers via spin-coating method need high-temperature sintering process to obtain a relatively compact structure with decent crystalline quality, which is incompatible with polymer substrates. So many strategies have been proposed to fabricate efficient charge transporting layers at low temperatures. For example, the plasma-enhanced atomic layer deposition and the magnetron sputtering technique have been employed to fabricate c-TiO_2 layers at low temperatures.[333, 334] Besides, it is also wise to seek for novel charge transporting materials which can be fabricated at low temperatures to replace those traditional metal oxides.[102, 336, 337]

2.7 Reference

[1] R. W. Miles, K. M. Hynes, I. Forbes, *Prog. Cryst. Growt. Ch. Mater.* **2005**, *51*, 1-42.

[2] A. Goetzberger, J. Luther, G. Willeke, *Sol. Energy Mater. Sol. Cells* **2002**, *74*, 1-11.

[3] K. L. Chopra, P. D. Paulson, V. Dutta, *Prog. Photovoltaics: Res. Appl.* **2004**, *12*, 69-92.

[4] P. Jackson, D. Hariskos, E. Lotter, S. Paetel, R. Wuerz, R. Menner, W. Wischmann, M. Powalla, *Prog. Photovoltaics: Res. Appl.* **2011**, *19*, 894-897.

[5] X. Wu, *Sol. Energy* **2004**, *77*, 803-814.

[6] J. Gong, K. Sumathy, Q. Qiao, Z. Zhou, *Renew. Sust. Energy Rev.* **2017**, *68*, 234-246.

[7] N.-G. Park, *Mater. Today* **2015**, ***18***, 65-72.

[8] M. A. Green, *Prog. Photovoltaics: Res. Appl.* **2009**, *17*, 183-189.

[9] B. Rech, T. Repmann, M. N. van den Donker, M. Berginski, T. Kilper, J. Hüpkes, S. Calnan, H. Stiebig, S. Wieder, *Thin Solid Films* **2006**, *511-512*, 548-555.

[10] M. A. Green, A. Ho-Baillie, H. J. Snaith, *Nat. Photonics* **2014**, *8*, 506-514.

[11] H. S. Jung, N.-G. Park, *Small* **2015**, *11*, 10-25.

[12] I. Mesquita, L. Andrade, A. Mendes, *Renew. Sust. Energy Rev.* **2018**, *82*, 2471-2489.

[13] N. Marinova, S. Valero, J. L. Delgado, *J. Colloid Interf. Sci.* **2017**, *488*, 373-389.

[14] H.-S. Kim, C.-R. Lee, J.-H. Im, K.-B. Lee, T. Moehl, A. Marchioro, S.-J. Moon, R. Humphry-Baker, J.-H. Yum, J. E. Moser, M. Grätzel, N.-G. Park, *Sci. Rep.* **2012**, *2*, 591.

[15] H.-S. Kim, S. H. Im, N.-G. Park, *J. Phys. Chem. C* **2014**, *118*, 5615-5625.

[16] M. M. Lee, J. Teuscher, T. Miyasaka, T. N. Murakami, H. J. Snaith, *Science* **2012**, *338*, 643-647.

[17] W. Wang, M. O. Tadé, Z. Shao, *Chem. Soc. Rev.* **2015**, *44*, 5371-5408.

[18] G. E. Eperon, G. M.释Paternò, R. J. Sutton, A. Zampetti, A. A. Haghighirad, F. Cacialli, H. J. Snaith, *J. Mater. Chem. A* **2015**, *3*, 19688-19695.

[19] N. K. Noel, S. D. Stranks, A. Abate, C. Wehrenfennig, S. Guarnera, A.-A. Haghighirad, A. Sadhanala, G. E. Eperon, S. K. Pathak, M. B. Johnston, A. Petrozza, L. M. Herz, H. J. Snaith, *Energy Environ. Sci.* **2014**, *7*, 3061-3068.

[20] S. D. Stranks, G. E. Eperon, G. Grancini, C. Menelaou, M. J. P. Alcocer, T. Leijtens, L. M. Herz, A. Petrozza, H. J. Snaith, *Science* **2013**, *342*, 341-344.

[21] G. Xing, N. Mathews, S. Sun, S. S. Lim, Y. M. Lam, M. Grätzel, S. Mhaisalkar, T. C. Sum, *Science* **2013**, *342*, 344-347.

[22] S. D. Stranks, H. J. Snaith, *Nat. Nanotechnol.* 2015, **10**, 391-402.

[23] G. Giorgi, J.-I. Fujisawa, H. Segawa, K. Yamashita, *J. Phys. Chem. Lett.* **2013**, *4*, 4213-4216.

[24] Y. Bai, X. Meng, S. Yang, *Adv.Energy Mater.* **2018**, **8**, 1701883.

[25] J. M. Ball, M. M. Lee, A. Hey, H. J. Snaith, *Energy Environ.Sci.* **2013**, *6*, 1739-1743.

[26] P. Liu, W. Wang, S. Liu, H. Yang, Z. Shao, *Adv. Energy Mater.* **2019**, *9*, 1803017.

[27] T. Leijtens, G. E. Eperon, S. Pathak, A. Abate, M. M. Lee, H. J. Snaith, *Nat. Commun.* **2013**, *4*, 2885.

[28] M. Liu, M. B. Johnston, H. J. Snaith, *Nature* **2013**, *501*, 395-398.

[29] S. Wang, T. Sakurai, W. Wen, Y. Qi, *Adv. Mater. Interfaces* **2018**, *5*, 1800260.

[30] J. Chen, N.-G. Park, *ACS Energy Lett.* **2020**, *5*, 2742-2786.

[31] S. Ryu, J. H. Noh, N. J. Jeon, Y. Chan Kim, W. S. Yang, J. Seo, S. I. Seok, *Energy Environ. Sci.* **2014**, *7*, 2614-2618.

[32] Q. Wang, Y. Shao, H. Xie, L. Lyu, X. Liu, Y. Gao, J. Huang, *Appl. Phys. Lett.* **2014**, *105*, 163508.

[33] D. Shin, D. Kang, J. Jeong, S. Park, M. Kim, H. Lee, Y. Yi, *J. Phys. Chem. Lett.* **2017**, *8*, 5423-5429.

[34] E. M. Miller, Y. Zhao, C. C. Mercado, S. K. Saha, J. M. Luther, K. Zhu, V. Stevanović, C. L. Perkins. J. van de Lagemaat, *Phys. Chem. Chem. Phys.***2014**, *16*, 22122-22130.

[35] P. Schulz, L. L. Whittaker-Brooks, B. A. MacLeod, D. C. Olson, Y.-L. Loo, A. Kahn, *Adv. Mater. Interfaces* **2015**, *2*, 1400532.

[36] G. Yang, C. Wang, H. Lei, X. Zheng, P. Qin, L. Xiong, X. Zhao, Y. Yan, G. Fang, *J. Mater. Chem. A* **2017**, *5*, 1658-1666.

[37] N. Marinova, W. Tress, R. Humphry-Baker, M. I. Dar, V. Bojinov, S. M. Zakeeruddin, M. K. Nazeeruddin, M. Grätzel, *ACS Nano* **2015**, *9*, 4200-4209.

[38] P. Yadav, S.-H. Turren-Cruz, D. Prochowicz, M. M. Tavakoli, K. Pandey, S. M. Zakeeruddin, M. Grätzel, A. Hagfeldt, M. Saliba, *J. Phys. Chem. C* **2018**, *122*, 15149-15154.

[39] S. Shao, Y. Cui, H. Duim, X. Qiu, J. Dong, G. H. ten Brink, G. Portale, R. C. Chiechi, S. Zhang, J. Hou and M. A. Loi, *Adv. Mater.* **2018**, *30*, 1803703.

[40] W. A. Laban and L. Etgar, *Energy Environ. Sci.* **2013**, *6*, 3249-3253.

[41] E. Edri, S. Kirmayer, A. Henning, S. Mukhopadhyay, K. Gartsman, Y. Rosenwaks, G. Hodes, D. Cahen, *Nano Lett.* **2014**, *14*, 1000-1004.

[42] B. Chen, M. Yang, S. Priya, K. Zhu, *J. Phys. Chem. Lett.* **2016**, *7*, 905-917.

[43] L. Atourki, E. Vega, B. Marí, M. Mollar, H. Ait Ahsaine, K. Bouabid, A. Ihlal, *Appl. Surf. Sci.* **2016**, *371*, 112-117.

[44] A. Kojima, K. Teshima, Y. Shirai, T. Miyasaka, *J. Am.Chem. Soc.* **2009**, *131*, 6050-6051.

[45] J.-H. Im, C.-R. Lee, J.-W. Lee, S.-W. Park, N.-G. Park, *Nanoscale* **2011**, *3*, 4088-4093.

[46] J. Burschka, N. Pellet, S.-J. Moon, R. Humphry-Baker, P. Gao, M. K. Nazeeruddin, M. Grätzel, *Nature* **2013**, *499*, 316-319.

[47] C. C. Stoumpos, C. D. Malliakas, M. G. Kanatzidis, *Inorg. Chem.* **2013**, *52*, 9019-9038.

[48] S. Pang, H. Hu, J. Zhang, S. Lv, Y. Yu, F. Wei, T. Qin, H. Xu, Z. Liu, G. Cui, *Chem. Mater.* **2014**, *26*, 1485-1491.

[49] G. E. Eperon, S. D. Stranks, C. Menelaou, M. B. Johnston, L. M. Herz, H. J. Snaith, *Energy Environ. Sci.* **2014**, *7*, 982-988.

[50] J.-W. Lee, D.-J. Seol, A.-N. Cho, N.-G. Park, *Adv. Mater.* **2014**, *26*, 4991-4998.

[51] W. S. Yang, J. H. Noh, N. J. Jeon, Y. C. Kim, S. Ryu, J. Seo, S. I. Seok, *Science* **2015**, *348*, 1234-1237.

[52] B. Cai, Y. Xing, Z. Yang, W.-H. Zhang, J. Qiu, *Energy Environ. Sci.* **2013**, *6*, 1480-1485..

[53] Y. Liang, Y. Wang, C. Mu, S. Wang, X. Wang, D. Xu, L. Sun, *Adv. Energy Mater.* **2018**, *8*, 1701159.

[54] W. S. Subhani, K. Wang, M. Du, X. Wang, N. Yuan, J. Ding, S. Liu, *J. Energy Chem.* **2019**, *34*, 12-19.

[55] N. Pellet, P. Gao, G. Gregori, T.-Y. Yang, M. K. Nazeeruddin, J. Maier, M. Grätzel, *Angew. Chem. Int. Ed.* **2014**, *53*, 3151-3157.

[56] N. J. Jeon, J. H. Noh, W. S. Yang, Y. C. Kim, S. Ryu, J. Seo, S. I. Seok, *Nature* **2015**, *517*, 476-480.

[57] S. Dastidar, D. A. Egger, L. Z. Tan, S. B. Cromer, A. D. Dillon, S. Liu, L. Kronik, A. M. Rappe, A. T. Fafarman, *Nano Lett.* **2016**, *16*, 3563-3570.

[58] B. Li, Y. Zhang, L. Fu, T. Yu, S. Zhou, L. Zhang, L. Yin, *Nat. Commun.* **2018**, *9*, 1076.

[59] P. Luo, W. Xia, S. Zhou, L. Sun, J. Cheng, C. Xu, Y. Lu, *J. Phys. Chem. Lett.* **2016**, *7*, 3603-3608.

[60] A. Swarnkar, A. R. Marshall, E. M. Sanehira, B. D. Chernomordik, D. T. Moore, J. A. Christians, T. Chakrabarti, J. M. Luther, *Science* **2016**, *354*, 92-95.

[61] T. Zhang, M. I. Dar, G. Li, F. Xu, N. Guo, M. Grätzel, Y. Zhao, *Sci. Adv.* **2017**, *3*, e1700841.

[62] C. Zuo, A. D. Scully, D. Vak, W. Tan, X. Jiao, C. R. McNeill, D. Angmo, L. Ding, M. Gao, *Adv. Energy Mater.* 2**019**, *9*, 1803258.

[63] Z. Yang, A. Surrente, K. Galkowski, A. Miyata, O. Portugall, R. J. Sutton, A. A. Haghighirad, H. J. Snaith, D. K. Maude, P. Plochocka, R. J. Nicholas, *ACS Energy Lett.* **2017**, *2*, 1621-1627.

[64] R. J. Sutton, G. E. Eperon, L. Miranda, E. S. Parrott, B. A. Kamino, J. B. Patel, M. T. Hörantner, M. B. Johnston, A. A. Haghighirad, D. T. Moore, H. J. Snaith, *Adv. Energy Mater.* **2016**, *6*, 1502458.

[65] J. K. Nam, S. U. Chai, W. Cha, Y. J. Choi, W. Kim, M. S. Jung, J. Kwon, D. Kim, J. H. Park, *Nano Lett.* **2017**, *17*, 2028-2033.

[66] C.-Y. Chen, H.-Y. Lin, K.-M. Chiang, W.-L. Tsai, Y.-C. Huang, C.-S. Tsao, H.-W. Lin, *Adv. Mater.* **2017**, *29*, 1605290.

[67] C. F. J. Lau, M. Zhang, X. Deng, J. Zheng, J. Bing, Q. Ma, J. Kim, L. Hu, M. A. Green, S. Huang, A. Ho-Baillie, *ACS Energy Lett.* **2017**, *2*, 2319-2325.

[68] D. Bai, H. Bian, Z. Jin, H. Wang, L. Meng, Q. Wang, S. Liu, *Nano Energy* **2018**, *52*, 408-415.

[69] C. Liu, W. Li, C. Zhang, Y. Ma, J. Fan, Y. Mai, *J. Am. Chem. Soc.* **2018**, *140*, 3825-3828.

[70] J. Tian, Q. Xue, X. Tang, Y. Chen, N. Li, Z. Hu, T. Shi, X. Wang, F. Huang, C. J. Brabec, H.-L. Yip, Y. Cao, *Adv. Mater.* **2019**, *31*, 1901152.

[71] S. Öz, A. K. Jena, A. Kulkarni, K. Mouri, T. Yokoyama, I. Takei, F. Ünlü, S. Mathur, T. Miyasaka, *ACS Energy Lett.* **2020**, *5*, 1292-1299.

[72] Y. Han, H. Zhao, C. Duan, S. Yang, Z. Yang, Z. Liu, S. Liu, *Adv. Funct. Mater.* **2020**, *30*, 1909972.

[73] Q. Ma, S. Huang, X. Wen, M. A. GreenA. W. Y. Ho-Baillie, *Adv. Energy Mater.* **2016**, *6*, 1502202.

[74] C. F. J. Lau, X. Deng, Q. Ma, J. Zheng, J. S. Yun, M. A. Green, S. Huang, A. W. Y. Ho-Baillie, *ACS Energy Lett.* **2016**, *1*, 573-577.

[75] C. Liu, W. Li, J. Chen, J. Fan, Y. Mai, R. E. I. Schropp, *Nano Energy* **2017**, *41*, 75-83.

[76] W. Zhu, Q. Zhang, D. Chen, Z. Zhang, Z. Lin, J. Chang, J. Zhang, C. Zhang, Y. Hao, *Adv. Energy Mater.* **2018**, *8*, 1802080.

[77] W. Zhu, Q. Zhang, C. Zhang, Z. Zhang, D. Chen, Z. Lin, J. Chang, J. Zhang, Y. Hao, *ACS Appl. Energy Mater.* **2018**, *1*, 4991-4997.

[78] Q. Zhang, W. Zhu, D. Chen, Z. Zhang, Z. Lin, J. Chang, J. Zhang, C. Zhang, Y. Hao, *ACS Appl. Mater. Interfaces* **2019**, *11*, 2997-3005..

[79] Y. Guo, X. Yin, J. Liu, W. Que, *J. Mater. Chem. A* **2019**, *7*, 19008-19016.

[80] B. Zhang, W. Bi, Y. Wu, C. Chen, H. Li, Z. Song, Q. Dai, L. Xu, H. Song, *ACS Appl. Mater. Interfaces* **2019**, *11*, 33868-33878.

[81] J. Liang, Z. Liu, L. Qiu, Z. Hawash, L. Meng, Z. Wu, Y. Jiang, L. K. Ono, Y. Qi, *Adv. Energy Mater.* **2018**, *8*, 1800504.

[82] X. Tan, X. Liu, Z. Liu, B. Sun, J. Li, S. Xi, T. Shi, Z. Tang, G. Liao, *Appl. Surf. Sci.* **2020**, *499*, 143990.

[83] P. Liu, X. Yang, Y. Chen, H. Xiang, W. Wang, R. Ran, W. Zhou, Z. Shao, *ACS Appl. Mater. Interface* **2020**, *12*, 23984-23994.

[84] H. Wang, S. Cao, B. Yang, H. Li, M. Wang, X. Hu, K. Sun, Z. Zang, *Sol. RRL* **2020**, *4*, 1900363..

[85] W. S. Subhani, K. Wang, M. Du, X. Wang, S. Liu, *Adv. Energy Mater.* **2019**, *9*, 1803785.

[86] H. Wang, H. Li, S. Cao, M. Wang, J. Chen, Z. Zang, *Sol. RLL* **2020**, *4*, 2000226.

[87] M. Kulbak, D. Cahen, G. Hodes, *J. Phys. Chem. Lett.* **2015**, *6*, 2452-2456.

[88] M. Kulbak, S. Gupta, N. Kedem, I. Levine, T. Bendikov, G. Hodes, D. Cahen, *J. Phys. Chem. Lett.* **2016**, *7*, 167-172.

[89] X. Chang, W. Li, L. Zhu, H. Liu, H. Geng, S. Xiang, J. Liu, H. Chen, *ACS Appl. Mater. Interfaces* **2016**, *8*, 33649-33655.

[90] J. Duan, T. Hu, Y. Zhao, B. He, Q. Tang, *Angew. Chem. Int. Ed.* 2018, **57**, 5746-5749.

[91] J. Duan, Y. Zhao, X. Yang, Y. Wang, B. He, Q. Tang, *Adv. Energy Mater.* **2018**, *8*, 1802346.

[92] Y. Li, J. Duan, H. Yuan, Y. Zhao, B. He, Q. Tang, *Sol. RRL* **2018**, *2*, 1800164.

[93] Y. Chen, Y. Sun, J. Peng, J. Tang, K. Zheng, Z. Liang, *Adv. Mater.* **2018**, *30*, 1703487.

[94] Y. Zheng, T. Niu, X. Ran, J. Qiu, B. Li, Y. Xia, Y. Chen, W. Huang, *J. Mater. Chem. A* **2019**, *7*, 13860-13872.

[95] P. Liu, N. Han, W. Wang, R. Ran, W. Zhou, Z. Shao, *Adv. Mater.* **2021**, *33*, 2002582.

[96] Y. Wei, H. Chu, Y. Tian, B. Chen, K. Wu, J. Wang, X. Yang, B. Cai, Y. Zhang, J. Zhao, *Adv. Energy Mater.* **2019**, *9*, 1900612.

[97] J. Qing, X.-K. Liu, M. Li, F. Liu, Z. Yuan, E. Tiukalova, Z. Yan, M. Duchamp, S. Chen, Y. Wang, S. Bai, J.-M. Liu, H. J. Snaith, C.-S. Lee, T. C. Sum, F. Gao, *Adv. Energy Mater.* **2018**, *8*, 1800185.

[98] D. H. Cao, C. C. Stoumpos, O. K. Farha, J. T. Hupp, M. G. Kanatzidis, *J. Am. Chem. Soc.* **2015**, *137*, 7843-7850.

[99] Z. Chen, Y. Guo, E. Wertz, J. Shi, *Adv. Mater.* **2019**, *31*, 1803514.

[100] P. Mao, J. Zhuang, Y. Wei, N. Chen, Y. Luan, J. Wang, *Sol. RRL* **2019**, *3*, 1800357.

[101] I. C. Smith, E. T. Hoke, D. Solis-Ibarra, M. D. McGehee, H. I. Karunadasa, *Angew. Chem. Int. Ed.* **2014**, *53*, 11232-11235.

[102] H. Tsai, W. Nie, J.-C. Blancon, C. C. Stoumpos, R. Asadpour, B. Harutyunyan, A. J. Neukirch, R. Verduzco, J. J. Crochet, S. Tretiak, L. Pedesseau, J. Even, M. A. Alam, G. Gupta, J. Lou, P. M. Ajayan, M. J. Bedzyk, M. G. Kanatzidis, A. D. Mohite, *Nature* **2016**, *536*, 312-316.

[103] J. Shi, Y. Gao, X. Gao, Y. Zhang, J. Zhang, X. Jing, M. Shao, *Adv.Mater.* **2019**, *31*, 1901673.

[104] Y. Liu, S. Akin, L. Pan, R. Uchida, N. Arora, J. V. Milić, A. Hinderhofer, F. Schreiber, A. R. Uhl, S. M. Zakeeruddin, A. Hagfeldt, M. I. Dar and M. Grätzel, *Sci. Adv.* **2019**, *5*, eaaw2543.

[105] Y. Yan, S. Yu, A. Honarfar, T. Pullerits, K. Zheng, Z. Liang, *Adv. Sci.* **2019**, *6*, 1900548.

[106] H. Lai, B. Kan, T. Liu, N. Zheng, Z. Xie, T. Zhou, X. Wan, X. Zhang, Y. Liu, Y. Chen, *J. Am. Chem. Soc.* **2018**, *140*, 11639-11646.

[107] H. Ren, S. Yu, L. Chao, Y. Xia, Y. Sun, S. Zuo, F. Li, T. Niu, Y. Yang, H. Ju, B. Li, H. Du, X. Gao, J. Zhang, J. Wang, L. Zhang, Y. Chen, W. Huang, *Nat. Photonics*, **2020**, *14*, 154-163

[108] Y. Li, H. Cheng, K. Zhao, Z.-S. Wang, *ACS Appl. Mater. Interfaces* **2019**, *11*, 37804-37811.

[109] Y. Wei, H. Chu, B. Chen, Y. Tian, X. Yang, B. Cai, Y. Zhang, J. Zhao, *Sol. Energy* **2020**, *201*, 13-20.

[110] Z. Xu, D. Lu, F. Liu, H. Lai, X. Wan, X. Zhang, Y. Liu, Y. Chen, *ACS Nano* **2020**, *14*, 4871-4881.

[111] Z. Wang, Q. Lin, F. P. Chmiel, N. Sakai, L. M. Herz, H. J. Snaith, *Nat. Energy* **2017**, *2*, 17135.

[112] L. R. V. Buizza, T. W. Crothers, Z. Wang, J. B. Patel, R. L. Milot, H. J. Snaith, M. B. Johnston, L. M. Herz, *Adv. Funct. Mater.* 2**019**, *29*, 1902656.

[113] Y. Hu, J. Schlipf, M. Wussler, M. L. Petrus, W. Jaegermann, T. Bein, P. Müller-Buschbaum, P. Docampo, *ACS Nano* **2016**, ***10***, 5999-6007.

[114] D. Yao, C. Zhang, S. Zhang, Y. Yang, A. Du, E. Waclawik, X. Yu, G. J. Wilson, H. Wang, *ACS Appl. Mater. Interfaces* **2019**, *11*, 29753-29764

[115] P. Chen, Y. Bai, S. Wang, M. Lyu, J.-H. Yun, L. Wang, *Adv. Funct. Mater.* **2018**, *28*, 1706923.

[116] D. Lin, T. Zhang, J. Wang, M. Long, F. Xie, J. Chen, B. Wu, T. Shi, K. Yan, W. Xie, P. Liu, J. Xu, *Nano Energy* **2019**, *59*, 619-625.

[117] F. Zhang, Q. Huang, J. Song, Y. Zhang, C. Ding, F. Liu, D. Liu, X. Li, H. Yasuda, K. Yoshida, J. Qu, S. Hayase, T. Toyoda, T. Minemoto, Q. Shen, *Sol. RRL* **2020**, *4*, 1900243.

[118] Y. Lin, Y. Bai, Y. Fang, Z. Chen, S. Yang, X. Zheng, S. Tang, Y. Liu, J. Zhao, J. Huang, *J. Phys.Chem. Lett.* **2018**, *9*, 654-658.

[119] G. Grancini, C. Roldán-Carmona, I. Zimmermann, E. Mosconi, X. Lee, D. Martineau, S. Narbey, F. Oswald, F. De Angelis, M. Graetzel, M. K. Nazeeruddin, *Nat. Commun.* **2017**, *8*, 15684.

[120] Y. Bai, S. Xiao, C. Hu, T. Zhang, X. Meng, H. Lin, Y. Yang, S. Yang, *Adv. Energy Mater.* **2017**, *7*, 1701038.

[121] Z. Xu, M. Chen, S. F. Liu, *J. Phys. Chem. Lett.* **2019**, *10*, 3670-3675.

[122] M.-H. Tremblay, J. Bacsa, B. Zhao, F. Pulvirenti, S. Barlow, S. R. Marder, *Chem. Mater.* **2019**, *31*, 6145-6153.

[123] Y. Li, J. V. Milić, A. Ummadisingu, J.-Y. Seo, J.-H. Im, H.-S. Kim, Y. Liu, M. I. Dar, S. M. Zakeeruddin, P. Wang, A. Hagfeldt, M. Grätzel, *Nano Lett.* **2019**, *19*, 150-157.

[124] L. Mao, W. Ke, L. Pedesseau, Y. Wu, C. Katan, J. Even, M. R. Wasielewski, C. C. Stoumpos, M. G. Kanatzidis, *J. Am. Chem. Soc.* **2018**, *140*, 3775-3783.

[125] S. Ahmad, P. Fu, S. Yu, Q. Yang, X. Liu, X. Wang, X. Wang, X. Guo, C. Li, *Joule* **2019**, *3*, 794-806.

[126] P. Huang, S. Kazim, M. Wang, S. Ahmad, *ACS Energy Lett.* **2019**, *4*, 2960-2974.

[127] M. Safdari, P. H. Svensson, M. T. Hoang, I. Oh, L. Kloo, J. M. Gardner, *J. Mater. Chem. A* **2016**, *4*, 15638-15646.

[128] M. Safdari, D. Phuyal, B. Philippe, P. H. Svensson, S. M. Butorin, K. O. Kvashnina, H. Rensmo, L. Kloo, J. M. Gardner, *J. Mater. Chem. A* **2017**, *5*, 11730-11738.

[129] W. Zhao, Q. Dong, J. Zhang, S. Wang, M. Chen, C. Zhao, M. Hu, S. Jin, N. P. Padture, Y. Shi, *J. Mater. Chem. A* **2020**, *8*, 9919-9926.

[130] B.-E. Cohen, Y. Li, Q. Meng and L. Etgar, *Nano Lett.* **2019**, *19*, 2588-2597.

[131] D. Lu, G. Lv, Z. Xu, Y. Dong, X. Ji and Y. Liu, *J. Am. Chem. Soc.* **2020**, *142*, 11114-11122.

[132] S. Yu, Y. Yan, M. Abdellah, T. Pullerits, K. Zheng, Z. Liang, *Small* **2019**, *15*, 1905081.

[133] Y. Zheng, T. Niu, J. Qiu, L. Chao, B. Li, Y. Yang, Q. Li, C. Lin, X. Gao, C. Zhang, Y. Xia, Y. Chen, W. Huang, *Sol. RRL* **2019**, *3*, 1900090.

[134] W. Ke, L. Mao, C. C. Stoumpos, J. Hoffman, I. Spanopoulos, A. D. Mohite, M. G. Kanatzidis, *Adv. Energy Mater.* **2019**, *9*, 1803384.

[135] Z. Fang, M. Shang, Y. Zheng, T. Zhang, Z. Du, G. Wang, X. Duan, K.-C. Chou, C.-H. Lin, W. Yang, X. Hou, T. Wu, *Materi. Horiz.* **2020**, *7*, 1042-1050.

[136] F. Li, J. Zhang, S. Jo, M. Qin, Z. Li, T. Liu, X. Lu, Z. Zhu, A. K.-Y. Jen, *Small Methods* **2020**, *4*, 1900831.

[137] H. Wu, X. Lian, S. Tian, Y. Zhang, M. Qin, Y. Zhang, F. Wang, X. Lu, G. Wu, H. Chen, *Sol. RRL* **2020**, *4*, 2000087.

[138] J. Peng, Y. Chen, K. Zheng, T. Pullerits, Z. Liang, *Chem. Soc. Rev.* **2017**, *46*, 5714-5729.

[139] J.-C. Blancon, W. Nie, A. J. Neukirch, G. Gupta, S. Tretiak, L. Cognet, A. D. Mohite and J. J. Crochet, *Adv. Funct. Mater.* **2016**, *26*, 4283-4292.

[140] M. B. Price, J. Butkus, T. C. Jellicoe, A. Sadhanala, A. Briane, J. E. Halpert, K. Broch, J. M. Hodgkiss, R. H. Friend, F. Deschler, *Nat. Commun.* **2015**, *6*, 8420.

[141] Z. Guo, Y. Wan, M. Yang, J. Snaider, K. Zhu, L. Huang, *Science* **2017**, *356*, 59-62.

[142] D. Shi, V. Adinolfi, R. Comin, M. Yuan, E. Alarousu, A. Buin, Y. Chen, S. Hoogland, A. Rothenberger, K. Katsiev, *Science* **2015**, *347*, 519-522.

[143] J. Peng, Y. Sun, Y. Chen, Y. Yao, Z. Liang, *ACS Energy Lett.* **2016**, *1*, 1000-1006.

[144] 144. Q. Han, S.-H. Bae, P. Sun, Y.-T. Hsieh, Y. Yang, Y. S. Rim, H. Zhao, Q. Chen, W. Shi, G. Li, Y. Yang, *Adv. Mater.* **2016**, *28*, 2253-2258.

[145] F. Thouin, S. Neutzner, D. Cortecchia, V. A. Dragomir, C. Soci, T. Salim, Y. M. Lam,

R. Leonelli, A. Petrozza, A. R. S. Kandada, *Phys. Rev. Mater.* **2018**, *2*, 034001.

[146] C. Liang, D. Zhao, Y. Li, X. Li, S. Peng, G. Shao, G. Xing, *Energy Environ. Mater.* **2018**, *1*, 221-231.

[147] J.-C. Blancon, H. Tsai, W. Nie, C. C. Stoumpos, L. Pedesseau, C. Katan, M. Kepenekian, C. M. M. Soe, K. Appavoo, M. Y. Sfeir, S. Tretiak, P. M. Ajayan, M. G. Kanatzidis, J. Even, J. J. Crochet, A. D. Mohite, *Science* **2017**, *355*, 1288-1292.

[148] Y. Zhou, O. S. Game, S. Pang and N. P. Padture, *J. Phys. Chem. Lett.* **2015**, *6*, 4827-4839

[149] Y. Zhao, K. Zhu, *J. Phys. Chem. Lett.* **2014**, *5*, 4175-4186.

[150] W. Liu, L. Li, M. Chen, X. Ding, M. Wang, G. Liu, X. Wang, *J. Alloys Compd.* **2017**, *697*, 374-379.

[151] K. Meng, X. Wang, Q. Xu, Z. Li, Z. Liu, L. Wu, Y. Hu, N. Liu, G. Chen, *Adv. Funct. Mater.* **2019**, *29*, 1902319.

[152] Z. Xiao, C. Bi, Y. Shao, Q. Dong, Q. Wang, Y. Yuan, C. Wang, Y. Gao, J. Huang, *Energy Environ. Sci.* **2014**, *7*, 2619-2623.

[153] Q. Chen, H. Zhou, Z. Hong, S. Luo, H.-S. Duan, H.-H. Wang, Y. Liu, G. Li, Y. Yang, *J. Am. Chem. Soc.* **2014**, *136*, 622-625.

[154] X. Wan, Z. Yu, W. Tian, F. Huang, S. Jin, X. Yang, Y.-B. Cheng, A. Hagfeldt and L. Sun, *J. Energy Chem.* **2020**, *46*, 8-15.

[155] J. Duan, Y. Zhao, B. He, Q. Tang, *Angew. Chem. Int. Ed.* **2018**, *57*, 3787-3791.

[156] G. Niu, X. Guo, L. Wang, *J. Mater. Chem. A* **2015**, *3*, 8970-8980.

[157] D. Wang, M. Wright, N. K. Elumalai, A. Uddin, *Sol. Energy Mater. Sol. Cells* **2016**, *147*, 255-275.

[158] J. H. Noh, S. H. Im, J. H. Heo, T. N. Mandal, S. I. Seok, *Nano Lett.* **2013**, *13*, 1764-1769.

[159] J. M. Frost, K. T. Butler, F. Brivio, C. H. Hendon, M. van Schilfgaarde, A. Walsh, *Nano Lett.* **2014**, *14*, 2584-2590.

[160] J. A. Christians, P. A. Miranda Herrera, P. V. Kamat, *J. Am. Chem. Soc.* **2015**, *137*, 1530-1538.

[161] A. Fujishima, T. N. Rao, D. A. Tryk, *J. Photoch. Photobio. C: Photoch. Rev.* **2000**, *1*, 1-21.

[162] S. Ito, S. Tanaka, K. Manabe, H. Nishino, *J. Phys. Chem. C* **2014**, *118*, 16995-17000.

[163] N. Chander, A. F. Khan, P. S. Chandrasekhar, E. Thouti, S. K. Swami, V. Dutta, V. K. Komarala, *Appl.Phys. Lett.* **2014**, *105*, 033904.

[164] B. Philippe, B.-W. Park, R. Lindblad, J. Oscarsson, S. Ahmadi, E. M. J. Johansson, H. Rensmo, *Chem. Mater.* **2015**, *27*, 1720-1731.

[165] J. Yang, B. D. Siempelkamp, E. Mosconi, F. De Angelis, T. L. Kelly, *Chem. Mater.* **2015**, *27*, 4229-4236.

[166] Y. Fang, X. Wang, Q. Wang, J. Huang, T. Wu, *Phys. Status Solidi A* **2014**, *211*, 2809-2816.

[167] L. Xiong, M. Qin, C. Chen, J. Wen, G. Yang, Y. Guo, J. Ma, Q. Zhang, P. Qin, S. Li, G. Fang, *Adv. Funct.Mater.* **2018**, *28*, 1706276.

[168] Y. Zhang, M. Liu, G. E. Eperon, T. C. Leijtens, D. McMeekin, M. Saliba, W. Zhang, M. de Bastiani, A. Petrozza, L. M. Herz, *Mater. Horiz.* **2015**, *2*, 315-322.

[169] H. J. Snaith, A. Abate, J. M. Ball, G. E. Eperon, T. Leijtens, N. K. Noel, S. D. Stranks, J. T.-W. Wang, K. Wojciechowski, W. Zhang, *J. Phys. Chem. Lett.* **2014**, *5*, 1511-1515.

[170] W. Tress, J. P. Correa Baena, M. Saliba, A. Abate, M. Graetzel, *Adv. Energy Mater.* **2016**, *6*,1600396

[171] Y. Rong, Y. Hu, S. Ravishankar, H. Liu, X. Hou, Y. Sheng, A. Mei, Q. Wang, D. Li, M. Xu, *Energy Environ. Sci.* **2017**, *10*, 2383-2391.

[172] S. Ravishankar, S. Gharibzadeh, C. Roldán-Carmona, G. Grancini, Y. Lee, M. Ralaiarisoa, A. M. Asiri, N. Koch, J. Bisquert, M. K. Nazeeruddin, *Joule* **2018**, *2*, 788-798.

[173] F. Fabregat-Santiago, M. Kulbak, A. Zohar, M. Vallés-Pelarda, G. Hodes, D. Cahen, I. n. Mora-Seró, *ACS Energy Lett.* **2017**, *2*, 2007-2013.

[174] Z. Liu, Q. Chen, J. W. Lee, Z. Zhao, X. Xu, Y. T. Hsieh, L. Meng, P. Sun, N. D. Marco, H. Zhou, *Adv. Energy Mater.* **2018**, 1800568.

[175] S. A. L. Weber, I. M. Hermes, S.-H. Turren-Cruz, C. Gort, V. W. Bergmann, L. Gilson, A. Hagfeldt, M. Graetzel, W. Tress, R. Berger, *Energy Environ. Sci.* **2018**, *11*, 2404-2413.

[176] A. Guerrero, A. Bou, G. Matt, O. Almora, T. Heumüller, G. Garcia-Belmonte, J. Bisquert, Y. Hou, C. Brabec, *Adv. Energy Mater.* **2018**, 1703376.

[177] H.-S. Kim, I.-H. Jang, N. Ahn, M. Choi, A. Guerrero, J. Bisquert, N.-G. Park, *J. Phys. Chem. Lett.* **2015**, *6*, 4633-4639.

[178] G. A. Sepalage, S. Meyer, A. R. Pascoe, A. D. Scully, U. Bach, Y.-B. Cheng, L. Spiccia, *Nano Energy* **2017**, *32*, 310-319.

[179] W. Tress, N. Marinova, T. Moehl, S. Zakeeruddin, M. K. Nazeeruddin, M. Grätzel, *Energy Environ. Sci.* **2015**, *8*, 995-1004.

[180] F. Wu, B. Bahrami, K. Chen, S. Mabrouk, R. Pathak, Y. Tong, X. Li, T. Zhang, R. Jian, Q. Qiao, *ACS Appl. Mater. Interfaces* **2018**, *10*, 25604-25613.

[181] G. A. Nemnes, C. Besleaga, V. Stancu, D. E. Dogaru, L. N. Leonat, L. Pintilie, K. Torfason, M. Ilkov, A. Manolescu, I. Pintilie, *J. Phys. Chem. C* **2017**, *121*, 11207-11214.

[182] H. Shen, D. A. Jacobs, Y. Wu, T. Duong, J. Peng, X. Wen, X. Fu, S. K. Karuturi, T. P. White, K. Weber, K. R. Catchpole, *J. Phys. Chem. Lett.* **2017**, *8*, 2672-2680.

[183] A. Babayigit, A. Ethirajan, M. Muller, B. Conings, *Nat. Mater.* **2016**, *15*, 247-251.

[184] A. Abate, *Joule* **2017**, *1*, 659-664.

[185] Y. Rong, Y. Hu, A. Mei, H. Tan, M. I. Saidaminov, S. I. Seok, M. D. McGehee, E. H. Sargent, H. Han, *Science* **2018**, *361*, eaat8235.

[186] A. Binek, M. L. Petrus, N. Huber, H. Bristow, Y. Hu, T. Bein, P. Docampo, *ACS Appl. Mater. Interfaces* **2016**, *8*, 12881-12886.

[187] F. Ünlü, E. Jung, J. Haddad, A. Kulkarni, S. Öz, H. Choi, T. Fischer, S. Chakraborty, T. Kirchartz, S. Mathur, *APL Mater.* **2020**, *8*, 070901.

[188] J. Gong, P. Guo, S. E. Benjamin, P. G. Van Patten, R. D. Schaller, T. Xu, *J. Energy Chem.* **2018**, *27*, 1017-1039.

[189] Z. Wang, Z. Shi, T. Li, Y. Chen, W. Huang, *Angew. Chem. Int. Ed.* **2017**, *56*, 1190-1212.

[190] H. J. Snaith, *J. Phys. Chem. Lett.* **2013**, 4, 3623-3630

[191] Y. Zhao, K. Zhu, *Chem. Soc. Rev.* **2016**, *45*, 655-689.

[192] J.-W. Lee, D.-H. Kim, H.-S. Kim, S.-W. Seo, S. M. Cho, N.-G. Park, *Adv. Energy*

Mater. **2015**, *5*, 1501310.

[193] C. Yi, J. Luo, S. Meloni, A. Boziki, N. Ashari-Astani, C. Grätzel, S. M. Zakeeruddin, U. Röthlisberger, M. Grätzel, *Energy Environ. Sci.* **2016**, *9*, 656-662.

[194] M. Saliba, T. Matsui, J.-Y. Seo, K. Domanski, J.-P. Correa-Baena, M. K. Nazeeruddin, S. M. Zakeeruddin, W. Tress, A. Abate, A. Hagfeldt, M. Grätzel, *Energy Environ. Sci.* **2016**, *9*, 1989-1997.

[195] M. Saliba, T. Matsui, K. Domanski, J.-Y. Seo, A. Ummadisingu, S. M. Zakeeruddin, J.-P. Correa-Baena, W. R. Tress, A. Abate, A. Hagfeldt, M. Grätzel, *Science* **2016**, ***354***, 206-209.

[196] T. Bu, X. Liu, Y. Zhou, J. Yi, X. Huang, L. Luo, J. Xiao, Z. Ku, Y. Peng, F. Huang, Y.-B. Cheng, J. Zhong, *Energy Environ. Sci.* **2017**, *10*, 2509-2515.

[197] D. J. Kubicki, D. Prochowicz, A. Hofstetter, M. Saski, P. Yadav, D. Bi, N. Pellet, J. Lewiński, S. M. Zakeeruddin, M. Grätzel, L. Emsley, *J. Am. Chem. Soc.* **2018**, 140, 3345-3351.

[198] A. D. Jodlowski, C. Roldán-Carmona, G. Grancini, M. Salado, M. Ralaiarisoa, S. Ahmad, N. Koch, L. Camacho, G. de Miguel, M. K. Nazeeruddin, *Nat. Energy* **2017**, *2*, 972-979.

[199] X. Hou, Y. Hu, H. Liu, A. Mei, X. Li, M. Duan, G. Zhang, Y. Rong, H. Han, *J. Mater. Chem. A* **2017**, *5*, 73-78.

[200] N. D. Pham, C. Zhang, V. T. Tiong, S. Zhang, G. Will, A. Bou, J. Bisquert, P. E. Shaw, A. Du, G. J. Wilson, H. Wang, *Adv. Funct. Mater.* **2019**, *29*, 1806479.

[201] W. Zhang, J. Xiong, J. Li, W. A. Daoud, *J. Mater. Chem. A* **2019**, *7*, 9486-9496.

[202] Y. Zhou, H. Xue, Y.-H. Jia, G. Brocks, S. Tao, N. Zhao, *Adv. Funct. Mater.* **2019**, *29*, 1905739.

[203] D. Liu, Q. Li, K. Wu, *RSC Adv.* **2019**, *9*, 7356-7361.

[204] Y. Wang, T. Zhang, G. Li, F. Xu, T. Wang, Y. Li, Y. Yang, Y. Zhao, *J. Energy Chem.* **2018**, *27*, 215-218.

[205] H.-L. Hsu, C.-C. Chang, C.-P. Chen, B.-H. Jiang, R.-J. Jeng, C.-H. Cheng, *J. Mater. Chem. A* **2015**, *3*, 9271-9277.

[206] M. Mateen, Z. Arain, X. Liu, A. Iqbal, Y. Ren, X. Zhang, C. Liu, Q. Chen, S. Ma, Y. Ding, M. Cai, S. Dai, *Sci. China Mater.* **2020**, DOI: 10.1007/s40843-020-1383-3.

[207] A. Buin, R. Comin, J. Xu, A. H. Ip, E. H. Sargent, *Chem. Mater.* **2015**, *27*, 4405-4412.

[208] P. Fedeli, F. Gazza, D. Calestani, P. Ferro, T. Besagni, A. Zappettini, G. Calestani, E. Marchi, P. Ceroni, R. Mosca, *J. Phys. Chem. C* **2015**, *119*, 21304-21313.

[209] Y. Chen, T. Chen, L. Dai, *Adv. Mater.* **2015**, *27*, 1053-1059.

[210] S. A. Kulkarni, T. Baikie, P. P. Boix, N. Yantara, N. Mathews, S. Mhaisalkar, *J. Mater. Chem. A* **2014**, *2*, 9221-9225.

[211] S. Dharani, H. A. Dewi, R. R. Prabhakar, T. Baikie, C. Shi, D. Yonghua, N. Mathews, P. P. Boix, S. G. Mhaisalkar, *Nanoscale* **2014**, *6*, 13854-13860.

[212] Q. Wang, M. Lyu, M. Zhang, J.-H. Yun, H. Chen, L. Wang, *J. Phys. Chem. Lett.* **2015**, *6*, 4379-4384.

[213] Q. Jiang, D. Rebollar, J. Gong, E. L. Piacentino, C. Zheng, T. Xu, *Angew. Chem. Int. Ed.* **2015**, *54*, 7617-7620.

[214] Y. Chen, B. Li, W. Huang, D. Gao, Z. Liang, *Chem. Commun.* **2015**, *51*, 11997-11999.

[215] Q. Tai, P. You, H. Sang, Z. Liu, C. Hu, H. L. W. Chan, F. Yan, *Nat. Commun.* **2016**, *7*, 11105.

[216] J. Chen, Y. Rong, A. Mei, Y. Xiong, T. Liu, Y. Sheng, P. Jiang, L. Hong, Y. Guan, X. Zhu, X. Hou, M. Duan, J. Zhao, X. Li, H. Han, *Adv. Energy Mater.* **2016**, *6*, 1502009.

[217] J. Zhang, S. Wu, T. Liu, Z. Zhu, A. K.-Y. Jen, *Adv. Funct. Mater.* **2019**, *29*, 1808833.

[218] J. Chen, S.-G. Kim, N.-G. Park, *Adv. Mater.* **2018**, *30*, 1801948.

[219] Y. Ohishi, T. Oku, A. Suzuki, *AIP Conf. Proc.* **2016**, *1709*, 020020.

[220] M. T. Klug, A. Osherov, A. A. Haghighirad, S. D. Stranks, P. R. Brown, S. Bai, J. T. W. Wang, X. Dang, V. Bulović, H. J. Snaith, A. M. Belcher, *Energy Environ. Sci.* **2017**, *10*, 236-246.

[221] P. Singh, P. J. S. Rana, P. Dhingra, P. Kar, *J. Mater. Chem. C* **2016**, *4*, 3101-3105.

[222] P.-P. Sun, Q.-S. Li, S. Feng, Z.-S. Li, *Phys. Chem. Chem. Phys.* **2016**, *18*, 14408-14418.

[223] F. Liu, C. Ding, Y. Zhang, T. S. Ripolles, T. Kamisaka, T. Toyoda, S. Hayase, T. Minemoto, K. Yoshino, S. Dai, M. Yanagida, H. Noguchi, Q. Shen, *J. Am. Chem. Soc.*

2017, *139*, 16708-16719.

[224] Y. Zong, N. Wang, L. Zhang, M.-G. Ju, X. C. Zeng, X. W. Sun, Y. Zhou, N. P. Padture, *Angew. Chem. Int. Ed.* **2017**, *56*, 12658-12662.

[225] F. Hao, C. C. Stoumpos, R. P. H. Chang, M. G. Kanatzidis, *J. Am. Chem. Soc.* **2014**, *136*, 8094-8099.

[226] Y. Zhou, Z. Zhou, M. Chen, Y. Zong, J. Huang, S. Pang, N. P. Padture, *J. Mater. Chem. A* **2016**, *4*, 17623-17635.

[227] M. M. Tavakoli, S. M. Zakeeruddin, M. Grätzel, Z. Fan, *Adv. Mater.* **2018**, *30*, 1705998.

[228] T. Jiang, Z. Chen, X. Chen, T. Liu, X. Chen, W. E. I. Sha, H. Zhu, Y. Yang, *Sol. RRL* **2020**, *4*, 1900467.

[229] M. Li, Z.-K. Wang, M.-P. Zhuo, Y. Hu, K.-H. Hu, Q.-Q. Ye, S. M. Jain, Y.-G. Yang, X.-Y. Gao, L.-S. Liao, *Adv. Mater.* **2018**, *30*, 1800258.

[230] X. Wang, Z. Zhang, J. Qin, W. Shi, Y. Liu, H. Gao, Y. Mao, *Electroch. Acta* **2017**, *245*, 839-845.

[231] D. H. Kim, G. S. Han, W. M. Seong, J.-W. Lee, B. J. Kim, N.-G. Park, K. S. Hong, S. Lee, H. S. Jung, *ChemSusChem* **2015**, *8*, 2392-2398.

[232] T. Singh, S. Öz, A. Sasinska, R. Frohnhoven, S. Mathur, T. Miyasaka, *Adv. Funct. Mater.* **2018**, *28*, 1706287.

[233] J. K. Kim, S. U. Chai, Y. Ji, B. Levy-Wendt, S. H. Kim, Y. Yi, T. F. Heinz, J. K. Nørskov, J. H. Park, X. Zheng, *Adv. Energy Mater.* **2018**, *8*, 1801717.

[234] Y. Xiao, N. Cheng, K. K. Kondamareddy, C. Wang, P. Liu, S. Guo, X.-Z. Zhao, *J. Power Sources* **2017**, *342*, 489-494.

[235] F. Zhang, K. Zhu, *Adv. Energy Mater.* **2020**, ***10***, 1902579.

[236] A. Mahapatra, D. Prochowicz, M. M. Tavakoli, S. Trivedi, P. Kumar and P. Yadav, *J. Mater. Chem. A* **2020**, *8*, 27-54.

[237] Q. Chen, H. Zhou, T.-B. Song, S. Luo, Z. Hong, H.-S. Duan, L. Dou, Y. Liu, Y. Yang, *Nano Lett.* **2014**, *14*, 4158-4163.

[238] Y. C. Kim, N. J. Jeon, J. H. Noh, W. S. Yang, J. Seo, J. S. Yun, A. Ho-Baillie, S. Huang,

M. A. Green, J. Seidel, T. K. Ahn, S. I. Seok, *Adv. Energy Mater.* **2016**, *6*, 1502104.

[239] C. Bi, X. Zheng, B. Chen, H. Wei, J. Huang, *ACS Energy Lett.* **2017**, *2*, 1400-1406.

[240] Z. Li, C. Xiao, Y. Yang, S. P. Harvey, D. H. Kim, J. A. Christians, M. Yang, P. Schulz, S. U. Nanayakkara, C.-S. Jiang, J. M. Luther, J. J. Berry, M. C. Beard, M. M. Al-Jassim, K. Zhu, *Energy Environ. Sci.* **2017**, *10*, 1234-1242.

[241] M. Abdi-Jalebi, Z. Andaji-Garmaroudi, S. Cacovich, C. Stavrakas, B. Philippe, J. M. Richter, M. Alsari, E. P. Booker, E. M. Hutter, A. J. Pearson, S. Lilliu, T. J. Savenije, H. Rensmo, G. Divitini, C. Ducati, R. H. Friend, S. D. Stranks, *Nature* **2018**, *555*, 497-501.

[242] M. Abdi-Jalebi, M. I. Dar, A. Sadhanala, S. P. Senanayak, M. Franckevičius, N. Arora, Y. Hu, M. K. Nazeeruddin, S. M. Zakeeruddin, M. Grätzel, R. H. Friend, *Adv. Energy Mater.* **2016**, *6*, 1502472.

[243] T. Li, Y. Pan, Z. Wang, Y. Xia, Y. Chen, W. Huang, *J. Mater. Chem. A* **2017**, *5*, 12602-12652.

[244] C. Liu, W. Li, H. Li, C. Zhang, J. Fan, Y. Mai, *Nanoscale* **2017**, *9*, 13967-13975.

[245] M. Li, Y.-H. Chao, T. Kang, Z.-K. Wang, Y.-G. Yang, S.-L. Feng, Y. Hu, X.-Y. Gao, L.-S. Liao, C.-S. Hsu, *J. Mater. Chem. A* **2016**, *4*, 15088-15094.

[246] K. Wang, C. Liu, P. Du, J. Zheng, X. Gong, *Energy Environ. Sci.* **2015**, *8*, 1245-1255.

[247] C.-H. Chiang, C.-G. Wu, *Nat. Photonics* **2016**, *10*, 196-200.

[248] J. Xu, A. Buin, A. H. Ip, W. Li, O. Voznyy, R. Comin, M. Yuan, S. Jeon, Z. Ning, J. J. McDowell, P. Kanjanaboos, J.-P. Sun, X. Lan, L. N. Quan, D. H. Kim, I. G. Hill, P. Maksymovych, E. H. Sargent, *Nat. Commun.* **2015**, *6*, 7081.

[249] . Wu, X. Yang, W. Chen, Y. Yue, M. Cai, F. Xie, E. Bi, A. Islam, L. Han, *Nat. Energy* **2016**, *1*, 16148.

[250] F. Zhang, W. Shi, J. Luo, N. Pellet, C. Yi, X. Li, X. Zhao, T. J. S. Dennis, X. Li, S. Wang, Y. Xiao, S. M. Zakeeruddin, D. Bi, M. Grätzel, *Adv. Mater.* **2017**, *29*, 1606806.

[251] X. Liu, F. Lin, C.-C. Chueh, Q. Chen, T. Zhao, P.-W. Liang, Z. Zhu, Y. Sun, A. K. Y. Jen, *Nano Energy* **2016**, *30*, 417-425.

[252] J. Yang, S. Xiong, T. Qu, Y. Zhang, X. He, X. Guo, Q. Zhao, S. Braun, J. Chen, J. Xu, Y. Li, X. Liu, C. Duan, J. Tang, M. Fahlman, Q. Bao, *ACS Appl. Mater. Interfaces* **2019**,

11, 13491-13498.

[253] D. Bi, C. Yi, J. Luo, J.-D. Décoppet, F. Zhang, Shaik M. Zakeeruddin, X. Li, A. Hagfeldt, M. Grätzel, *Nat. Energy* **2016**, *1*, 16142.

[254] N. K. Noel, A. Abate, S. D. Stranks, E. S. Parrott, V. M. Burlakov, A. Goriely, H. J. Snaith, *ACS Nano* **2014**, *8*, 9815-9821.

[255] Q. Zeng, X. Zhang, X. Feng, S. Lu, Z. Chen, X. Yong, S. A. T. Redfern, H. Wei, H. Wang, H. Shen, W. Zhang, W. Zheng, H. Zhang, J. S. Tse, B. Yang, *Adv. Mater.* **2018**, *30*, 1705393.

[256] H. Zhang, J. Cheng, D. Li, F. Lin, J. Mao, C. Liang, A. K.-Y. Jen, M. Grätzel, W. C. H. Choy, *Adv. Mater.* **2017**, *29*, 1604695.

[257] Z. Liu, F. Cao, M. Wang, M. Wang, L. Li, *Angew. Chem. Int. Ed.* **2020**, *59*, 4161-4167.

[258] X. Li, W. Zhang, W. Zhang, H.-Q. Wang, J. Fang, *Nano Energy* **2019**, *58*, 825-833.

[259] J. H. Heo, D. H. Song, H. J. Han, S. Y. Kim, J. H. Kim, D. Kim, H. W. Shin, T. K. Ahn, C. Wolf, T.-W. Lee, S. H. Im, *Adv. Mater.* **2015**, *27*, 3424-3430.

[260] 260. J. Huang, M. Wang, L. Ding, Z. Yang, K. Zhang, *RSC Advances* **2016**, *6*, 55720-55725.

[261] J. H. Heo, D. H. Song, S. H. Im, *Adv. Mater.* **2014**, *26*, 8179-8183.

[262] W. Zhang, M. Saliba, S. D. Stranks, Y. Sun, X. Shi, U. Wiesner, H. J. Snaith, *Nano Lett.* **2013**, *13*, 4505-4510.

[263] T.-H. Chang, C.-W. Kung, H.-W. Chen, T.-Y. Huang, S.-Y. Kao, H.-C. Lu, M.-H. Lee, K. M. Boopathi, C.-W. Chu, K.-C. Ho, *Adv. Mater.* **2015**, *27*, 7229-7235.

[264] S. N. Habisreutinger, T. Leijtens, G. E. Eperon, S. D. Stranks, R. J. Nicholas, H. J. Snaith, *Nano Lett.* **2014**, *14*, 5561-5568.

[265] Y. Zhang, L. Tan, Q. Fu, L. Chen, T. Ji, X. Hu, Y. Chen, *Chem. Commun.* **2016**, *52*, 5674-5677.

[266] Z. Arain, C. Liu, Y. Yang, M. Mateen, Y. Ren, Y. Ding, X. Liu, Z. Ali, M. Kumar, S. Dai, *Sci. China Mater.* **2019**, *62*, 161-172.

[267] Y. Wu, A. Islam, X. Yang, C. Qin, J. Liu, K. Zhang, W. Peng, L. Han, *Energy Environ. Sci.* **2014**, *7*, 2934-2938.

[268] H. Zai, D. Zhang, L. Li, C. Zhu, S. Ma, Y. Zhao, Z. Zhao, C. Chen, H. Zhou, Y. Li, Q. Chen, *J. Mater. Chem.A* **2018**, *6*, 23602-23609.

[269] J. Zhang, L. Zhang, X. Li, X. Zhu, J. Yu, K. Fan, *ACS Sustain. Chem. Eng.* **2019**, *7*, 3487-3495.

[270] G. R. Perumallapelli, S. R. Vasa, J. Jang, *Org. Electron.* **2016**, *31*, 142-148.

[271] N. J. Jeon, J. H. Noh, Y. C. Kim, W. S. Yang, S. Ryu and S. I. Seok, *Nat. Mater.* **2014**, *13*, 897-903.

[272] X. Fang, Y. Wu, Y. Lu, Y. Sun, S. Zhang, J. Zhang, W. Zhang, N. Yuan, J. Ding, *J. Materi. Chem.C* **2017**, *5*, 842-847.

[273] 273. X. Liu, K. Yan, D. Tan, X. Liang, H. Zhang and W. Huang, *ACS Energy Lett.* **2018**, *3*, 2701-2707.

[274] 274. D. Bi, W. Tress, M. I. Dar, P. Gao, J. Luo, C. Renevier, K. Schenk, A. Abate, F. Giordano, J.-P. Correa Baena, J.-D. Decoppet, S. M. Zakeeruddin, M. K. Nazeeruddin, M. Grätzel, A. Hagfeldt, *Sci. Adv.* **2016**, *2*, e1501170.

[275] X. Zheng, B. Chen, C. Wu and S. Priya, *Nano Energy* **2015**, *17*, 269-278.

[276] S. Paek, P. Schouwink, E. N. Athanasopoulou, K. T. Cho, G. Grancini, Y. Lee, Y. Zhang, F. Stellacci, M. K. Nazeeruddin, P. Gao, *Chem. Mater.* **2017**, *29*, 3490-3498.

[277] P. Zhao, B. J. Kim, X. Ren, D. G. Lee, G. J. Bang, J. B. Jeon, W. B. Kim, H. S. Jung, *Adv. Mater.* **2018**, *30*, 1802763.

[278] M. Zhang, Z. Wang, B. Zhou, X. Jia, Q. Ma, N. Yuan, X. Zheng, J. Ding, W.-H. Zhang, *Sol. RRL* **2018**, *2*, 1700213.

[279] D. Xin, Z. Wang, M. Zhang, X. Zheng, Y. Qin, J. Zhu, W.-H. Zhang, *ACS Sustain.Chem. Eng.* **2019**, *7*, 4343-4350.

[280] W. Xu, Y. Gao, W. Ming, F. He, J. Li, X.-H. Zhu, F. Kang, J. Li, G. Wei, *Adv. Mater.* **2020**, *32*, 2003965.

[281] L. Wang, X. Wang, L.-L. Deng, S. Leng, X. Guo, C.-H. Tan, W. C. H. Choy, C.-C. Chen, *Mater. Horiz.* **2020**, *7*, 934-942.

[282] W. Zhang, Y. Li, X. Liu, D. Tang, X. Li, X. Yuan, *Chem. Eng. J.* **2020**, *379*, 122298.

[283] S. Sanchez, X. Hua, N. Phung, U. Steiner, A. Abate, *Adv. Energy Mater.* **2018**, *8*,

1702915.

[284] B. Chaudhary, A. Kulkarni, A. K. Jena, M. Ikegami, Y. Udagawa, H. Kunugita, K. Ema, T. Miyasaka, *ChemSusChem* **2017**, *10*, 2473-2479.

[285] J. Peng, J. I. Khan, W. Liu, E. Ugur, T. Duong, Y. Wu, H. Shen, K. Wang, H. Dang, E. Aydin, X. Yang, Y. Wan, K. J. Weber, K. R. Catchpole, F. Laquai, S. De Wolf, T. P. White, *Adv. Energy Mater.* **2018**, *8*, 1801208.

[286] F. Meng, K. Liu, S. Dai, J. Shi, H. Zhang, X. Xu, D. Li, X. Zhan, *Mater. Chem. Front.* **2017**, *1*, 1079-1086.

[287] X. Zheng, B. Chen, J. Dai, Y. Fang, Y. Bai, Y. Lin, H. Wei, Xiao C. Zeng, J. Huang, *Nat. Energy* **2017**, *2*, 17102.

[288] M. M. Byranvand, T. Kim, S. Song, G. Kang, S. U. Ryu, T. Park, *Adv. Energy Mater.* **2018**, *8*, 1702235.

[289] J. Cao, B. Wu, R. Chen, Y. Wu, Y. Hui, B.-W. Mao, N. Zheng, *Adv. Mater.* **2018**, *30*, 1705596.

[290] Q. Wang, Q. Dong, T. Li, A. Gruverman, J. Huang, *Adv. Mater.* **2016**, *28*, 6734-6739.

[291] W. Chen, Y. Wu, J. Liu, C. Qin, X. Yang, A. Islam, Y.-B. Cheng, L. Han, *Energy Environ. Sci.* **2015**, *8*, 629-640.

[292] Z. Gu, L. Zuo, T. T. Larsen-Olsen, T. Ye, G. Wu, F. C. Krebs,H. Chen, *J.Mater. Chem. A* **2015**, *3*, 24254-24260.

[293] M. Li, X. Yan, Z. Kang, Y. Huan, Y. Li, R. Zhang, Y. Zhang, *ACS Appl. Mater. Interfaces* **2018**, *10*, 18787-18795.

[294] 294. F. Hao, C. C. Stoumpos, D. H. Cao, R. P. H. Chang, M. G. Kanatzidis, *Nat. Photonics* **2014**, *8*, 489-494.

[295] T. M. Koh, T. Krishnamoorthy, N. Yantara, C. Shi, W. L. Leong, P. P. Boix, A. C. Grimsdale, S. G. Mhaisalkar, N. Mathews, *J. Mater. Chem. A* **2015**, *3*, 14996-15000.

[296] W. Liao, D. Zhao, Y. Yu, C. R. Grice, C. Wang, A. J. Cimaroli, P. Schulz, W. Meng, K. Zhu, R.-G. Xiong, Y. Yan, *Adv. Mater.* **2016**, *28*, 9333-9340.

[297] D. Sabba, H. K. Mulmudi, R. R. Prabhakar, T. Krishnamoorthy, T. Baikie, P. P. Boix, S. Mhaisalkar, N. Mathews, *J. Phys. Chem. C* **2015**, *119*, 1763-1767.

[298] M. H. Kumar, S. Dharani, W. L. Leong, P. P. Boix, R. R. Prabhakar, T. Baikie, C. Shi, H. Ding, R. Ramesh, M. Asta, M. Graetzel, S. G. Mhaisalkar, N. Mathews, *Adv. Mater.* **2014**, *26*, 7122-7127.

[299] K. P. Marshall, M. Walker, R. I. Walton, R. A. Hatton, *Nat. Energy* **2016**, *1*, 16178.

[300] E. W.-G. Diau, E. Jokar, M. Rameez, *ACS Energy Lett.* **2019**, *4*, 1930-1937.

[301] W. Li, J. Li, J. Li, J. Fan, Y. Mai, L. Wang, *J. Mater. Chem. A* **2016**, *4*, 17104-17110.

[302] C. Wang, F. Gu, Z. Zhao, H. Rao, Y. Qiu, Z. Cai, G. Zhan, X. Li, B. Sun, X. Yu, B. Zhao, Z. Liu, Z. Bian, C. Huang, *Adv. Mater.* **2020**, *32*, 1907623.

[303] S. Tsarev, A. G. Boldyreva, S. Y. Luchkin, M. Elshobaki, M. I. Afanasov, K. J. Stevenson, P. A. Troshin, *J. Mater. Chem. A* **2018**, *6*, 21389-21395.

[304] M. Roknuzzaman, K. Ostrikov, H. Wang, A. Du, T. Tesfamichael, *Sci. Rep.* **2017**, *7*, 14025.

[305] D. Liu, Q. Li, H. Jing, K. Wu, *J. Phys. Chem. C* **2019**, *123*, 3795-3800.

[306] T. Krishnamoorthy, H. Ding, C. Yan, W. L. Leong, T. Baikie, Z. Zhang, M. Sherburne, S. Li, M. Asta, N. Mathews, S. G. Mhaisalkar, *J. Mater. Chem. A* **2015**, *3*, 23829-23832.

[307] I. Kopacic, B. Friesenbichler, S. F. Hoefler, B. Kunert, H. Plank, T. Rath, G. Trimmel, *ACS Appl. Energy Mater.* **2018**, *1*, 343-347.

[308] M. Chen, M.-G. Ju, H. F. Garces, A. D. Carl, L. K. Ono, Z. Hawash, Y. Zhang, T. Shen, Y. Qi, R. L. Grimm, D. Pacifici, X. C. Zeng, Y. Zhou, N. P. Padture, *Nat. Commun.* **2019**, *10*, 16.

[309] A. H. Slavney, T. Hu, A. M. Lindenberg, H. I. Karunadasa, *J. Am. Chem. Soc.* **2016**, *138*, 2138-2141.

[310] C. Wu, Q. Zhang, Y. Liu, W. Luo, X. Guo, Z. Huang, H. Ting, W. Sun, X. Zhong, S. Wei, S. Wang, Z. Chen, L. Xiao, *Adv. Sci.* **2018**, *5*, 1700759.

[311] M. Wang, P. Zeng, S. Bai, J. Gu, F. Li, Z. Yang, M. Liu, *Sol. RRL* **2018**, *2*, 1800217.

[312] M. Pantaler, K. T. Cho, V. I. E. Queloz, I. García Benito, C. Fettkenhauer, I. Anusca, M. K. Nazeeruddin, D. C. Lupascu, G. Grancini, *ACS Energy Lett.* **2018**, *3*, 1781-1786.

[313] C.-W. Chen, H.-W. Kang, S.-Y. Hsiao, P.-F. Yang, K.-M. Chiang, H.-W. Lin, *Adv. Mater.* **2014**, *26*, 6647-6652.

[314] H. Chen, F. Ye, W. Tang, J. He, M. Yin, Y. Wang, F. Xie, E. Bi, X. Yang, M. Grätzel, L. Han, *Nature* **2017**, *550*, 92-95.

[315] X. Li, D. Bi, C. Yi, J.-D. Décoppet, J. Luo, S. M. Zakeeruddin, A. Hagfeldt, M. Grätzel, *Science* **2016**, *353*, 58-62.

[316] A. T. Barrows, A. J. Pearson, C. K. Kwak, A. D. F. Dunbar, A. R. Buckley, D. G. Lidzey, *Energy Environ. Sci.* **2014**, *7*, 2944-2950.

[317] S. Das, B. Yang, G. Gu, P. C. Joshi, I. N. Ivanov, C. M. Rouleau, T. Aytug, D. B. Geohegan, K. Xiao, *ACS Photonics* **2015**, *2*, 680-686.

[318] H. Huang, J. Shi, L. Zhu, D. Li, Y. Luo, Q. Meng, *Nano Energy*, **2016**, *27*, 352-358.

[319] Y. Chen, L. Zhang, Y. Zhang, H. Gao, H. Yan, *RSC Adv.* **2018**, *8*, 10489-10508.

[320] S. Razza, F. Di Giacomo, F. Matteocci, L. Cinà, A. L. Palma, S. Casaluci, P. Cameron, A. D'Epifanio, S. Licoccia, A. Reale, T. M. Brown, A. Di Carlo, *J. Power Sources* **2015**, *277*, 286-291.

[321] S.-G. Li, K.-J. Jiang, M.-J. Su, X.-P. Cui, J.-H. Huang, Q.-Q. Zhang, X.-Q. Zhou, L.-M. Yang, Y.-L. Song, *J. Mater. Chem. A* **2015**, *3*, 9092-9097.

[322] J. H. Kim, S. T. Williams, N. Cho, C.-C. Chueh, A. K.-Y. Jen, *Adv. Energy Mater.* **2015**, *5*, 1401229.

[323] P. Li, C. Liang, B. Bao, Y. Li, X. Hu, Y. Wang, Y. Zhang, F. Li, G. Shao, Y. Song, *Nano Energy* **2018**, *46*, 203-211.

[324] C. Li, J. Yin, R. Chen, X. Lv, X. Feng, Y. Wu, J. Cao, *J. Am.. Chem. Soc.* **2019**, *141*, 6345-6351.

[325] S.-W. Lee, S. Bae, D. Kim, H.-S. Lee, *Adv. Mater.* **2020**, DOI: 10.1002/adma.202002202.

[326] C. Yin, J. Lu, Y. Xu, Y. Yun, K. Wang, J. Li, L. Jiang, J. Sun, A. D. Scully, F. Huang, J. Zhong, J. Wang, Y.-B. Cheng, T. Qin, W. Huang, *Adv. Energy Mater.* **2018**, *8*, 1800538.

[327] D. Yang, R. Yang, S. Priya, S. Liu, *Angew. Chem. Int. Ed.* **2019**, *58*, 4466-4483.

[328] Z. Wang, X. Liu, Y. Lin, Y. Liao, Q. Wei, H. Chen, J. Qiu, Y. Chen, Y. Zheng, *J. Mater. Chem. A* **2019**, *7*, 2773-2779.

[329] F. Deng, X. Li, X. Lv, J. Zhou, Y. Chen, X. Sun, Y.-Z. Zheng, X. Tao, J.-F. Chen, *ACS*

Appl. Energy Mater. **2020**, *3*, 401-410.

[330] H. Rao, S. Ye, F. Gu, Z. Zhao, Z. Liu, Z. Bian, C. Huang, *Adv. Energy Mater.* **2018**, *8*, 1800758.

[331] Y. Wang, T. Zhang, F. Xu, Y. Li and Y. Zhao, *Sol. RRL* **2018**, *2*, 1700180.

[332] M. B. Faheem, B. Khan, C. Feng, M. U. Farooq, F. Raziq, Y. Xiao, Y. Li, *ACS Energy Lett.* **2020**, *5*, 290-320.

[333] B. J. Kim, D. H. Kim, Y.-Y. Lee, H.-W. Shin, G. S. Han, J. S. Hong, K. Mahmood, T. K. Ahn, Y.-C. Joo, K. S. Hong, N.-G. Park, S. Lee, H. S. Jung, *Energy Environ. Sci.* **2015**, *8*, 916-921.

[334] D. Yang, R. Yang, J. Zhang, Z. Yang, S. Liu, C. Li, *Energy Environ. Sci.* **2015**, *8*, 3208-3214.

[335] S. S. Shin, W. S. Yang, J. H. Noh, J. H. Suk, N. J. Jeon, J. H. Park, J. S. Kim, W. M. Seong, S. I. Seok, *Nat. Commun.* **2015**, 6, 7410.

[336] K. Wang, Y. Shi, L. Gao, R. Chi, K. Shi, B. Guo, L. Zhao, T. Ma, *Nano Energy* 2017, *31*, 424-431.

Chapter 3 A Bilateral Cyano Molecule Serving as an Effective Additive Enables High-Efficiency and Stable Perovskite Solar Cells

Abstract

The existence of defects in perovskite films is a major obstacle that prevents perovskite solar cells (PSCs) from high efficiency and long-term stability. A variety of additives have been introduced into perovskite films for reducing the number of defects. Lewis base-based additive engineering has been considered as an effective way to eliminate defects, especially the defects caused by the uncoordinated Pb^{2+}. In this work, for the first time, a bilateral cyano molecule (succinonitrile, SN) which is a commonly used plasticizer in solid electrolyte of solid-state lithium batteries was selected as an additive to modify organic-inorganic hybrid perovskite films in PSCs. SN is featured with two cyano groups (-C≡N) distributing at both terminals of the carbon chain, providing two cross-linking points to interact with perovskites crystals via coordinating with uncoordinated Pb^{2+} and forming hydrogen bonds with $-NH_2$ groups in perovskite. It was found that the addition of SN into perovskite precursor solution could effectively reduce defects, particularly inhabit the appearance of Pb^0 and thus suppress trap-assisted nonradiative charge carrier recombination. As a result, the efficiency of $CH_3NH_3PbI_3(Cl)$ ($MAPbI_3(Cl)$)-based PSCs was improved from 18.4% to 20.3% with enhanced long-term stability at N_2 and humid air atmosphere. This work provides a facile and effective strategy to enhance the PCE and stability of PSCs simultaneously, facilitating the commercialization of PSCs.

3.1 Introduction

During the past 10 years, perovskite solar cells (PSCs) as a rising star in the photovoltaic field have experienced rapid increase in the photovoltaic performance. Particularly, the power conversion efficiency (PCE) of PSCs has been boosted to exceed 25%, which is almost comparable to that of commercialized silicon solar cells.[1–4] According to the Shockley-Queisser theory, the PCE of PSCs can reach as high as 30%, so there is still a long way to go for further improving the PCE of PSCs.[5,6] From the perspective of stability, the inorganic-organic hybrid halide perovskite-based PSCs which have been reported to deliver higher efficiency than other perovskite light absorbers-based PSCs however suffer from severe stability problem and are sensitive to high temperatures and water. To settle this issue, numerous efforts have been devoted to improve the long-term operational stability of PSCs.[7–11]

Among various factors influencing the PCE and stability of PSCs, defect-induced nonradiative recombination is a major obstacle that impedes the realization of high PCE and long-term stability of PSCs.[12–16] Defects not only exist in the interfaces between different functional layers but also appear in the grain boundaries and the bulk grains of perovskite films, because the inorganic-organic hybrid halide perovskite film is polycrystalline and is composed of many small perovskite grains.[17,18] Previous reports have pointed out various types of defects in $MAPbI_3$ perovskite films, including vacancy defects (V_I, V_{Pb}, V_{MA}), interstitial defects (I_i, Pb_i, MA_i) and substitution defects (MA_I, Pb_I, MA_{Pb}, Pb_{MA}, I_{MA}, I_{Pb}).[19,20] These defects would trap electrons and holes during the charge transporting process and these trapped immobile charges will recombine with free-moving electrons or holes, consequently degrading the photovoltaic performance. Furthermore, due to the presence of defects, grain boundaries are more easily invaded by water and have been regarded as the performance deterioration factor.[21] Thus, it is very imperative and significant to reduce defects in perovskite films via a variety of effective strategies.[15,19,22,23]

Additive engineering has become one of effective approaches to eliminate various defects via introducing some functional materials into perovskite films.[20,24,25] The existence of the uncoordinated Pb^{2+} has an adverse impact on the device photovoltaic performance, particularly preventing PSCs from high fill factor (FF) and open-circuit voltage (V_{oc}) as they act as deep-level traps to lead to nonradiative charge carrier recombination. On the other hand, these uncoordinated Pb^{2+} jeopardize the long-term stability of PSCs because they will result in the formation of new deep-level defects during the aging process, which will further weaken the device performance.[26–29] In consideration of the positive charge of uncoordinated Pb^{2+}, Lewis bases as electron donors can perform well in reducing these defects via interacting with uncoordinated Pb^{2+} .[20]

Various O-donor, S-donor and N-donor Lewis bases have been presented to regulate the crystal growth and the perovskite film formation process to minimize the defects via coordinating with uncoordinated Pb^{2+}. [30] Moreover, Lewis bases often have the ability to form hydrogen-bonding interactions with organic-inorganic hybrid halide perovskites, potentially providing possibilities for the passivation of defects at grain boundaries.[20,31,32] For example, a O-donor Lewis base, ethyl cellulose (EC) as an additive has been reported to passivate defects via the formed hydrogen-bonding interactions.[33] As for S-donor and N-donor Lewis base additives, thiourea is a typical representative which has two amino groups and one S-donor. When introducing it into $MAPbI_3$ perovskites, amino groups and S-donor can generate hydrogen-bonding interactions with I and the $-NH_2$ groups in the perovskite, respectively, while the S-donor also plays an important role in forming Lewis acid-base adducts with Pb, thereby significantly reducing defects and enhancing device performance.[34,35] In addition, numerous $-NH_2$ derivatives have been extensively studied as Lewis base additives to eliminate defects in perovskites.[36,37] Long-chain oleylamine (OA) ligands have been reported to spontaneously anchor on the $MAPbI_3$ perovskite films to reduce defects, simultaneously enhancing efficiency and stability of PSCs.[38] In another case, bilateral alkylamine additives have been proven to be capable of passivating defects at the perovskite film surface and reinforcing grain boundaries.[39] However, there is rare report on employing bilateral cyano molecules as additives to lessen defects in perovskite films.

Herein, for the first time, a bilateral cyano molecule, succinonitrile (SN) with two cyano groups ($-C\equiv N$) distributing at both ends of the short carbon chain, which is a commonly used plasticizer in solid electrolyte of solid-state lithium batteries, is utilized as an additive to modify the $MAPbI_3(Cl)$ perovskite films to effectively reduce defects in the perovskite film for highly efficient and stable PSCs.[40,41] It is found that SN additive could reduce the appearance of Pb^0 in the perovskite film and allow perovskite grains to grow in contact with each other more tightly because -N with lone-pair electrons in cyano group can coordinate with uncoordinated Pb^{2+} and form hydrogen bonding with $-NH_2$ groups in perovskite crystals. As a result, the PCE of $MAPbI_3(Cl)$-based PSCs was enhanced from 18.4% to 20.3% with obviously increased *FF* and V_{oc}. At the same time, the incorporation of SN protected the perovskite film from water invasion and other environmental factors such as air, thereby improving the device stability. By carefully tailoring the amount of SN additive, the device with optimized SN amount remained over 90% of their initial PCE after storage in N_2 for a long period of 7 months and in humid air for 530 h. This work provides some useful guidelines for the design and fabrication of high-efficiency and stable PSCs, promoting the commercialization of this technology.

3.2 Experimental section

3.2.1 Materials

All materials and reagents used in this work were directly utilized as received without any purification. 75% titanium diisopropoxide bis(acetylacetonate in isopropoxide (Sigma-Aldrich, 99.999%), TiO_2 paste (30NR-D), Methylammonium iodide (MAI, ≥99.5%, 6 times purification, Xi'an Polymer Light Technology Corp.), lead iodide (PbI_2, >99.99%, Xi'an Polymer Light Technology Corp.), lead chloride ($PbCl_2$, >99.99%, Xi'an Polymer Light Technology Corp.) 2,2′,7,7′-tetrakis (N,N-di-p-methoxyphenylamine)-9,9′-spirobifluorene (Spiro-OMeTAD, Xi'an Polymer Light Technology Corp.), Li-bis(trifluoromethanesulfonyl)imide (Li-TFSI, 99.95%, Sigma-Aldrich), Tris(2-(1H-pyrazol-1-yl)-4-tert-butylpyridine)-cobalt(III)Tris(bis(trifluoromethylsulfonyl)imide)) (FK209, 99.5%, Xi'an Polymer Light Technology), PEDOT:PSS (1-3 wt % solution in water, Xi'an Polymer Light Technology Corp.), N,N-Dimethylformamide (DMF, 99.8%, anhydrous, Aladdin), dimethyl sulfoxide (DMSO, 99.8%, anhydrous, Aladdin), chlorobenzene (CB, 99.5%, anhydrous, Aladdin), n-Butanol (99.8%, anhydrous, Aladdin)

3.2.2 Device fabrication

F^- doped tin oxide (FTO) glass was successively cleaned with acetone, isopropanol, deionized water and ethanol for 30 min, respectively. After the treatment of oxygen plasma cleaning for 5 min, compact TiO_2 (c-TiO_2) layer was fabricated via spin-coating 0.15 M titanium diisopropoxide bis(acetylacetonate) solution and then annealing at 500 ºC for 30 min.

Followed by this, mesoporous TiO_2 (m-TiO_2) layer was prepared via spin-coating TiO_2 paste (Great cell, 30NR-D) in ethanol (1:6, mass ratio) and annealing at 500 °C for 30 min. After the treatment of oxygen plasma cleaning for 5 min, the substrates were transferred into a N_2-filled glove box to prepare the perovskite layer. The perovskite layer was obtained via spin-coating 1.2 M perovskite precursor solution for 30 s, in which (0.005 g $PbCl_2$, 0.5532 g PbI_2, 0.1907 g MAI were dissolved in the mixed solvents of DMF and DMSO (7:3 in volume). For SN modified perovskite layers, different amounts of SN in DMF and DMSO solution (0.33, 0.66 and 1.00 mg mL^{-1}) were introduced into the perovskite precursor solution. During the spin-coating process, 100 uL chlorobenzene as antisolvent was added, followed by annealing at 100 °C for 5 min. Then, hole-transporting layer (HTL) was fabricated via spin-coating the spiro-OMeTAD solution on top of the formed perovskite layer at 4000 rpm for 30 s. Finally, a 100 nm-thick Ag electrode layer with the active area of 0.0625 cm^2 was thermally evaporated onto the HTL to obtain complete PSCs with the configuration of FTO/c-TiO_2/m-TiO_2/$MAPbI_3$(Cl)/spiro-OMeTAD/Ag.

3.2.3 Characterization

The crystallinity of perovskites was examined by X-ray diffraction (XRD) patterns (Rigaku Smartlab equipped with Cu $K\alpha$ radiation). PerkinElmer (PE) Lambda 750s spectrometer (PerkinElmer, USA) and PE fluorescence spectrometer (FL 6500) were utilized to measure ultraviolet-visible (UV-vis) spectra and photoluminescence (PL) spectra, respectively. The time-resolved photoluminescence (TRPL) curves were carried out on a fluorescence spectrophotometer (Edinburgh Instruments, FLS980). As for PL spectra and TRPL spectra test, the perovskite films were deposited on glass substrates and the excitation light irradiated from the perovskite film side. X-ray photoelectron spectroscopy (XPS) spectra were obtained by XPS spectrometer (PHI5000 Versa Probe) with an Al $K\alpha$ X-ray source. The surface morphology of perovskite films and the cross-sectional morphology of devices were observed by field emission SEM (HITACHI S-4800). The surface roughness of perovskite films was measured via AFM (Horiba, SmartSPM).

Photocurrent density-voltage (J-V) curves of PSCs were tested under AM 1.5G illumination at 100 mW cm^{-2} via using a solar simulator (Zolix). A standard silicon solar cell was used to calibrate the light intensity. External quantum efficiency (EQE) spectra were conducted by a Zolix Solar Cell Scan 100 instrument. The electrochemical impedance spectroscopy (EIS) measurements were carried out on an electrochemical workstation (CHI760E) under dark conditions at a fixed bias of 0.9 V.

3.3 Results and discussion

In this study, a small amount of $PbCl_2$ was utilized to fabricate $MAPbI_3$ perovskite so we defined the pristine perovskite as $MAPbI_3(Cl)$. Mesoporous-structured PSCs (**Figure 3.1a**) were fabricated, in which $MAPbI_3(Cl)$ served as the light absorber and different amounts of SN additive were introduced into this perovskite layer. To investigate whether the SN incorporation was beneficial to the enhancement of photovoltaic performance of $MAPbI_3(Cl)$-based PSCs or not, we first tested J-V curves of the corresponding PSCs without and with different amounts of SN additive. As shown in **Figure 3.1b**, PSCs with SN modified $MAPbI_3(Cl)$ as light absorbers exhibited significantly improved photovoltaic performance compared with pristine PSCs without the SN modification. The champion PCE that the pristine PSCs without SN achieved was 18.4% (average: 17.1%) with a J_{sc} of 23.8 mA cm^{-2} (average: 23.2 mA cm^{-2}), a V_{oc} of 1.04 V (average: 1.03 V) and an FF of 0.739 (average: 0.719). By contrast, a small quantity of SN addition (0.33 mg mL^{-1}) noticeably boosted the PCE to 20.3% (average: 19.5%) but further increasing the SN addition amount slightly decreased the PCE of PSC, which was still higher than that of pristine PSCs without SN. The PSCs with 0.66 and 1.00 mg mL^{-1} SN addition delivered the champion PCE of 19.6% (average: 19.2%) and 19.4% (average: 18.9%), respectively. **Figure 3.1c** gives the external quantum efficiency (EQE) spectra, where the integrated J_{sc} from the EQE spectra is well coincident with the J_{sc} obtained from the corresponding J-V curves. In addition, the short-term (200 s) stability under a given voltage near the maximum power point voltage with continuous light illumination and exposure to the humid ambient air is displayed in **Figure 3.1d**. 0.33 mg ml^{-1} SN modified PSCs possessed higher stabilized PCE than pristine PSCs without BAN addition.

The distribution of various photovoltaic performance parameters is summarized in **Figure 3.2** via testing 30 devices of every sample. 0.33 mg mL^{-1} SN modified PSCs exhibited a narrower PCE distribution range than pristine PSCs, indicating better reproducibility and higher reliability. From **Figure 3.2c** and **d**, it can be found that V_{oc} and FF were obviously improved to 1.08 V (average: 1.07 V) and 0.776 (average: 0.753) after 0.33 mg mL^{-1} SN was added, contributing to the improved PCE and implying the important role of SN addition in reducing defects.[19,38,42–44] The detailed photovoltaic performance parameters from *J-V* curves are listed in **Table 3.1**. Besides, it is well known that hysteresis is a common problem of PSCs, which can be reflected by the deviation of the photovoltaic performance measured at different scan directions.[45] Hysteresis index ($HI= (PCE_{reverse}-PCE_{forward})/PCE_{reverse}$) has been calculated to evaluate the influence of SN addition on the hysteresis behavior. As shown in **Figure 3.3**, although all PSCs in this work exhibited relatively obvious hysteresis phenomenon, the SN addition relieved this hysteresis behavior with reducing the HI value from 0.35 to 0.25. The relieved hysteresis phenomenon may be attributed to the merits brought by SN, such as the reduced defects and the suppressed charge recombination, which have been explored in detail later.

Table 3.1 Photovoltaic performance parameters from *J-V* curves

Device	J_{sc} (mA cm^{-2})		V_{oc} (V)		FF		PCE (%)	
	Best	Average	Best	Average	Best	Average	Best	Average
w/o	23.8	23.2	1.04	1.03	0.739	0.719	18.4	17.1
0.33 mg mL^{-1}	24.2	24.2	1.08	1.07	0.776	0.753	20.3	19.5
0.66 mg mL^{-1}	24.1	24.1	1.09	1.06	0.741	0.748	19.6	19.2
1.00 mg mL^{-1}	23.8	24.0	1.09	1.06	0.744	0.744	19.4	18.9

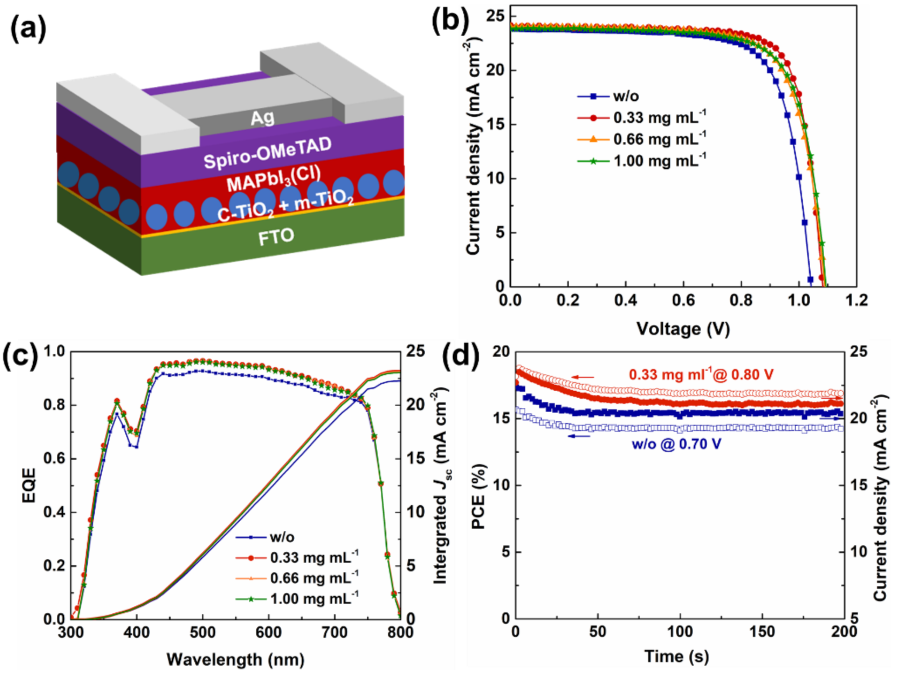

Figure 3.1 (a) Device structure of $MAPbI_3(Cl)$-based PSCs. (b) *J-V* curves, (c) EQE spectra, of $MAPbI_3(Cl)$-based PSCs without and with SN addition. (d) Short-term stability test under a given voltage near the maximum power point of $MAPbI_3(Cl)$-based PSCs without and with 0.33 mg ml^{-1} SN.

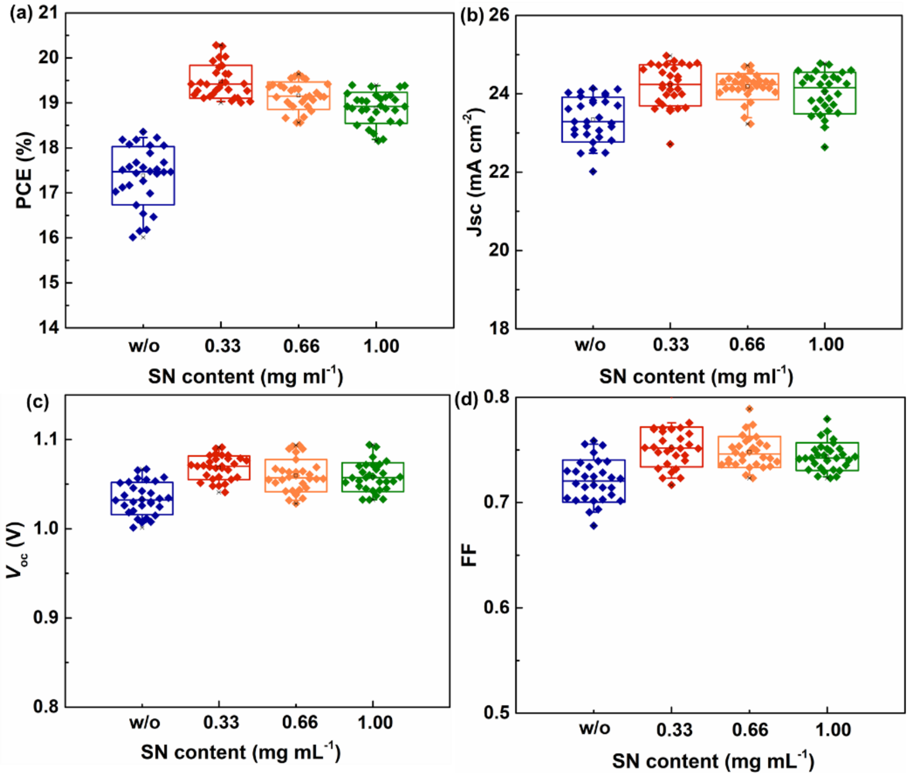

Figure 3.2 The distribution of (a) PCE, (b) FF, (c) J_{sc} and (d) V_{oc} of tested 30 devices.

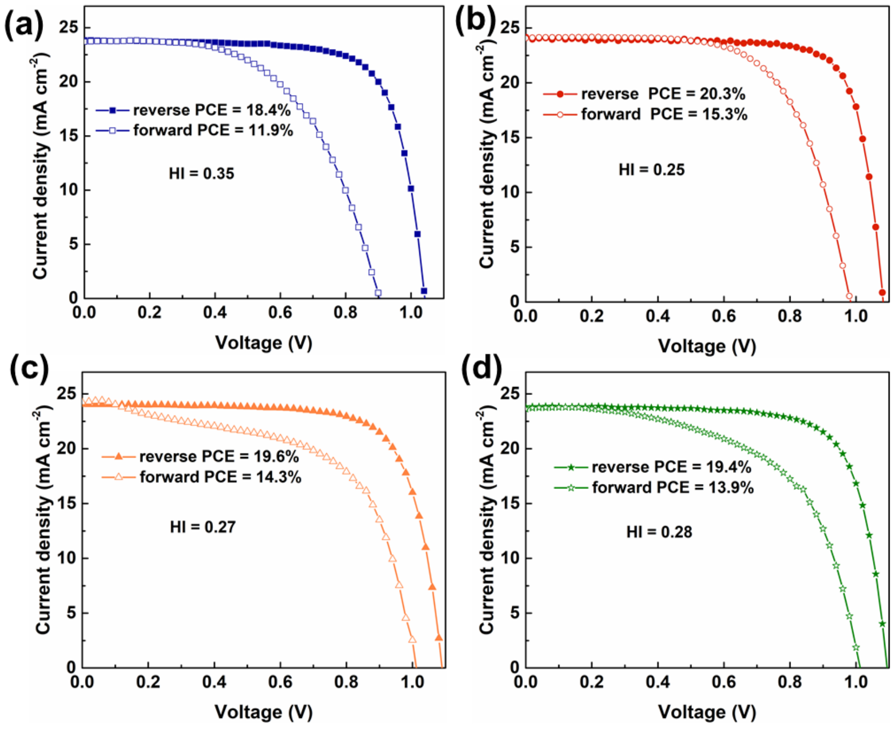

Figure 3.3 *J-V* curves measured at forward and reverse scan directions.

To clarify the influences of SN addition on the photovoltaic performance of the PSCs and how it worked in the $MAPbI_3(Cl)$ perovskite films, we first investigated the crystallinity of the perovskite films via XRD patterns as shown in **Figure 3.4a.** The main diffraction peaks at 14.2° and 28.5 ° can be assigned to (110) and (220) planes of halide perovskite. No significant shift of peaks was found, suggesting that SN was not incorporated into the $MAPbI_3$ crystal structure. This may be because too large molecular size makes it difficult to enter into the perovskite crystal and only allows them to locate at the periphery of the perovskite grains via the two cyano groups interacting with uncoordinated Pb^{2+} exposed at the surface.[39] The intensity and the full width at half maximum (FWHM) of the (110) diffraction peak are shown in **Figure 3.4b**. It is clear that a small amount of SN enhanced the intensity and decreased the FWHM, demonstrating that a small amount of SN addition improved the crystallinity of the perovskite film but the crystallinity slightly decreased with further increased SN amount.

To investigate the effects of SN addition on the light absorption intensity of perovskite light absorbers, UV-vis spectra and PL spectra were tested and presented in **Figure 3.5a** and **Figure 3.5c** respectively. The SN addition did not change the absorption onset but enhanced the light absorption intensity, suggesting that the SN addition showed negligible effect on the band gap (~1.60 eV, **Figure 3.5b**) and just improved the light absorbing capability of perovskite films, which is beneficial to the generation of higher photocurrent density. In addition, PL spectra tested via fabricating perovskite films on non-conductive glass showed that the PL intensity was obviously improved after SN addition, demonstrating that SN addition helped to reduce defects in perovskite films, benefiting to the photovoltaic performance.[46] Additionally, TRPL spectroscopy was performed to investigate the impact of SN addition on the excitonic behavior of perovskites films as shown in **Figure 3.5d**. The TRPL curves were fitted to biexponential decay equation of $I\ (t) = I_0 + A_1\exp\ (-t/\tau_1) + A_2\exp\ (-t/\tau_2)$, where τ_1 and τ_2 represent the fast decay time and slow decay time, respectively, reflecting the trap-assisted nonradiative charge recombination lifetime and the radiative charge recombination lifetime, respectively.[37,44, 47] According to the fitting results of TRPL profiles (**Figure 3.5d**), the fast decay time for pristine $MAPbI_3(Cl)$ and 0.33, 0.66 and 1.00 mg mL^{-1} SN modified $MAPbI_3(Cl)$ was 34.53, 47.99, 42.96 and 15.35 ns, respectively, while the corresponding slow decay time was 154.8, 280.9, 251.0 and 160.1 ns, respectively. Additionally, the average charge lifetime of perovskite films was calculated. With the assistance of 0.33 and 0.66 mg mL^{-1} SN addition, the average charge lifetime of $MAPbI_3(Cl)$ was improved from 136.5 ns to 259.2 and 229.2 ns, respectively. This result is indicative of the effectively suppressed nonradiative charge recombination via decreasing trap densities, thereby achieving the obvious increase in V_{oc}.

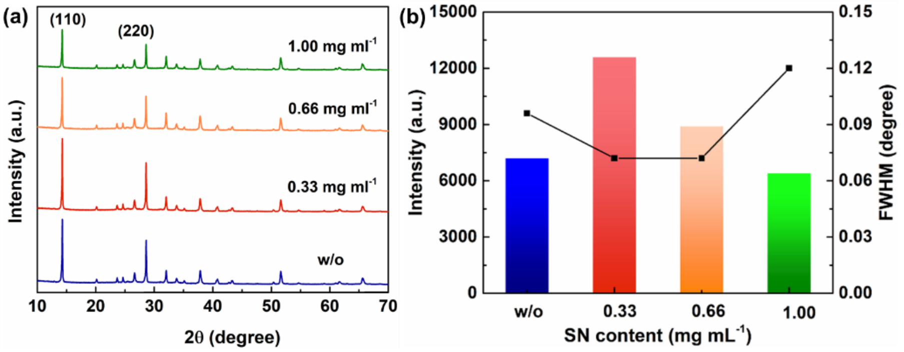

Figure 3.4 (a) XRD patterns and (b) intensity and FWHM of (110) diffraction peaks for

perovskite films without and with different amount of SN fabricated in glove box after annealing treatment.

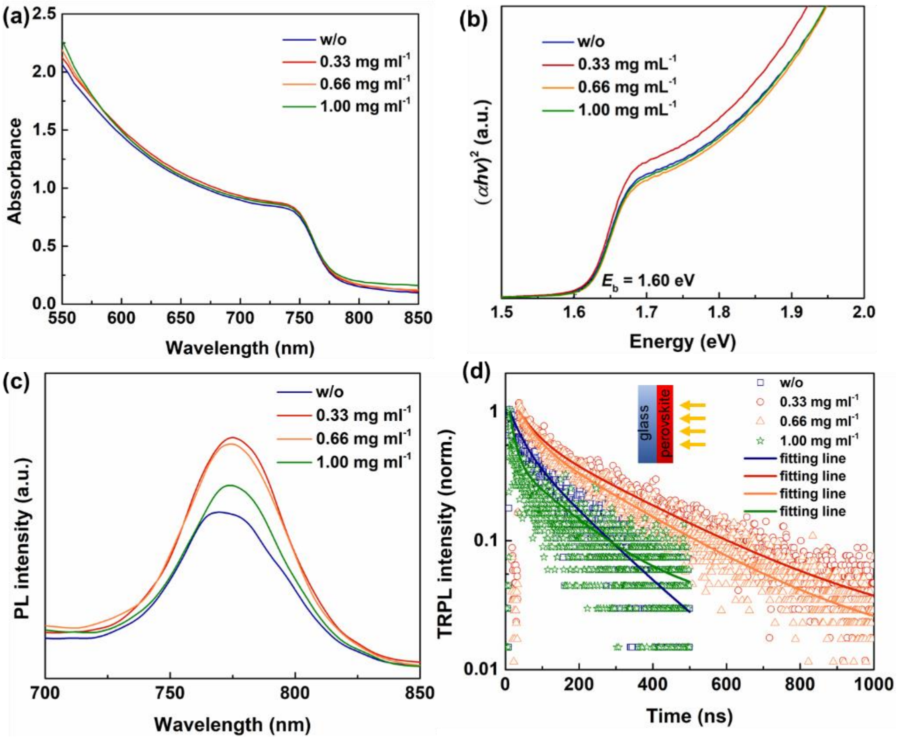

Figure 3.5 (a) UV-vis spectra, (b) Tauc plots, (c) PL spectra and (d) TRPL spectra of $MAPbI_3(Cl)$ perovskite films without and with different amounts of SN additive.

Table 3.2 Fitted results of TRPL spectroscopy

Sample	τ_1 (ns)	τ_1 ratio (%)	τ_2 (ns)	τ_2 ratio (%)	average τ (ns)
w/o	34.53	15.22	154.8	84.78	136.5
0.33 mg mL^{-1}	47.99	9.29	280.9	90.71	259.2
0.66 mg mL^{-1}	42.96	10.50	251.0	89.50	229.2
1.00 mg mL^{-1}	15.35	13.37	160.1	86.63	141.3

XPS was carried out to investigate whether SN still existed in the final perovskite films or it just participated in the film formation process and was removed during the annealing process and to study the interactive effect between SN and perovskites. In the C 1*s* spectrum (**Figure 3.6a**) of $MAPbI_3(Cl)$ perovskite films, the peaks at about 284.8 and 286.6 eV represent the -C-C and -C-N bonds from MA^+ and the peak at about 402.3 eV in the N 1*s* spectrum (**Figure 3.6b**) also corresponds to -C-N bond.[48,49] After the SN incorporation, the peaks around 285.7 eV in the C 1*s* spectrum and 400.2 eV in the N 1*s* spectrum were observed, which can be ascribed to the -C≡N bonds, confirming the presence of SN in the final perovskite films. In addition, a small peak of Pb^0 $4f_{7/2}$ at around 136.8 eV was observed in pristine perovskite films but it disappeared in SN-modified perovskites films (**Figure 3.6c**). Based on previous reports, uncoordinated Pb^{2+} in perovskite films is susceptible to reduction reactions, thus leading to the formation of metallic Pb (Pb^0).[29,43,50] Thus, the disappearance of Pb^0 after SN addition indicates that SN can interact with uncoordinated Pb^{2+} to reduce the defects. We also estimated the Pb/I ratio in the film via XPS spectra (**Table 3.3**), which decreased from 0.4444 for the pristine film to 0.4279 for 0.33 mg mL^{-1} SN modified films. Stoichiometrically, the Pb/I ratio should be 0.33. The larger Pb/I means the existence of uncoordinated Pb^{2+} at the surface of these perovskite films but the relatively smaller Pb/I ratio for SN-modified films proves again that SN addition is capable to reduce defects via interacting with uncoordinated Pb^{2+}.[50,51] Furthermore, the signal peaks of N 1*s*, Pb 4*f* and I 3*d* (**Figure 3.6d**) shifted to lower binding energy after SN incorporation, indicative of the change of the chemical environment caused by the interaction between SN additive and $MAPbI_3(Cl)$. Specifically, the nitrogen atom in -C≡N with lone-pair electrons can coordinate with those uncoordinated Pb^{2+} of perovskite and also form hydrogen bonding interaction with the $-NH_2$ in perovskite, which is favorable for defect passivation. Additionally, no characteristic peak of Cl was detected in all samples (**Figure 3.6e**), indicating that Cl^- just aided to optimize the film formation process and it would not retain in the films, which was consistent with previous reports discussing about the role of Cl^- for perovskite films.[52,53]

Table 3.3 Atomic concentration (%) of various elements at the surface of different perovskite films from XPS spectra.

Samples	I 3*d*	Pb 4*f*	C 1*s*	N 1*s*	Cl 2*p*	Pb/I ratio
w/o	35.62	15.83	41.67	6.87	0.00	0.444413
0.33 mg mL^{-1}	25.73	11.01	51.95	11.31	0.00	0.427905
0.66 mg mL^{-1}	20.03	8.77	59.63	11.57	0.00	0.437843

1.00 mg mL^{-1}	19.38	8.17	59.16	13.29	0.00	0.421569

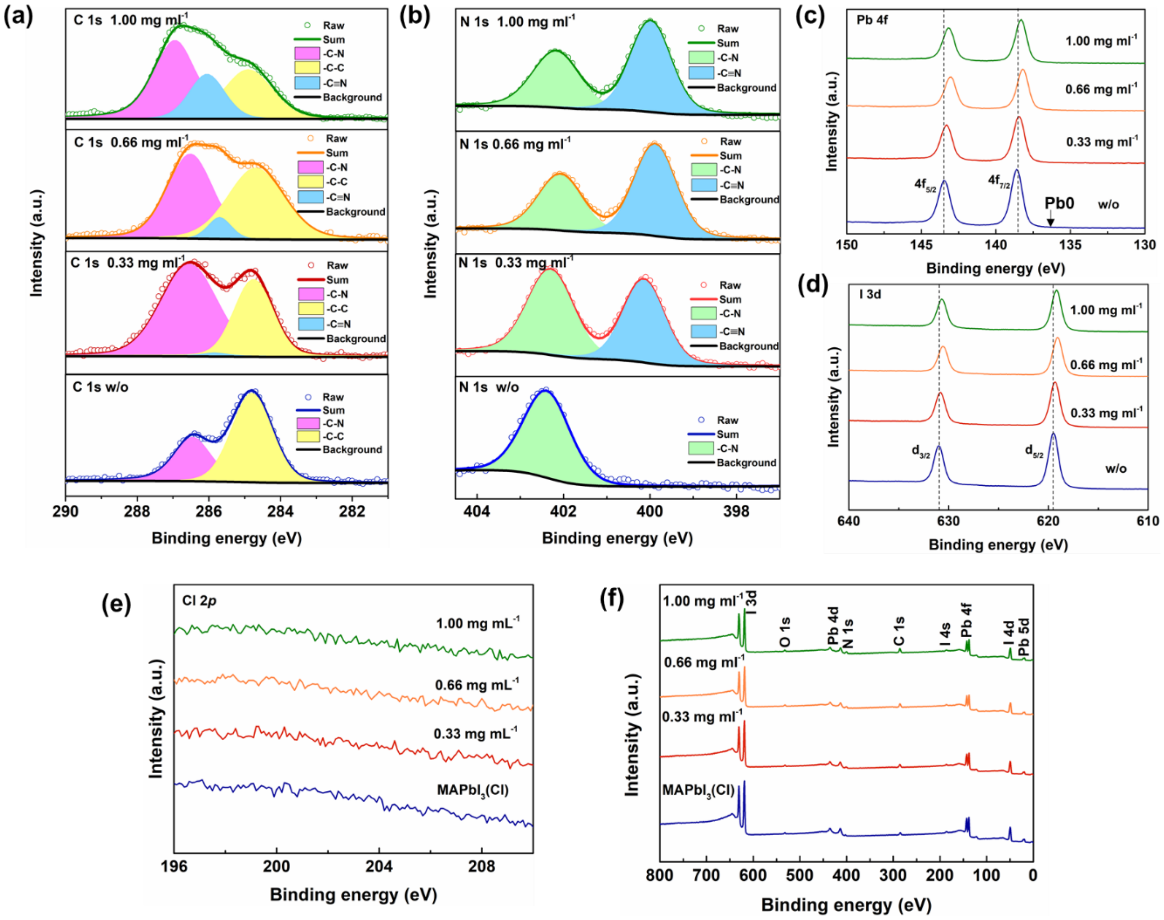

Figure 3.6 (a) C 1*s* spectrum, (b) N 1*s* spectrum, (c) Pb 4*f* spectrum, (d) I 3*d* spectrum, (e) Cl 2*p* and (f) wide-range XPS spectra of perovskite films without and with different amount of SN addition.

Then, we performed SEM and AFM to observe the variation of the perovskite film surface induced by the SN addition. **Figure 3.7a-h** show the top-view SEM images of perovskite films with different amounts of SN additive. Compared with pristine MAPbI$_3$(Cl) perovskite films with clear grain boundaries and many cracks, SN modified films were featured with less obvious grain boundaries and reduced cracks. It seemed that a large number of grains tightly gathered together after adding SN, leading to the decrease of grain boundaries. The reduced grain boundaries led to the decrease in the number of defects, thereby suppressing the nonradiative charge recombination. The more uniform perovskite film with tightly gathered perovskite grains and reduced grain boundaries after SN modification was also observed in the cross-section SEM images compared to the pristine perovskite film **(Figure 3.7i-l**). The improved film quality is also favorable to light absorption, which leads to the increased J_{sc}. In addition, the uneven surface of pristine perovskite films became smoother by the addition of SN, which can be confirmed from AFM images (**Figure 3.8**). The measured root-mean-square (RMS) surface roughness decreased from 55.5 nm of pristine perovskite film to 32.3, 37.0 and 41.8 nm of modified perovskite films with 0.33, 0.66 and 1.00 mg mL^{-1} SN, respectively. The smoother perovskite film surface allowed this layer to contact better with its upper HTL, promoting the hole separation and transportation.

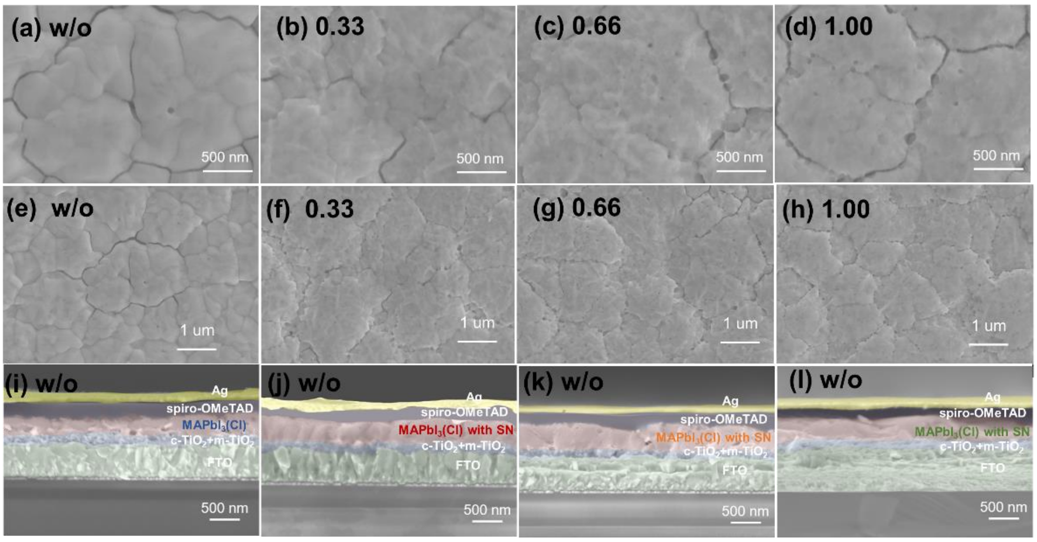

Figure 3.7 (a-h) Top-view SEM and (i-l) cross-sectional images of MAPbI$_3$(Cl) perovskite layer without and with different amount of SN addition.

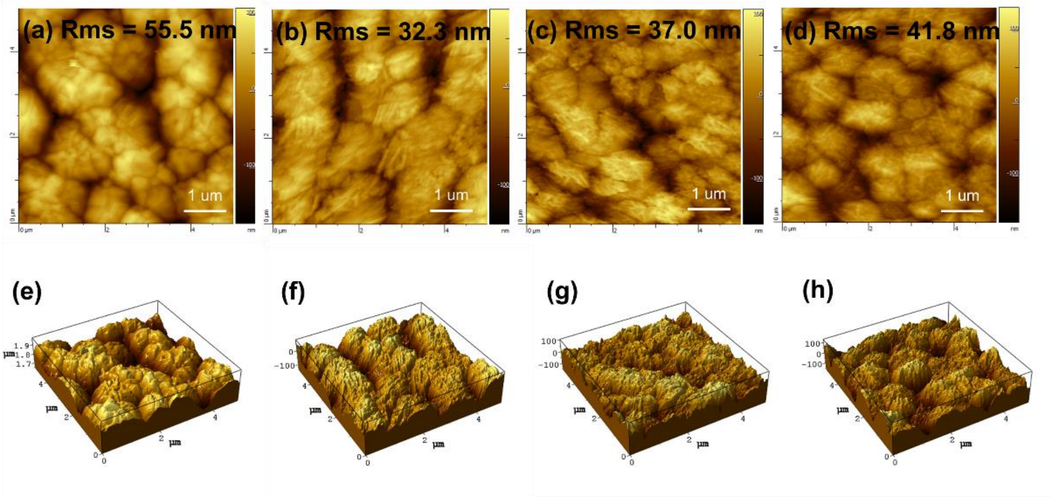

Figure 3.8 (a-d) AFM images and (e-h) the corresponding 3D models of MAPbI$_3$(Cl) perovskite films without and with different amount of SN addition.

To shed light on the internal formation mechanism of perovskite films with the assistance of SN, we paid attention to the analysis of the molecular structure of SN. **Figure 3.9** gives a schematic to show the role of SN in perovskite film. As for SN molecule, -C≡N with lone-pair electrons can present an interaction with uncoordinated Pb^{2+} and form hydrogen bonding with -NH$_2$ groups in perovskite, which provided a linking point for SN to anchor to perovskite grain boundaries.[54,55] More importantly, two -C≡N functional groups distribute at the ends of the short carbon chain (N≡C-CH$_2$-CH$_2$-C≡N), which presented the interaction with perovskite crystals from two directions and generated an aggregation strength to enable perovskite grains to tightly gather and cross-link together. Therefore, for pristine perovskite films without the assistance of SN, the absence of the coordination strength from additives made perovskite grains not tightly gather together, so grain boundaries and even cracks clearly appeared in the pristine perovskite film. By contrast, for SN modified perovskite films, SN can cross link with perovskite grains, thereby passivating grain boundaries, enhancing the surface compactness and smoothness and showing a positive effect on the light absorption and charge transfer.

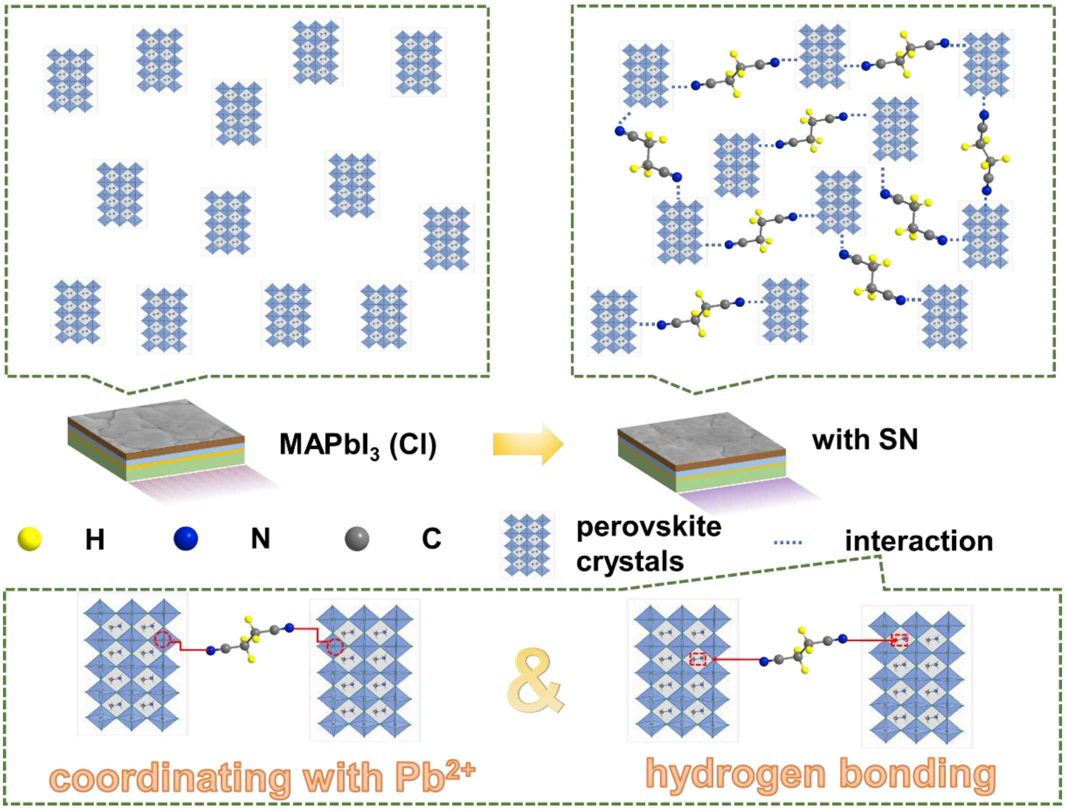

Figure 3.9 Schematic diagram of the perovskite film surface formed without and with the assistance of SN.

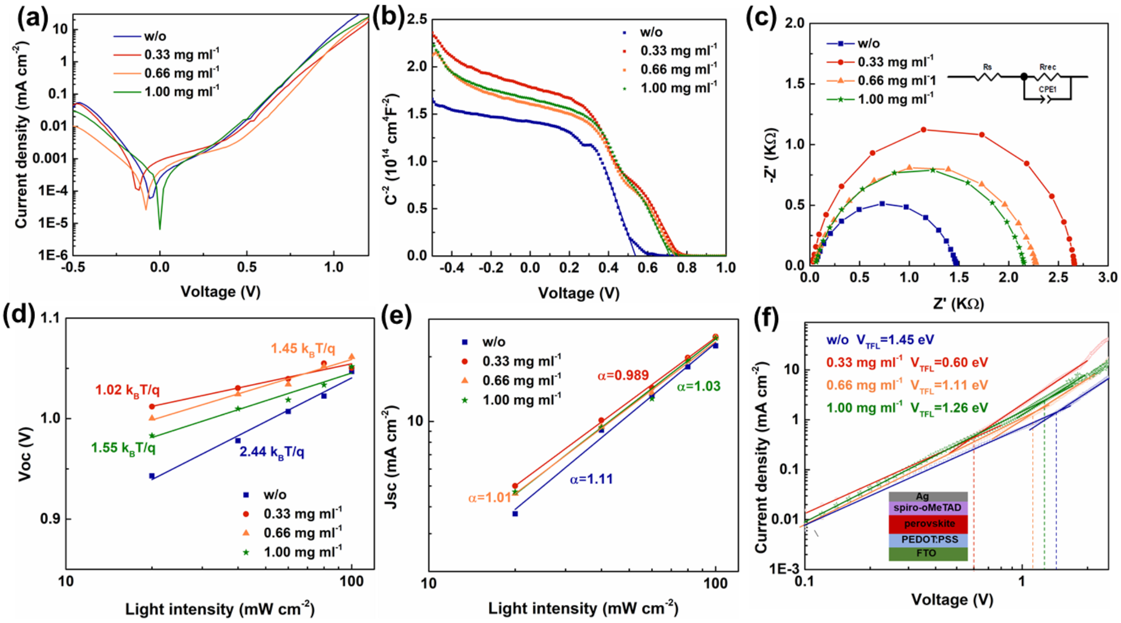

Figure 3.10 (a) Dark *J-V* curves (b) Mott-Schottky curves (c) Nyquist plots of PSCs without and with SN. The relationship curves between light intensity and (d) V_{oc}, (e) J_{sc}. (f) Dark *J-V*

curves of hole-only devices with a device structure schematic inside.

We then measured the dark *J-V* curves of devices to investigate the photovoltaic performance. As shown in **Figure 3.10a**, SN modified devices produced relatively lower dark current from -0.5 to -0.25 V and 0.25 to 1.2 V than pristine devices. The lower loss in current for SN modified PSCs signaled the smoother charge transfer at the interface, which may be attributed to the passivated surface and reduced defects at the interface.[56] We also tested Mott-Schottky (MS) curves (**Figure 3.10b**) of PSCs to determine the built-in voltage of devices. The relationship between capacitance and bias voltage can be defined as $1/C^2 = (2/e\varepsilon\varepsilon_0 N_D)(V_{bi} - V_{app} - kT/q)$, in which C represents the capacitance of the space charge region, ε refers to the dielectric constant of the semiconductor, ε_0 means the vacuum permittivity, N_D represents the carrier density, V_app refers to the applied potential, V_bi means the built-in potential, k represents Boltzmann's constant, q means the electron charge and T means the absolute temperature. Thus, the intercept of the MS curve with the x-axis represents V_{bi}.[57] The obtained V_{bi} of PSCs without and with various SN were 0.52, 0.76, 0.73, 0.71 V, respectively, which manifested that SN modification significantly improved the electrical field of PSCs, beneficial to the V_{oc} improvement. Then, EIS was measured to probe into the interfacial charge transfer kinetics of PSCs. Nyquist plots were tested under dark condition and the fitted Nyquist plots are shown in **Figure 3.10c**. The fitted Nyquist plots exhibited a low-frequency arc, which reflects the charge carrier recombination process occurring at the interfaces. Pristine PSCs had a small recombination resistance (R_{rec}) of 1428 Ω, while PSCs with 0.33, 0.66 and 1.00 mg ml^{-1} SN showed larger R_{rec} of 2636, 2241 and 2108 Ω, respectively. The obviously increased R_{rec} for BAN-modified devices means the suppressed charge carrier recombination behavior at the interfaces, thus giving rise to an improved photovoltaic performance.[58]

The dependance of J_{sc} and V_{oc} on light intensity was measured to gain deeper insight into the recombination kinetics within the PSCs. In **Figure 3.10d**, the degree of the deviation of the slope from kT/q can reflect the severity of trap-assisted carrier recombination. The slope of pristine devices was 2.44 kT/q, while the slope of SN-modified PSCs with different amounts was decreased to 1.02, 1.45 and 1.55 kT/q, which suggested that SN addition into perovskite films brought about an effective suppression of the non-radiative (trap-assisted) recombination via reducing the presence of defects. In **Figure 3.10e**, the slope was 1.11 for pristine PSCs, which decreased to 0.989, 1.01 and 1.03 for PSCs with different amount of SN additives. According to the general power law of $J_{sc} \propto (\text{light intensity})^{\alpha}$, if α approaches to 1, it means that the recombination adopts the monomolecular path.[59] In this work, the reduced slope for SN modified devices suggested that SN incorporation was capable of inhibiting the monomolecular recombination.[60] The specific *J-V* curves of devices measured at different light intensities are displayed in **Figure 3.11**.

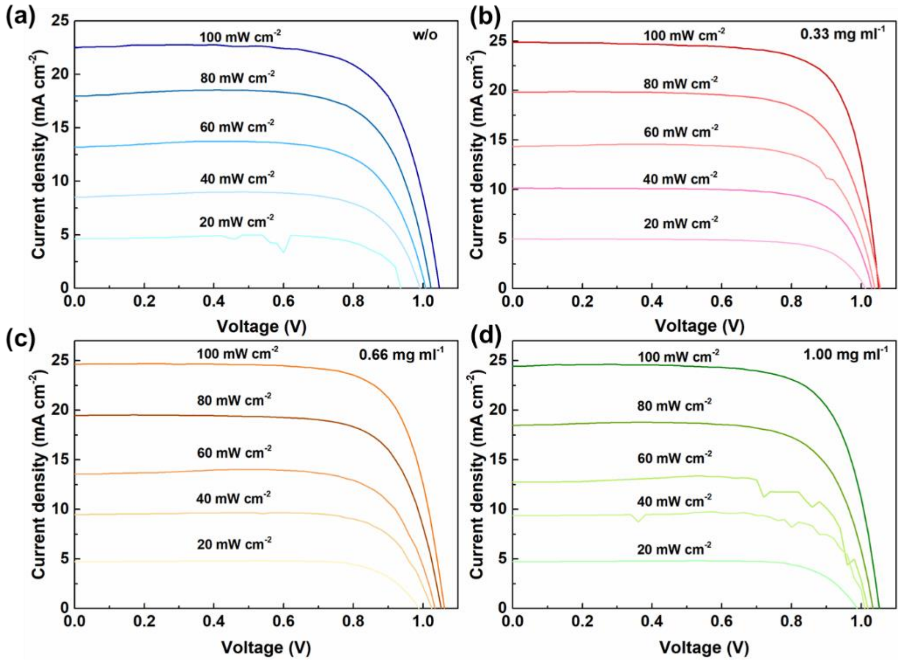

Figure 3.11 *J-V* curves of PSCs without and with different amount of SN addition measured at different light intensity.

The reduced non-radiative recombination is closely associated with the defect density in perovskite films, thus we then measured the dark *J-V* curves of hole-only devices with the structure of FTO/PEDOT:PSS/perovskite/spiro-OMeTAD/Ag to further investigate the influence of SN addition on the hole defect density of perovskite films. The hole defect density can be calculated according to the equation: $N_{\text{defects}} = 2\varepsilon\varepsilon_0 V_{\text{TFL}}/eL^2$, where ε refers to the relative dielectric constant of perovskite, ε_0 represents the vacuum permittivity, V_{TFL} represents the trap filled limit voltage, e represents the electron charge, and L means the thickness of the perovskite.[54,61] V_{TFL} can be obtained from **Figure 3.10f**, which was 1.45 eV for pristine devices. By contrast, V_{TFL} was dramatically decreased to 0.60 eV for devices with 0.33 mg ml^{-1} SN. Under the circumstance of the same perovskite film thickness, the dramatically decreased V_{TFL} was indicative of the obviously reduced numbers of defects in perovskite films via SN passivating the surface and cross-linking perovskite grains.[48] This result was coincident with the above-mentioned suppressed charge non-radiative recombination. Besides, the electron trap density was also calculated via testing the dark I-V curves of devices with the structure of FTO/c-TiO_2/m-TiO_2/perovskite/PCBM/Ag. As shown in **Figure 3.12**, the SN addition created a non-obvious effect on the VTFL for electron-only devices, signaling the negligible effect of SN addition on the electron defect density. Thai may be because SN mainly modified the interface of perovskite layer/HTL, thus affecting holes more significantly than electrons.

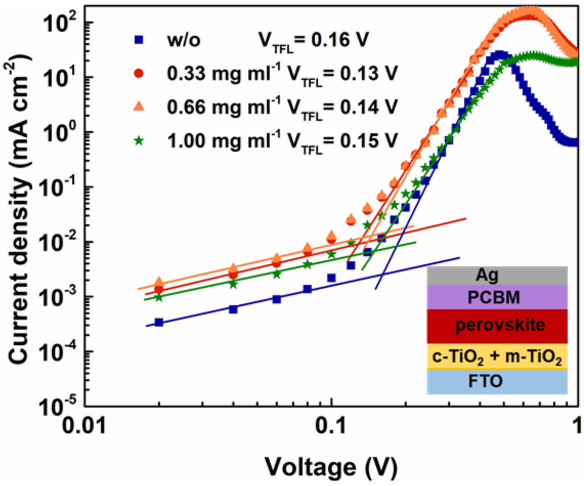

Figure 3.12 Dark *J-V* curves of electron-only devices with the structure of FTO/c-TiO_2/m-TiO_2/perovskite/PCBM/Ag.

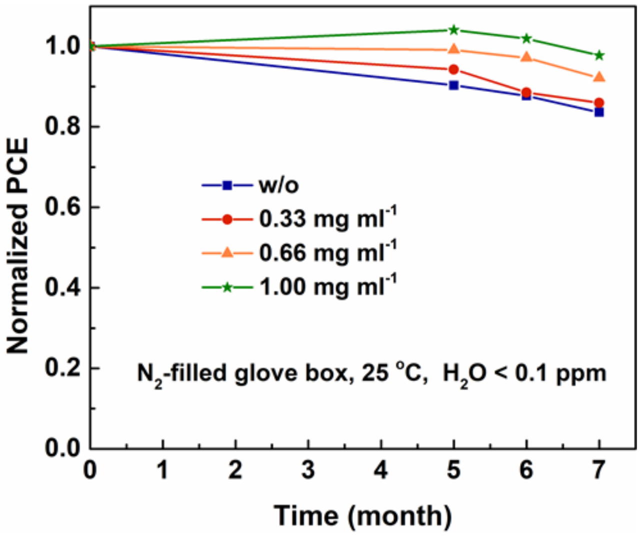

Figure 3.13 PCE evolution of PSCs without and with SN modification after storing in N_2 for 7 months.

To evaluate the impact of SN addition on the stability of PSCs, long-term stability of devices was tested at dry nitrogen (N_2) and humid air atmosphere without encapsulation. After storing devices without and with BAN modification in N_2-filled glove box for 7 months, pristine devices without SN modification lost about 20% of their initial PCE, while devices with increasing SN addition exhibited better stability. The PCE of devices with 1.00 mg ml^{-1} N remained almost unchanged (**Figure 3.13**). **Figure 3.14** gives the *J-V* curves of devices stored in N_2 atmosphere and tested at different time points. In terms of air stability with ~ 30% humid for 530 h, pristine devices without SN modification experienced a 30% decrease in their initial PCE (**Figure 3.15**), while SN-modified devices witnessed lesser PCE loss (Figure 5b). Particularly, devices with 0.66 mg ml^{-1} SN exhibited best air stability, remaining almost 95% of their initial PCE after storing in the air for 530h. The related *J-V* curves tested at different time points are shown in **Figure 3.16**.

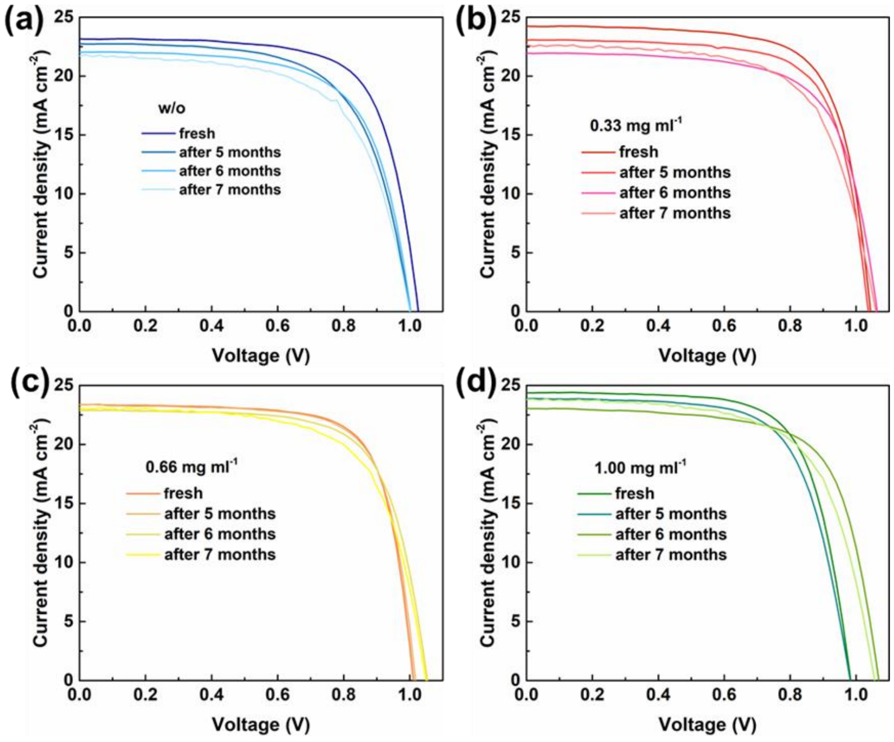

Figure 3.14 The variation of *J-V* curves of PSCs without and with different amount of SN addition when storing in N_2 atmosphere.

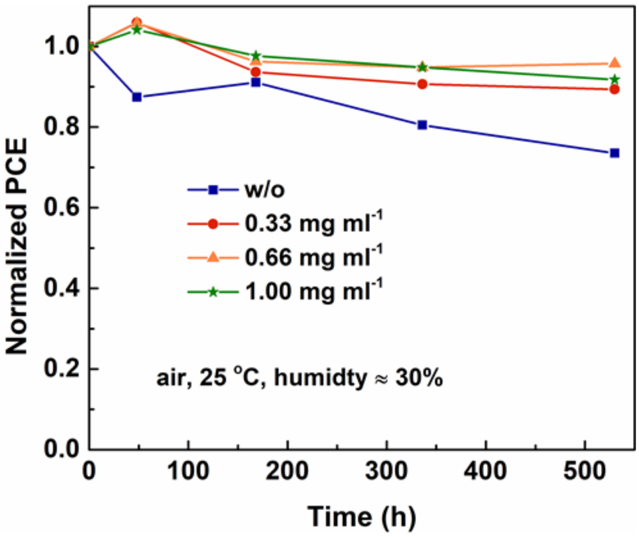

Figure 3.15 PCE evolution of PSCs without and with SN modification after storing in air atmosphere without encapsulation for 530h.

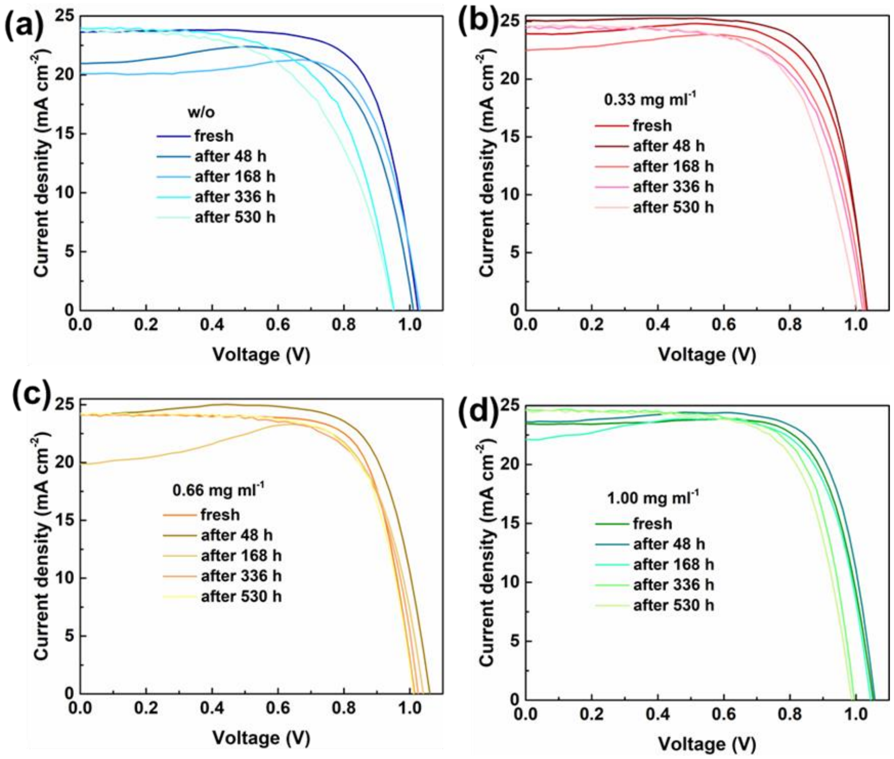

Figure 3.16 The variation of *J-V* curves of PSCs without and with different amount of SN addition when storing at humid air atmosphere.

We guess the improved moisture stability by SN addition is related to the change of surface hydrophobicity induced by defect passivation. We then evaluated the surface hydrophobicity via testing the contact angle of water droplets on $MAPbI_3(Cl)$ perovskite films without and with different amount of SN modification. As shown in **Figure 3.17a-d**, in comparison with pristine $MAPbI_3(Cl)$ perovskite film with a water contact angle of 35 ^{o}, SN modified perovskite films exhibited larger water contact angle with 53 ^{o} for 1.00 mg ml^{-1} SN modified perovskite films, suggesting that SN incorporation-induced surface passivation enhanced the film surface hydrophobicity, which can be responsible for the enhancement of the stability of devices. We further tested the long-term moisture stability of perovskite films via exposing them to highly humid air (~ 60% humidity). **Figure 3.17e** displays the photographs of freshly-fabricated perovskite films. When placing them in the humid air for 2 months, the photographs of these samples are shown in **Figure 3.17f**. The initial black color of the pristine perovskite films completely became light yellow, indicating that $MAPbI_3(Cl)$ had completely decomposed to PbI_2. By contrast, SN-modified perovskite films remained most of their initial black brown color, manifesting that the SN incorporation inhibited the decomposition of perovskites under the humid atmosphere and enhanced the film resistance to water. The significantly enhanced stability of SN-modified devices was mainly ascribed to the spontaneous surface passivation induced by SN addition. The disappearance of grain boundaries can block the pathway of water invasion, thereby protecting the perovskite films from water-caused degradation.

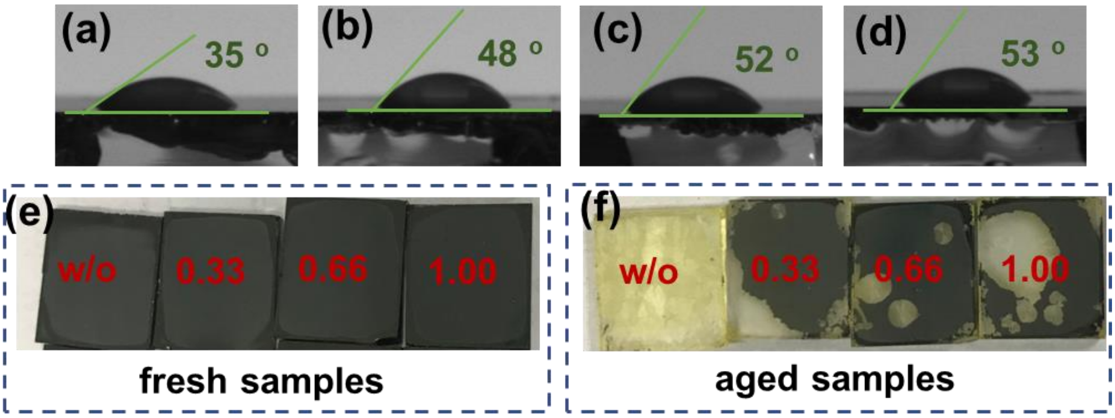

Figure 3.17 (a-d) Images of the angles of water contact of perovskite films without and with different amount of SN. Photographs of (e) freshly fabricated perovskite films and (f) aged perovskite films in the humid air atmosphere.

3.4 Conclusions

In summary, this work provides an effective and convenient way to enhance the efficiency and stability of $MAPbI_3(Cl)$-based PSCs via adding SN additive into perovskite precursor solution and provides a systematic investigation to clarify the effect of SN addition on the properties of perovskite films and the performance of PSCs. SN with two -C≡N functional groups distributing at the two terminals of the short carbon chain can coordinate with uncoordinated Pb^{2+} and form hydrogen bonding with $-NH_2$ in $MAPbI_3(Cl)$ perovskite, offering strong aggregation force to cross link perovskite grains. Benefitting from this, the defects in perovskite films were significantly reduced, thereby effectively suppressing trap-assisted nonradiative charge recombination and improving the device performance. Simultaneously, the defect passivation also stabilizes the perovskite film and enhances the film surface hydrophobicity, making devices with better stability in N_2 and humid air atmospheres

3.5 Reference

[1] M. Kim, G.-H. Kim; T. K. Lee, I. W. Choi, H. W. Choi, Y. Jo, Y. J. Yoon, J. W. Kim, J. Lee, D. Huh, H. Lee, S. K. Kwak, J. Y. Kim, D. S. Kim, *Joule* **2019**, *3*, 2179–2192.

[2] B. Shi, L. Duan, Y. Zhao, J. Luo, X. Zhang, *Adv. Mater.* **2020**, *32*, 1806474.

[3] J. Y. Kim, J.-W. Lee, H. S. Jung, H. Shin, N.-G. Park, *Chem. Rev.* 120 (2020) 7867–7918.

[4] M. A. Green, A. Ho-Baillie, H. J. Snaith, *Nat. Photonics* **2014**, *8*, 506–514.

[5] S. Rühle, *Sol. Energy* **2016**, *130*, 139–147.

[6] N.-G. Park, H. Segawa, *ACS Photonics* **2018**, *5*, 2970–2977.

[7] W. Wang, Z. Shao, N. S. Arul, V. D. Nithya, *Eds. Springer Singapore: Singapore* **2020**, 175–207.

[8] J.-W. Lee, N.-G. Park, *Adv. Energy Mater.* **2020**, *10*, 1903249.

[9] Y.-H. Lin, N. Sakai, P. Da, J. Wu, H. Sansom, A. J. Ramadan, S. Mahesh, J. Liu, R. D. J. Oliver, J. Lim, L. Aspitarte, K. Sharma, P. K. Madhu, A. B. Morales-Vilches, P. K. Nayak, S. Bai, F. Gao, C. R. M. Grovenor, M. B. Johnston, J. G. Labram, J. R. Durrant, J. M. Ball, B. Wenger, B. Stannowski, H. J. Snaith, *Science* **2020**, *369*, 96–102.

[10] X. Yang, Y. Chen, P. Liu, H. Xiang, W. Wang, R. Ran, W. Zhou, Z. Shao, *Adv. Funct. Mater.* **2020**, *30*, 2001557.

[11] P. Liu, X. Yang, H. Xiang, W. Wang, R. Ran, W. Zhou, Z. Shao, *ACS Appl. Mater. Interfaces* **2020**, *12*, 23984–23994.

[12] P. Schulz, *ACS Energy Lett.* **2018**, *3*, 1287–1293.

[13] M. Stolterfoht, C. M. Wolff, J. A. Márquez, S. Zhang, C. J. Hages, D. Rothhardt, S. Albrecht, P. L. Burn, P. Meredith, T. Unold, D. Neher, *Nat. Energy* **2018**, *3*, 847–854.

[14] H. Xiang, P. Liu, W. Wang, R. Ran, W. Zhou, Z. Shao, *Chem. Eng. J.* **2020**, DOI: 10.1016/j.cej.2020.127599.

[15] S. Akin, N. Arora, S. M. Zakeeruddin, M. Grätzel, R. H. Friend, M. I. Dar, *Adv. Energy Mater.* **2020**, *10*, 1903090.

[16] X. Yang, W. Wang, R. Ran, W. Zhou, Z. Shao, *Energy Fuels* **2020**, *34*, 10513–10528.

[17] J. Kim, A. Ho-Baillie, S. Huang, *Sol. RRL* **2019**, *3*, 1800302.

[18] Z. Ni, C. Bao, Y. Liu, Q. Jiang, W.-Q. Wu, S.Chen, X. Dai, B. Chen, B. Hartweg, Z. Yu, Z. Holman, J. Huang, *Science* **2020**, *367*, 1352–1358.

[19] E. Aydin, M. De Bastiani, S. De Wolf, *Adv. Mater.* **2019**, *31*, 1900428.

[20] F. Zhang, K. Zhu, *Adv. Energy Mater.* **2020**, *10*, 1902579.

[21] F. Gao, Y. Zhao, X. Zhang, J. You, *Adv. Energy Mater.* 10 (2020) 1902650.

[22] Y. Chen, X. Yang, P. Liu, W. Wang, R. Ran, W. Zhou, Z. Shao, *Sol. RRL* **2021**, *5*, 2000621. DOI:10.1002/solr.202000621.

[23] T.-H. Han, J.-W. Lee, C. Choi, S. Tan, C. Lee, Y. Zhao, Z. Dai, N. De Marco, S.-J. Lee, S.-H. Bae,Y. Yuan, H. M. Lee, Y. Huang, Y. Yang, *Nat. Commun.* **2019**, *10*, 520.

[24] S. Xiong, T. Hao, Y. Sun, J. Yang, R. Ma, J. Wang, S. Gong, X. Liu, L. Ding, M. Fahlman, Q. Bao, *J. Energy Chem.* **2021**, *55*, 265–271.

[25] J. Zhang, H. Yu, *J. Energy Chem.* **2021**, *54*, 291–300.

[26] Y. Li, X. Xu, C. Wang, B. Ecker, J. Yang, J. Huang, Y. Gao, *J. Phys. Chem. C* **2017**, *121*, 3904–3910.

[27] S. Svanström, T. J. Jacobsson, T. Sloboda, E. Giangrisostomi, R. Ovsyannikov, H. Rensmo, U. B. Cappel, *J. Mater. Chem. A* **2018**, *6*, 22134–22144.

[28] M. Anaya, J. F. Galisteo-López, M. E. Calvo, J. P. Espinós, H. Míguez, *J. Phys. Chem. Lett.* **2018**, *9*, 3891–3896.

[29] L. Yang, Q. Xiong, Y. Li, P. Gao, B. Xu, H. Lin, X. Li, T. Miyasaka, *J. Mater. Chem. A* **2021**, *9*, 1574-1582.

[30] J. Xie, Z. Zhou, H. Qiao, M. Chen, L. Wang, S. Yang, Y. Hou, H. Yang, *J. Energy Chem.* **2021**, *56*, 179–185.

[31] L. Zhu, Y. Xu, P. Zhang, J. Shi, Y. Zhao, H. Zhang, J. Wu, Y. Luo, D. Li, Q. Meng, *J. Mater. Chem. A* **2017**, *5*, 20874–20881.

[32] J.-W. Lee, S.-H. Bae, Y.-T. Hsieh, N. De Marco, M. Wang, P. Sun, Y. Yang, *Chem* **2017**, *3*, 290–302.

[33] J. Yang, S. Xiong, T. Qu, Y. Zhang, X. He, X. Guo, Q. Zhao, S. Braun, J. Chen, J. Xu, Y.

Li, X. Liu, C. Duan, J. Tang, M. Fahlman, Q. Bao, *ACS Appl. Mater. Interfaces* **2019**, *11*, 13491–13498.

[34] S.-G. Ko, G.-I. Ryu, B. Kim, G.-J. Cha, J.-H. Ri, G.-S. Sonu, U.-C. Kim, *Sol. Energy Mater. Sol. Cells* **2019**, *196*, 105–110.

[35] C. Fei, B. Li, R. Zhang, H. Fu, J. Tian, G. Cao, *Adv. Energy Mater.* **2017**, *7*, 1602017.

[36] H. Zhao, S. Wang, M. Sun, F. Zhang, X. Li, Y. Xiao, *J. Mater. Chem. A* **2018**, *6*, 10825–10834.

[37] S. Yang, J. Dai, Z. Yu, Y. Shao, Y. Zhou, X. Xiao, X. C. Zeng, J. Huang, *J. Am. Chem. Soc.* **2019**, *141*, 5781–5787.

[38] W.-Q. Wu, J.-X. Zhong, J.-F. Liao, C. Zhang, Y. Zhou, W. Feng, L. Ding, L. Wang, D.-B. Kuang, *Nano Energy* **2020**, *75*, 104929.

[39] W.-Q. Wu, Z. Yang, P. N. Rudd, Y. Shao, X. Dai, H. Wei, J. Zhao, Y. Fang, Q. Wang, Y. Liu, Y. Deng, X. Xiao, Y. Feng, J. Huang, *Sci. Adv.* **2019**, *5*, eaav8925.

[40] W. Zha, F. Chen, D. Yang, Q. Shen, L. Zhang, *J. Power Sources* **2018**, *397*, 87–94.

[41] J. Bi, D. Mu, B. Wu, J. Fu, H. Yang, G. Mu, L. Zhang, F. Wu, *J. Mater. Chem. A* **2020**, *8*, 706–713.

[42] Y. Cho, A. M. Soufiani, J S. Yun, J. Kim, D. S. Lee, J. Seidel, X. Deng, M. A. Green, S. Huang, A. W. Y. Ho-Baillie, *Adv. Energy Mater.* **2018**, *8*, 1703392.

[43] B. Chen, P. N. Rudd, S. Yang, Y. Yuan, J. Huang, Chem. Soc. Rev. 48 (2019) 3842-3867.

[44] S. Li, L. Zhu, Z. Kan, Y. Hua, F. Wu, *J. Mater. Chem. A* 2020, 8, 19555.

[45] P. Liu, W. Wang, S. Liu, H. Yang, Z. Shao, *Adv. Energy Mater.* **2019**, *9*, 1803017.

[46] Z. Liu, F. Cao, M. Wang, M. Wang, L. Li, *Angew. Chem. Int. Ed.* **2020**, *132*, 4190–4196.

[47] M. Maiberg, T. Hölscher, S. Zahedi-Azad, R. Scheer, *J. Appl. Phys.* **2015**, *118*, 105701.

[48] X. Jiang, J. Zhang, S. Ahmad, D. Tu, X. Liu, G. Jia, X. Guo, C. Li, *Nano Energy* **2020**, *75*, 104892.

[49] Y. Lv, Y. Shi, X. Song, J. Liu, M. Wang, S. Wang, Y. Feng, S. Jin, C. Hao, *ACS Appl. Mater. Interfaces* **2018**, *10*, 31755–31764.

[50] W. Zhang, S. Pathak, N. Sakai, T. Stergiopoulos, P. K. Nayak, N. K. Noel, A. A. Haghighirad, V. M. Burlakov, D. W. deQuilettes, A. Sadhanala, W. Li, L. Wang, D. S. Ginger,

R. H. Friend, H. J. Snaith, *Nat. Commun.* **2015**, *6*, 10030.

[51] R. Lindblad, D. Bi, B.-W. Park, J. Oscarsson, M. Gorgoi, H. Siegbahn, M. Odelius, E. M. J. Johansson, H. Rensmo, *J. Phys. Chem. Lett.* **2014**, *5*, 648–653.

[52] M. I. Dar, N. Arora, P. Gao, S. Ahmad, M. Grätzel, M. K. Nazeeruddin, *Nano Lett.* **2014**, *14*, 6991–6996.

[53] E. L. Unger, A. R. Bowring, C. J. Tassone, V. L. Pool, A. Gold-Parker, R. Cheacharoen, K. H. Stone, E. T. Hoke, M. F. Toney, M. D. McGehee, *Chem. Mater.* **2014**, *26*, 7158–7165.

[54] X. Li, W. Zhang, W. Zhang, H.-Q. Wang, J. Fang, *Nano Energy* **2019**, *58*, 825–833.

[55] K. Wang, J. Liu, J. Yin, E. Aydin, G. T. Harrison, W. Liu, S. Chen, O. F. Mohammed, S. De Wolf, *Adv. Funct. Mater.* **2020**, *30*, 2002861.

[56] K. Gao, Z. Zhu, B. Xu, S. B. Jo, Y. Kan, X. Peng, A. K.-Y. Jen, *Adv. Mater.* **2017**, *29*, 1703980.

[57] W. S. Subhani, K. Wang, M. Du, S. F. Liu, *Nano Energy* **2019**, *61*, 165–172.

[58] Z. Guo, S. H. Teo, Z. Xu, C. Zhang, Y. Kamata, S. Hayase, T. Ma, *J. Mater. Chem. A* **2019**, *7*, 1227–1232.

[59] X. Liu, B. Xie, C. Duan, Z. Wang, B. Fan, K. Zhang, B. Lin, F. J. M. Colberts, W. Ma, R. A. J. Janssen, F. Huang, Y. Cao, *J. Mater. Chem. A* **2018**, *6*, 395–403.

[60] G. Wu, X. Li, J. Zhou, J. Zhang, X. Zhang, X. Leng, P. Wang, M. Chen, D. Zhang, K. Zhao, S. Liu, H. Zhou, Y. Zhang, *Adv. Mater.* **2019**, *31*, 1903889.

[61] Z. Liu, J. Hu, H. Jiao, L. Li, G. Zheng, Y. Chen, Y. Huang, Q. Zhang, C. Shen, Q. Chen, H. Zhou, *Adv. Mater.* **2017**, *29*, 1606774.

Chapter 4 Benefitting from Synergistic Effect of Anion and Cation in Antimony Acetate for Stable $CH_3NH_3PbI_3$-Based Perovskite Solar Cell with Efficiency Beyond 21%

Abstract

Both the film quality and the electronic structure of halide perovskites have significant influences on the photovoltaic performance of perovskite solar cells (PSCs) because both of them are closely related to the charge carrier transportation, separation and recombination processes in PSCs. In this work, an additive engineering strategy using antimony acetate ($Sb(Ac)_3$) is employed to enhance the photovoltaic performance of methylammonium lead iodide ($MAPbI_3$)-based PSCs by improving the film quality and optimizing the photo-electronic properties of halide perovskites. It is found that Ac^- and Sb^{3+} of $Sb(Ac)_3$ played different roles and their synergistic effect contributed to the eventual excellent photovoltaic performance of $MAPbI_3$-based PSCs with an efficiency of above 21%. The Ac^- anions act as a crystal growth controller and are more involved in the improvement of perovskite film morphology. By comparison, Sb^{3+} cations are more involved in the optimization of electronic structure of perovskite to tailor the energy levels of the perovskite film. Furthermore, with the assistance of $Sb(Ac)_3$, $MAPbI_3$-based PSCs delivered much improved moisture, air and thermal stability. This work can provide scientific insights on the additive engineering for improving the efficiency and long-term stability of $MAPbI_3$-based PSCs, facilitating the further development of perovskite-based optoelectronics.

4.1 Introduction

$MAPbI_3$ has become a promising photovoltaic material because of the long charge carrier diffusion length, intensive light absorption and tunable band gap.[1-4] Since it was firstly utilized as a light-absorbing material to fabricate dye-sensitized solar cells in 2009, perovskite solar cells (PSCs) using $MAPbI_3$ or other organic-inorganic hybrid halide perovskites as light absorbers have experienced an unprecedented development during the past 12 years.[5] Up to now, the certificated highest power conversion efficiency (PCE) of single-junction PSCs has reached >25%,[6,7] which is approaching to that of mature silicon solar cells. Comparing with formamidinium lead iodide perovskite ($FAPbI_3$) and MA-FA mixed cation halide perovskites-based PSCs, the photovoltaic performance of $MAPbI_3$-based PSCs is still inferior due to the formation of defective perovskite film and the limitation of well-matched energy levels. [8-11]

During the past several years, tremendous efforts have been made to boost the performance of $MAPbI_3$-based PSCs from the improvement of fabrication protocols,[12-14] the optimization of device configuration[15,16] and the adjustment of chemical compositions.[17,18] Additive engineering has been regarded as a facile and efficacious approach to enhance the photovoltaic performance of PSCs.[19,20] A large number of substances including polymers, organics, inorganic acid and metal halides have been added into perovskite precursor solutions to fabricate decent perovskite films with high quality and tailor the optical and electronic properties of perovskite films.[21,22] For example, typical Lewis base and Lewis acid additives can reduce defects via interacting with uncoordinated Pb^{2+} and I^-.[23,24] Some organic additives can participate in the crystal growth and film formation processes to manipulate the crystallization of perovskites and regulate the film morphology via forming intermediate phases with perovskite precursors.[25] As for some metal halide additives, they not only can affect the crystallization process but also can dope into the perovskite lattice to tune the optoelectronic properties.[26]

In addition to metal halides, metal acetate and other acetate salts are also promising additives due to the existence of carbonyl (C=O) group in acetate ion (Ac^-), which can coordinate with Pb^{2+} in the precursor solution to tune the crystallization process and also interact with uncoordinated Pb^{2+} in the formed perovskite film to reduce defects.[27-32] For example, lead acetate ($Pb(Ac)_2$) that was widely used as lead precursor source to synthesize perovskites have been employed as an effective additive to retard the perovskite crystallization process.[33,34] The addition of $Pb(Ac)_2$ resulted in the formation of full-coverage and uniform perovskite films with large grains and low defect densities as well as the passivation of grain boundaries.[34] In another case, liquid zirconium acetate ($Zr(Ac)_4$) as additive also improved the $MAPbI_3$ perovskite film quality and reduced the defects.[35] The addition of $Zr(Ac)_4$ can release the crystal microstrain and Zr^{4+} was found to be concentrated at grain boundaries to interact with uncoordinated I^- and reduce the amount of detrimental metallic Pb. With the assistance of $Zr(Ac)_4$, the modified $MAPbI_3$-based device delivered a high PCE of 20.9% and exhibited decent stability.[35] In addition, barium acetate ($Ba(Ac)_2$) as additive in $MAPbI_3$ perovskite precursor solution not only lowered defect density but also optimized the energy level alignment, thus contributing to the much improved PCE and stability of devices.[36]

Previous reports have pointed out that Sb^{3+} was capable to improve the optical and electronic properties of halide perovskites for the application in solar cells, giving rise to the enhanced photovoltaic performance of the corresponding devices.[37,38] In consideration of the positive effects of both Ac^- and Sb^{3+}, antimony acetate ($Sb(Ac)_3$) was selected as a new additive to optimize $MAPbI_3$ perovskite film quality and then to enhance the photovoltaic performance of the corresponding PSCs. With the assistance of optimized amount of $Sb(Ac)_3$, $MAPbI_3$-based PSCs delivered a boosted PCE of 21.04% (19.00% for pristine device) with much enhanced moisture, air and thermal stability. Particularly, the individual roles of Ac^- and Sb^{3+} in promoting the film quality and optical/electronic properties of halide perovskites were investigated in detail by comparing $Sb(Ac)_3$, $Pb(Ac)_2$ and SbI_3 additives in this work. The enhanced photovoltaic performance of device was attributed to the synergistic effect of Ac^- and Sb^{3+}, in which Ac^- serves as a crystal growth regulator to improve the film morphology while Sb^{3+} shows more influence on electronic structure to tune the energy levels of $MAPbI_3$ film. Overall, the synergistic effect of the anion and cation in $Sb(Ac)_3$ additive contributed to the much improved efficiency and long-term durability of PSCs and our work may provide a new research direction for the development of high-performance PSCs.

4.2 Experimental sections

4.2.1 Materials and device fabrication

MAI (99.95%), PbI_2 (99.95%), spiro-OMeTAD (99.98%) were purchased from Xi'an Polymer Light Technology Corp. SbI_3 (99.99%), chlorobenzene (CB, 99.5%, anhydrous), N, N-dimethylformamide (DMF, 99.8%, anhydrous) and dimethyl sulfoxide (DMSO, 99.8%, anhydrous) were purchased from Aladdin. All these materials and regents were directly used as received without any purification. The fabrication process of compact TiO_2 (c-TiO_2) layer and mesoporous TiO_2 (m-TiO_2) layer is same as that mentioned in Chapter 3. 0.2 M $Sb(Ac)_3$, $Pb(Ac)_2$, SbI_3 solution were added into 1.2 M perovskite precursor solution with 1.2 M MAI and PbI_2 dissolving in mixed DMF and DMSO (3:7, in volume). Perovskite layer was fabricated via spin-coating the perovskite precursor solution on the top of m-TiO_2 layer with dropping 100 μL CB into the film as antisolvents and annealing the film at 100 °C for 5 min. The modified spiro-OMeTAD solution with Li- and Co-salts was then spin-coated on the top of perovskite layer to prepare HTL, which was then oxidized in dry air overnight. Finally, Ag electrode with a thickness of 100 nm and an active area of 0.0625 cm^2 was deposited on top of HTL by the thermal evaporation method.

4.2.2 Film and device characterization

XRD patterns were measured via Rigaku Smartlab equipped with Cu Kα radiation to analyze the crystal structure and crystallinity of perovskite films. The field emission SEM images were obtained via HITACHI S-4800 to observe the film morphology and the thicknesses of each layer in PSCs. AFM images were obtained via Horiba, SmartSPM. UV-vis spectra were carried out via PerkinElmer Lambda 750s spectrometer (PerkinElmer, USA) to observe light absorption and analyze band gaps. Steady-state PL spectra and TRPL spectra were surveyed via PerkinElmer fluorescence spectrometer (FL 6500) and fluorescence spectrophotometer (Edinburgh Instruments, FLS980), respectively. XPS spectra were conducted via XPS spectrometer (PHI5000 Versa Probe) with an Al Kα X-ray source. J-V curves of fabricated PSCs were tested via a solar simulator (Zolix) under AM 1.5G illumination at 100 mW cm^{-2}. EQE spectra of the devices were tested via a Zolix Solar Cell Scan 100 instrument. EIS spectra and MS curves of PSCs were performed on CHI760E electrochemical workstation under dark conditions.

4.3 Results and discussion

To assess the effect of $Sb(Ac)_3$ additive on the perovskite film morphology, top-view scanning electron microscopy (SEM) images of perovskite films were measured and shown in **Figure 4.1a-f** with the grain size statistics shown inset. Pristine $MAPbI_3$ film exhibited poor surface morphology with small grain sizes, many pinholes and microcracks. By contrast, the addition of suitable amount of $Sb(Ac)_3$ can improve the film quality. With the assistance of 0.1 mol.% and 0.2 mol.% $Sb(Ac)_3$, the perovskite film became more compact and flat with increased grain sizes, which is favorable for the improvement of device performance. Further increasing the amount of $Sb(Ac)_3$ additive, the grain size of the perovskite film displayed no obvious change but the surface flatness of the film slightly decreased. Then, the influence of $Sb(Ac)_3$ additive on the crystallinity and the crystal structure of $MAPbI_3$ perovskite films was analyzed via X-ray diffraction (XRD) patterns. As shown in **Figure 4.1g**, the main characteristic peaks appeared at 2θ of 14.29, 28.38° in all samples, corresponding to the (110) and (220) crystal planes of the tetragonal perovskite structure, respectively.[39,40] The peak intensity of 0.1 mol.% $Sb(Ac)_3$-modified sample increased compared with pristine $MAPbI_3$ film, indicative of the improved crystallinity, which was consistent with the SEM results. In addition, it was found that the (110) and (220) diffraction peaks (**Figure 4.1h**) gradually shifted to a smaller angle with the increased amount of $Sb(Ac)_3$ additive, meaning the expanded crystal lattice induced by Ac^- or Sb^{3+} doping. However, the ionic radius of Ac^- and Sb^{3+} were 0.162 nm and 0.076 nm, which were much smaller than the ionic radius of I^- (0.220 nm) and the ionic radius of Pb^{2+} (0.119 nm), respectively. [37,41] Thus, we inferred that the Ac^- and Sb^{3+} were more likely to enter into the crystal lattice as interstitial ions to cause the crystal lattice expansion.[42,43]

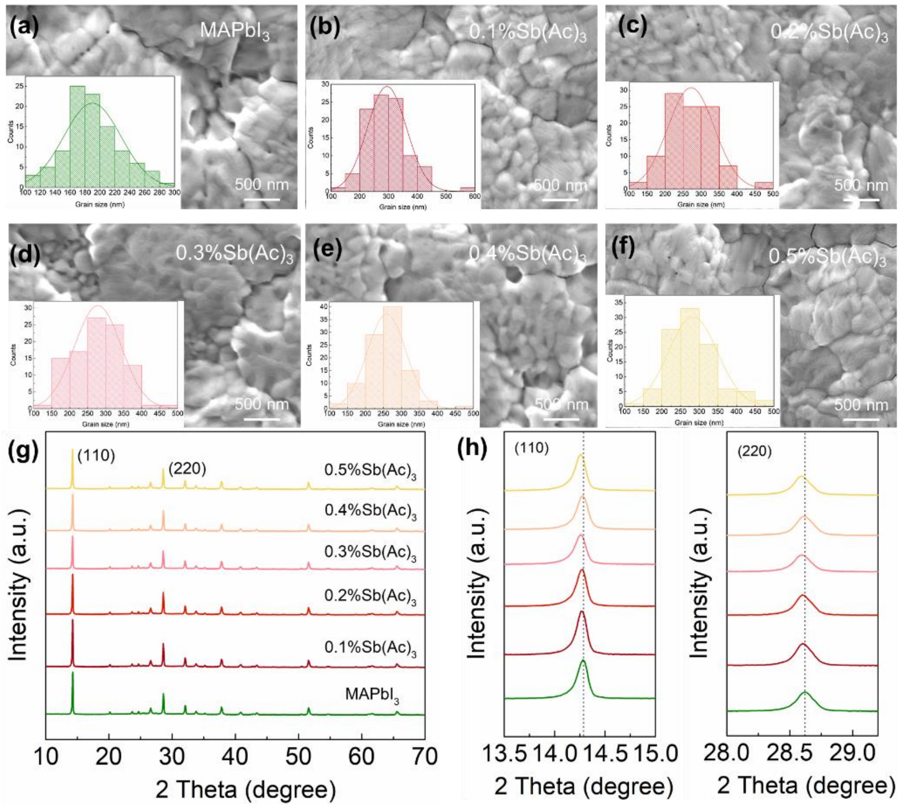

Figure 4.1 (a-f) Top-view SEM images of $MAPbI_3$ perovskite films without and with different amounts of $Sb(Ac)_3$ additive with the grain size distribution statistics shown inset. (g) XRD patterns and (h) relevant enlarged (110) and (220) diffraction peaks of the corresponding perovskite films.

To investigate the effect of $Sb(Ac)_3$ additive on the light absorption capability and the band gap (E_g) of perovskite films, UV-vis spectra were tested and presented in **Figure 4.2a**. The introduction of small amounts of $Sb(Ac)_3$ additive (0.1 mol.% and 0.2 mol.%) was observed to slightly increase the light absorption capability but further increasing the amount of $Sb(Ac)_3$ additive weakened the light absorption, which was closely related to the surface quality and the crystallinity of the films. Through the UV-vis spectra, the Kubelka-Munk spectra was obtained to calculate E_g values as shown in **Figure 4.2b**.[44] It is clear to find that E_g of $MAPbI_3$ perovskite film became larger with increasing the amount of $Sb(Ac)_3$. For example, the addition of 0.2 mol.% $Sb(Ac)_3$ increased E_g from 1.618 to 1.621 eV. In addition, steady-state photoluminescence (PL) spectra (**Figure 4.2c**) were measured to evaluate the defect variation behavior caused by the addition of $Sb(Ac)_3$. The significant increase of PL intensity was observed with adding 0.1 mol.% and 0.2 mol.% $Sb(Ac)_3$ into the perovskite. The PL intensity gradually declined with further increasing $Sb(Ac)_3$ amount but was still higher than the pristine $MAPbI_3$ perovskite film. Meanwhile, a gradual blue shift was observed with increasing amount of $Sb(Ac)_3$ until 0.3 mol.%. Both the increased PL peak intensity and the blue shift of PL peaks indicated the reduced defects in the perovskite films, which can inhibit non-radiative charge carrier recombination induced by the trap sites.[45]

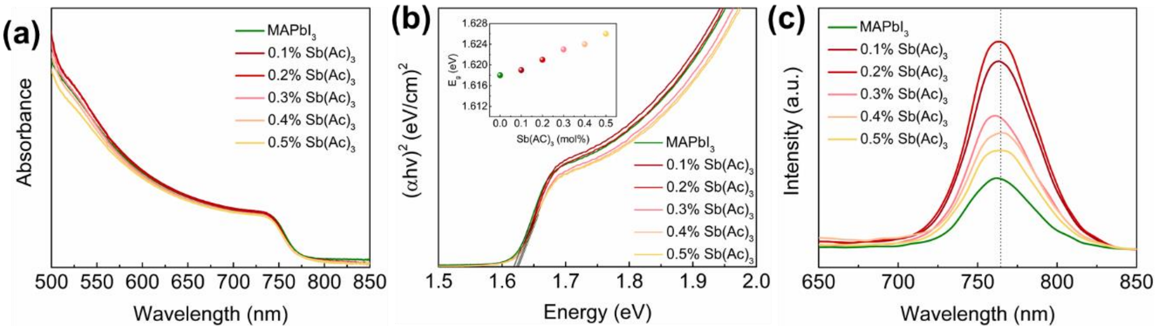

Figure 4.2 (a) UV-vis spectra, (b) Kubelka-Munk spectra and (c) Steady-state PL spectra of $MAPbI_3$ perovskite films without and with different amounts of $Sb(Ac)_3$ additive.

Mesoporous PSCs with a device configuration of FTO/c-TiO_2/m-TiO_2/$MAPbI_3$/spiro-OMeTAD/Ag where c-TO_2 and m-TiO_2 serve as electron transporting layer (ETL) and spiro-OMeTAD acts as hole transporting layer (HTL) were fabricated to explore the effect of $Sb(Ac)_3$ addition on the photovoltaic performance of PSCs. **Figure 4.3a** displays a cross-sectional SEM image of a PSC device with approximate 450 nm-thick perovskite layer. The *J-V* curves tested under AM 1.5 G illumination for the champion devices are displayed in **Figure 4.3b** and the relevant photovoltaic parameters are listed in **Table 4.1**. The pristine $MAPbI_3$ device without $Sb(Ac)_3$ additive achieved a champion PCE of 19.01% (average 17.95%) with J_{sc} of 23.21 mA cm^{-2} (average: 23.35 mA cm^{-2}), V_{oc} of 1.079 V (average: 1.061 V) and FF of 0.7586 (average: 0.7241). After the incorporation of 0.1 mol.% and 0.2 mol.% $Sb(Ac)_3$ additive, the PCEs of corresponding PSCs were significantly enhanced to 20.14% (average: 18.91%) and 21.04% (average: 19.76%), respectively, with improvements in all photovoltaic parameters, especially in V_{oc} and FF, hinting that appropriate amount of $Sb(Ac)_3$ additive can remarkably reduce the defects in the perovskite films.[46,47] However, further increasing the addition amount of

$Sb(Ac)_3$ additive to 0.5 mol.% notably reduced the J_{sc}, V_{oc} and FF of PSCs, leading to the much lowered PCE. **Figure 4.3c** shows the photovoltaic parameter distributions of various devices with different $Sb(Ac)_3$ additive amounts (25 cells for each type of devices). Overall, 0.2 mol.% $Sb(Ac)_3$ addition conferred $MAPbI_3$-based PSCs with better photovoltaic performance, higher and reproducible PCE. **Figure 4.3d** exhibits the external quantum efficiency (EQE) of $MAPbI_3$-based PSCs without and with 0.2 mol.% $Sb(Ac)_3$ additive, in which the device with 0.2 mol.% $Sb(Ac)_3$ exhibited higher EQE throughout the wavelength range from 350 to 750 nm and gives higher integrated J_{sc}. In addition, we compared our PCE obtained by 0.2 mol.% $Sb(Ac)_3$ modified PSC with the PCEs of some reported $MAPbI_3$-based PSCs using acetic acid or acetate salts as additives.[28-30,32,34-36] As shown in **Figure 4.3e**, the PCE obtained in this work is the highest PCE value of acetate-assisted $MAPbI_3$-based PSCs reported so far, suggesting $Sb(Ac)_3$ is a more efficient additive to improve the PCE of $MAPbI_3$-based PSCs than other acetate-based additives.

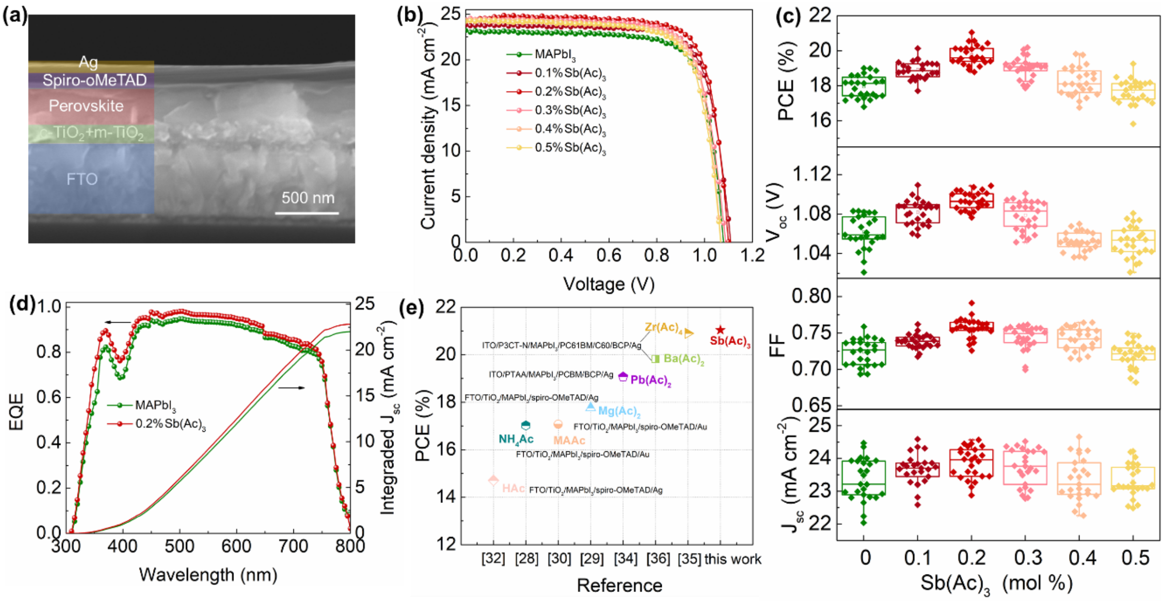

Figure 4.3 (a) Cross-sectional SEM images of the fabricated PSCs. (b) *J-V* curves of best-performing $MAPbI_3$-based PSCs without and with different amounts of $Sb(Ac)_3$ additive. (c) The distribution of photovoltaic parameters for the corresponding devices. (d) EQE spectra of $MAPbI_3$-based PSCs without and with 0.2 mol.% $Sb(Ac)_3$ additive. (e) PCE comparison between $Sb(Ac)_3$-modified $MAPbI_3$ devices in this work and other reported acetate acid and

salts-modified $MAPbI_3$-based PSCs in the literature.

Table 4.1 The influence of different amounts of $Sb(Ac)_3$ additive on the photovoltaic performance parameters of PSCs.

Device	PCE (%)		J_{sc} (mA cm^{-2})		V_{oc} (V)		FF	
	best	average	best	average	best	average	best	average
$MAPbI_3$	19.01	17.95	23.21	23.35	1.079	1.061	0.7586	0.7241
0.1%$Sb(Ac)_3$	20.14	18.91	23.82	23.67	1.109	1.082	0.7620	0.7383
0.2%$Sb(Ac)_3$	21.04	19.76	24.19	23.86	1.100	1.094	0.7910	0.7570
0.3%$Sb(Ac)_3$	20.06	19.03	24.4	23.72	1.088	1.079	0.7558	0.7436
0.4%$Sb(Ac)_3$	19.82	18.23	24.29	23.36	1.068	1.052	0.7644	0.7418
0.5%$Sb(Ac)_3$	19.25	17.66	24.22	23.32	1.067	1.052	0.7449	0.7119

According to previous reports, both Ac^- and Sb^{3+} can exert a positive effect on $MAPbI_3$ perovskite films and were capable of improving the photovoltaic performance of devices. Thus, we speculated that the enhanced photovoltaic performance by $Sb(Ac)_3$ additive in this work is determined by the synergistic effect of Ac^- and Sb^{3+}.[34,37] The same idea was also put forward when $Zr(Ac)_4$ and $Ba(Ac)_2$ were utilized to modify $MAPbI_3$-based PSCs, but the internal mechanism of how the cation and anion cooperated with each other to improve the device performance synergistically is still unclear.[35,36] To clarify this, we also added $Pb(Ac)_2$ and SbI_3 into precursor solution to investigate the individual role of Ac^- and Sb^{3+} on the film properties and their contribution to the final photovoltaic performance. According to the above investigation, the amount of $Pb(Ac)_2$ and SbI_3 additive was fixed at 0.3 mol.% and 0.2 mol.%, respectively and the $Sb(Ac)_3$, $Pb(Ac)_2$ and SbI_3-modified $MAPbI_3$ were written as $MAPbI_3$-$Sb(Ac)_3$, $MAPbI_3$-$Pb(Ac)_2$ and $MAPbI_3$-SbI_3, respectively. Frist, we analyzed the crystallinity and crystal structure of $MAPbI_3$ and $MAPbI_3$-$SbAc_3$, $MAPbI_3$-$Pb(Ac)_2$ and $MAPbI_3$-SbI_3 and found that these four samples showed a typical tetragonal perovskite structure (**Figure 4.4a**). For the (110) diffraction peak, no matter which additive ($Sb(Ac)_3$, $Pb(Ac)_2$ and SbI_3) was added, it exhibited a slight shift to lower angles, indicating that both Ac^- and Sb^{3+} can be doped into the crystal lattice as interstitial ions. We also compared their full width at half maximum (FWHM) and calculated the average crystallite size of perovskite via the Scherrer equation[48,49] as shown in **Figure 4.4b**. It was found that $MAPbI_3$-$Pb(Ac)_2$ exhibited smallest FWHM and largest average crystallite size and $MAPbI_3$-$Sb(Ac)_3$ displayed similar FWHM and average crystallite size to those of $MAPbI_3$-$Pb(Ac)_3$, while $MAPbI_3$-SbI_3 just displayed a slight variation in FWHM and average crystallite size as compared with pristine $MAPbI_3$. Thus, we inferred that Ac^- played a vital role in expanding the crystal lattice and promoting the crystallization.

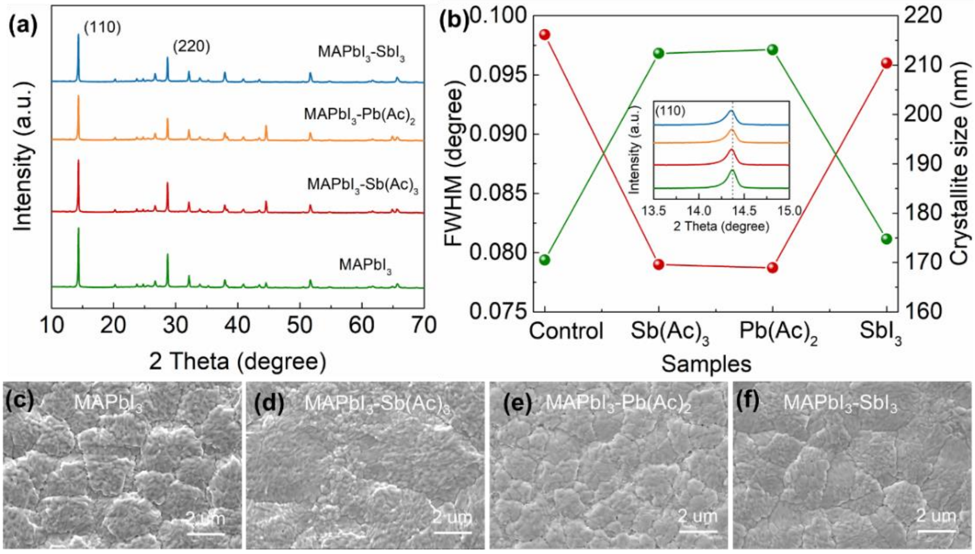

Figure 4.4 (a) XRD patterns of $MAPbI_3$, $MAPbI_3$-$Sb(Ac)_3$, $MAPbI_3$-$Pb(Ac)_2$ and $MAPbI_3$-SbI_3 perovskite films. (b) FWHM and corresponding average crystallite sizes obtained via the Scherrer equation. (c-f) Top-view SEM of $MAPbI_3$, $MAPbI_3$-$Sb(Ac)_3$, $MAPbI_3$-$Pb(Ac)_2$ and $MAPbI_3$-SbI_3 perovskite films.

The morphological effects of Ac^- and Sb^{3+} on $MAPbI_3$ perovskite film were examined by SEM as shown in **Figure 4.4c-f**. $MAPbI_3$-$Pb(Ac)_2$ perovskite film showed an improved surface morphology with obviously enlarged grain sizes while $MAPbI_3$-SbI_3 showed a very slight increase in grain size compared with pristine $MAPbI_3$ perovskite film, which was accordant with XRD results. With the assistance of Ac^- and Sb^{3+}, in which Ac^- plays a main role, $MAPbI_3$-$Sb(Ac)_3$ perovskite film exhibited optimized surface morphology with enlarged grain size. More importantly, the compactness and flatness of perovskite film was more obviously improved after $Sb(Ac)_3$ additive was incorporated, which was verified by atomic force microscope (AFM) images (**Figure 4.5**). The surface roughness was significantly reduced for $MAPbI_3$-$Sb(Ac)_3$ perovskite films, which was superior to $MAPbI_3$-$Pb(Ac)_2$, $MAPbI_3$-SbI_3 and pristine $MAPbI_3$ perovskite films. The reduced surface roughness means a smoother surface with less pinholes or sharp traps, thus affording a better contact between perovskite layer and HTL and benefitting the charge transfer.[50,51] Compared with pristine $MAPbI_3$ perovskite film, the addition of $Pb(Ac)_2$ and SbI_3 also deceased the surface roughness, which was still inferior to that of $Sb(Ac)_3$. Combining XRD and top-view SEM images, it is safe to say that both Ac^- and Sb^{3+} have influence on the final perovskite film morphology in different degree but Ac^- serves more as a film formation regulator to determine the film crystallinity and grain size. This may be because the C=O group in Ac^- which has lone-pair electrons can interact with Pb^{2+} in the precursor solution to manage the crystallization and growth of perovskite crystals.[35,52]

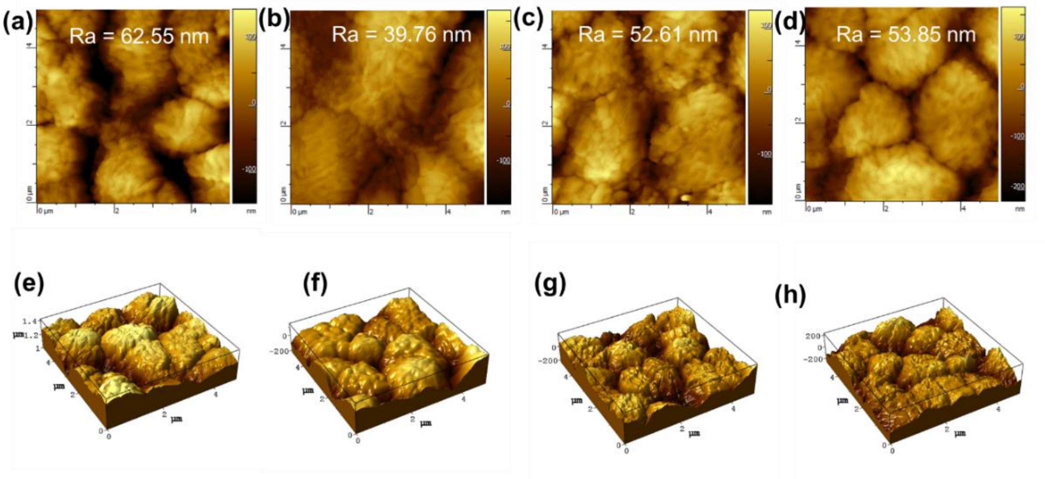

Figure 4.5 AFM images of (a) $MAPbI_3$, (b) $MAPbI_3$-$Sb(Ac)_3$, (c) $MAPbI_3$-$Pb(Ac)_2$ and (d) $MAPbI_3$-SbI_3 perovskite films. (e-f) The corresponding 3D AFM models.

To confirm the appearance of Ac^- and Sb^{3+} in perovskite films, XPS spectra of C 1*s* and Sb 3*d* were measured and shown in **Figure 4.6a** and **Figure 4.6b**, respectively. In C 1*s* XPS spectrum, the peaks at 284.8 and 286.3 eV represent C-C and C-N bonds, respectively.[53] An additional peak at around 288.0 eV for $MAPbI_3$-$Pb(Ac)_2$ and $MAPbI_3$-$Sb(Ac)_3$ perovskite films represent the C=O group, meaning the existence of Ac^- in these two perovskite films.[54] In Sb 3*d* XPS spectrum, the peaks at around 540.0 and 530.6 eV belong to Sb^{3+} $3d_{3/2}$ and $3d_{5/2}$, respectively, in $MAPbI_3$-$Sb(Ac)_3$ and $MAPbI_3$-SbI_3 perovskite films, indicative of the presence of Sb^{3+} in both films.[55] The peaks at around 532.7 eV are associated with O 1*s* which is from TiO_2 or the absorbed O_2 in air for all samples. The XPS spectra of I 3*d*, Pb 4*f* and N 1*s* were also analyzed to investigate the change of chemical environment caused by the incorporation of Ac$^-$ and Sb^{3+}. As shown in **Figure 4.6c**, N 1*s* peaks for $\mathrm{MAPbI_3}$-$\mathrm{Sb(Ac)_3}$ and $\mathrm{MAPbI_3}$-$\mathrm{Pb(Ac)_2}$ shifted to a higher binding energy, which may be caused by the hydrogen-bond interaction between C=O and -$\mathrm{NH_2}$ group in perovskite. The Pb 4*f* peaks shifted to higher binding energy for $\mathrm{MAPbI_3}$-$\mathrm{Sb(Ac)_3}$ and $\mathrm{MAPbI_3}$-$\mathrm{Pb(Ac)_2}$ (**Figure 4.6d**), which may be ascribed to the interaction between Pb^{2+} and Ac$^-$.[56] In addition, a slight shift was observed in I 3*d* peaks (**Figure 4.6e**) for $\mathrm{MAPbI_3}$-$\mathrm{Sb(Ac)_3}$ and $\mathrm{MAPbI_3}$-$\mathrm{SbI_3}$, meaning the interaction between Sb^{3+} and I$^-$. Based on this analysis, it can be concluded that both Ac$^-$ and Sb^{3+} existed in the final perovskite films and were capable to cause the variations of chemical environment via interacting with -$\mathrm{NH_2}$ group, Pb^{2+} and I$^-$ in perovskite.

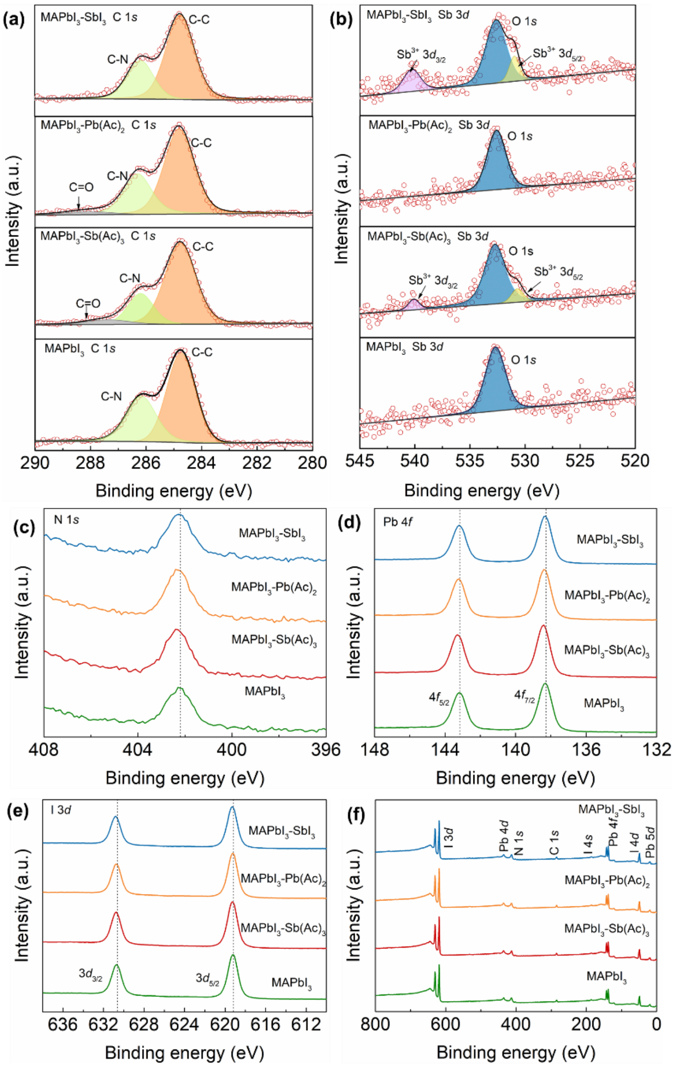

Figure 4.6 (a) C 1*s*, (b) Sb 3*d*, (c)N 1*s*, (d) Pb 4*f* and (e)I 3*d* XPS spectra for the $\mathrm{MAPbI_3}$, $\mathrm{MAPbI_3}$-$\mathrm{Sb(Ac)_3}$, $\mathrm{MAPbI_3}$-$\mathrm{Pb(Ac)_2}$ and $\mathrm{MAPbI_3}$-$\mathrm{SbI_3}$ perovskite films. (f) XPS survey spectra.

To evaluate the impact of Ac^- and Sb^{3+} on optical properties, we first compared the E_g values of various perovskite films, which were estimated from UV-vis spectra (**Figure 4.7a**). As shown in **Figure 4.7b**, the addition of $Pb(Ac)_2$ showed a negligible influence on E_g while the addition of SbI_3 increased E_g of $MAPbI_3$ perovskite film from 1.618 to 1.625 eV. Thus, it is reasonable to attribute such increase in E_g for $MAPbI_3$-$Sb(Ac)_3$ perovskite films (1.621 eV) to the function of Sb^{3+}. Then, ultraviolet photoelectron spectroscopy (UPS) was employed to study the influence of Ac^- and Sb^{3+} on the electronic structures of the perovskite films with results shown in **Figure 4.8a**. **Figure 4.8b** and **c** (Supporting Information) displays the valence band maximum (VBM) onset (E_{onset}) and secondary-electron cutoff energy boundary (E_{cutoff}). E_{VBM} can be calculated by the equation of $E_{VBM} = 21.21 - E_{cutoff} + E_{onset}$. According to the obtained E_g, the conduction band minimum (E_{CBM}) can be defined as $E_{CBM} = E_{VBM} - E_g$.[35,50] All these parameters are summarized in **Table 4.2**. Ac^- actually showed insignificant effect on the electronic structure as the addition of $Pb(Ac)_2$ did not cause the changes in E_{VBM} and E_{CBM}. By contrast, the introduction of SbI_3 obviously altered the electronic structure, upshifting E_{CBM} to -4.26 eV and E_{VBM} to -5.88 eV. Thus, Sb^{3+} should be mainly responsible for the variations of E_{CBM} and E_{VBM} of $MAPbI_3$-$Sb(Ac)_3$, which moved up to -4.28 and -5.90 eV, respectively. The upshift of E_{VBM} can narrow the gap between E_{VBM} of perovskite layer and HTL and the rise of E_{CBM} can provide an increased driving force to facilitate the injection of electrons from the photoactive layer to the ETL.[57,58] The optimized energy level alignment is shown in **Figure 4.8d**.

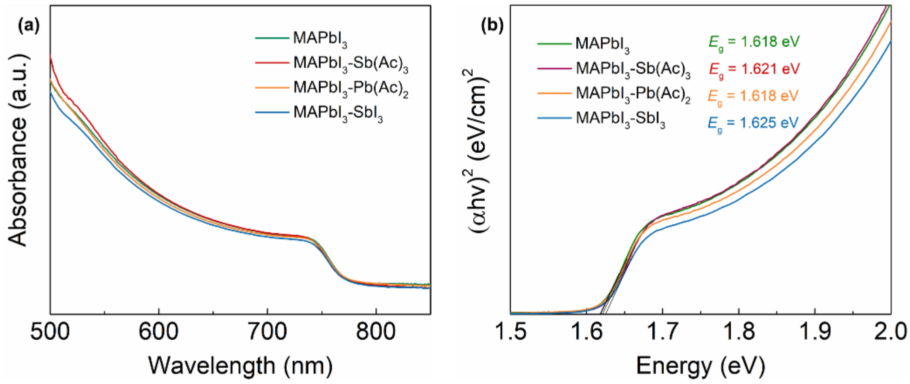

Figure 4.7 (a)UV-Vis spectra and (b) Kubelka-Munk spectra of $MAPbI_3$, $MAPbI_3$-$Sb(Ac)_3$,

MAPbI$_3$-Pb(Ac)$_2$ and MAPbI$_3$-SbI$_3$ perovskite films.

Table 4.2 Energy level parameters of MAPbI$_3$, MAPbI$_3$-Sb(Ac)$_3$, MAPbI$_3$-Pb(Ac)$_2$ and MAPbI$_3$-SbI$_3$ perovskite films.

Sample	E_{onset} (eV)	E_{cutoff} (eV)	E_{g} (eV)	E_{VBM} (eV)	E_{CBM} (eV)
MAPbI$_3$	1.730	17.01	1.618	5.930	4.312
MAPbI$_3$-Sb(Ac)$_3$	1.630	16.94	1.621	5.900	4.279
MAPbI$_3$-Pb(Ac)$_2$	1.730	17.01	1.618	5.930	4.312
MAPbI$_3$-SbI$_3$	1.790	17.12	1.625	5.880	4.255

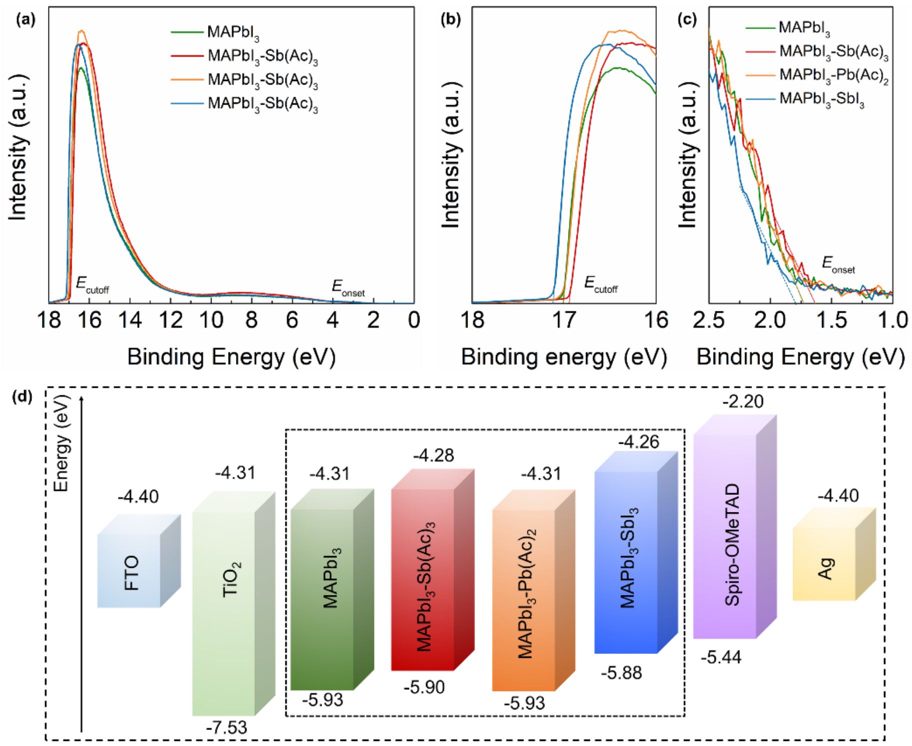

Figure 4.8 (a) UPS spectra, (b) secondary-electron cutoff energy boundary and (c) VBM onset of MAPbI$_3$, MAPbI$_3$-Sb(Ac)$_3$, MAPbI$_3$-Pb(Ac)$_2$ and MAPbI$_3$-SbI$_3$ perovskite films. (d) Energy level alignment among different functional layers in PSCs.

By comparing the PL spectra of various perovskite films (**Figure 4.9a**), we observed that the addition of both Pb(Ac)$_2$ and SbI$_3$ can to varying degree enhance the PL peak intensity and

$MAPbI_3$-$Sb(Ac)_3$ perovskite film displayed the largest PL peak intensity. In addition, different blue shift levels of PL peaks were observed after introducing $Sb(Ac)_3$, $Pb(Ac)_2$ and SbI_3 into $MAPbI_3$ perovskite. These results may reflect that Ac^- and Sb^{3+} jointly help to reduce the defects in perovskite films, which was beneficial for suppressing the nonradiative charge carrier recombination.[59] To analyze the charge carrier lifetime, time-resolved photoluminescence (TRPL) decay measurements were performed as shown in **Figure 4.9b**. The average charge carrier lifetime values of $MAPbI_3$-$Pb(Ac)_2$ and $MAPbI_3$-SbI_3 were 193.8 and 189.5 ns, respectively, which were longer than that of pristine $MAPbI_3$ (184.7 ns). With the joint effect of Ac^- and Sb^{3+}, $MAPbI_3$-$Sb(Ac)_3$ displayed the longest average charge carrier lifetime of 225.0 ns. The fitted charge carrier lifetime parameters are listed in **Table 4.3**. The prolonged charge carrier lifetime may be attributed to the reduced defect density, which was favorable for the enhancement of photovoltaic performance.[41,60] The space charge-limited current (SCLC) model was utilized to analyze the defect density via measuring the dark *J*-*V* curves of hole-only devices as shown in **Figure 4.9c**. The defect density (N_t) can be calculated via the following equation of $N_t = 2\varepsilon\varepsilon_0 V_{TFL}/eL^2$, where ε and ε_0 represent dielectric constant of perovskite and the vacuum permittivity, respectively, V_{TFL} means the trap-filled limit voltage, e is the elementary charge and L represents the thickness of perovskite film.[61] The V_{TFL} values obtained from **Figure 4.9c** were 1.14, 0.71, 0.91 and 0.95 V for $MAPbI_3$, $MAPbI_3$-$Sb(Ac)_3$, $MAPbI_3$-$Pb(Ac)_2$ and $MAPbI_3$-SbI_3 perovskite films, respectively and corresponding N_t values were 1.792×10^{16}, 1.116×10^{16}, 1.430×10^{16} and 1.493×10^{16} cm^{-3}, which further confirms that Ac^- and Sb^{3+} collaborated with each other to significantly reduce the defect density.

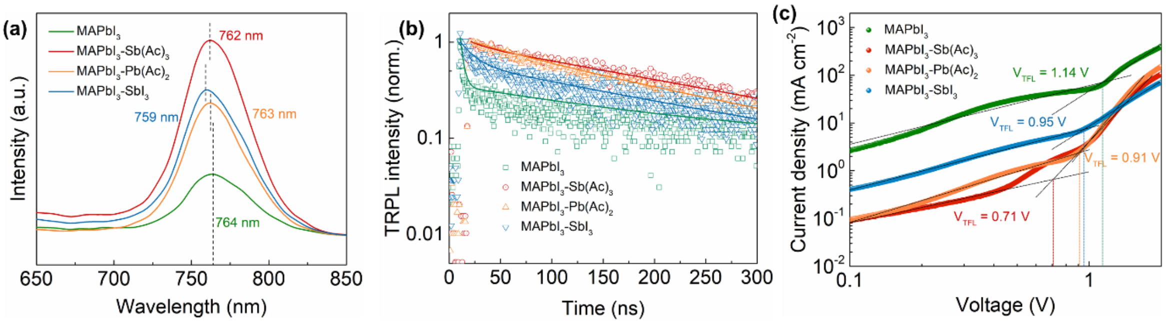

Figure 4.9 (a) Steady-state PL spectra and (b) TRPL spectra of $MAPbI_3$, $MAPbI_3$-$Sb(Ac)_3$, $MAPbI_3$-$Pb(Ac)_2$ and $MAPbI_3$-SbI_3 perovskite films. (c) Dark *J*-*V* curves of $MAPbI_3$, $MAPbI_3$-$Sb(Ac)_3$, $MAPbI_3$-$Pb(Ac)_2$ and $MAPbI_3$-SbI_3-based hole-only devices.

Table 4.3 Fitted charge carrier lifetime parameters of $MAPbI_3$, $MAPbI_3$-$Sb(Ac)_3$, $MAPbI_3$-$Pb(Ac)_2$ and $MAPbI_3$-SbI_3 perovskite films.

Sample	τ_1 (ns)	τ_1 ratio (%)	τ_2 (ns)	τ_2 ratio (%)	average τ (ns)
$MAPbI_3$	3.23	5.30	194.84	94.70	184.7
$MAPbI_3$-$Sb(Ac)_3$	15.59	0.86	226.83	99.14	225.0
$MAPbI_3$-$Pb(Ac)_2$	61.34	7.73	204.95	92.27	193.8
$MAPbI_3$-SbI_3	14.08	5.03	196.91	95.88	189.5

To study the effect of Ac^- and Sb^{3+} on the photovoltaic performance and their individual contribution to the photovoltaic parameters, *J-V* curves of $MAPbI_3$-$Pb(Ac)_2$ and $MAPbI_3$-SbI_3-based PSCs were tested and compared with that of pristine $MAPbI_3$ and $MAPbI_3$-$Sb(Ac)_3$-based PSCs. The *J-V* curves of best-performing devices are displayed in **Figure 4.10a**. The corresponding dark J-V curves were also measured and shown in **Figure 4.10b**. The distribution of photovoltaic parameters is shown in Figure **4.10c-f** and **Table 4.4**. It was found that $MAPbI_3$-$Pb(Ac)_2$-based PSCs delivered a champion PCE of 20.59% (average: 18.99%) with a large V_{oc} of 1.116 V (average: 1.094 V), a J_{sc} of 24.15 mA cm^{-2} (average: 23.38 mA cm^{-2}) and a FF of 0.7643 (average: 0.7420) while the best-performing $MAPbI_3$-SbI_3-based PSC produced a boosted PCE of 19.63% with a high J_{sc} of 24.88 mA cm^{-2} (average: 23.87 mA cm^{-2}), a V_{oc} of 1.088 V (average: 1.064 V) and a FF of 0.7387 (average: 0.7255). The significantly increased FF and V_{oc} for $MAPbI_3$-$Pb(Ac)_2$ device may be attributed to the improved film morphology and the increased crystallinity, which can help to reduce defects and suppress the charge carrier recombination.[62] The obviously enhanced J_{sc} for $MAPbI_3$-SbI_3 device may be credited to the optimized energy levels, which provided a large diving force to promote the electron injection into ETL.[58,63] In comparison with the photovoltaic performance of $MAPbI_3$-$Sb(Ac)_3$ device, it can be concluded that the incorporation of Ac^- contributed more to the enhancement of V_{oc} and FF while the addition of Sb^{3+} contributed more to the increase in J_{sc}, which finally gave rise to the greatly improved PCEs of $MAPbI_3$-$Sb(Ac)_3$-based PSCs.

Table 4.4 Comparison of photovoltaic performance parameters of PSCs based on $MAPbI_3$,

$MAPbI_3$-$Sb(Ac)_3$, $MAPbI_3$-$Pb(Ac)_2$ and $MAPbI_3$-SbI_3.

Device	PCE (%)		J_{sc} (mA cm^{-2})		V_{oc} (V)		FF	
	best	average	best	average	best	average	best	average
$MAPbI_3$	19.01	17.95	23.21	23.35	1.079	1.061	0.7586	0.7241
$MAPbI_3$-$Sb(Ac)_3$	21.04	19.76	24.19	23.86	1.100	1.094	0.7910	0.7570
$MAPbI_3$-$Pb(Ac)_2$	20.59	18.98	24.15	23.38	1.116	1.094	0.7643	0.7420
$MAPbI_3$-SbI_3	19.63	18.75	24.88	23.87	1.088	1.064	0.7387	0.7255

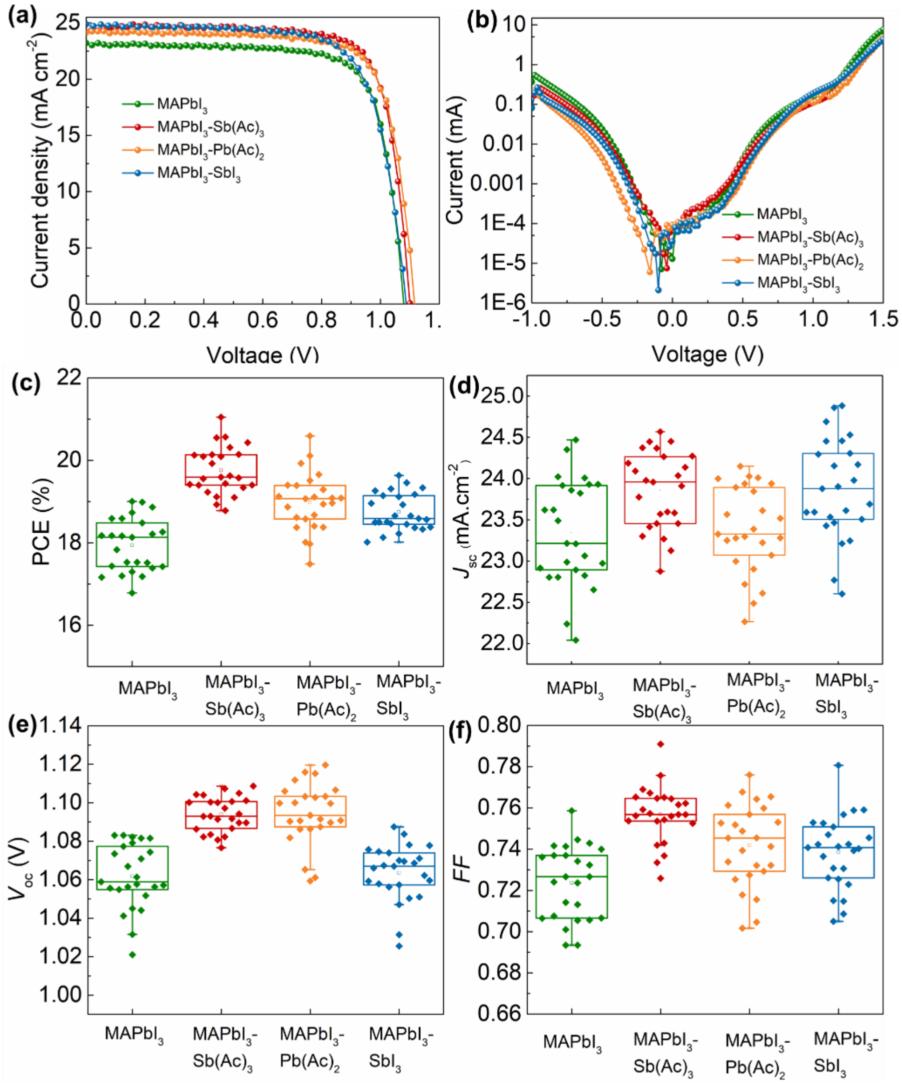

Figure 4.10 (a) *J*-*V* curves and (b) dark *J*-*V* curves of $MAPbI_3$, $MAPbI_3$-$Sb(Ac)_3$, $MAPbI_3$-$Pb(Ac)_2$ and $MAPbI_3$-SbI_3-based PSCs. The distribution of various photovoltaic parameters for $MAPbI_3$, $MAPbI_3$-$Sb(Ac)_3$, $MAPbI_3$-$Pb(Ac)_2$ and $MAPbI_3$-SbI_3-based PSCs: (c) PCE, (d) J_{sc},

(e) V_{oc} and (f) FF.

Mott-Schottky (MS) curves of the corresponding devices were measured to determine the influence of Ac^- and Sb^{3+} on the built-in voltage and free charge density (shown in **Figure 4.11a**). The capacitance and bias voltage have the relationship of $1/C^2 = (2/e\varepsilon\varepsilon_0 N_d)(V_{bi} - V_{app} - kT/e)$, where C means the capacitance of the space charge region, N_d means the free charge density, V_{bi} is the built-in voltage, V_{app} is the applied voltage, k is the Boltzmann's Constant and T means the absolute temperature.[64] V_{bi} can be obtained from the intercept of the MS curves with the x-axis, which were 0.57, 0.72, 0.69 and 0.57 eV for $MAPbI_3$, $MAPbI_3$-$Sb(Ac)_3$, $MAPbI_3$-$Pb(Ac)_2$ and $MAPbI_3$-SbI_3 devices, respectively. The introduction of SbI_3 had negligible influence on V_{bi} while the addition of $Pb(Ac)_2$ obviously increased V_{bi}, meaning that Ac^- played a more dominant role in improving V_{bi} than Sb^{3+}, which was consistent with their contribution to the enhancement of V_{oc}. N_d values were calculated to be 6.544×10^{15}, 3.938×10^{15}, 3.341×10^{15} and 3.339×10^{15} cm^{-3} for $MAPbI_3$ with $Sb(Ac)_3$, $Pb(Ac)_2$, SbI_3 and without additives, respectively. Although $Pb(Ac)_2$ and SbI_3 additives just slightly increased the free charge density, the addition of $Sb(Ac)_3$ can almost double the free charge density, which was closely related to the cooperation of Ac^- and Sb^{3+} to maximize each other's advantages. Furthermore, charge recombination resistance (R_{rec}) was evaluated via the electrochemical impedance spectra (EIS) measurements, which were tested under dark conditions and shown in **Figure 4.11b**. One clear low-frequency arc is observed in EIS spectra, which is related to interfacial charge carrier recombination.[65] Compared with pristine $MAPbI_3$ device, the greatly increased R_{rec} was observed after the addition of $Sb(Ac)_3$, $Pb(Ac)_2$ and SbI_3, which magnified that the charge carrier recombination, especially occurring at the interfaces between perovskite layer and ETL/HTL, can be effectively suppressed. For $Pb(Ac)_2$ modified device, this was derived from the improved surface morphology and increased grain size. For SbI_3 modified counterpart, the suppressed charge carrier recombination was ascribed to the optimized energy levels, which promoted the charge transfer and decrease charge carrier recombination at the perovskite/ETL interface. All these results suggested that Ac^- and Sb^{3+} collaborate with each other to maximize their individual advantage to endow $MAPbI_3$-$SbAc_3$-based PSCs with the best photovoltaic performance.

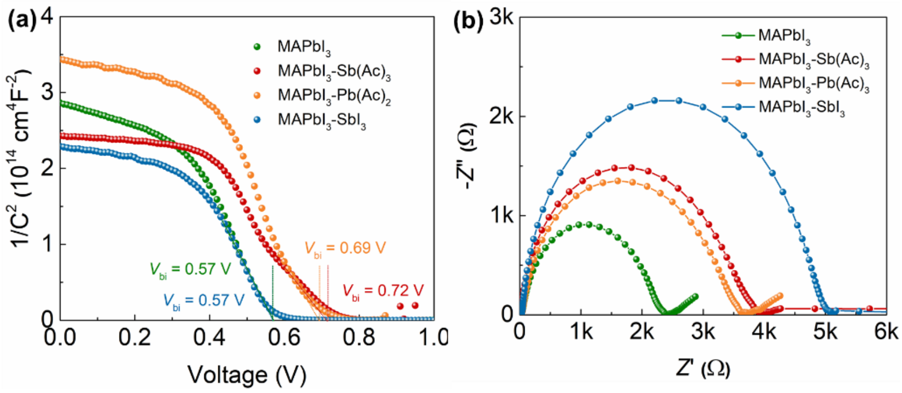

Figure 4.11 (a) MS curves and (b) EIS spectra tested at a bias of 0.9 V under dark condition of $MAPbI_3$, $MAPbI_3$-$Sb(Ac)_3$, $MAPbI_3$-$Pb(Ac)_2$ and $MAPbI_3$-SbI_3-based devices.

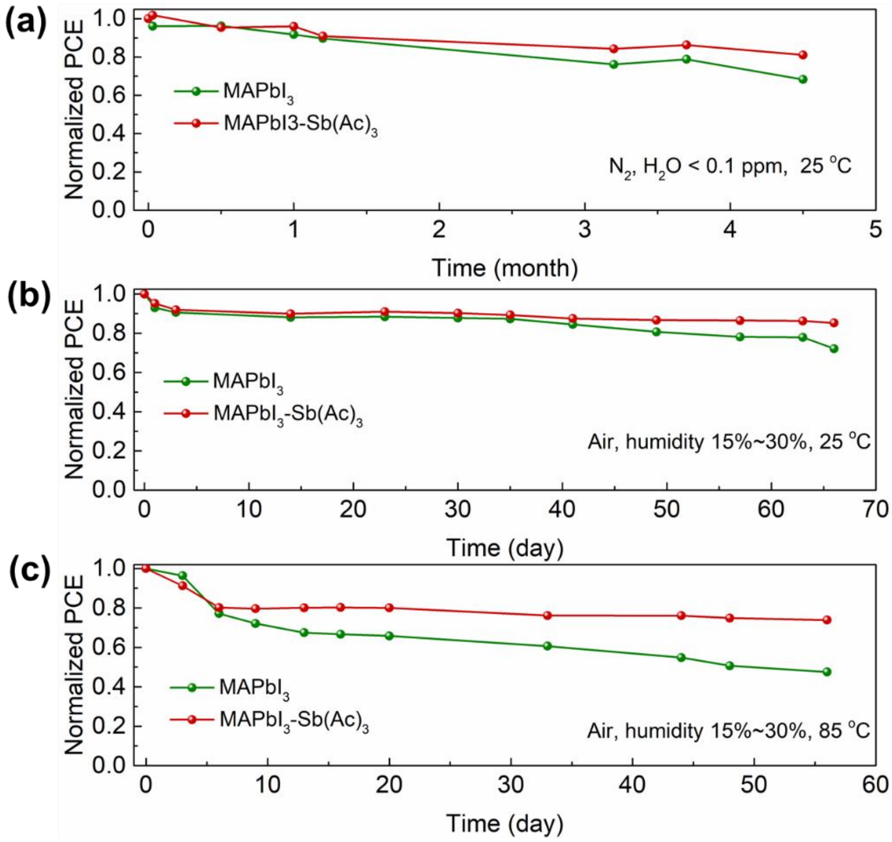

Figure 4.12 PCE evolution in various stability tests under different conditions (a) N_2, (b) humid air and (c) 85 °C in humid air of $MAPbI_3$ and $MAPbI_3$-$Sb(Ac)_3$-based PSCs without encapsulation.

Finally, the long-term stability of $MAPbI_3$-based PSCs without and with $Sb(Ac)_3$ additive was tested and analyzed. After storing the fabricated devices in a N_2-filled glove box for over 4 months, $MAPbI_3$-$Sb(Ac)_3$ device remained about 80% of their initial PCE while the PCE of pristine $MAPbI_3$ declined to below 70% as shown in **Figure 4.12a** and **Figure 4.13a**. To test the long-term stability in humid air, Ag electrode was replaced with Au to exclude the effect of the Ag oxidation on the durability. $MAPbI_3$-$Sb(Ac)_3$-based PSCs exhibited a better durability in the air with a relative humidity of 15-30%, keeping almost 85% of its initial PCE after a 65 days' storage in the air (**Figure 4.12b** and **Figure 4.13b**). In addition, the thermal stability of PSCs in the air was also tested via fabricating HTL-free devices with a cell configuration of FTO/c-TiO_2/m-TiO_2/perovskite/carbon. The J-V curves of best-performing HTL-free $MAPbI_3$ and $MAPbI_3$-$Sb(Ac)_3$ devices are displayed in **Figure 4.13c** and the photovoltaic parameters are listed in **Table 4.5**. The best-performing HTL-free $MAPbI_3$-based PSC delivered a PCE of 9.958% with a J_{sc} of 21.22 mA cm^{-2}, V_{oc} of 0.7830 V and a FF of 0.5993, while the best-performing HTL-free $MAPbI_3$-$Sb(Ac)_3$-based PSC produced a higher PCE of 11.27% with a J_{sc} of 21.71 mA cm^{-2}, a V_{oc} of 0.8282 V and a FF of 0.6265. Such a result further confirms the effectiveness of $Sb(Ac)_3$ additive in improving the device photovoltaic performance. When heating the devices at 85 °C in the air for 55 days, a decrease of over 50% in the PCE was observed for pristine $MAPbI_3$ device while only 25% of the initial PCE was lost for $MAPbI_3$-$Sb(Ac)_3$ counterpart as shown in **Figure 4.12c** and **Figure 4.13d**. All these parameters experienced different degrees of deterioration in the thermal stability test, among which the loss of FF should be the main responsibility for the eventual PCE degradation of $MAPbI_3$ device. Through analyzing the evolution of XRD patterns of $MAPbI_3$ and $MAPbI_3$-$Sb(Ac)_3$ perovskite films during the process of the thermal stability test as shown in **Figure 4.14** (Supporting Information), it was found that a new peak at around 12.75° appeared, assigning to PbI_2 phase,[36,62] which was caused by the decomposition of $MAPbI_3$ perovskite. Such PbI_2 phase appeared in both $MAPbI_3$ and $MAPbI_3$-$Sb(Ac)_3$ films but the growth rate of PbI_2 characteristic peak for $MAPbI_3$-$Sb(Ac)_3$ was much slower than that of pristine $MAPbI_3$ perovskite film, implying that the addition of $Sb(Ac)_3$ additive can slow the decomposition rate of $MAPbI_3$, thus improving its resistance to heat.[66]

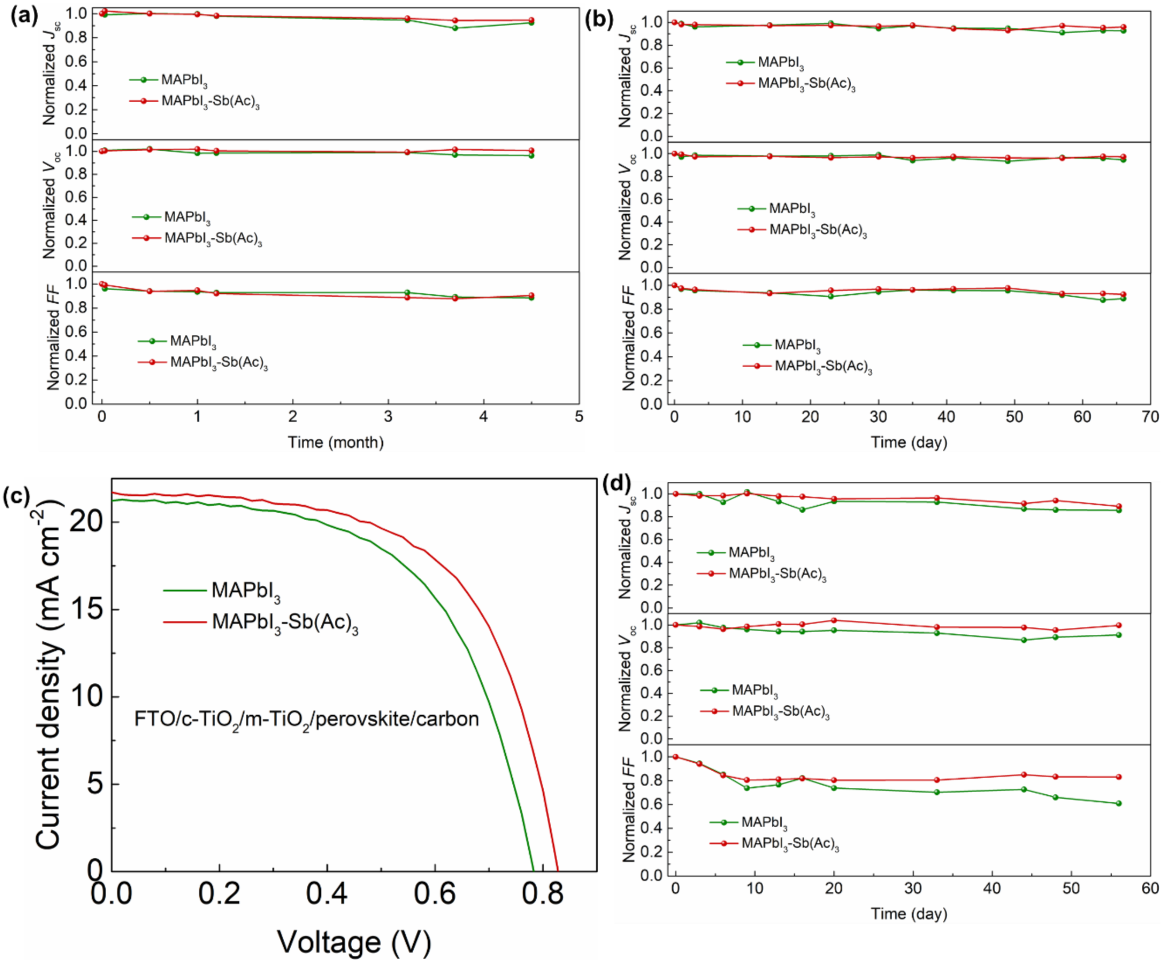

Figure 4.13 J_{sc}, V_{oc} and FF evolution during the long-term stability test in (a) N_2 and (b) humid air for PSCs based on $MAPbI_3$ and $MAPbI_3$-$Sb(Ac)_3$. (c) *J*-*V* curves of HTL-free PSCs based on $MAPbI_3$ and $MAPbI_3$-$Sb(Ac)_3$ for the thermal stability test. (d) J_{sc}, V_{oc} and FF evolution during the long-term thermal stability test for HTL-free PSCs based on $MAPbI_3$ and $MAPbI_3$-$Sb(Ac)_3$.

Table 4.5 Photovoltaic performance parameters of HTL-free devices based on $MAPbI_3$ and $MAPbI_3$-$Sb(Ac)_3$.

Device	PCE (%)	J_{sc} (mA cm^{-2})	V_{oc} (V)	FF
$MAPbI_3$	9.958	21.22	0.7830	0.5993
$MAPbI_3$-$Sb(Ac)_3$	11.27	21.71	0.8282	0.6265

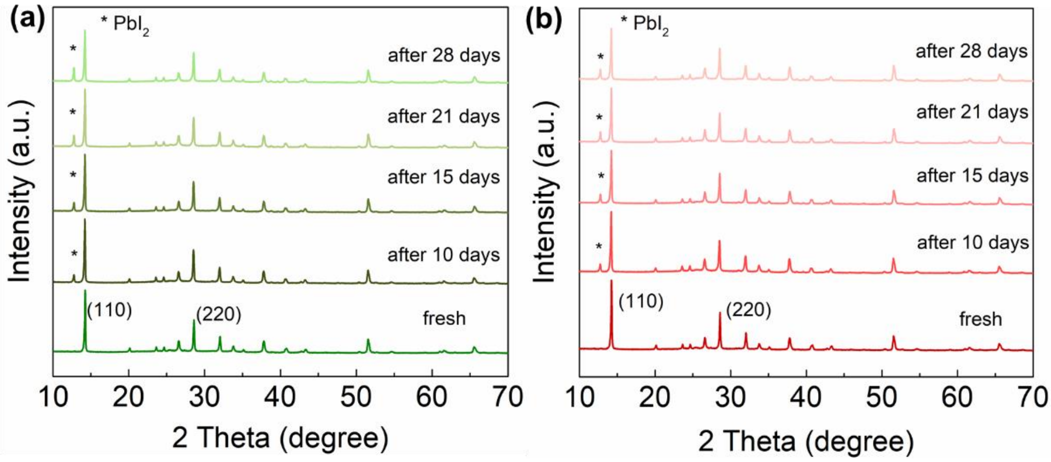

Figure 4.14 The investigation of XRD patterns during the long-term thermal stability test at 85 °C in air for PSCs based on $MAPbI_3$ and $MAPbI_3$-$Sb(Ac)_3$.

4.4 Conclusions

In this work, additive engineering utilizing $Sb(Ac)_3$ enabled the fabrication of high-performance $MAPbI_3$-based PSCs, delivering a PCE of above 21% and decent long-term stability against water and heat. The enhanced performance was credited to the synergistic effect of the anion (Ac^-) and the cation (Sb^{3+}) in the $Sb(Ac)_3$ additive. Ac^- acts as a crystal growth regulator to increase grain size and tailor the film surface morphology while Sb^{3+} is more effective in tuning the energy levels of perovskite films. Benefiting from the synergistic effect of Ac^- and Sb^{3+}, the incorporation of $Sb(Ac)_3$ additive into $MAPbI_3$ perovskite significantly reduced the defect density, suppressed the charge carrier recombination and promoted the charge transfer. This work presents a feasible avenue to improve the photovoltaic performance of $MAPbI_3$-based PSCs, providing useful guidance for promoting the further development of PSC technology.

4.5 Reference

[1] M. A. Green, A. Ho-Baillie, H. J. Snaith, *Nat. Photonics* **2014**, *8*, 506.

[2] S. D. Stranks, H. J. Snaith, *Nat. Nanotechnol*. **2015**, *10*, 391.

[3] Q. Lin, A. Armin, R.C. R. Nagiri, P. L. Burn, P. Meredith, *Nat. Photonics* **2015**, *9*, 106.

[4] N.-G. Park, *Mater. Today* **2015**, *18*, 65.

[5] A. Kojima, K. Teshima, Y. Shirai, T. Miyasaka, *J. Am. Chem. Soc.* **2009**, *131*, 6050.

[6] J. J. Yoo, G. Seo, M. R. Chua, T. G. Park, Y. Lu, F. Rotermund, Y.-K. Kim, C. S. Moon, N. J. Jeon, J.-P. Correa-Baena, V. Bulović, S. S. Shin, M. G. Bawendi, J. Seo, *Nature* **2021**, *590*, 587.

[7] J. Jeong, M. Kim, J. Seo, H. Lu, P. Ahlawat, A. Mishra, Y. Yang, M. A. Hope, F. T. Eickemeyer, M. Kim, Y. J. Yoon, I. W. Choi, B. P. Darwich, S. J. Choi, Y. Jo, J. H. Lee, B. Walker, S. M. Zakeeruddin, L. Emsley, U. Rothlisberger, A. Hagfeldt, D. S. Kim, M. Grätzel, J. Y. Kim, *Nature* DOI: 10.1038/s41586-021-03406-5.

[8] Y. Zou, H.-Y. Wang, Y. Qin, C. Mu, Q. Li, D. Xu, J. P. Zhang, *Adv. Funct. Mater.* **2019**, *29*, 1805810.

[9] A. Dobrovolsky, A. Merdasa, J. Li, K. Hirselandt, E. L. Unger, I. G. Scheblykin, *J. Phys. Chem. Lett.* **2020**, *11*, 1714.

[10] S. Wang, T. Sakurai, W. Wen, Y. Qi, *Adv. Mater. Interfaces* **2018**, *5*, 1800260.

[11] X. Yang, W. Wang, R. Ran, W. Zhou, Z. Shao, *Energy Fuels* **2020**, *34*, 10513.

[12] K. Wang, C. Wu, Y. Hou, D. Yang, T. Ye, J. Yoon, M. Sanghadasa, S. Priya, *Energy Environ. Sci.* **2020**, *13*, 3412.

[13] J. Burschka, N. Pellet, S.-J. Moon, R. Humphry-Baker, P. Gao, M. K. Nazeeruddin, M. Grätzel, *Nature* **2013**, *499*, 316.

[14] C.-H. Chiang, C.-G. Wu, *ACS Nano* **2018**, *12*, 10355.

[15] Y. Huang, T. Liu, C. Liang, J. Xia, D. Li, H. Zhang, A. Amini, G. Xing, C. Cheng, *Adv. Funct. Mater.* **2020**, *30*, 2000863.

[16] H. Xiang, P. Liu, W. Wang, R. Ran, W. Zhou, Z. Shao, Z., *Chem. Eng. J.*, DOI: 10.1016/j.cej.2020.127599.

[17] N. J. Jeon, J. H. Noh, Y. C. Kim, W. S. Yang, S. Ryu, S. I. Seok, *Nat. Mater.* **2014**, *13*, 897.

[18] N. J. Jeon, J. H. Noh, W. S. Yang, Y. C. Kim, S. Ryu, J. Seo, S. I. Seok, *Nature* **2015**, *517*, 476.

[19] F. Zhang, K. Zhu, *Adv. Energy Mater.* **2020**, *10*, 1902579.

[20] P. Liu, N. Han, W. Wang, R. Ran, W. Zhou, Z. Shao, *Adv. Mater*. **2021**, *33*, 2002582.

[21] Y. Zhang, J. Chen, X. Lian, W. Yang, J. Li, S. Tian, G. Wu, H. Chen, *Sci. China Chem.* **2019**, *62*, 859.

[22] P. Liu, H. Xiang, W. Wang, R. Ran, W. Zhou, Z. Shao, *J. Energy Chem.*, DOI: 10.1016/j.jechem.2021.03.024.

[23] Y. Yang, H. Peng, C. Liu, Z. Arain, Y. Ding, S. Ma, X. Liu, T. Hayat, A. Alsaedi, S. Dai, *J. Mater. Chem. A* **2019**, *7*, 6450.

[24] J.-W. Lee, H.-S. Kim, N.-G. Park, *Acc. Chem. Res.* **2016**, *49*, 311.

[25] B. J. Foley, J. Girard, B. A. Sorenson, A. Z. Chen, J. Scott Niezgoda, M. R. Alpert, A. F. Harper, D.-M. Smilgies, P. Clancy, W. A. Saidi, J. J. Choi, *J. Mater. Chem. A* **2017**, *5*, 113.

[26] T. Li, Y. Pan, Z. Wang, Y. Xia, Y. Chen, W. Huang, *J. Mater. Chem. A* **2017**, *5*, 12602.

[27] X. Li, C.-C. Chen, M. Cai, X. Hua, F. Xie, X. Liu, J. Hua, Y.-T. Long, H. Tian, L. Han, *Adv. Energy Mater.* **2018**, *8*, 1800715.

[28] Q. Wu, P. Zhou, W. Zhou, X. Wei, T. Chen, S. Yang, *ACS Appl. Mater. Interfaces* **2016**, *8*, 15333.

[29] L. Yang, G. Han, Y. Chang, Y. Zhang, Y. Xiao, *Mater. Sci. Semicon. Process.* **2019**, *104*, 104671.

[30] Y. Xiao, L. Yang, G. Han, Y. Li, M. Li, H. Li, *Org. Electron.* **2019**, *65*, 201.

[31] Z. Zhang, W. Fan, X. Wei, L. Zhang, Z. Yang, Z. Wei, T. Shen, H. Si, J. Qi, *J. Alloys Compd.* **2019**, *802*, 694.

[32] Q. Zhao, G. R. Li, J. Song, Y. Zhao, Y. Qiang, X. P. Gao, *Sci. Rep.* **2016**, 6, 38670.

[33] D. Forgács, M. Sessolo, H. J. Bolink, *J. Mater. Chem. A* **2015**, *3*, 14121.

[34] G. Tang, P. You, Q. Tai, R. Wu, F. Yan, *Sol. RRL* **2018**, *2*, 1800066.

[35] Y. Wu, L. Wan, S. Fu, W. Zhang, X. Li, J. Fang, *J. Mater. Chem. A* **2019**, *7*, 14136.

[36] Y. Wang, Y. Wu, S. Fu, C. Song, L.Wan, W. Zhang, X. Li, W. Yang, W. Song, J. Fang, *J. Mater. Chem. C* **2019**, *7*, 11411.

[37] J. Zhang, M.-h. Shang, P. Wang, X. Huang, J. Xu, Z. Hu, Y. Zhu, L. Han, *ACS Energy Lett.* **2016**, *1*, 535.

[38] H. W. Qiao, S. Yang, Y. Wang, X. Chen, T. Y. Wen, L. J. Tang, Q. Cheng, Y. Hou, H. Zhao, H. G. Yang, *Adv. Mater.* **2019**, *31*, 1804217.

[39] Y. Xiao, G. Han, Y. Chang, Y. Zhang, Y. Li, M. Li, *J. Power Sources* **2015**, *286*, 118.

[40] W. Zhou, D. Li, Z. Xiao, Z. Wen, M. Zhang, W. Hu, X. Wu, M. Wang, W.-H. Zhang, Y. Lu, S. Yang, S. Yang, *Adv. Funct. Mater.* **2019**, *29*, 1901026.

[41] S. Yang, H. Zhao, Y. Han, C. Duan, Z. Liu, S. Liu, *Small* **2019**, *15*, 1904387.

[42] H. Sun, J. Zhang, X. Gan, L. Yu, H. Yuan, M. Shang, C. Lu, D. Hou, Z. Hu, Y. Zhu, L. Han, *Adv. Energy Mater.* **2019**, *9*, 1900896.

[43] L. Chen, L. Wan, X. Li, W. Zhang, S. Fu, Y. Wang, S. Li, H.-Q. Wang,W. Song, J. Fang, *Chem. Mater.* **2019**, *31*, 9032.

[44] Z. Yang, C.-C. Chueh, P.-W. Liang, M. Crump, F. Lin, Z. Zhu, A. K. Jen, *Nano Energy* **2016**, *22*, 328.

[45] F. Bai, J. Zhang, Y. Yuan, H. Liu, X. Li, C.-C. Chueh, H. Yan, Z. Zhu, A. K.-Y. Jen, *Adv. Mater.* **2019**, *31*, 1904735.

[46] B. Chen, P. N. Rudd, S. Yang, Y. Yuan, J. Huang, *Chem. Soc. Rev.* **2019**, *48*, 3842.

[47] E. Aydin, M. De Bastiani, S. De Wolf, *Adv. Mater.* **2019**, *31*, 1900428.

[48] W. Xu, G. Lei, C. Tao, J. Zhang, X. Liu, X. Xu, W.-Y. Lai, F. Gao, W. Huang, *Adv. Funct. Mater.* **2018**, *28*, 1802320.

[49] H. Kim, J. W. Lee, G. R. Han, S. K. Kim, J. H. Oh, *Adv. Funct. Mater.* **2021**, *31*, 2008801.

[50] P. Liu, X. Yang, Y. Chen, H. Xiang, W. Wang, R. Ran, W. Zhou, Z. Shao, *ACS Appl. Mater. Interfaces* **2020**, *12*, 23984.

[51] K. Wang, C. Liu, P. Du, H.-L. Zhang, X. Gong, *Small* **2015**, *11*, 3369.

[52] J. Peng, J. I. Khan, W. Liu, E. Ugur, T. Duong, Y. Wu, H. Shen, K. Wang, H. Dang, E. Aydin, X. Yang, Y. Wan, K. J. Weber, K. R. Catchpole, F. Laquai, S. De Wolf, T. P. White, *Adv. Energy Mater.* **2018**, *8*, 1801208.

[53] X. Jiang, J. Zhang, S. Ahmad, D. Tu, X. Liu, G. Jia, X. Guo, C. Li, *Nano Energy* **2020**, *75*, 104892.

[54] Q. Sun, P. Fassl, D. Becker-Koch, A. Bausch, B. Rivkin, S. Bai, P. E. Hopkinson, H. J. Snaith, Y. Vaynzof, *Adv. Energy Mater.* **2017**, *7*, 1700977.

[55] G. Chen, P. Wang, Y. Wu, Q. Zhang, Q. Wu, Z. Wang, Z. Zheng,Y. Liu, Y. Dai, B. Huang, *Adv. Mater.* **2020**, *32*, 2001344.

[56] Y. Chen, X. Yang, P. Liu, W. Wang, R. Ran, W. Zhou, Z. Shao, *Sol. RRL* **2021**, *5*, 2000621.

[57] D. Luo, W. Yang, Z. Wang, A. Sadhanala, Q. Hu, R. Su, R. Shivanna, G. F. Trindade, J. F. Watts, Z. Xu, T. Liu, K. Chen, F. Ye, P. Wu, L. Zhao, J. Wu, Y. Tu, Y. Zhang, X. Yang, W. Zhang, R. H. Friend, Q. Gong, H. J. Snaith, R. Zhu, *Science* **2018**, *360*, 1442.

[58] Q. Zhang, W. Zhu, D. Chen, Z. Zhang, Z. Lin, J. Chang, J. Zhang, C. Zhang, Y. Hao, *ACS Appl. Mater. Interfaces* **2019**, *11*, 2997.

[59] R. Wang, J. Xue, L. Meng, J.-W. Lee, Z. Zhao, P. Sun, L. Cai, T. Huang, Z.Wang, Z.-K. Wang, Y. Duan, J. L. Yang, S.Tan, Y. Yuan, Y. Huang, Y. Yang, *Joule* **2019**, *3*, 1464.

[60] Q. Jiang, Y. Zhao, X. Zhang, X. Yang, Y. Chen, Z. Chu, Q. Ye, X. Li, Z. Yin, J. You, *Nat. Photonics* **2019**, *13*, 460.

[61] X. Yang, Y. Chen, P. Liu, H. Xiang, W. Wang, R. Ran, W. Zhou, Z. Shao, *Adv. Funct. Mater.* **2020**, *30*, 2001557.

[62] J. Chen, S.-G. Kim, X. Ren, H. S. Jung, N.-G. Park, *J. Mater. Chem. A* **2019**, *7*, 4977.

[63] J. H. Heo, M. S. You, M. H. Chang, W. Yin, T. K. Ahn, S.-J. Lee, S.-J. Sung, D. H. Kim, S. H. Im, *Nano Energy* **2015**, *15*, 530.

[64] J. J. He, Z. R. Zhou, Z. Q. Lin, B. Ge, H. W. Qiao, Y. Hou, S. Yang, H. G. Yang, *ACS Appl. Energy Mater.* **2020**, *3*, 4121.

[65] B. Yang, M. Wang, X. Hu, T. Zhou, Z. Zang, *Nano Energy* **2019**, *57*, 718.

[66] W. Zhang, Y. Li, X. Liu, D. Tang, X. Li, X. Yuan, *Chem. Eng. J.* **2020**, *379*, 122298.

Chapter 5 Promoting the Efficiency and Stability of $CsPbIBr_2$-Based All-Inorganic Perovskite Solar Cells through a Functional Cu^{2+} Doping Strategy

Abstract

Although organic-inorganic halide perovskite solar cells (PSCs) have shown dramatically enhanced power conversion efficiencies (PCEs) in the last decade, their long-term stability is still a critical challenge for commercialization. To address this issue, tremendous research efforts have been devoted to exploring all-inorganic PSCs because of their intrinsically high structural stability. Among them, $CsPbIBr_2$-based all-inorganic PSCs have drawn increasing attention owing to their suitable bandgap and favorable stability. However, the PCEs of $CsPbIBr_2$-based PSCs are still far from those of their organic-inorganic counterparts, thus inhibiting their practical applications. Herein, we demonstrate that by simply doping an appropriate amount of Cu^{2+} into a $CsPbIBr_2$ perovskite lattice (0.5 at.% to Pb^{2+}), the perovskite crystallinity and grain size are increased, the perovskite film morphology is improved, the energy level alignment is optimized and the trap density and charge recombination are reduced. As a consequence, a decent PCE improvement from 7.81% to 10.4% is achieved along with an enhancement ratio of 33% with a $CsPbIBr_2$-based PSC. Furthermore, the long-term stability of $CsPbIBr_2$-based PSCs against moisture and heat is also remarkably improved by Cu^{2+} doping. This work provides a facile and effective route to improve the PCE and long-term stability of $CsPbIBr_2$-based all-inorganic PSCs.

5.1 Introduction

Organic-inorganic hybrid halide PSCs have been recognized as a promising class of photovoltaics owing to their high efficiency, tuneable bandgap and relatively simple fabrication process. During the past decade, organic-inorganic hybrid halide PSCs have witnessed a great boost in their power conversion efficiencies (PCEs) from 3.8% in 2009 to a current value of over 25%.[1,2] Despite the high efficiency of organic-inorganic hybrid halide PSCs, which have been almost comparable with commercial silicon solar cells, the further development of organic-inorganic hybrid halide PSCs is limited by their poor stability, as they are very sensitive to humidity and heat.[3] To overcome this drawback, remarkable efforts have been devoted to enhancing the stability of organic-inorganic hybrid halide PSCs by optimizing the device architecture, compositional engineering, interfacial engineering and utilizing encapsulation technology, which have achieved modest progress.[4-9] All-inorganic perovskites have much higher intrinsic stability compared to organic-inorganic hybrid perovskites because inorganic cations have much lower sensitivity towards humidity and heat than that of organic groups; thus, all-inorganic halide PSCs have attracted remarkable interest as an alternative avenue for managing the stability issue.[10]

To date, the most investigated Pb-based inorganic perovskites include $CsPbI_3$, $CsPbI_2Br$, $CsPbIBr_2$ and $CsPbBr_3$, which possess some distinct advantages as well disadvantages in terms of PSC applications. Specifically, $CsPbI_3$ with an appropriate bandgap (1.73 eV) has achieved the highest PCE among the various all-inorganic halide PSCs. However, it suffers from severe instability in its phase structure because the valid α-$CsPbI_3$ perovskite structure for light absorbers in solar cells is only stable at temperatures over 330 °C; unfortunately at room temperature, the structure exists in the form of a non-photoactive phase (δ-$CsPbI_3$), which shows a negative effect on the PCEs of PSCs.[11-13] In contrast, $CsPbBr_3$ shows superior stability in its phase structure and even a strong resistance to heat and humidity, but its wide bandgap (2.3 eV) negatively influences sunlight absorption; the above bandgap leads to a low generation of photocurrent in PSCs.[14-16] Auspiciously, mixed halide all-inorganic perovskites ($CsPbI_xBr_{3-x}$) bring new hope for the fabrication of highly efficient and durable PSCs by fully balancing the bandgap (light absorption capability) and stability.[17,18] For example, brown $CsPbI_2Br$ with a narrow bandgap of 1.92 eV shows a higher stability of phase structure than that of $CsPbI_3$, but it is also sensitive to high humidity and temperature.[19,20] Further increasing the Br^- amount in the X site of the perovskites contributes to an increased stability. As a result, $CsPbIBr_2$ shows satisfactory stability and a suitable bandgap (2.05 eV), making it a good choice as a light absorber in PSCs.

Despite the high structural stability and favourable bandgap of $CsPbIBr_2$ perovskite, the

PCEs of $CsPbIBr_2$-based PSCs are currently still not satisfactory and far from that of typical organic-inorganic halide PSCs as well as $CsPbI_3$ and $CsPbI_2Br$-based PSCs. The above inadequacy in PCE is mainly attributed to the poor quality of the perovskite film. Actually, it is highly challenging to deposit a high-quality $CsPbIBr_2$ film via a conventional solution-based spin-coating method; instead, pinholes and small grains are apparent and massive grain boundaries easily appear on the surface.[21] Previous studies have demonstrated that such pinholes and massive grain boundaries display a negative impact on the device performance, as they may disturb charge carrier diffusion and cause severe charge recombination.[22] In pursuit of high-quality $CsPbIBr_2$ films, a variety of strategies have been implemented that focus on optimizing the spin-coating process[23-25], adopting a dual source thermal evaporation technique[26], conducting an interfacial modification[27] and applying a posttreatment process to passivate the grain boundaries and defects.[28] Very recently, high PCEs of 9.17% and 9.86% have been obtained by $CsPbIBr_2$-based PSCs via precisely optimizing the substrate-preheating temperature and choosing antisolvents and organic-ion surface passivation strategies.[29,30] However, the additional fabrication steps inevitably increase the fabrication cost and scale-up difficulty.

Among the variety of available strategies, functional elemental doping is widely applied for fine tuning the photoelectronic properties of perovskites. In addition, it is also a facile, feasible, effective and easily controllable approach to improve the quality of a perovskite film. For example, Mn^{2+} and Li^{+} doped into $CsPbIBr_2$ has been found to enhance the crystallinity and morphology of perovskite films in comparison with their undoped counterparts, thus alleviating the hole transfer energy loss, facilitating charge transfer and significantly improving the PCE and air stability of $CsPbIBr_2$-based PSCs.[31,32] Sn^{2+} has also been reported as a dopant for $CsPbIBr_2$ perovskites, in which Sn^{2+} plays a vital role in appropriately tuning the bandgap of $CsPbIBr_2$ and improving the perovskite film morphology. As a result, remarkably enhanced PCEs of over 11% and an improved long-term stability of $CsPbIBr_2$-based PSCs have been achieved.[33,34] In another study, Liu et al. broke the limit of the Goldschmidt tolerance factor (t, whose value is between 0.8 and 1.0) and successfully incorporated Ba^{2+} into a $CsPbIBr_2$ perovskite. Intriguingly, Ba^{2+} doping was capable of enlarging the grain size and enhancing the crystallinity of $CsPbIBr_2$, which led to an increase in the PCE of Ba^{2+}-doped $CsPbIBr_2$-based devices to 10.51% and prevailed over that of the undoped pristine counterpart (8.40%).[35] It is well known that manganese changes to multiple oxidation states while Sn^{2+} is easily oxidized to Sn^{4+}. Thus, to bring about a beneficial effect, the raw materials should be well selected, and the synthesis conditions should be strictly controlled to ensure that Mn and Sn are in a 2+ oxidation state when doped into a perovskite lattice.

Herein, we demonstrated that the incorporation of stable Cu^{2+} into the $CsPbIBr_2$ perovskite lattice through functional doping in the B-site could effectively improve the $CsPbIBr_2$ film quality and enhance the PCE and operational stability. The influences of Cu^{2+} doping on the perovskite film quality, photoelectronic properties, photovoltaic performance and long-term stability were systematically investigated. It was found that a small amount of Cu^{2+} doping brought about significant changes, clearly increasing the crystallinity and particle sizes, improving the surface morphology, optimizing the energy level alignment, lowering the trap densities and suppressing the charge carrier recombination in the perovskite films. By optimizing the doping amount of Cu^{2+} (0.50 at.%), a PSC with $CsPbIBr_2$-0.50%Cu displayed a much superior PCE of 10.4% with an enhancement factor of 33% and a much better moisture stability and thermal stability compared with that of the pristine $CsPbIBr_2$-based PSC. This study could provide a new avenue for the design and fabrication of highly efficient and stable $CsPbIBr_2$-based PSCs and promote the practical application of all-inorganic PSCs.

5.2 Experimental section

5.2.1 Materials

All materials and reagents were directly used as received without any purification, including titanium tetrachloride ($TiCl_4$, GR, 99.5%, Aladdin), caesium iodide (CsI, 99.999% trace metals basis, Sigma-Aldrich), lead bromide ($PbBr_2$, 99.999% trace metals basis, Sigma-Aldrich), 2,2′,7,7′-Tetrakis (N,N-di-p-methoxyphenylamine)-9,9′-spirobifluorene (Spiro-OMeTAD, Xi'an Polymer Light Technology Corp.), phenyl-C61-butyric acid methyl ester (PCBM, 99%, Xi'an Polymer Light Technology Corp.), poly(3,4-ethylenedioxythiophene)-

poly(styrenesulfonate) (PEDOT:PSS, 1-3 wt% solution in water, Xi'an Polymer Light Technology Corp.) and dimethyl sulfoxide (DMSO, 99.8%, anhydrous, Aladdin).

5.2.2 Fabrication of solar cells

Fluorine-doped tin oxide (FTO) glass was successively cleaned with acetone, isopropanol, deionized water, and ethanol. Before preparing a compact TiO_2 (c-TiO_2) layer, the FTO glass was treated via oxygen plasma cleaning for 5 min. Then, the c-TiO_2 layer was deposited by immersing the FTO substrates in a 40 mM $TiCl_4$ aqueous solution for 90 min at 70 °C. Sequentially, the obtained substrates were washed with deionized water and ethanol and dried with N_2 followed by annealing the prepared TiO_2 layer at 200 °C for 30 min in air. Before transferring the substrates into glove box for the preparation of perovskite layers, the substrates with c-TiO_2 were treated via oxygen plasma cleaning for 5 min.

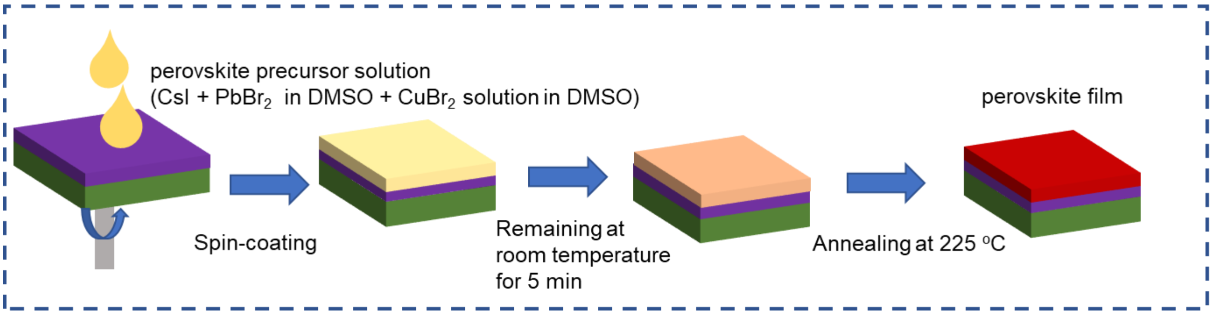

Figure 5.1 The schematic of the fabrication process of $CsPbIBr_2$ perovskite films.

After that, the perovskite layers were obtained via spin-coating a 1 M $CsPbIBr_2$ precursor solution (in which 367 mg $PbBr_2$ and 260 mg CsI were dissolved in 1 mL DMSO) on top of the c-TiO_2 layer at 2000 rpm for 100 s as shown in **Figure 5.1**. After spin-coating, the obtained film was remained at room temperature for 5 min. Then, the above samples were annealed at 225 °C for 10 min. For Cu^{2+}-doped $CsPbIBr_2$ perovskites, 0.2 M $CuBr_2$-DMSO solution was prepared, and different amounts of this solution were introduced into the perovskite precursor solution to fabricate 0.25%, 0.50%, 0.75% and 1.0% Cu^{2+} (molar ratio)-doped $CsPbIBr_2$. For the HTL, a solution was prepared according to a previous report. The HTL was obtained by spin coating spiro-OMeTAD solution onto the perovskite layers at 4000 rpm for 30 s. Finally, a Ag layer with a thickness of approximately 100 nm was thermally evaporated on top of the

HTL to complete the whole fabrication process. The active area of the device in this work was 0.0625 cm^2.

5.2.3 Characterization

XRD (Rigaku Smartlab equipped with Cu Kα radiation) was utilized to examine the crystal structure. The morphology was observed by using field emission scanning electron microscopy (FESEM, HITACHI S-4800). The chemical states of ions were analysed by XPS (PHI550), and all spectra were corrected using the C 1s line at 284.6 eV before analysis. The surface smoothness of films was obtained through atomic force microscopy (AFM, Horiba, SmartSPM). UV-visible (UV-vis) spectra were obtained with a PerkinElmer (PE) Lambda 750s spectrometer (Perkin Elmer, USA). The photoluminescence spectra (PL) were obtained by utilizing a PE fluorescence spectrometer (FL 6500). The *J-V* curves of the fabricated devices were tested under AM 1.5G illumination at 100 mW cm^{-2} under a solar simulator (Zolix), which was calibrated by a standard silicon solar cell. EQE was performed by using a Zolix Solar Cell Scan 100 instrument and setting the wavelength region from 300 to 700 nm. The EIS measurements were conducted on a computer-controlled electrochemical workstation (CHI760E) under dark conditions. The frequency range was between 0.1 Hz and 1 MHz with an amplitude of 20 mV and a fixed bias of 0.5 V.

5.3 Results and discussion

Four different doping amounts of Cu^{2+} (0.25%, 0.50%, 0.75% and 1%, molar ratio) were doped into $CsPbIBr_2$ perovskite films. For simplicity, we wrote these perovskites as pristine $CsPbIBr_2$, $CsPbIBr_2$-0.25%Cu, $CsPbIBr_2$-0.50%Cu, $CsPbIBr_2$-0.75%Cu and $CsPbIBr_2$-1.0%Cu. **Figure 5.2** shows photos of the $CsPbIBr_2$ precursor solution with the incorporation of different amounts of Cu^{2+} in which the precursor solution colour gradually changes from light yellow to brown with an increasing amount of doped Cu^{2+}.

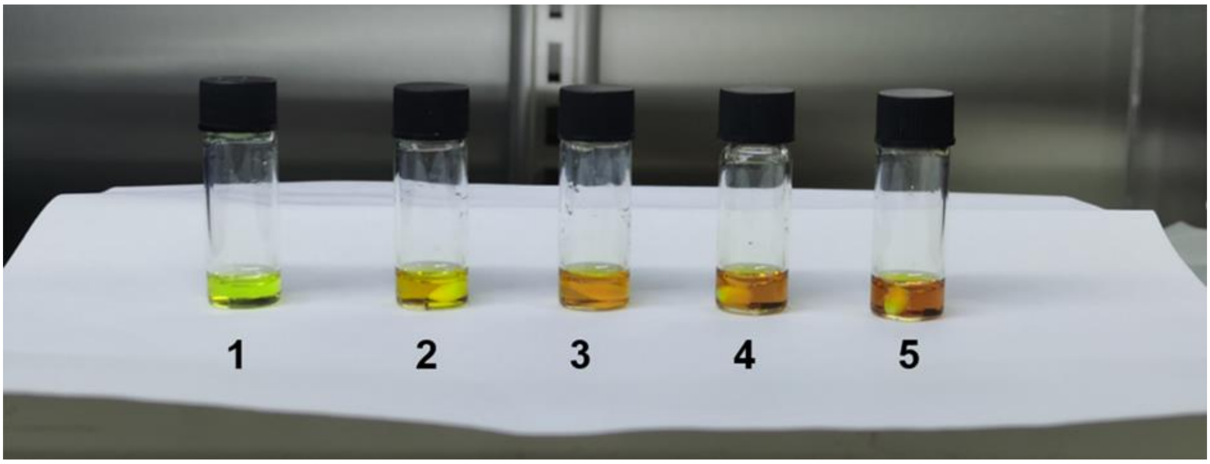

Figure 5.2 The photographs of $CsPbIBr_2$ precursor solution with different amount of Cu^{2+} incorporation (1: Pristine $CsPbIBr_2$, 2: $CsPbIBr_2$-0.25%Cu, 3: $CsPbIBr_2$-0.50%Cu, 4: $CsPbIBr_2$-0.75%Cu, 5: $CsPbIBr_2$-1.0%Cu).

Figure 5.3a shows the X-ray diffraction (XRD) patterns of $CsPbIBr_2$ films with various doping amounts of Cu^{2+} after annealing at 225 °C for 10 min in a glovebox. The main XRD diffraction peaks at 2-theta of 15.6° and 30.8° could be indexed to the (100) and (200) planes of α-phase perovskite $CsPbIBr_2$, respectively, implying a preferential growth direction along the [100] plane of the grains in the $CsPbIBr_2$ films.[36] No impurity peaks were found, indicating that all the as-prepared $CsPbIBr_2$ samples with different doping amounts of Cu^{2+} were pure-phase perovskites with cubic structures. From the enlarged (100) and (200) diffraction peaks in **Figure 5.3b**, it was observed that after Cu^{2+} incorporation, the main peaks shifted to a higher angle in conjunction with an increasing amount of Cu^{2+}. The above result further demonstrated the successful doping of Cu^{2+}, with a smaller cation size (72 pm) than Pb^{2+} (120 pm), into the B-site of the $CsPbIBr_2$ lattice, which caused the shrinkage of the perovskite lattice. In addition, after doping with Cu^{2+}, the main peak intensity of the perovskites first increased and then decreased with Cu^{2+} doping and reached the maximum for the $CsPbIBr_2$-0.50%Cu sample. Meanwhile, $CsPbIBr_2$-0.50%Cu showed the narrowest full width at half maximum (FWHM) of the (200) diffraction peaks (**Figure 5.3c**). These results were indicative of the enhanced crystallinity brought about by an optimized doping amount of Cu^{2+}.[37] The increased crystallinity of perovskite films is favorable to light absorption, thus improving PCE of the corresponding PSCs via enhancing photocurrent density.

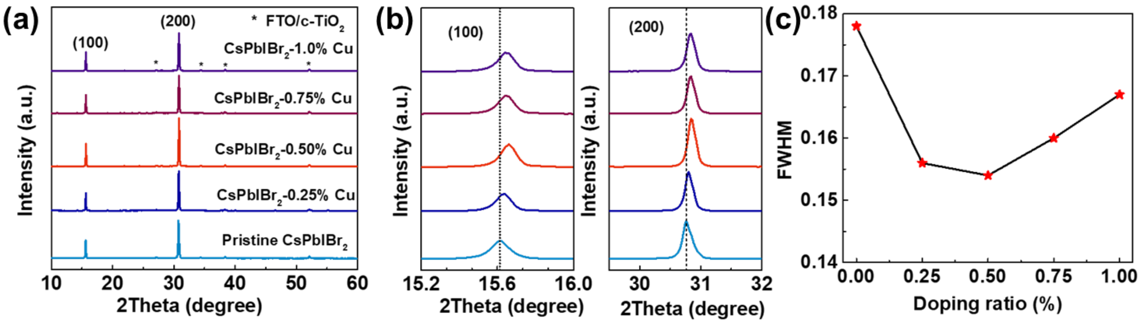

Figure 5.3 (a) XRD patterns of the pristine CsPbIBr$_2$ films and doped films with different amounts of Cu^{2+}. (b) Enlarged XRD peaks of the (100) and (200) diffraction peaks. (c) The FWHM of (200) diffraction peaks for CsPbIBr$_2$ films with different doping ratio.

The effect of Cu^{2+} doping on the sunlight absorption capability (bandgap), chemical states, energy level match and surface morphology was then investigated. As shown in **Figure 5.4a,** doping with a low concentration of Cu^{2+} into the CsPbIBr$_2$ perovskite did not cause any noticeable changes in the absorption edge in the UV-vis spectra. All five samples with different doping amounts of Cu^{2+} showed an almost identical absorption onset at ~605 nm, corresponding to an ~2.05 eV bandgap, which was obtained from the Tauc plots shown in **Figure 5.4b**; the above result is in accordance with previously reported results of CsPbIBr$_2$ perovskites.[32,38] Despite the unchanged bandgap, the absorption intensity in the 350-600 nm wavelength range was obviously enhanced after Cu^{2+} doping, which was indicative of better light absorption capability. This benefit might be due to the full coverage of the film as well as the improved film morphology with large-sized grains and enhanced crystallinity, which will be discussed later.

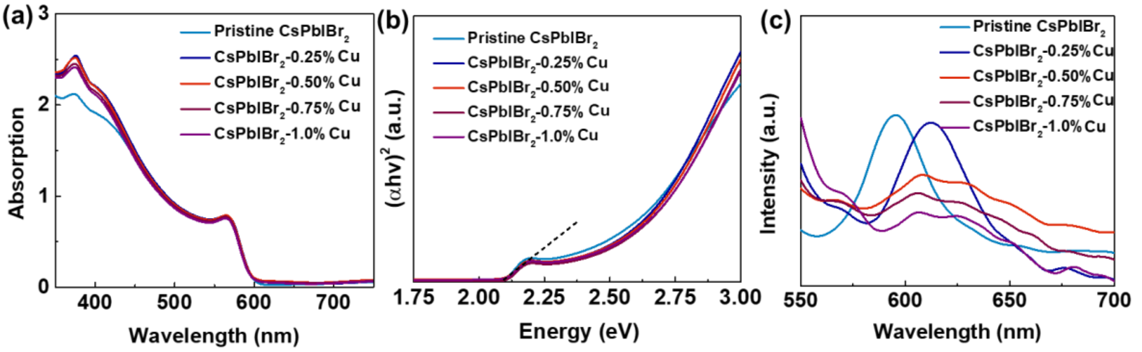

Figure 5.4 (a) UV-vis spectra, (b) Tauc plots and (c) steady-state PL spectra of the $CsPbIBr_2$ films with different doping amounts of Cu^{2+} (Perovskite films were fabricated on top of a c-TiO_2/FTO substrate for UV-vis spectra and a nonconductive glass for the PL test).

According to the steady-state PL spectra in **Figure 5.4c** of $CsPbIBr_2$ films with different doping amounts of Cu^{2+} fabricated on nonconductive glass, the pristine $CsPbIBr_2$ film showed a distinct PL spectrum at approximately 600 nm. After doping 0.25% Cu (relative to Pb) into the $CsPbIBr_2$ perovskite, the main PL peak red-shifted from 600 to 612 nm, and some weak peak shoulders appeared at approximately 570 and 680 nm. Notably, after further increasing the Cu^{2+} content to 0.5%, the PL spectra experienced a noticeable change. Specifically, the main peak at 600 nm for pristine $CsPbIBr_2$ turned into a small peak at approximately 570, 612, 629, 650 and 682 nm, demonstrating the occurrence of phase separation in the $CsPbIBr_2$ perovskite films if an excessive amount of Cu^{2+} was introduced. For higher Cu^{2+} doping level, the multiple PL peaks also appeared but with reduced intensity, meaning more defects in $CsPbIBr_2$-0.75%Cu and $CsPbIBr_2$-1.0%Cu perovskite films. Similar steady-state PL spectra were also observed in Guo's work in which a preheating-assisted spin-coating method was employed as an effective way to prepare high-quality $CsPbIBr_2$ perovskite films for optimized performance.[30] Yi-Bing Cheng's group also confirmed that phase segregation occurred in $CsPbIBr_2$ perovskite films, which generated a large number of mobile ions that moved along grain boundaries and served as ion-migration "highways". They also concluded that the phase segregation should be responsible for the significant hysteresis of the planar PSCs with $CsPbIBr_2$ perovskite.[39] In our work, Cu^{2+} doping created a more obvious phase segregation in the $CsPbIBr_2$ perovskite films. However, the photovoltaic performance was also improved through the use of Cu^{2+} doping, which indicated that appropriate phase separation might benefit the efficiency under certain circumstances rather than always weakening it. For instance, the incorporation Ba^{2+} into $CsPbI_2Br$ induced beneficial phase segregation, significantly enhancing the device performance.[40]

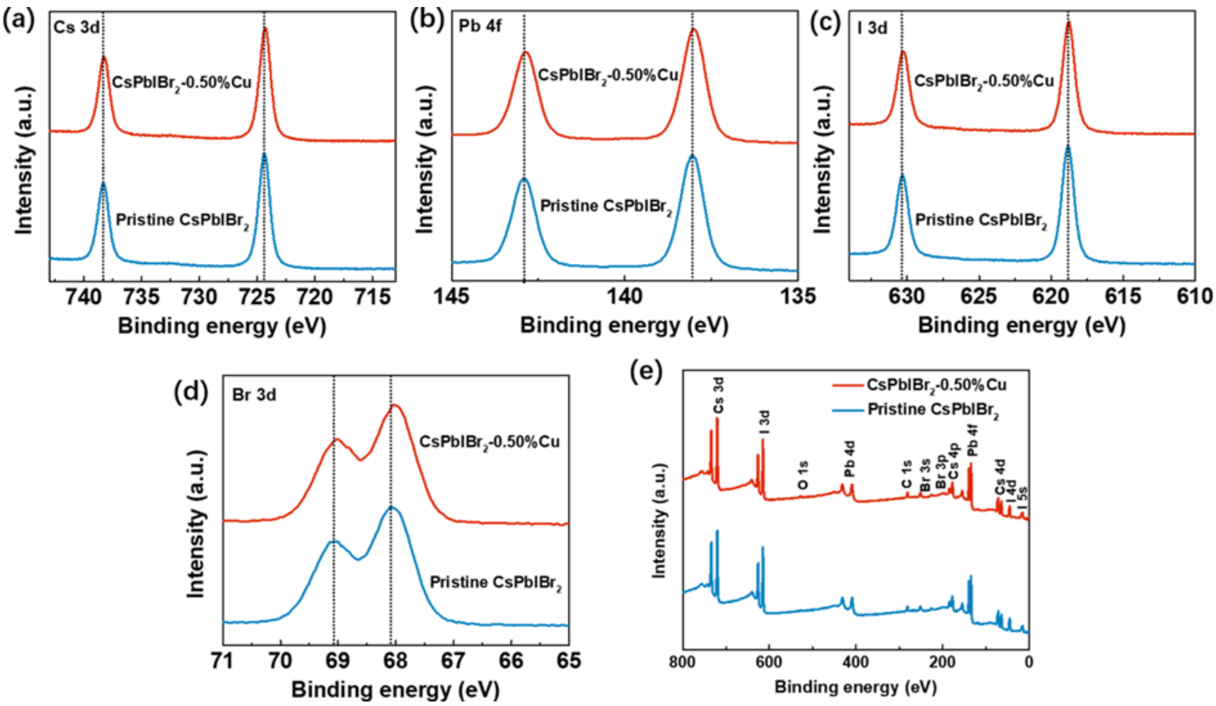

Figure 5.5 XPS spectra of the pristine CsPbIBr$_2$ (blue line) and CsPbIBr$_2$-0.50% Cu (red line) films: (a) Cs 3*d*, (b) Pb 4*f*, (c) I 3*d*, (d) Br 3*d*. (e) XPS survey spectra of pristine CsPbIBr$_2$ and CsPbIBr$_2$-0.50%Cu films.

X-ray photoelectron spectroscopy (XPS) was performed to investigate whether Cu^{2+} doping caused a change in the chemical states of ions in the perovskite lattice. As shown in **Figure 5.5**, all the peaks of the CsPbIBr$_2$-0.50%Cu perovskite film shifted to lower binding energies compared with the pristine CsPbIBr$_2$ film without Cu^{2+} doping. The shifts were correlated with the insertion of Cu^{2+} ions, verifying the successful introduction of Cu^{2+} dopants in the CsPbIBr$_2$ perovskite; the above results were coincident with the literature about Mn^{2+} doping in CsPbIBr$_2$[31] and also consistent with the XRD results in this study. Specifically, the BX$_6$ (B= Pb^{2+} or Cu^{2+}, X= Br$^-$ and I$^-$) octahedral shrinkage caused by the replacement of Pb^{2+} with Cu^{2+} brought about changes in the chemical bonding properties, which was reflected in the shift of the XPS peaks for all elements.

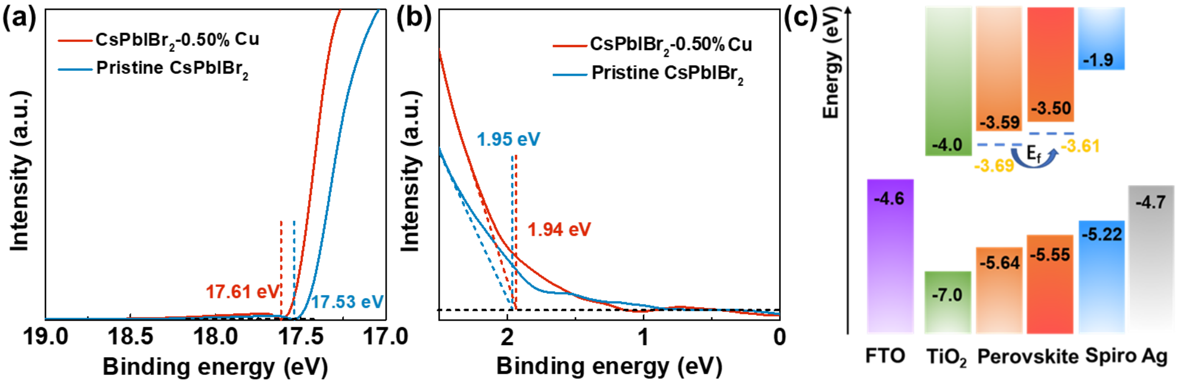

Figure 5.6 UPS spectra showing the (a) secondary-electron cutoff energy boundary and (b) VBM onset of pristine $CsPbIBr_2$ and $CsPbIBr_2$-0.50%Cu perovskite films. (c) Energy level alignment of devices.

In addition, ultraviolet photoelectron spectroscopy (UPS) was performed to investigate the variation of electronic structures resulting from Cu^{2+} doping. The valence band maximum (VBM) onset and secondary-electron cutoff energy boundary of the pristine $CsPbIBr_2$ and $CsPbIBr_2$-0.50%Cu perovskite films are displayed in **Figure 5.6a** and **b**. The VBM can be calculated via the following formula, VBM = 21.2 eV - (E_{cutoff} -E_{onset}), where the intersection points of the linear sections represent the values of E_{cutoff} and E_{onset}. The calculated VBM values for pristine $CsPbIBr_2$ and $CsPbIBr_2$-0.50%Cu are -5.64 and -5.55 eV, respectively. Based on a band gap of 2.05 eV, the CBM of pristine $CsPbIBr_2$ and $CsPbIBr_2$-0.50%Cu was calculated to be -3.59 and -3.50 eV, respectively. Furthermore, the Fermi level of pristine $CsPbIBr_2$ was raised from -3.69 to -3.61 eV after the incorporation of 0.50% Cu^{2+}. The Fermi level moved up and was closer to the CBM (-3.50 eV), indicative of a n-type nature of Cu^{2+} doped $CsPbIBr_2$.[37] The upshift of the VBM caused by Cu^{2+} doping allowed the energy distinction between the VBM of perovskite and spiro-OMeTAD to decrease from 0.42 to 0.33 eV. Moreover, the large energy distinction between the CBM of perovskite and TiO_2 provided a large driving force for electrons to be injected from the photoactive layer to the ETL. Overall, this optimized energy level alignment (**Figure 5.6c**) among the ETL, perovskite and HTL layers not only inhibited the energy loss during the hole transfer process from the perovskite layer to the HTL but also promoted electron separation and extraction from the perovskite layer to the ETL, which is helpful to the increase of PCE of PSCs.[23,41]

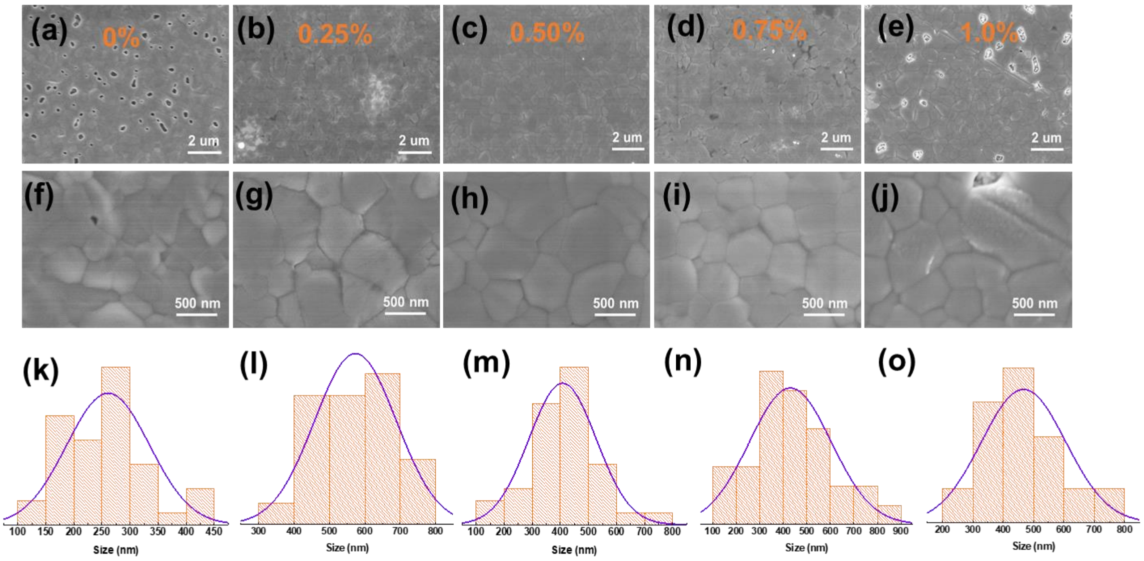

Figure 5.7 (a-j) Top-view SEM images of $CsPbIBr_2$ without and with different amount of Cu^{2+} doping. (k-o) The statistical chart of grain size distribution.

In consideration of the important role of perovskite film morphology on device performance, we investigated the effect of the doping amount of Cu^{2+} on the surface morphologies of $CsPbIBr_2$ perovskite films. SEM images from the top view of the various perovskite films with different doping amounts of Cu^{2+} were obtained, and the results are shown in **Figure 5.7a-j**. After thermal annealing at 225 °C for 10 min, the color of all samples remained almost unchanged, which was consistent with the unchanged bandgap of the various perovskites. However, the microscopic morphology was distinctly altered. The pristine $CsPbIBr_2$ perovskite film displayed a poor film quality with a large number of voids and small grain sizes (**Figure 5.7a** and **f**). After doping with 0.25% Cu^{2+}, the pinholes were distinctly eliminated, and the grain sizes became larger. The $CsPbIBr_2$-0.50%Cu perovskite film exhibited a compact and homogenous morphology with significantly increased grain sizes (**Figure 5.7c** and **h**). When the doping amount of Cu^{2+} was further increased to 0.75%, the film quality remained similar to that of the $CsPbIBr_2$-0.50% film but with slightly reduced grain sizes. However, an excessive doping amount of 1.0% Cu^{2+} severely damaged the film morphology; the film became inhomogeneous with many pinholes. From the statistical chart of grain size distribution inside the SEM images (**Figure 5.7k-o**), a remarkably enlarged grain size was evident after the introduction of Cu^{2+} into the CsPbIBr$_2$ perovskite, which might reduce the recombination of charge carriers.[42,43]

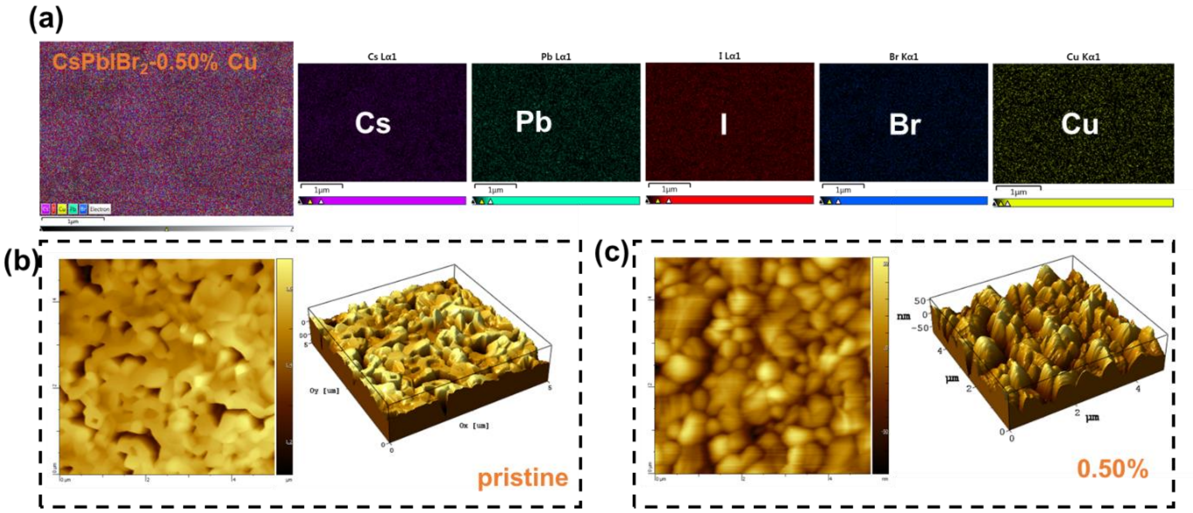

Figure 5.8 (a) EDX mapping images of Cs, Pb, Br, I, and Cu in the CsPbIBr$_2$-0.50%Cu perovskite film. (b) and (c) AFM images of CsPbIBr$_2$ without and with 0.50% Cu^{2+} doping.

To confirm the existence of Cu^{2+} and observe its distribution in the CsPbIBr$_2$-0.50%Cu perovskite film, energy-dispersive X-ray (EDX) spectroscopy was conducted. As displayed in **Figure 5.8a**, all elements, including Cs, Pb, Cu, I and Br, were distributed evenly over the perovskite film. We also tested the top-view AFM height images (5 × 5 μm) and the corresponding 3D models of pristine CsPbIBr$_2$ and CsPbIBr$_2$-0.50%Cu perovskite films, shown in **Figure 5.8b** and **c**, which again manifested the decrease in the number of pinholes and the improved coverage of the perovskite film after 0.50% Cu^{2+} was introduced. In addition, the root-mean-square (RMS) roughness of the CsPbIBr$_2$-0.50% Cu film (14.9 nm) was smaller than that of the pristine CsPbIBr$_2$ film (54.1 nm), which was helpful for reducing the contact resistance in the presence of the hole transport layer (HTL). Therefore, it is safe to say that doping an appropriate amount of Cu^{2+} into the perovskite lattice facilitated the crystallization process of CsPbIBr$_2$, allowing them to grow to larger grains and form more compact and smooth perovskite films; however, excessive Cu^{2+} doping exerted a negative impact on the film quality. The improved perovskite film quality plays a critical role in obtaining the high-performance CsPbIBr$_2$-based PSCs as trap densities and charge recombination in the perovskite film can be thus reduced.

To explore the potential enhancement of the Cu^{2+} doping on the performance of PSCs, we investigated the effect of the doping amount of Cu^{2+} on the photovoltaic performance of PSCs with a configuration of FTO/TiO_2/perovskite/spiro-OMeTAD/Ag (**Figure 5.9a**). **Figure 5.9b** shows the cross-sectional SEM image of the $CsPbIBr_2$-based devices in which the perovskite layer has a thickness of approximately 350 nm. **Figure 5.9c** shows a comparison in which a small doping amount of Cu^{2+} significantly improves the PCEs of the PSCs. The best PCE of 10.4% was obtained by $CsPbIBr_2$-0.50%Cu-based PSCs, and all the related photovoltaic parameters are listed in **Table 5.1**. The PCE enhancement was mainly attributed to the fill factor (FF) and the short-circuit current density (J_{sc}) improvement with a slight increase in open-circuit voltage (V_{oc}). The FF values of the devices slightly improved from 0.611 for pristine $CsPbIBr_2$ to 0.648 for $CsPbIBr_2$-0.25%Cu and then notably to 0.671 for $CsPbIBr_2$-0.50%Cu. The J_{sc} of the devices was slightly enhanced from 12.6 to 12.7 mA cm^{-2} for $CsPbIBr_2$-0.25%Cu and 12.8 mA cm^{-2} for $CsPbIBr_2$-0.50%Cu. The V_{oc} of pristine $CsPbIBr_2$-based devices increased slightly from 1.19 V to 1.20, 1.21 and 1.20 V after 0.25%, 0.50% and 0.75% Cu^{2+} were introduced into pristine $CsPbIBr_2$, respectively. The FF, V_{oc} and J_{sc} enhancement were mainly derived from the optimized morphology, including the reduced number of pinholes, increased grain sizes, and reduced number of defects. **Figure 5.9d** shows the statistical distribution (45 devices) of the PCEs for devices utilizing pristine $CsPbIBr_2$ and $CsPbIBr_2$-0.50%Cu as light absorbing materials, demonstrating that target PSCs have a highly reproducible photovoltaic performance with a narrow PCE distribution range of 8.92% to 10.4%. **Figure 5.10** displays the distribution results of the PCE, J_{sc}, V_{oc} and FF values of various devices, further confirming the superior reproducibility of $CsPbIBr_2$-0.50%Cu-based PSCs to that of devices assembled by pristine $CsPbIBr_2$ and other Cu^{2+}-doped perovskites.

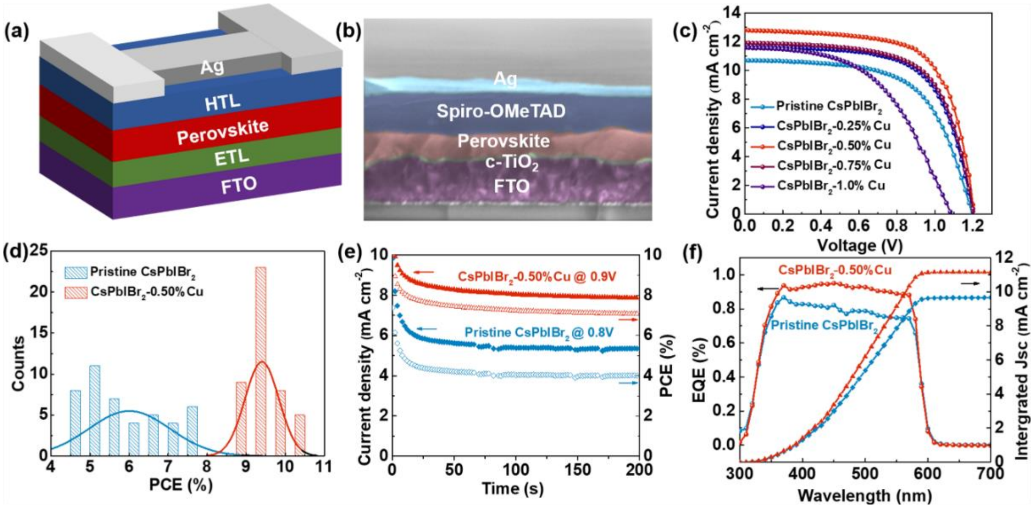

Figure 5.9 (a) Schematic diagram of the device architecture with a configuration of FTO/TiO_2/perovskite/spiro-OMeTAD/Ag. (b) Cross-sectional SEM images of the PSCs. (c) *J*-*V* curves of the champion devices using pristine $CsPbIBr_2$ and various Cu^{2+}-doped $CsPbIBr_2$ as light absorbers. (d) Statistical distribution of the PCE values of PSCs based on pristine $CsPbIBr_2$ and $CsPbIBr_2$-0.50%Cu. (e) MPPT profiles, (f) corresponding EQE spectra of pristine $CsPbIBr_2$ and $CsPbIBr_2$-0.50%Cu-based devices.

Table 5.1 Photovoltaic parameters of PSCs based on various perovskites

Sample	Scan direction	J_{sc} (mA cm^{-2})	V_{oc} (V)	FF	PCE (%)	HI
Pristine $CsPbIBr_2$	reverse	10.7	1.19	0.611	7.81	0.48
	forward	12.7	1.07	0.299	4.05	
$CsPbIBr_2$-0.25%Cu	reverse	11.6	1.20	0.648	9.06	0.44
	forward	12.5	1.08	0.374	5.04	
$CsPbIBr_2$-0.50%Cu	reverse	12.8	1.21	0.671	10.4	0.29
	forward	12.9	1.06	0.535	7.34	
$CsPbIBr_2$-0.75%Cu	reverse	11.9	1.20	0.649	9.32	0.33
	forward	12.1	1.05	0.494	6.26	
$CsPbIBr_2$-1.0%Cu	reverse	11.6	1.09	0.510	6.40	0.33
	forward	13.2	0.979	0.330	4.26	

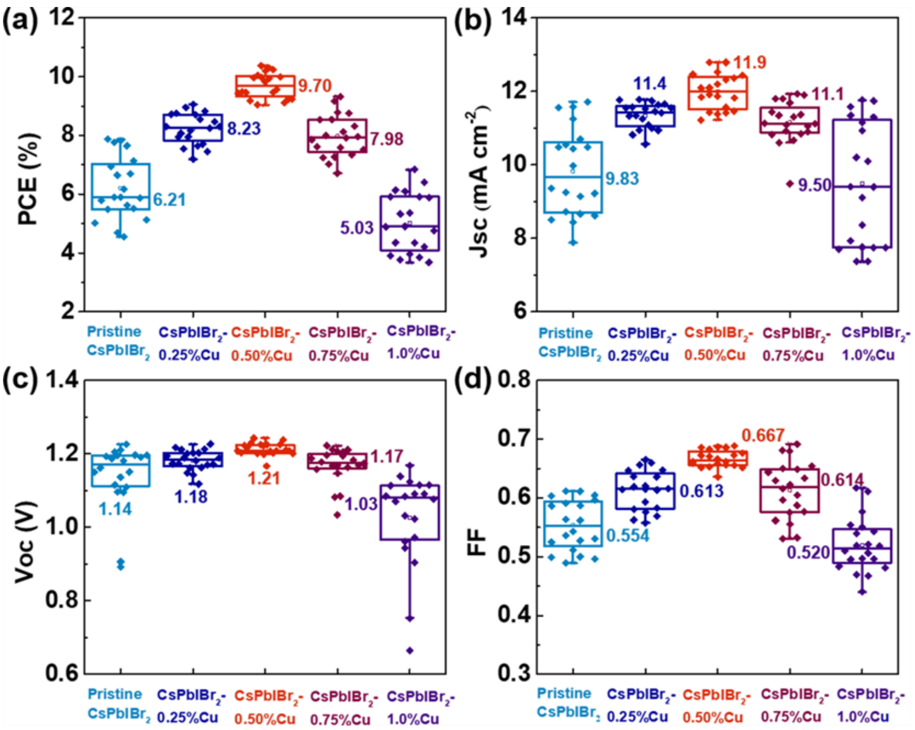

Figure 5.10 (a) PCE, (b) J_{sc}, (c) V_{oc} and (d) FF distributions of $CsPbIBr_2$-based PSCs without and with various Cu^{2+} doping amounts with the average value inside.

In addition, we performed maximum power point tracking (MPPT) of PSCs with $CsPbIBr_2$ and $CsPbIBr_2$-0.50%Cu, as shown in **Figure 5.9e**. PSCs with pristine $CsPbIBr_2$ presented a stabilized photocurrent density of 5.90 mA cm^{-2} at the maximum power output point (voltage = 0.80 V) and yielded a stabilized PCE of 4.72%. In contrast, $CsPbIBr_2$-0.50%Cu-based devices displayed a stabilized photocurrent density of 8.50 mA cm^{-2} at the maximum power output point (voltage = 0.90 V) and produced a PCE of 7.65%. Due to the presence of serious hysteresis phenomena in our work (which will be discussed next), the stabilized power output approached the forward scan results. The external quantum efficiency (EQE) spectra in **Figure 5.9f** show that the cells based on $CsPbIBr_2$-0.50%Cu yielded a much higher EQE throughout the whole wavelength range. The integrated J_{sc} value was 11.2 mA cm^{-2} for $CsPbIBr_2$-0.50%Cu, which was much higher than that based on pristine perovskite with a J_{sc} value of 9.66 mA cm^{-2}. The obtained integrated J_{sc} values of pristine $CsPbIBr_2$ and $CsPbIBr_2$-0.50%Cu samples from the EQE spectra almost agreed with the average of their corresponding Jsc values (9.66 and 11.2 mA cm^{-2} in **Figure 5.10**) obtained from the *J-V* curves.

According to the EQE spectra of pristine $CsPbIBr_2$ and $CsPbIBr_2$-0.50%Cu-based PSCs, we also calculated the Urbach energy (Eu), which can embody the quality of the perovskite films. Based on the equation $EQE = EQE_0 \exp [(E - E_g)/E_u]$ (where EQE_0 means the EQE value at the bandgap), the slope of the exponential EQE tail describes Eu, as shown in **Figure 5.11**. It is worth mentioning that $CsPbIBr_2$-0.50%Cu-based PSCs exhibited lower Eu (15.14 eV) than pristine $CsPbIBr_2$-based PSCs (19.26 eV), thus manifesting a better $CsPbIBr_2$ perovskite film quality because of the Cu^{2+} doping. This result was in agreement with the increase in J_{sc}, FF and V_{oc}.[44]

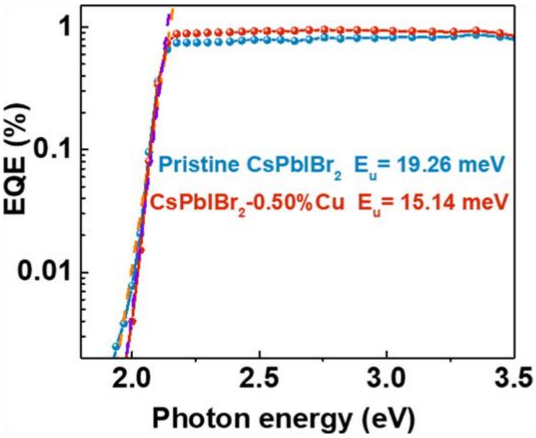

Figure 5.11 The semilog plot of the EQE values versus the photon energy of pristine $CsPbIBr_2$ and $CsPbIBr_2$-0.50%Cu-based devices.

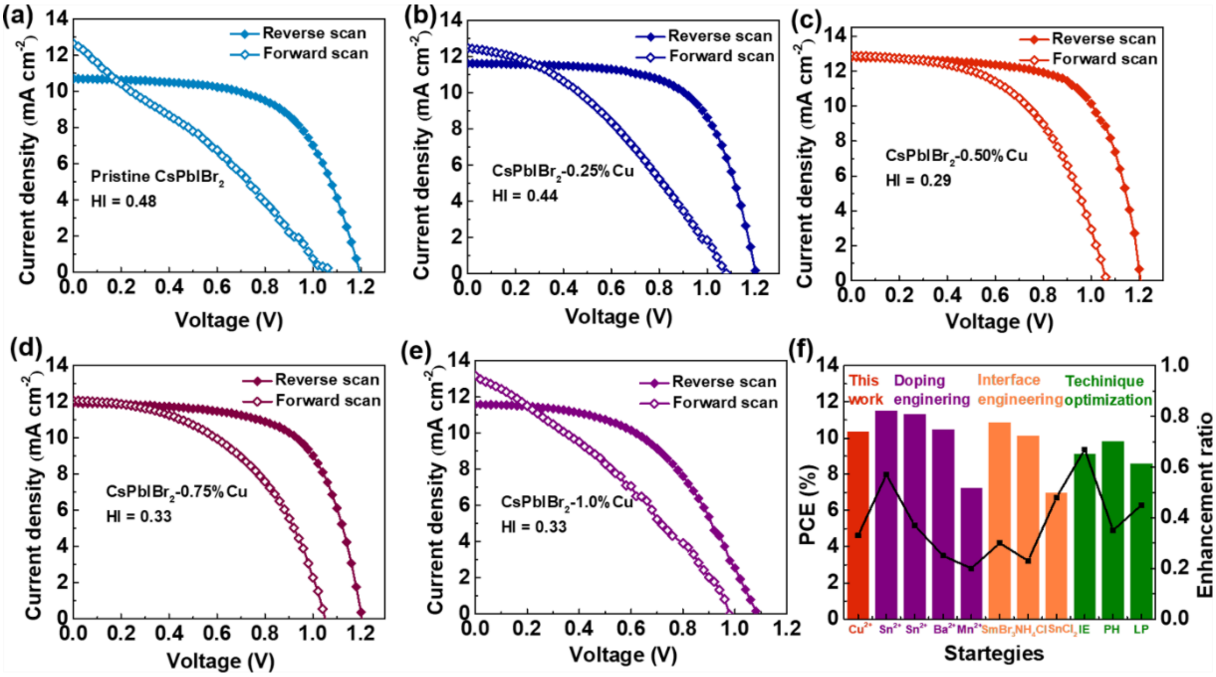

Figure 5.12 (a-e) *J-V* curves of $CsPbIBr_2$-based PSCs without and with various Cu^{2+} doping amounts at different scan directions. (f) The histogram comparison between our work and previously reported work (IE: intermolecular exchange, PH: preheating, LP: light processing).

It is well known that the PCE of PSCs strongly depends on the measurement conditions because of the well-known hysteresis effect. Thus, the hysteresis behaviour of $CsPbIBr_2$-based PSCs with and without Cu^{2+} doping was also investigated. **Figure 5.12a-e** displays the photocurrent-voltage (*J-V)* curves of various PSCs without and with the incorporation of Cu^{2+} in the perovskite film measured with different scan directions (reverse and forward). The hysteresis degree of PSCs can be reflected via the PCE gap between the *J-V* curves tested in the forward and reverse directions, which can be quantitatively defined by the hysteresis index (HI) using **Equation 5.1**.[45]

$$\mathrm{HI} = \frac{\mathrm{PCE(reverse)} - \mathrm{PCE(forward)}}{\mathrm{PCE(reverse)}} \tag{5.1}$$

The HI values of PSCs based on pristine $CsPbIBr_2$, $CsPbIBr_2$-0.25%Cu, $CsPbIBr_2$-0.50%Cu, $CsPbIBr_2$-0.75%Cu and $CsPbIBr_2$-1.0%Cu were calculated to be 0.48, 0.44, 0.29, 0.33 and 0.33 (**Table 5.1**), respectively, meaning that a small doping amount of Cu^{2+} was capable of reducing the hysteresis phenomenon, which was ascribed to the reduced charge recombination as the incorporation of 0.50% Cu^{2+} gave rise to a homogeneous and compact perovskite morphology with expanded gain sizes and reduced grain boundaries. However, it is noteworthy that despite the reduced hysteresis through the use of Cu^{2+} doping, the hysteresis phenomenon in this work was obviously more serious in comparison with the reported organic-inorganic hybrid halide perovskite-based devices. The serious hysteresis of pristine $CsPbIBr_2$-based devices in this study might be ascribed to the severe charge recombination caused by the poor quality of the perovskite film. In comparison, the hysteresis for the Cu^{2+}-doped samples in this study might be mainly ascribed to the phase separation behaviour of the $CsPbIBr_2$-based perovskites. Phase separation often occurs in mixed halide perovskites and can lead to excessive ion migration and accumulation at the interfaces of the perovskite and charge transporting layers.[39] All the items mentioned above might be the reason for the serious hysteresis. According to our previous review about the hysteresis in PSCs, hysteresis might be the result of the combination of many factors, and the dominant factor and reason need further research.[45] Finally, we compared the PCE of our work with those of previously reported results in the literature, as shown in **Figure 5.12f**. Clearly, high PCEs have been achieved through engineered doping, and the PCE obtained from Cu^{2+}-doped perovskite in this work surpassed most reported $CsPbIBr_2$-based PSCs in the literature.[23,24,27,30,31,33-35,41,46]

To further explain the improved PSC performance via Cu^{2+} doping, some important optoelectronic properties of pristine $CsPbIBr_2$ and $CsPbIBr_2$-0.50%Cu-based devices were studied. It is well known that trap-state density (n_{trap}) is an essential electronic property that can be determined via the space-charge-limited current (SCLC) model by utilizing single-charge carrier devices. **Figure 5.13a** and **b** display the dark *J-V* curves of electron-only and hole-only devices with cell configurations of FTO/TiO_2/perovskite/ phenyl-C61-butyric acid methyl ester (PCBM)/Ag and FTO/poly(3,4-ethylenedioxythiophene)-poly(styrenesulfonate) (PEDOT:PSS)/perovskite/spiro-OMeTAD/Ag, respectively. Generally, the current linearly response to a voltage in the low voltage region, signaling an ohmic response, while the current experienced a rapid nonlinear rise in the increasing voltage region. The nonlinear rise represented the transition to a trap-filled limit, a system where the injected charges, including electrons and holes, completely fill all the available trap states. Based on this, the junction points between the two mentioned regions represented the trap-filled limit voltage (V_{TFL}). The n_{trap} value can be calculated according to **Equation 5.2**:

$$n_{trap} = \frac{2V_{TFL}\varepsilon\varepsilon_0}{eL^2} \tag{5.2}$$

where L denotes the perovskite film thickness; ε represents the dielectric constant of $CsPbIBr_2$, which is approximately equal to 8 for $CsPbIBr_2$; and ε_0 and e refer to the vacuum permittivity and the elementary charge, respectively.[35] When the perovskite layer was the same thickness, a low V_{TFL} represented a low trap density. As shown in **Figure 5.13a** and **b**, the $CsPbIBr_2$ - 0.50%Cu-based device evidently showed a low V_{TFL}, which was indicative of reduced trap density in both the electron and hole transport sides. Based on a perovskite film thickness of 350 nm obtained from **Figure 5.9b**, the calculated electron trap densities of pristine $CsPbIBr_2$ and $CsPbIBr_2$-0.50%Cu films were 6.29×10^{15} and 2.60×10^{15} cm^{-3}, respectively. The calculated hole trap densities of pristine $CsPbIBr_2$ and $CsPbIBr_2$-0.50%Cu films were 7.30 ×

10^{15} and 5.78×10^{15} cm^{-3}, respectively. These results demonstrated that Cu^{2+} doping into $CsPbIBr_2$ was capable of reducing the trap density because of the improved perovskite film quality.

Additionally, to investigate the interfacial charge transfer properties in $CsPbIBr_2$-based PSCs with and without Cu^{2+} doping, we carried out electrochemical impedance spectroscopy (EIS) measurements. The Nyquist plots included one clear low-frequency arc, which was connected to the charge carrier recombination process at the interface of perovskite/TiO_2 and perovskite/spiro-OMeTAD and represented the recombination resistance (R_{rec}).[36,47] Generally, an increase in the low-frequency arc corresponds to a reduced charge recombination. As shown in **Figure 5.13c**, $CsPbIBr_2$-0.50%Cu-based PSCs exhibited a larger R_{rec} than that based on pristine $CsPbIBr_2$. In brief, Cu^{2+} doping effectively reduced charge recombination at the interface, thus contributing to an enhanced device performance.

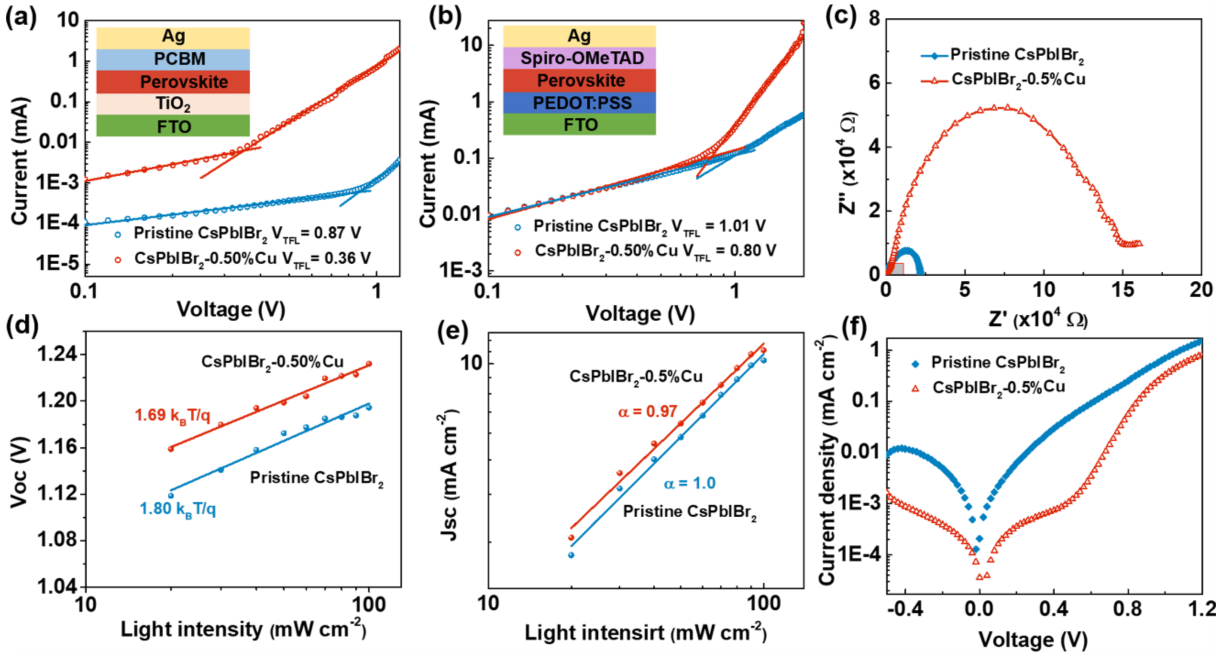

Figure 5.13 *J-V* curves for the (a) electron-only devices and (b) hole-only devices based on pristine $CsPbIBr_2$ and $CsPbIBr_2$-0.50%Cu under dark conditions. (c) Nyquist plots of pristine $CsPbIBr_2$ and $CsPbIBr_2$-0.50%Cu-based PSCs under dark conditions at an applied bias of 0.5 V. (d) V_{oc} values and (e) J_{sc} values versus light intensity and their linear fitting curves. (f) *J-V* curves of pristine $CsPbIBr_2$ and $CsPbIBr_2$-0.50%Cu-based devices under dark conditions.

To further confirm the reduced charge recombination and the facilitated charge extraction via Cu^{2+} doping, light intensity-dependent *J-V* measurements were performed. The dependence of V_{oc} and J_{sc} on various light intensities is shown in **Figure 5.13d** and **e**. V_{oc} can be expressed according to **Equation 5.3**:

$$\mathrm{Voc} = \mathrm{n}\frac{\mathrm{k_B T}}{\mathrm{q}}\ln\left(\frac{\mathrm{Jsc}}{\mathrm{J_0}} + 1\right) \tag{5.3}$$

where n, T, k_B, q and J_0 represent the ideality factor, absolute temperature, Boltzmann constant, elementary charge and saturated current density (in the dark), respectively. Since J_{sc} is much larger than J_0 and increases with increasing light intensity, V_{oc} is linearly dependent on the natural logarithm of light intensity, and n can be extracted from the slope of $nkTq^{-1}$, which can reflect the carrier recombination inside devices. The n value is normally between 1 and 2. An n value of 1 signifies the absence of trap-assisted carrier recombination (monomolecular recombination) in the solar cell except for direct free-carrier recombination. A small n value means there is reduced carrier recombination inside the device, and thus, better device performance; if the n value is large, the opposite occurs.[48,49] As shown in **Figure 5.13d**, $CsPbIBr_2$-0.50%Cu-based devices showed a smaller n value of 1.69 than that of the pristine $CsPbIBr_2$-based device (1.80), which was indicative of reduced trap-assisted nonradiative recombination after Cu^{2+} doping. **Figure 5.13e** shows the J_{sc} variation with the dependence of light intensity, in which the two parameters conform to the general power law of $J_{sc} \propto$ (light intensity)$^{\alpha}$, where the power α is an exponential factor. Generally, the power α should approach 1 in solar cells in which the recombination adopts a monomolecular path.[50] Thus, a small value of α is a symbol of reduced recombination in solar cells. Through linear fittings, we extracted α values of 1 and 0.97 for the pristine $CsPbIBr_2$ and $CsPbIBr_2$-0.50%Cu-based devices, respectively. This result confirmed again that Cu^{2+} doping into $CsPbIBr_2$ effectively suppressed monomolecular recombination in PSCs. Furthermore, we tested the *J-V* curves of the devices in the dark. As shown in **Figure 5.13f**, the $CsPbIBr_2$-0.50%Cu-based device exhibited small current densities within a voltage range of -0.4 V to 1.2 V in the dark. The above result demonstrated a reduced current leak and provided a reasonable explanation for the V_{oc} improvement after Cu^{2+} doping in $CsPbIBr_2$.

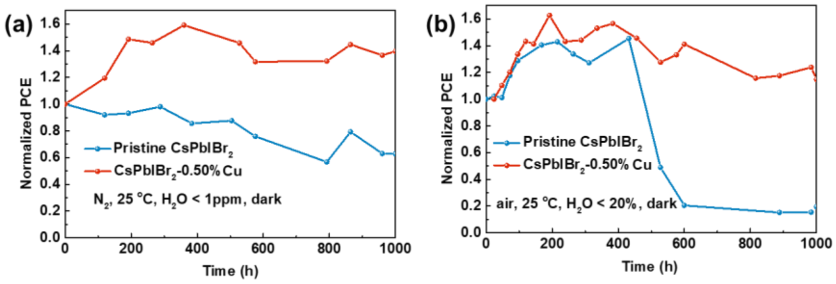

Figure 5.14 Normalized PCE for the pristine $CsPbIBr_2$ and $CsPbIBr_2$-0.50%Cu-based PSCs stored in a (a) N_2 atmosphere and (b) dry air atmosphere (without encapsulation).

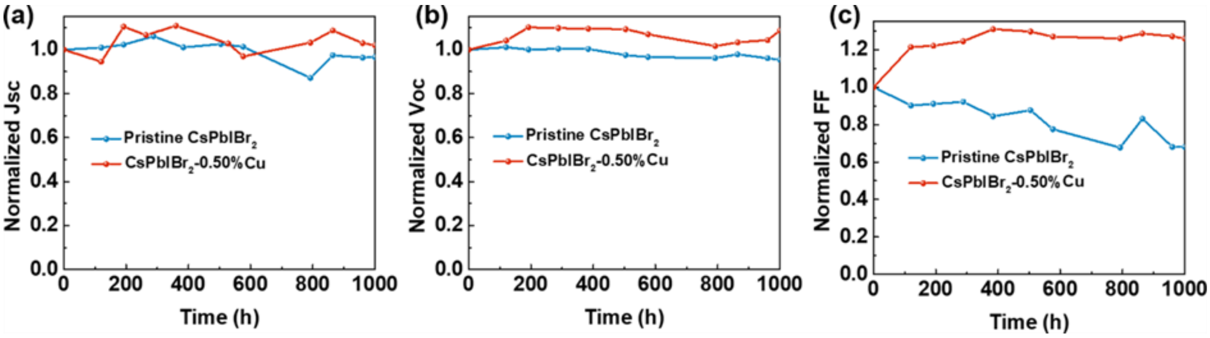

Figure 5.15 Normalized (a) J_{sc}, (b) V_{oc} and (c) FF of PSCs with pristine $CsPbIBr_2$ and $CsPbIBr_2$-0.50%Cu under N_2 atmosphere.

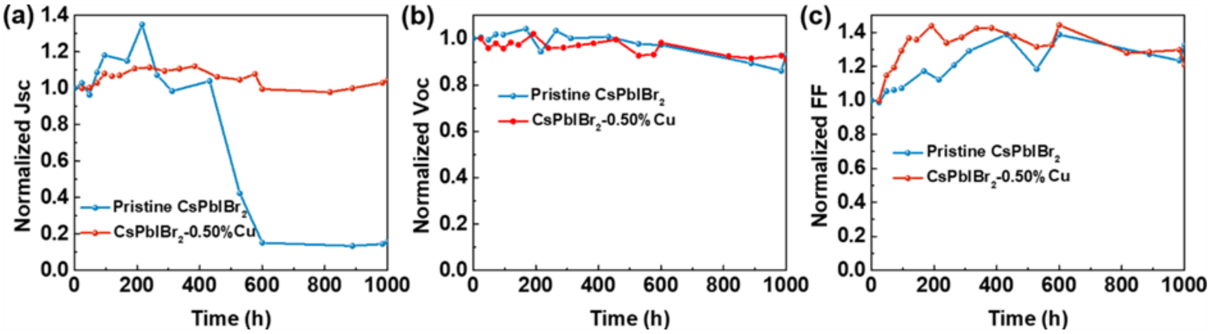

Figure 5.16 Normalized (a) J_{sc}, (b) V_{oc} and (c) FF of PSCs with pristine $CsPbIBr_2$ and $CsPbIBr_2$-0.50%Cu under dry air atmosphere.

To continue the pursuit of highly stable $CsPbIBr_2$-based PSCs that benefit the commercialization of this technology, we investigated the influence of Cu^{2+} doping into $CsPbIBr_2$ on the device stability in a N_2 and dry air atmosphere and fabricated PSCs with gold (Au) as the electrode (FTO/TiO_2/perovskite/spiro-OMeTAD/Au). The variation of PCEs as well as other parameters is displayed in **Figure 5.14a-b** and **Figure 5.15** and **5.16**. When stored in a N$_2$ atmosphere, CsPbIBr$_2$-0.50%Cu-based PSCs did not show an obvious decrease in the PCE or other parameters, while the PCE of pristine CsPbIBr$_2$-based PSCs decreased by 40% (**Figure 5.14a**). The decrease in PCE for pristine CsPbIBr$_2$ devices was mainly attributed to the decrease in FF (**Figure 5.15**). The air stability was tested at room temperature (25 °C) with the humidity below 20%. In comparison with the pristine CsPbIBr$_2$-based PSC whose PCE experienced a significant degradation after 500 h, the PSC with CsPbIBr$_2$-0.50%Cu showed no significant changes in the PCE (**Figure 5.14b**), thus demonstrating the enhanced air stability provided by Cu^{2+} doping. Notably, both of them witnessed an apparent increase in PCE in the beginning 200 h, which was credited to the gradual oxidation of spiro-OMeTAD and the increased hole transport capability.[51] The enhanced long-term stability in a N$_2$ and dry air atmosphere was attributed to the reduced number of defects in the CsPbIBr$_2$-0.50%Cu film due to the enlarged grain boundaries.

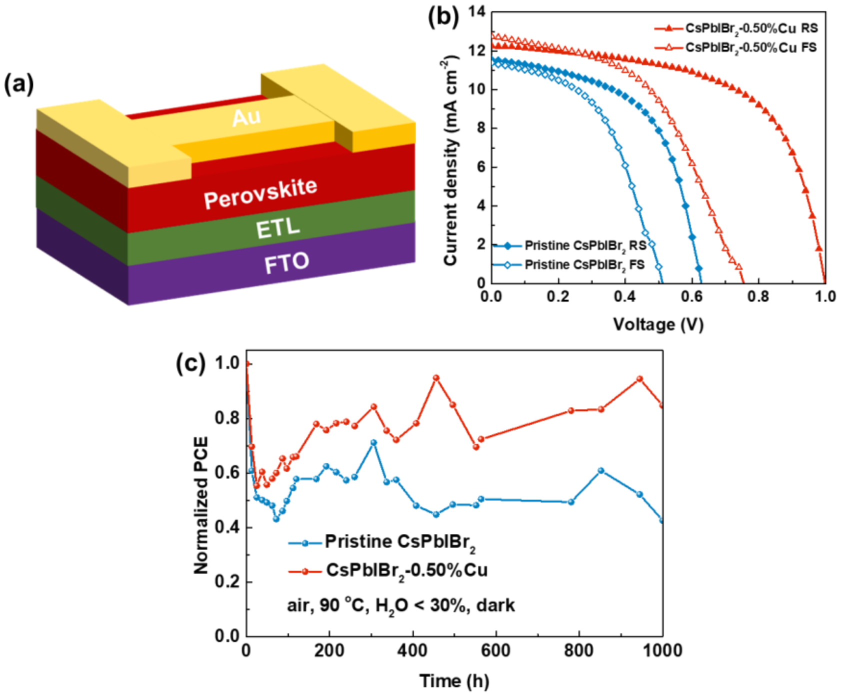

Figure 5.17 *J-V* curves of HTL-free pristine CsPbIBr$_2$ and CsPbIBr$_2$-0.50%-based PSCs at different scan directions.

Table 5.2 Photovoltaic parameters of Au-based HTL-free PSCs

Sample	Scan direction	J_{sc} (mA cm^{-2})	V_{oc} (V)	FF	PCE (%)
Pristine $CsPbIBr_2$	reverse	11.6	0.628	0.559	4.06
	forward	11.4	0.512	0.492	2.87
$CsPbIBr_2$-0.50%Cu	reverse	12.3	0.998	0.604	7.39
	forward	12.7	0.755	0.493	4.74

Furthermore, we compared the thermal stability between pristine $CsPbIBr_2$ and $CsPbIBr_2$-0.50%Cu-based devices at 90 °C with 30% humidity in an ambient atmosphere. Considering that Spiro-OMeTAD was very sensitive to heat, we fabricated Au-based HTL-free PSCs with a device configuration of FTO/TiO_2/perovskite/Au, as shown in **Figure 5.17a**. The maximum PCE obtained by the Au-based HTL-free pristine $CsPbIBr_2$ and $CsPbIBr_2$-0.50%Cu PSCs was 4.06% and 7.39% (**Figure 5.17b**), respectively, which confirmed again the effectiveness of Cu^{2+} doping for an enhanced PCE. The detailed J-V test results are shown in **Table 5.2**. For the thermal stability, it was interesting to observe that the pristine $CsPbIBr_2$-based PSCs lost 50% of their initial PCE after 500 h of operation, while $CsPbIBr_2$-0.50%Cu-based PSCs retained almost 75% of their original PCE after 1000 h of operation despite a slight decrease in the beginning period. From the thermal stability test results of other parameters (**Figure 5.18**), it was clear that the PCE reduction was mainly attributed to the decrease in J_{sc} and FF but especially Jsc (**Figure 5.18a-b**). However, an interesting phenomenon was that V_{oc} decreased first and then increased with the heat treatment process (**Figure 5.18b**), which might be attributed to the heat process accelerating the ion migration and accumulation at the perovskite/Au or perovskite/TiO_2 interfaces. Ion migration might lead to serious charge recombination at the interface, causing a decrease in Jsc and FF. On the other hand, ion migration may form I^-/Br^--enriched separated phases, which might have various existing ratios and conditions during the thermal stability test process that would finally give rise to a V_{oc} increase after heating for a period of time.

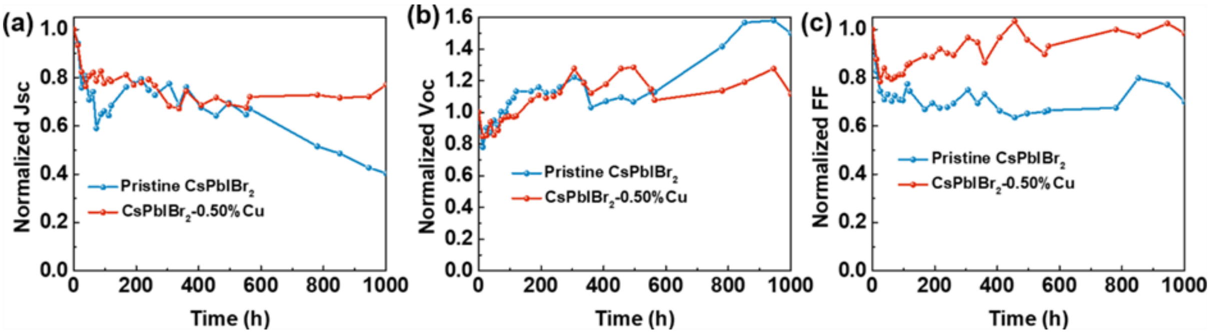

Figure 5.18 Normalized (a) J_{sc}, (b) V_{oc} and (c) FF of PSCs with pristine $CsPbIBr_2$ and $CsPbIBr_2$-0.50%Cu under air atmosphere at 90 °C with 30% humidity.

5.4 Conclusion

In summary, by incorporating an appropriate amount of Cu^{2+} (0.50 at.%) into $CsPbIBr_2$ perovskite, an enhanced film quality with the increased crystallinity and the expanded grain sizes, an optimized energy level alignment, a reduced trap density, and a decreased charge carrier recombination were achieved for the solar cell perovskite film. Benefiting from the merits mentioned above, a maximum PCE value of 10.4% was obtained on the $CsPbIBr_2$-0.50%Cu-based device with a cell configuration of FTO/c-TiO_2/$CsPbIBr_2$-0.50%Cu/spiro-OMeTAD/Ag. The PCE of $CsPbIBr_2$-0.50%Cu-based devices in this study was superior to those of most of the reported $CsPbIBr_2$-PSCs so far. Furthermore, Cu^{2+} doping also played a critical role in the stability enhancement of PSCs, which allowed $CsPbIBr_2$ PSCs to experience no obvious degradation in a N_2 and dry air atmosphere and retained almost 75% of their initial PCE when heated at 90 °C in an ambient atmosphere with 30% humidity. This work provides a facile and effective approach for the enhancement of efficiency and long-term stability of $CsPbIBr_2$-based PSCs, which may accelerate the commercialization of this technology.

5.5 Reference

[1] S. D. Stranks, H. J. Snaith, *Nat. Nanotech.* **2015**, *10*, 391-402.

[2] Research Cell Efficiency Records, N. R. E. L. N. https://www. nrel.gov/pv/cell-efficiency.html.

[3] Y. Rong, Y. Hu, A. Mei, H.Tan, M. I. Saidaminov, S. I. Seok, M. D. McGehee, E. H. Sargent, H. Han, *Science* **2018**, *361*, 8235.

[4] Z. Wang, Z. Shi, T. Li, Y. Chen, W. Huang, *Angew. Chem. Int. Ed.* **2017**, *56*, 1190-1212.

[5] Y. H. Park, I. Jeong, S. Bae, H. J. Son, P. Lee, J. Lee, C.-H. Lee, M. J. Ko, *Adv. Funct. Mater.* **2017**, *27*, 1605988.

[6] Y. Fan, H. Meng, L. Wang, S. Pang, *Sol. RRL* **2019**, *3*, 1900215.

[7] J. Zhao, Y. Deng, H. Wei, X. Zheng, Z. Yu, Y. Shao, J. E. Shield, J. Huang, *Sci. Adv.* **2017**, *3*, 5616.

[8] W.-Q. Wu, Z. Yang, P. N. Rudd, Y. Shao, X. Dai, H. Wei, J. Zhao, Y. Fang, Q. Wang, Y. Liu, Y. Deng, X. Xiao, Y. Feng, J. Huang, *Sci. Adv.* **2019**, 5, 8925.

[9] N.-G. Park, M. Grätzel, T. Miyasaka, K. Zhu, K. Emery, *Nat. Energy* **2016**, *1*, 16152.

[10] J. Zhang, G. Hodes, Z. Jin , S. Liu, *Angew. Chem. Int. Ed.* **2019**, *58*, 15596-15618.

[11] W. Xiang, W. Tress, *Adv. Mater.* **2019**, *31*, 1902851.

[12] S. Dastidar, C. J. Hawley, A. D. Dillon, A. D. Gutierrez-Perez, J. E. Spanier, A. T. Fafarman, *J. Phys. Chem. Lett.* **2017**, *8*, 1278-1282.

[13] A. K. Jena, A. Kulkarni, Y. Sanehira, M. Ikegami, T. Miyasaka, *Chem. Mater.* **2018**, *30*, 6668-6674.

[14] G. Tong, T. Chen, H. Li, L. Qiu, Z. Liu, Y. Dang, W. Song, L. K. Ono, Y. Jiang, Y. Qi, *Nano Energy* **2019**, *65*, 104015.

[15] B. Li, L. Fu, S. Li, H. Li, L. Pan, L. Wang, B. Chang, L. Yin, *J. Mater. Chem. A* **2019**, *7*, 20494-20518.

[16] J. Liang, C. Wang, Y. Wang, Z. Xu, Z. Lu, Y. Ma, H. Zhu, Y. Hu, C. Xiao, X. Yi, G. Zhu, H. Lv, L. Ma, T. Chen, Z. Tie, Z. Jin, J. Liu, *J. Am. Chem. Soc.* **2016**, *138*, 15829-15832.

[17] J. Duan, H. Xu, W. E. I. Sha, Y. Zhao, Y. Wang, X. Yang, Q. Tang. *J. Mater. Chem. A* **2019**, *7*, 21036-21068.

[18] A. Ho-Baillie, M. Zhang, C. F. J. Lau, F.-J Ma, S. Huang, *Joule* **2019**, *3*, 938-955.

[19] S. S. Mali,J. V. Patil, C. K. Hong, *Nano Lett.* **2019**, *19*, 6213-6220.

[20] S. Mariotti, O. S. Hutter, L. J. Phillips, P. J. Yates, B. Kundu, K. Durose, *ACS Appl. Mater. Interfaces* **2018**, *10*, 3750-3760.

[21] Y. Guo, X. Yin, J. Liu, S. Wen, Y. Wu, W. Que, *Sol. RRL* **2019**, *3*, 1900135.

[22] F. Wang, S. Bai, W. Tress, A. Hagfeldt, F. Gao, *npj Flexible Electronics* **2018**, *2*, 1-14.

[23] Q. Zhang, W. Zhu, D. Chen, Z. Zhang, Z. Lin, J. Chang, J. Zhang, C. Zhang, Y. Hao, *ACS Appl. Mater. Interfaces* **2019**, *11*, 2997-3005.

[24] W. Zhu, Q. Zhang, D. Chen, Z. Zhang, Z. Lin, J. Chang, J. Zhang, C. Zhang, Y. Hao, *Adv. Energy Mater.* **2018**, *8*, 1802080.

[25] W. Zhu, Q. Zhang, C. Zhang, Z. Zhang, D. Chen, Z. Lin, J. Chang, J. Zhang, Y. Hao, *ACS Appl. Energy Mater.* **2018**, *1*, 4991-4997.

[26] C. F. J. Lau, X. Deng, Q. Ma, J. Zheng, J. S. Yun, M. A. Green, S. Huang, A. W. Y. Ho-Baillie, *ACS Energy. Lett.* **2016**, *1*, 573-577.

[27] W. S. Subhani, K. Wang, M. Du, X. Wang, S. Liu, *Adv. Energy Mater.* **2019**, *9*, 1803785.

[28] J. Lu, S.-C. Chen, Q. Zheng, *ACS Appl. Energy Mater.* **2018**, *1*, 5872-5878.

[29] B. Zhang, W. Bi, Y. Wu, C. Chen, H. Li, Z. Song, Q. Dai, L. Xu, H. Song, *ACS Appl. Mater. Interfaces* **2019**, *11*, 33868-33878.

[30] Y. Guo, X. Yin, J. Liu, W. Que, *J. Mater. Chem. A* **2019**, *7*, 19008-19016.

[31] J. Liang, Z. Liu, L. Qiu, Z. Hawash, L. Meng, Z. Wu, Y. Jiang, L. K. Ono, Y. Qi, *Adv. Energy Mater.* **2018**, *8*, 1800504.

[32] X. Tan, X. Liu, Z. Liu, B. Sun, J. Li, S. Xi, T. Shi, Z. Tang, G. Liao, *Appl. Surf. Sci.* **2020**, *499*, 143990.

[33] J. Liang, P. Zhao, C. Wang, Y. Wang, Y. Hu, G. Zhu, L. Ma, J. Liu, Z. Jin, *J. Am. Chem. Soc.* **2017**, *139*, 14009-14012.

[34] N. Li, Z. Zhu, J. Li, A. Jen, L. Wang, *Adv. Energy Mater.* **2018**, *8*, 1800525.

[35] W. S. Subhani, K. Wang, M. Du, S. F. Liu, *Nano Energy* **2019**, *61*, 165-172.

[36] W. Zhu, W. Chai, Z. Zhang, D. Chen, J. Chang, S. Liu, J. Zhang, C. Zhang, Y. Hao, *Org. Electron.* **2019**, *74*, 103-109.

[37] Y. Han, H. Zhao, C. Duan, S. Yang, Z. Yang, Z. Liu, S. Liu, *Adv. Funct. Mater.* **2020**, DOI: 10.1002/adfm.201909972.

[38] Q. Ma, S. Huang, X. Wen, M. A. Green, A. W. Y. Ho-Baillie, *Adv. Energy Mater.* **2016**, *6*, 1502202.

[39] W. Li, M. U. Rothmann, A. Liu, Z. Wang, Y. Zhang, A. R. Pascoe, J. Lu, L. Jiang, Y. Chen, F. Huang, Y. Peng, Q. Bao, J. Etheridge, U. Bach, Y.-B. Cheng, *Adv. Energy Mater.* **2017**, *7*, 1700946.

[40] W. Xiang, Z. Wang D. J. Kubicki, X. Wang W. Tress J. Luo, J. Zhang, A. Hofstetter, L. Zhang, L. Emsley, M. Grätzel, A. Hagfeldt, *Nat. Commun.* **2019**, *10*, 1-8.

[41] H. Wang, S. Cao, B. Yang, H. Li, M. Wang, X. Hu, K. Sun, Z. Zang, *Sol. RRL* **2020**, *4*, 1900363.

[42] M. Xiao, F. Huang, W. Huang, Y. Dkhissi, Y. Zhu, J. Etheridge, A. Gray-Weale, U. Bach, Y.-B. Cheng, L. Spiccia, *Angew. Chem. Int. Ed.* **2014**, *53*, 9898-9903.

[43] H. Choi, K. Choi, Y. Choi, T. Kim, S. Lim, T. A. Park, *Small Methods* **2020**, 4, 1900569.

[44] P. You, G. Li, G. Tang, J. Cao, F. Yan, *Energy Environ. Sci.* **2020**, 13, 1187-1196.

[45] P. Liu, W. Wang, S. Liu, H. Yang, Z. Shao, *Adv. Energy Mater.* **2019**, *9*, 1803017.

[46] Z. Guo, S. Teo, Z. Xu, C. Zhang, Y. Kamata, S. Hayase, T. Ma, *J. Mater. Chem. A* **2019**, *7*, 1227-1232.

[47] B. Yang, M. Wang, X. Hu, T. Zhou, Z. Zang, *Nano Energy* **2019**, *57*, 718-727.

[48] X. Yi, Z. Zhang, A. Chang, Y. Mao, Y. Luan, T. Lin, Y. Wei, Y. Zhang, F. Wang, S. Cao, C. Li, J. Wang, *Adv. Energy Mater.* **2019**, *9*, 1901726.

[49] L. J. A. Koster, V. D. Mihailetchi, R. Ramaker, P. W. M. Blom, *Appl. Phys. Lett.* **2005**, *86*, 123509.

[50] G. Wu, X. Li, J. Zhou, J. Zhang, X. Zhang, X. Leng, P. Wang, M. Chen, D. Zhang, K. Zhao, S. Liu, H. Zhou, Y. Zhang, *Adv. Mater.* **2019**, *31*, 1903889.

[51] L. Xie, K. Lin, J. Lu, W. Feng, P. Song, C. Yan, K. Liu, L. Shen, C. Tian, Z. Wei, *J. Am. Chem. Soc.* **2019**, *141*, 20537-20546.

Chapter 6 Conclusions and Recommendations

6.1 Conclusions

During the past decade, PSCs have experienced a great boost in power conversion efficiency (PCE), improving from 3.8% to over 25.5%. However, there is still long way to go to commercialize PSCs. On one hand, the PCE is expected to be further improved although the current PCE is almost comparable with that achieved by the commercialized crystalline silicon solar cells. On the other hand, some problems restricted the development of PSCs. Stability has become the biggest obstacle that limits the development of PSCs as most PSCs are vulnerable to various environmental factors. Additionally, the hysteresis behavior in PSCs makes it difficult to evaluate the real performance of PSCs. Thus, it is very important to find effective ways to resolve these problems.

In this thesis, organic-inorganic hybrid halide perovskite $MAPbI_3$-based PSCs and all inorganic halide perovskite $CsPbIBr_2$-based PSCs were studied. In terms of $MAPbI_3$-based PSCs, the biggest advantage lies in the relatively high PCE due to the suitable properties of $MAPbI_3$ as light-absorbing materials. However, $MAPbI_3$-based PSCs suffer from unsatisfactory stability. With the assistance of SN and $Sb(Ac)_3$, $MAPbI_3$-based PSCs achieved significantly improved PCE and stability at the N_2 and humid air atmosphere. However, these devices also suffered from poor thermal stability. To fabricate PSCs with decent thermal stability, the attention was then paid to all-inorganic halide perovskites-based PSCs. Among various all-inorganic halide perovskites, $CsPbIBr_2$ was selected as the research object due to its suitable bandgap and good stability. Unfortunately, $CsPbIBr_2$-based PSCs delivered low PCE, which is still far from that of $MAPbI_3$-based devices due to the difficulty in fabricating high-quality $CsPbIBr_2$ perovskite films via the solution-processed spin-coating method. Thus, a strategy of Cu^{2+} doping was carried out to enhance the film quality and improve PCE as well as further improve long-term stability of $CsPbIBr_2$-based PSCs. The conclusions of the three research work mentioned in this thesis are listed as below.

Chapter 3 A Bilateral Cyano Molecule Serving as an Effective Additive Enables High-Efficiency and Stable Perovskite Solar Cells

- SN as a bilateral cyano molecule was utilized as an additive to tune the properties of $MAPbI_3(Cl)$ perovskite films.
- One SN molecule has two cyano groups (-C≡N) distributing at the terminals of the carbon chain, which provides two cross linking points to interact with perovskite crystals.
- The interaction between $MAPbI_3$ perovskites and the added SN formed strong aggregation strength among perovskite grains, enabling perovskite grains to gather together.
- The incorporation of SN reduced defects, thus effectively suppressing charge recombination.
- In addition, small amount of SN addition increased crystallinity and enhanced light absorption.
- As a result, the PCE of $MAPbI_3$-based PSCs was improved from 18.4% to 20.3% and the stability was also improved.

Chapter 4 Benefitting from Synergistic Effect of Anion and Cation in Antimony Acetate for Stable $CH_3NH_3PbI_3$-Based Perovskite Solar Cell with Efficiency Beyond 21%

- $Sb(Ac)_3$ was selected to modify $MAPbI_3$-based PSCs because both Sb^{3+} and Ac^- can improve the properties of $MAPbI_3$ perovskite films. $Pb(Ac)_2$ and SbI_3 were also utilized in this work to investigate the individual role of Sb^{3+} and Ac^-.
- It was found that Ac^- is more effective in optimizing the perovskite film morphology while Sb^{3+} is more involved in tuning the electronic properties of perovskite.
- Benefiting from the synergetic effect of Sb^{3+} and Ac^-, $Sb(Ac)_3$ modified perovskite films exhibited increased crystallinity, reduced defects and effectively suppressed charge carrier recombination.
- Consequently, $Sb(Ac)_3$-modified $MAPbI_3$ PSCs achieved a high PCE above 21% with improved stability in N_2 and humid atmosphere and enhanced thermal stability.

Chapter 5 Promoting the Efficiency and Stability of $CsPbIBr_2$-Based All-Inorganic Perovskite

Solar Cells through a Functional Cu^{2+} Doping Strategy

- By incorporating an appropriate amount of Cu^{2+} (0.50 at. %) into the $CsPbIBr_2$ perovskite, an enhanced film quality with the increased crystallinity and the expanded grain sizes was achieved.
- Cu^{2+} doping gave rise to an optimized energy level alignment, which is beneficial to charge transportation and separation.
- Trap densities were significantly reduced after Cu^{2+} doping, effectively suppressing charge carrier recombination.
- Benefiting from the merits mentioned above, a maximum PCE value of 10.4% was obtained on the $CsPbIBr_2$-0.50%Cu-based device with a cell configuration of FTO/c-TiO_2/$CsPbIBr_2$-0.50%Cu/spiro-OMeTAD/Ag.
- Cu^{2+} doping also played a critical role in the stability enhancement of PSCs, which allowed $CsPbIBr_2$ PSCs to experience no obvious degradation in a N_2 and dry air atmosphere and remained almost 75% of their initial PCE when heated at 90 °C in the ambient atmosphere with 30% humidity.

6.2 Recommendations

In spite of some progress that have been achieved in this PhD thesis, future work is still required to further improve the quality of these studies. As for the first research work, TEM images are recommended to test for the observation of the distribution of SN on the surface and to confirm whether SN only distributes at the grain boundaries. As for the second research work, it is meaningful to analyze the distribution of Ac^- and Sb^{3+} in perovskite films. In terms of the third research work, some other all-inorganic halide perovskite materials like $CsPbI_3$ and $CsPbI_2Br$-based PSCs should be paid some attention as they often showed higher PCE than $CsPbIBr_2$-based PSCs. Furthermore, it is meaningful to deepen the understanding of PSCs, particularly in terms of some important phenomenon and factors.

Appendix: Permission of Reproduction from the Copyright Owner

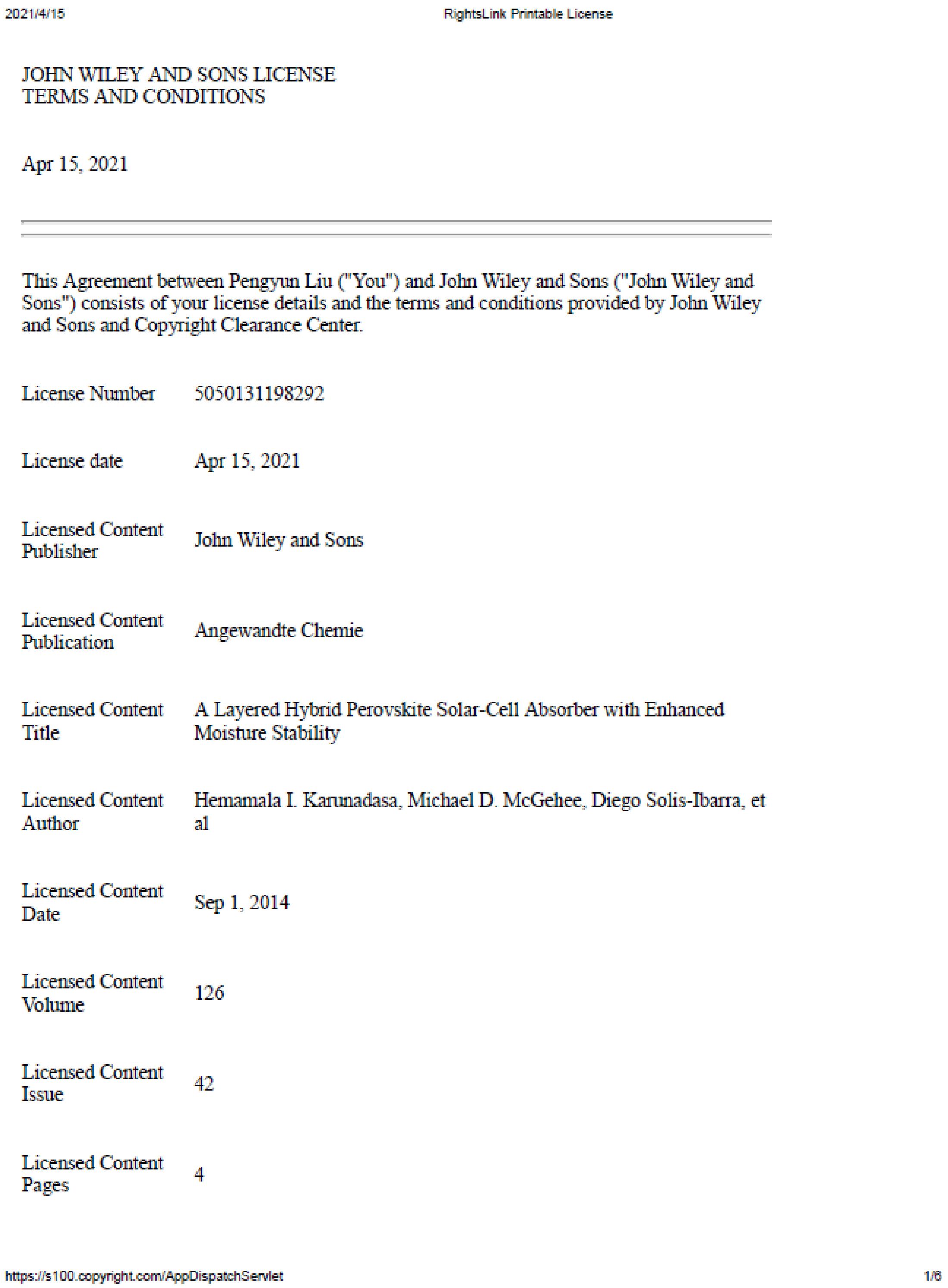

JOHN WILEY AND SONS LICENSE
TERMS AND CONDITIONS

Apr 15, 2021

This Agreement between Pengyun Liu ("You") and John Wiley and Sons ("John Wiley and Sons") consists of your license details and the terms and conditions provided by John Wiley and Sons and Copyright Clearance Center.

License Number	5050131198292
License date	Apr 15, 2021
Licensed Content Publisher	John Wiley and Sons
Licensed Content Publication	Angewandte Chemie
Licensed Content Title	A Layered Hybrid Perovskite Solar-Cell Absorber with Enhanced Moisture Stability
Licensed Content Author	Hemamala I. Karunadasa, Michael D. McGehee, Diego Solis-Ibarra, et al
Licensed Content Date	Sep 1, 2014
Licensed Content Volume	126
Licensed Content Issue	42
Licensed Content Pages	4

Type of use	Dissertation/Thesis
Requestor type	University/Academic
Format	Print and electronic
Portion	Figure/table
Number of figures/tables	1
Will you be translating?	No
Title	The optimization of perovskite solar cells from power conversion efficiency and operational stability
Institution name	Curtin University
Expected presentation date	Dec 2021
Portions	Figure 1
Requestor Location	Pengyun Liu 14 spyglass circle, canning vale Perth, WA 6155 Australia Attn:
Publisher Tax ID	EU826007151
Total	0.00 AUD

Terms and Conditions

TERMS AND CONDITIONS

This copyrighted material is owned by or exclusively licensed to John Wiley & Sons, Inc. or one of its group companies (each a"Wiley Company") or handled on behalf of a society with which a Wiley Company has exclusive publishing rights in relation to a particular work (collectively "WILEY"). By clicking "accept" in connection with completing this licensing transaction, you agree that the following terms and conditions apply to this transaction (along with the billing and payment terms and conditions established by the Copyright Clearance Center Inc., ("CCC's Billing and Payment terms and conditions"), at the time that you opened your RightsLink account (these are available at any time at http://myaccount.copyright.com).

Terms and Conditions

- The materials you have requested permission to reproduce or reuse (the "Wiley Materials") are protected by copyright.

- You are hereby granted a personal, non-exclusive, non-sub licensable (on a stand-alone basis), non-transferable, worldwide, limited license to reproduce the Wiley Materials for the purpose specified in the licensing process. This license, **and any CONTENT (PDF or image file) purchased as part of your order**, is for a one-time use only and limited to any maximum distribution number specified in the license. The first instance of republication or reuse granted by this license must be completed within two years of the date of the grant of this license (although copies prepared before the end date may be distributed thereafter). The Wiley Materials shall not be used in any other manner or for any other purpose, beyond what is granted in the license. Permission is granted subject to an appropriate acknowledgement given to the author, title of the material/book/journal and the publisher. You shall also duplicate the copyright notice that appears in the Wiley publication in your use of the Wiley Material. Permission is also granted on the understanding that nowhere in the text is a previously published source acknowledged for all or part of this Wiley Material. Any third party content is expressly excluded from this permission.

- With respect to the Wiley Materials, all rights are reserved. Except as expressly granted by the terms of the license, no part of the Wiley Materials may be copied, modified, adapted (except for minor reformatting required by the new Publication), translated, reproduced, transferred or distributed, in any form or by any means, and no derivative works may be made based on the Wiley Materials without the prior permission of the respective copyright owner.**For STM Signatory Publishers clearing permission under the terms of the STM Permissions Guidelines only, the terms of the license are extended to include subsequent editions and for editions in other languages, provided such editions are for the work as a whole in situ and does not involve the separate exploitation of the permitted figures or extracts,** You may not alter, remove or suppress in any manner any copyright, trademark or other notices displayed by the Wiley Materials. You may not license, rent, sell, loan, lease, pledge, offer as security, transfer or assign the Wiley Materials on a stand-alone basis, or any of the rights granted to you hereunder to any other person.

- The Wiley Materials and all of the intellectual property rights therein shall at all times remain the exclusive property of John Wiley & Sons Inc, the Wiley Companies, or their respective licensors, and your interest therein is only that of having possession of and the right to reproduce the Wiley Materials pursuant to Section 2 herein during the continuance of this Agreement. You agree that you own no right, title or interest in or to the Wiley Materials or any of the intellectual property rights therein. You shall have no rights hereunder other than the license as provided for above in Section 2. No right,

license or interest to any trademark, trade name, service mark or other branding ("Marks") of WILEY or its licensors is granted hereunder, and you agree that you shall not assert any such right, license or interest with respect thereto

- NEITHER WILEY NOR ITS LICENSORS MAKES ANY WARRANTY OR REPRESENTATION OF ANY KIND TO YOU OR ANY THIRD PARTY, EXPRESS, IMPLIED OR STATUTORY, WITH RESPECT TO THE MATERIALS OR THE ACCURACY OF ANY INFORMATION CONTAINED IN THE MATERIALS, INCLUDING, WITHOUT LIMITATION, ANY IMPLIED WARRANTY OF MERCHANTABILITY, ACCURACY, SATISFACTORY QUALITY, FITNESS FOR A PARTICULAR PURPOSE, USABILITY, INTEGRATION OR NON-INFRINGEMENT AND ALL SUCH WARRANTIES ARE HEREBY EXCLUDED BY WILEY AND ITS LICENSORS AND WAIVED BY YOU.

- WILEY shall have the right to terminate this Agreement immediately upon breach of this Agreement by you.

- You shall indemnify, defend and hold harmless WILEY, its Licensors and their respective directors, officers, agents and employees, from and against any actual or threatened claims, demands, causes of action or proceedings arising from any breach of this Agreement by you.

- IN NO EVENT SHALL WILEY OR ITS LICENSORS BE LIABLE TO YOU OR ANY OTHER PARTY OR ANY OTHER PERSON OR ENTITY FOR ANY SPECIAL, CONSEQUENTIAL, INCIDENTAL, INDIRECT, EXEMPLARY OR PUNITIVE DAMAGES, HOWEVER CAUSED, ARISING OUT OF OR IN CONNECTION WITH THE DOWNLOADING, PROVISIONING, VIEWING OR USE OF THE MATERIALS REGARDLESS OF THE FORM OF ACTION, WHETHER FOR BREACH OF CONTRACT, BREACH OF WARRANTY, TORT, NEGLIGENCE, INFRINGEMENT OR OTHERWISE (INCLUDING, WITHOUT LIMITATION, DAMAGES BASED ON LOSS OF PROFITS, DATA, FILES, USE, BUSINESS OPPORTUNITY OR CLAIMS OF THIRD PARTIES), AND WHETHER OR NOT THE PARTY HAS BEEN ADVISED OF THE POSSIBILITY OF SUCH DAMAGES. THIS LIMITATION SHALL APPLY NOTWITHSTANDING ANY FAILURE OF ESSENTIAL PURPOSE OF ANY LIMITED REMEDY PROVIDED HEREIN.

- Should any provision of this Agreement be held by a court of competent jurisdiction to be illegal, invalid, or unenforceable, that provision shall be deemed amended to achieve as nearly as possible the same economic effect as the original provision, and the legality, validity and enforceability of the remaining provisions of this Agreement shall not be affected or impaired thereby.

- The failure of either party to enforce any term or condition of this Agreement shall not constitute a waiver of either party's right to enforce each and every term and condition of this Agreement. No breach under this agreement shall be deemed waived or excused by either party unless such waiver or consent is in writing signed by the party granting such waiver or consent. The waiver by or consent of a party to a breach of any provision of this Agreement shall not operate or be construed as a waiver of or consent to any other or subsequent breach by such other party.

- This Agreement may not be assigned (including by operation of law or otherwise) by you without WILEY's prior written consent.

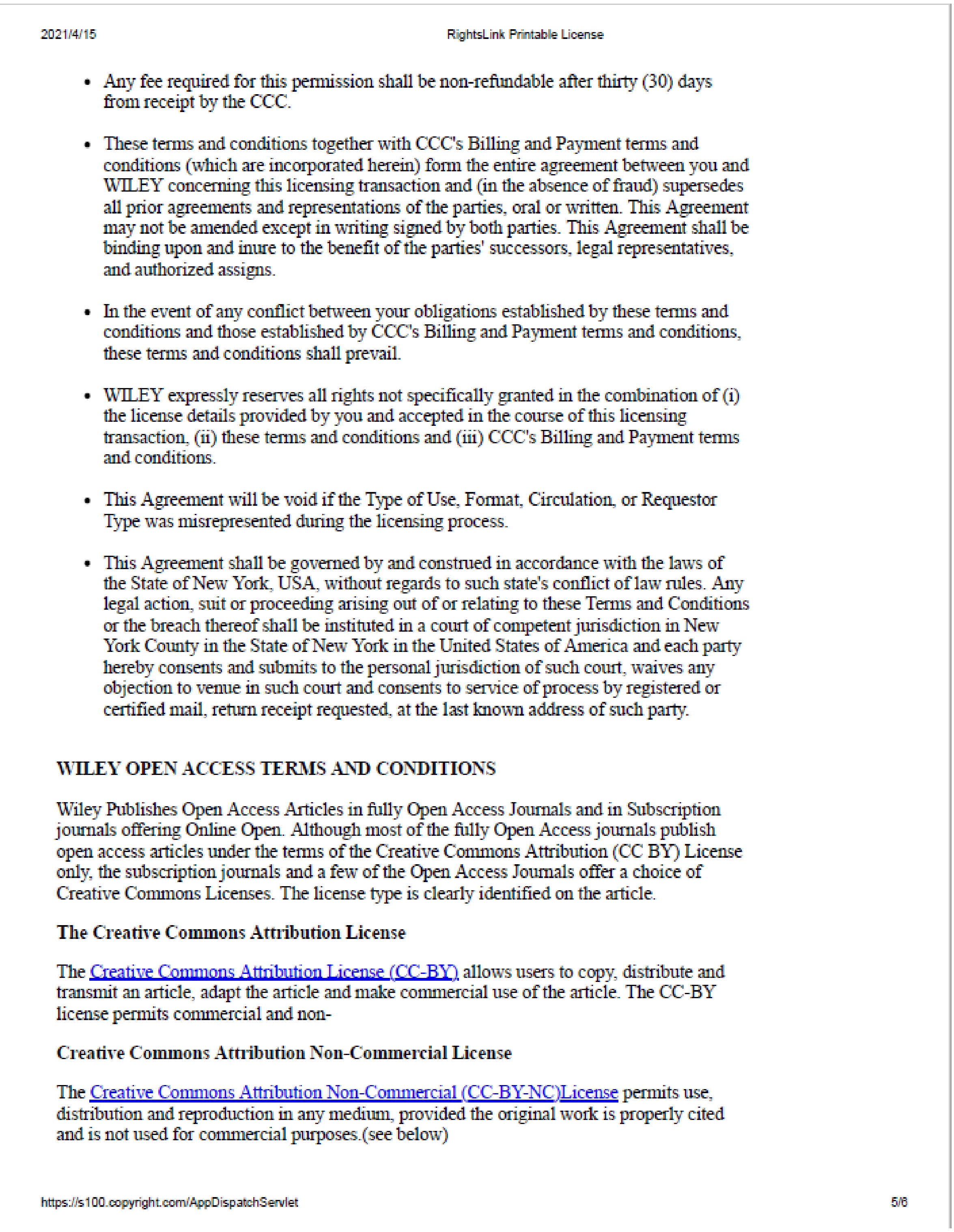

- Any fee required for this permission shall be non-refundable after thirty (30) days from receipt by the CCC.

- These terms and conditions together with CCC's Billing and Payment terms and conditions (which are incorporated herein) form the entire agreement between you and WILEY concerning this licensing transaction and (in the absence of fraud) supersedes all prior agreements and representations of the parties, oral or written. This Agreement may not be amended except in writing signed by both parties. This Agreement shall be binding upon and inure to the benefit of the parties' successors, legal representatives, and authorized assigns.

- In the event of any conflict between your obligations established by these terms and conditions and those established by CCC's Billing and Payment terms and conditions, these terms and conditions shall prevail.

- WILEY expressly reserves all rights not specifically granted in the combination of (i) the license details provided by you and accepted in the course of this licensing transaction, (ii) these terms and conditions and (iii) CCC's Billing and Payment terms and conditions.

- This Agreement will be void if the Type of Use, Format, Circulation, or Requestor Type was misrepresented during the licensing process.

- This Agreement shall be governed by and construed in accordance with the laws of the State of New York, USA, without regards to such state's conflict of law rules. Any legal action, suit or proceeding arising out of or relating to these Terms and Conditions or the breach thereof shall be instituted in a court of competent jurisdiction in New York County in the State of New York in the United States of America and each party hereby consents and submits to the personal jurisdiction of such court, waives any objection to venue in such court and consents to service of process by registered or certified mail, return receipt requested, at the last known address of such party.

WILEY OPEN ACCESS TERMS AND CONDITIONS

Wiley Publishes Open Access Articles in fully Open Access Journals and in Subscription journals offering Online Open. Although most of the fully Open Access journals publish open access articles under the terms of the Creative Commons Attribution (CC BY) License only, the subscription journals and a few of the Open Access Journals offer a choice of Creative Commons Licenses. The license type is clearly identified on the article.

The Creative Commons Attribution License

The Creative Commons Attribution License (CC-BY) allows users to copy, distribute and transmit an article, adapt the article and make commercial use of the article. The CC-BY license permits commercial and non-

Creative Commons Attribution Non-Commercial License

The Creative Commons Attribution Non-Commercial (CC-BY-NC)License permits use, distribution and reproduction in any medium, provided the original work is properly cited and is not used for commercial purposes.(see below)

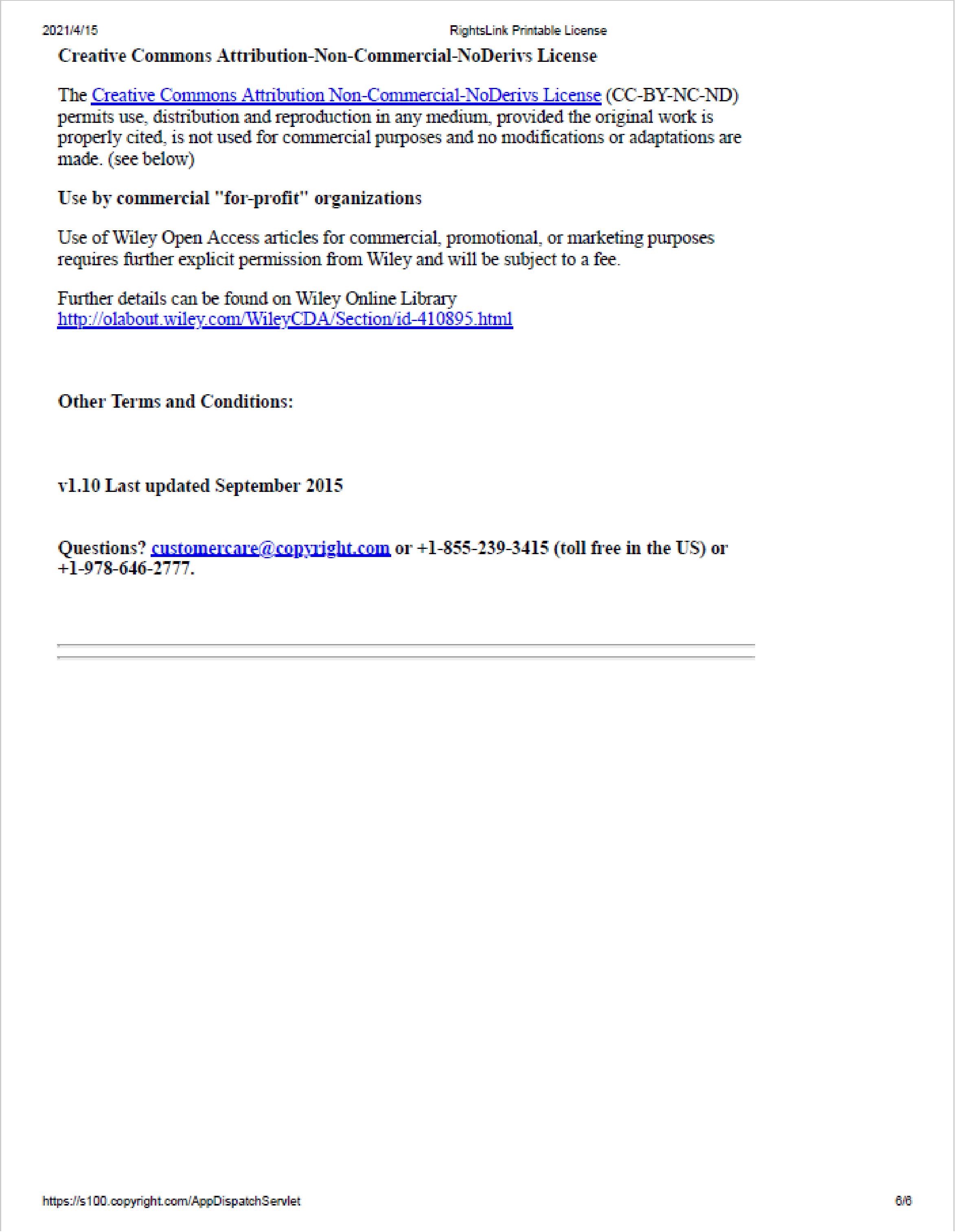

Creative Commons Attribution-Non-Commercial-NoDerivs License

The Creative Commons Attribution Non-Commercial-NoDerivs License (CC-BY-NC-ND) permits use, distribution and reproduction in any medium, provided the original work is properly cited, is not used for commercial purposes and no modifications or adaptations are made. (see below)

Use by commercial "for-profit" organizations

Use of Wiley Open Access articles for commercial, promotional, or marketing purposes requires further explicit permission from Wiley and will be subject to a fee.

Further details can be found on Wiley Online Library
http://olabout.wiley.com/WileyCDA/Section/id-410895.html

Other Terms and Conditions:

v1.10 Last updated September 2015

Questions? customercare@copyright.com or +1-855-239-3415 (toll free in the US) or +1-978-646-2777.

JOHN WILEY AND SONS LICENSE
TERMS AND CONDITIONS

Apr 17, 2021

This Agreement between Pengyun Liu ("You") and John Wiley and Sons ("John Wiley and Sons") consists of your license details and the terms and conditions provided by John Wiley and Sons and Copyright Clearance Center.

License Number	5051161116464
License date	Apr 17, 2021
Licensed Content Publisher	John Wiley and Sons
Licensed Content Publication	Advanced Materials
Licensed Content Title	High-Quality Ruddlesden–Popper Perovskite Film Formation for High -Performance Perovskite Solar Cells
Licensed Content Author	Zongping Shao, Wei Zhou, Ran Ran, et al
Licensed Content Date	Jan 29, 2021
Licensed Content Volume	33
Licensed Content Issue	10
Licensed Content Pages	40

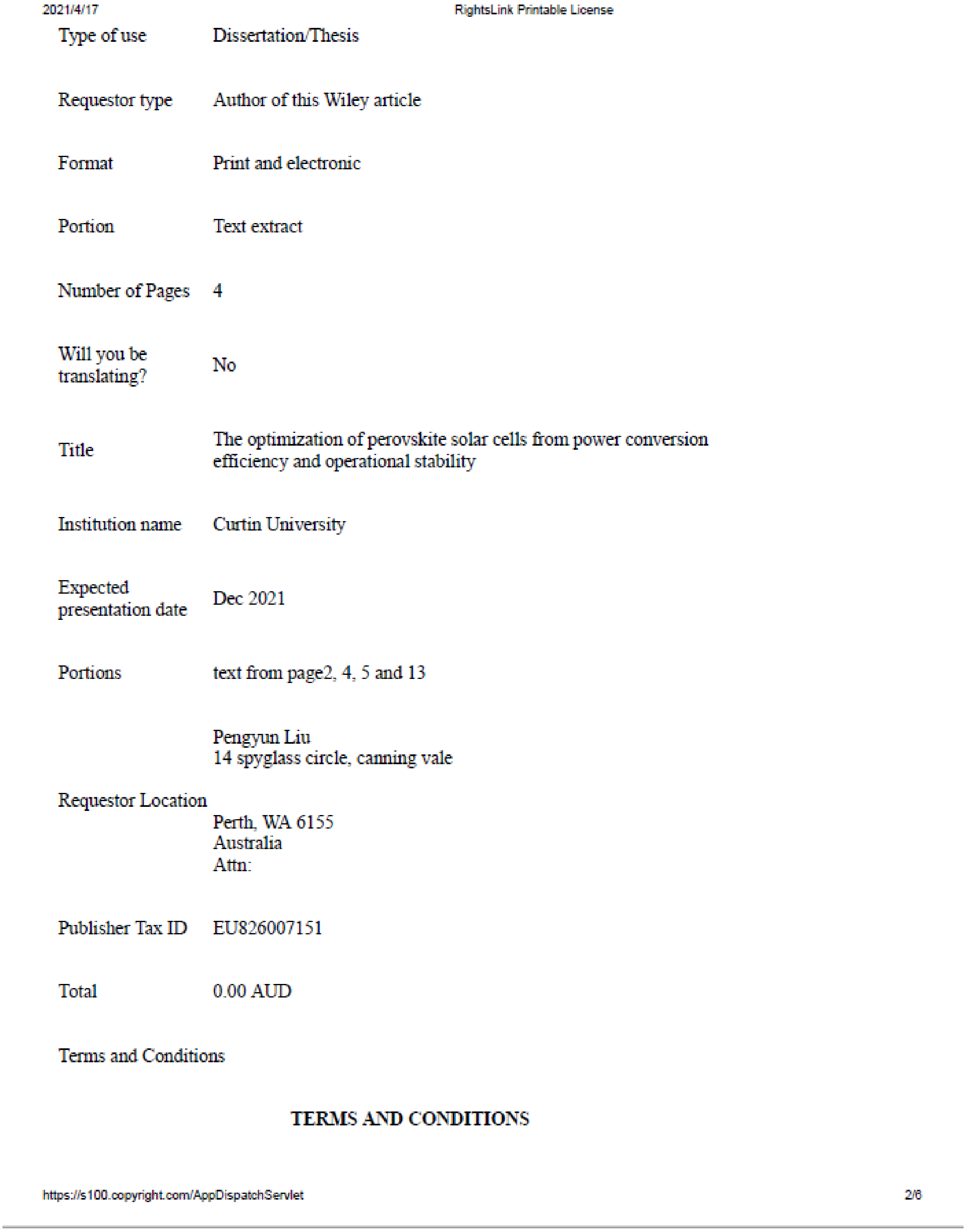

Type of use	Dissertation/Thesis
Requestor type	Author of this Wiley article
Format	Print and electronic
Portion	Text extract
Number of Pages	4
Will you be translating?	No
Title	The optimization of perovskite solar cells from power conversion efficiency and operational stability
Institution name	Curtin University
Expected presentation date	Dec 2021
Portions	text from page2, 4, 5 and 13
Requestor Location	Pengyun Liu 14 spyglass circle, canning vale Perth, WA 6155 Australia Attn:
Publisher Tax ID	EU826007151
Total	0.00 AUD

Terms and Conditions

TERMS AND CONDITIONS

This copyrighted material is owned by or exclusively licensed to John Wiley & Sons, Inc. or one of its group companies (each a"Wiley Company") or handled on behalf of a society with which a Wiley Company has exclusive publishing rights in relation to a particular work (collectively "WILEY"). By clicking "accept" in connection with completing this licensing transaction, you agree that the following terms and conditions apply to this transaction (along with the billing and payment terms and conditions established by the Copyright Clearance Center Inc., ("CCC's Billing and Payment terms and conditions"), at the time that you opened your RightsLink account (these are available at any time at http://myaccount.copyright.com).

Terms and Conditions

- The materials you have requested permission to reproduce or reuse (the "Wiley Materials") are protected by copyright.

- You are hereby granted a personal, non-exclusive, non-sub licensable (on a stand-alone basis), non-transferable, worldwide, limited license to reproduce the Wiley Materials for the purpose specified in the licensing process. This license, **and any CONTENT (PDF or image file) purchased as part of your order**, is for a one-time use only and limited to any maximum distribution number specified in the license. The first instance of republication or reuse granted by this license must be completed within two years of the date of the grant of this license (although copies prepared before the end date may be distributed thereafter). The Wiley Materials shall not be used in any other manner or for any other purpose, beyond what is granted in the license. Permission is granted subject to an appropriate acknowledgement given to the author, title of the material/book/journal and the publisher. You shall also duplicate the copyright notice that appears in the Wiley publication in your use of the Wiley Material. Permission is also granted on the understanding that nowhere in the text is a previously published source acknowledged for all or part of this Wiley Material. Any third party content is expressly excluded from this permission.

- With respect to the Wiley Materials, all rights are reserved. Except as expressly granted by the terms of the license, no part of the Wiley Materials may be copied, modified, adapted (except for minor reformatting required by the new Publication), translated, reproduced, transferred or distributed, in any form or by any means, and no derivative works may be made based on the Wiley Materials without the prior permission of the respective copyright owner.**For STM Signatory Publishers clearing permission under the terms of the STM Permissions Guidelines only, the terms of the license are extended to include subsequent editions and for editions in other languages, provided such editions are for the work as a whole in situ and does not involve the separate exploitation of the permitted figures or extracts,** You may not alter, remove or suppress in any manner any copyright, trademark or other notices displayed by the Wiley Materials. You may not license, rent, sell, loan, lease, pledge, offer as security, transfer or assign the Wiley Materials on a stand-alone basis, or any of the rights granted to you hereunder to any other person.

- The Wiley Materials and all of the intellectual property rights therein shall at all times remain the exclusive property of John Wiley & Sons Inc, the Wiley Companies, or their respective licensors, and your interest therein is only that of having possession of and the right to reproduce the Wiley Materials pursuant to Section 2 herein during the continuance of this Agreement. You agree that you own no right, title or interest in or to the Wiley Materials or any of the intellectual property rights therein. You shall have no rights hereunder other than the license as provided for above in Section 2. No right,

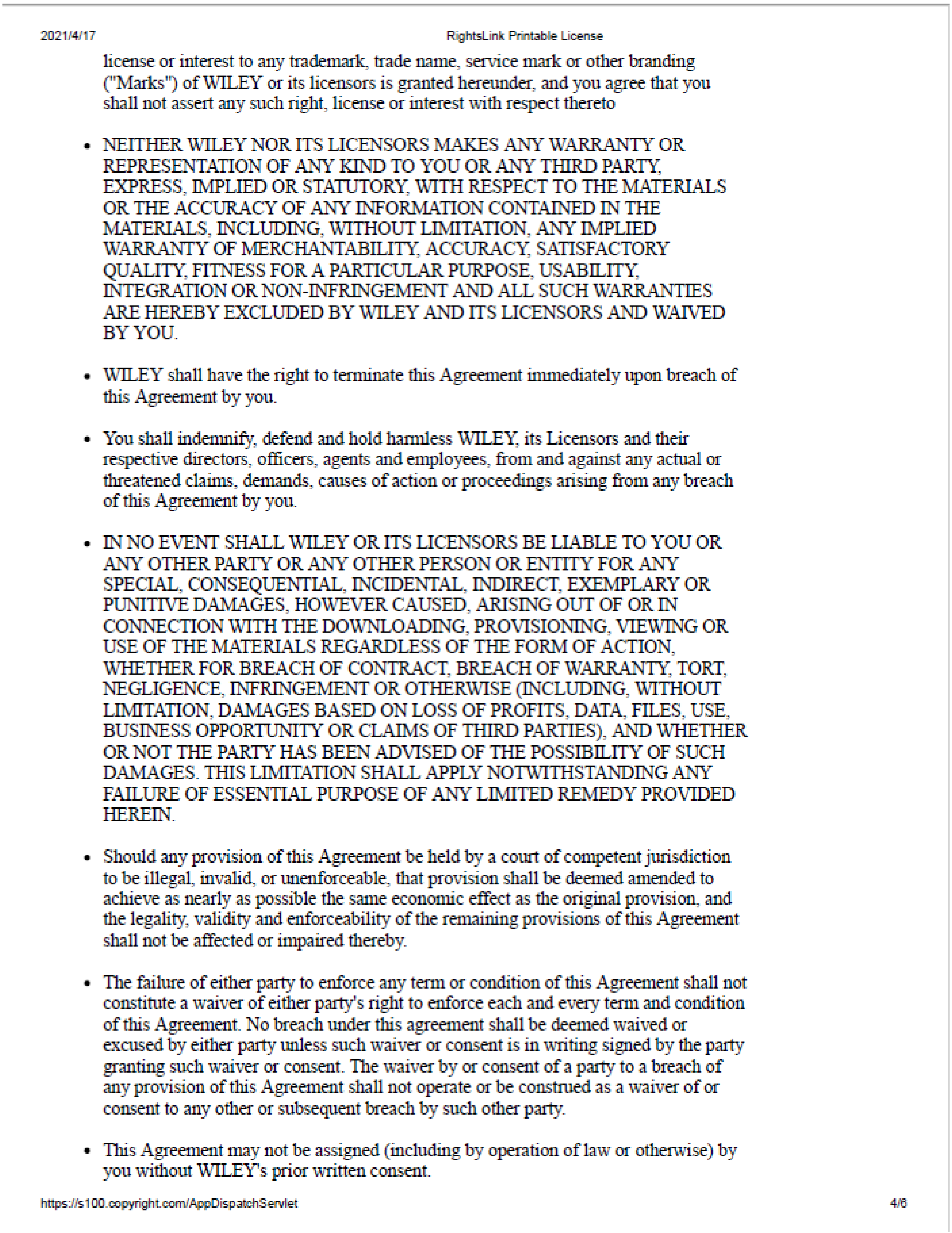

license or interest to any trademark, trade name, service mark or other branding ("Marks") of WILEY or its licensors is granted hereunder, and you agree that you shall not assert any such right, license or interest with respect thereto

- NEITHER WILEY NOR ITS LICENSORS MAKES ANY WARRANTY OR REPRESENTATION OF ANY KIND TO YOU OR ANY THIRD PARTY, EXPRESS, IMPLIED OR STATUTORY, WITH RESPECT TO THE MATERIALS OR THE ACCURACY OF ANY INFORMATION CONTAINED IN THE MATERIALS, INCLUDING, WITHOUT LIMITATION, ANY IMPLIED WARRANTY OF MERCHANTABILITY, ACCURACY, SATISFACTORY QUALITY, FITNESS FOR A PARTICULAR PURPOSE, USABILITY, INTEGRATION OR NON-INFRINGEMENT AND ALL SUCH WARRANTIES ARE HEREBY EXCLUDED BY WILEY AND ITS LICENSORS AND WAIVED BY YOU.

- WILEY shall have the right to terminate this Agreement immediately upon breach of this Agreement by you.

- You shall indemnify, defend and hold harmless WILEY, its Licensors and their respective directors, officers, agents and employees, from and against any actual or threatened claims, demands, causes of action or proceedings arising from any breach of this Agreement by you.

- IN NO EVENT SHALL WILEY OR ITS LICENSORS BE LIABLE TO YOU OR ANY OTHER PARTY OR ANY OTHER PERSON OR ENTITY FOR ANY SPECIAL, CONSEQUENTIAL, INCIDENTAL, INDIRECT, EXEMPLARY OR PUNITIVE DAMAGES, HOWEVER CAUSED, ARISING OUT OF OR IN CONNECTION WITH THE DOWNLOADING, PROVISIONING, VIEWING OR USE OF THE MATERIALS REGARDLESS OF THE FORM OF ACTION, WHETHER FOR BREACH OF CONTRACT, BREACH OF WARRANTY, TORT, NEGLIGENCE, INFRINGEMENT OR OTHERWISE (INCLUDING, WITHOUT LIMITATION, DAMAGES BASED ON LOSS OF PROFITS, DATA, FILES, USE, BUSINESS OPPORTUNITY OR CLAIMS OF THIRD PARTIES), AND WHETHER OR NOT THE PARTY HAS BEEN ADVISED OF THE POSSIBILITY OF SUCH DAMAGES. THIS LIMITATION SHALL APPLY NOTWITHSTANDING ANY FAILURE OF ESSENTIAL PURPOSE OF ANY LIMITED REMEDY PROVIDED HEREIN.

- Should any provision of this Agreement be held by a court of competent jurisdiction to be illegal, invalid, or unenforceable, that provision shall be deemed amended to achieve as nearly as possible the same economic effect as the original provision, and the legality, validity and enforceability of the remaining provisions of this Agreement shall not be affected or impaired thereby.

- The failure of either party to enforce any term or condition of this Agreement shall not constitute a waiver of either party's right to enforce each and every term and condition of this Agreement. No breach under this agreement shall be deemed waived or excused by either party unless such waiver or consent is in writing signed by the party granting such waiver or consent. The waiver by or consent of a party to a breach of any provision of this Agreement shall not operate or be construed as a waiver of or consent to any other or subsequent breach by such other party.

- This Agreement may not be assigned (including by operation of law or otherwise) by you without WILEY's prior written consent.

- Any fee required for this permission shall be non-refundable after thirty (30) days from receipt by the CCC.

- These terms and conditions together with CCC's Billing and Payment terms and conditions (which are incorporated herein) form the entire agreement between you and WILEY concerning this licensing transaction and (in the absence of fraud) supersedes all prior agreements and representations of the parties, oral or written. This Agreement may not be amended except in writing signed by both parties. This Agreement shall be binding upon and inure to the benefit of the parties' successors, legal representatives, and authorized assigns.

- In the event of any conflict between your obligations established by these terms and conditions and those established by CCC's Billing and Payment terms and conditions, these terms and conditions shall prevail.

- WILEY expressly reserves all rights not specifically granted in the combination of (i) the license details provided by you and accepted in the course of this licensing transaction, (ii) these terms and conditions and (iii) CCC's Billing and Payment terms and conditions.

- This Agreement will be void if the Type of Use, Format, Circulation, or Requestor Type was misrepresented during the licensing process.

- This Agreement shall be governed by and construed in accordance with the laws of the State of New York, USA, without regards to such state's conflict of law rules. Any legal action, suit or proceeding arising out of or relating to these Terms and Conditions or the breach thereof shall be instituted in a court of competent jurisdiction in New York County in the State of New York in the United States of America and each party hereby consents and submits to the personal jurisdiction of such court, waives any objection to venue in such court and consents to service of process by registered or certified mail, return receipt requested, at the last known address of such party.

WILEY OPEN ACCESS TERMS AND CONDITIONS

Wiley Publishes Open Access Articles in fully Open Access Journals and in Subscription journals offering Online Open. Although most of the fully Open Access journals publish open access articles under the terms of the Creative Commons Attribution (CC BY) License only, the subscription journals and a few of the Open Access Journals offer a choice of Creative Commons Licenses. The license type is clearly identified on the article.

The Creative Commons Attribution License

The Creative Commons Attribution License (CC-BY) allows users to copy, distribute and transmit an article, adapt the article and make commercial use of the article. The CC-BY license permits commercial and non-

Creative Commons Attribution Non-Commercial License

The Creative Commons Attribution Non-Commercial (CC-BY-NC)License permits use, distribution and reproduction in any medium, provided the original work is properly cited and is not used for commercial purposes.(see below)

Creative Commons Attribution-Non-Commercial-NoDerivs License

The Creative Commons Attribution Non-Commercial-NoDerivs License (CC-BY-NC-ND) permits use, distribution and reproduction in any medium, provided the original work is properly cited, is not used for commercial purposes and no modifications or adaptations are made. (see below)

Use by commercial "for-profit" organizations

Use of Wiley Open Access articles for commercial, promotional, or marketing purposes requires further explicit permission from Wiley and will be subject to a fee.

Further details can be found on Wiley Online Library
http://olabout.wiley.com/WileyCDA/Section/id-410895.html

Other Terms and Conditions:

v1.10 Last updated September 2015

Questions? customercare@copyright.com or +1-855-239-3415 (toll free in the US) or +1-978-646-2777.

JOHN WILEY AND SONS LICENSE
TERMS AND CONDITIONS

Jul 01, 2021

This Agreement between Pengyun Liu ("You") and John Wiley and Sons ("John Wiley and Sons") consists of your license details and the terms and conditions provided by John Wiley and Sons and Copyright Clearance Center.

License Number	5100531446295
License date	Jul 01, 2021
Licensed Content Publisher	John Wiley and Sons
Licensed Content Publication	Advanced Energy Materials
Licensed Content Title	Fundamental Understanding of Photocurrent Hysteresis in Perovskite Solar Cells
Licensed Content Author	Zongping Shao, Huagui Yang, Shaomin Liu, et al
Licensed Content Date	Feb 8, 2019
Licensed Content Volume	9
Licensed Content Issue	13
Licensed Content Pages	33

Type of use	Dissertation/Thesis
Requestor type	Author of this Wiley article
Format	Print and electronic
Portion	Figure/table
Number of figures/tables	1
Will you be translating?	No
Title	The optimization of perovskite solar cells from power conversion efficiency and operational stability
Institution name	Curtin University
Expected presentation date	Dec 2021
Portions	Figure 4
Requestor Location	Pengyun Liu 14 spyglass circle, canning vale Perth, WA 6155 Australia Attn:
Publisher Tax ID	EU826007151
Total	0.00 AUD

Terms and Conditions

TERMS AND CONDITIONS

This copyrighted material is owned by or exclusively licensed to John Wiley & Sons, Inc. or one of its group companies (each a"Wiley Company") or handled on behalf of a society with which a Wiley Company has exclusive publishing rights in relation to a particular work (collectively "WILEY"). By clicking "accept" in connection with completing this licensing transaction, you agree that the following terms and conditions apply to this transaction (along with the billing and payment terms and conditions established by the Copyright Clearance Center Inc., ("CCC's Billing and Payment terms and conditions"), at the time that you opened your RightsLink account (these are available at any time at http://myaccount.copyright.com).

Terms and Conditions

- The materials you have requested permission to reproduce or reuse (the "Wiley Materials") are protected by copyright.

- You are hereby granted a personal, non-exclusive, non-sub licensable (on a stand-alone basis), non-transferable, worldwide, limited license to reproduce the Wiley Materials for the purpose specified in the licensing process. This license, **and any CONTENT (PDF or image file) purchased as part of your order,** is for a one-time use only and limited to any maximum distribution number specified in the license. The first instance of republication or reuse granted by this license must be completed within two years of the date of the grant of this license (although copies prepared before the end date may be distributed thereafter). The Wiley Materials shall not be used in any other manner or for any other purpose, beyond what is granted in the license. Permission is granted subject to an appropriate acknowledgement given to the author, title of the material/book/journal and the publisher. You shall also duplicate the copyright notice that appears in the Wiley publication in your use of the Wiley Material. Permission is also granted on the understanding that nowhere in the text is a previously published source acknowledged for all or part of this Wiley Material. Any third party content is expressly excluded from this permission.

- With respect to the Wiley Materials, all rights are reserved. Except as expressly granted by the terms of the license, no part of the Wiley Materials may be copied, modified, adapted (except for minor reformatting required by the new Publication), translated, reproduced, transferred or distributed, in any form or by any means, and no derivative works may be made based on the Wiley Materials without the prior permission of the respective copyright owner.**For STM Signatory Publishers clearing permission under the terms of the STM Permissions Guidelines only, the terms of the license are extended to include subsequent editions and for editions in other languages, provided such editions are for the work as a whole in situ and does not involve the separate exploitation of the permitted figures or extracts,** You may not alter, remove or suppress in any manner any copyright, trademark or other notices displayed by the Wiley Materials. You may not license, rent, sell, loan, lease, pledge, offer as security, transfer or assign the Wiley Materials on a stand-alone basis, or any of the rights granted to you hereunder to any other person.

- The Wiley Materials and all of the intellectual property rights therein shall at all times remain the exclusive property of John Wiley & Sons Inc, the Wiley Companies, or their respective licensors, and your interest therein is only that of having possession of and the right to reproduce the Wiley Materials pursuant to Section 2 herein during the continuance of this Agreement. You agree that you own no right, title or interest in or to the Wiley Materials or any of the intellectual property rights therein. You shall have no rights hereunder other than the license as provided for above in Section 2. No right,

license or interest to any trademark, trade name, service mark or other branding ("Marks") of WILEY or its licensors is granted hereunder, and you agree that you shall not assert any such right, license or interest with respect thereto

- NEITHER WILEY NOR ITS LICENSORS MAKES ANY WARRANTY OR REPRESENTATION OF ANY KIND TO YOU OR ANY THIRD PARTY, EXPRESS, IMPLIED OR STATUTORY, WITH RESPECT TO THE MATERIALS OR THE ACCURACY OF ANY INFORMATION CONTAINED IN THE MATERIALS, INCLUDING, WITHOUT LIMITATION, ANY IMPLIED WARRANTY OF MERCHANTABILITY, ACCURACY, SATISFACTORY QUALITY, FITNESS FOR A PARTICULAR PURPOSE, USABILITY, INTEGRATION OR NON-INFRINGEMENT AND ALL SUCH WARRANTIES ARE HEREBY EXCLUDED BY WILEY AND ITS LICENSORS AND WAIVED BY YOU.

- WILEY shall have the right to terminate this Agreement immediately upon breach of this Agreement by you.

- You shall indemnify, defend and hold harmless WILEY, its Licensors and their respective directors, officers, agents and employees, from and against any actual or threatened claims, demands, causes of action or proceedings arising from any breach of this Agreement by you.

- IN NO EVENT SHALL WILEY OR ITS LICENSORS BE LIABLE TO YOU OR ANY OTHER PARTY OR ANY OTHER PERSON OR ENTITY FOR ANY SPECIAL, CONSEQUENTIAL, INCIDENTAL, INDIRECT, EXEMPLARY OR PUNITIVE DAMAGES, HOWEVER CAUSED, ARISING OUT OF OR IN CONNECTION WITH THE DOWNLOADING, PROVISIONING, VIEWING OR USE OF THE MATERIALS REGARDLESS OF THE FORM OF ACTION, WHETHER FOR BREACH OF CONTRACT, BREACH OF WARRANTY, TORT, NEGLIGENCE, INFRINGEMENT OR OTHERWISE (INCLUDING, WITHOUT LIMITATION, DAMAGES BASED ON LOSS OF PROFITS, DATA, FILES, USE, BUSINESS OPPORTUNITY OR CLAIMS OF THIRD PARTIES), AND WHETHER OR NOT THE PARTY HAS BEEN ADVISED OF THE POSSIBILITY OF SUCH DAMAGES. THIS LIMITATION SHALL APPLY NOTWITHSTANDING ANY FAILURE OF ESSENTIAL PURPOSE OF ANY LIMITED REMEDY PROVIDED HEREIN.

- Should any provision of this Agreement be held by a court of competent jurisdiction to be illegal, invalid, or unenforceable, that provision shall be deemed amended to achieve as nearly as possible the same economic effect as the original provision, and the legality, validity and enforceability of the remaining provisions of this Agreement shall not be affected or impaired thereby.

- The failure of either party to enforce any term or condition of this Agreement shall not constitute a waiver of either party's right to enforce each and every term and condition of this Agreement. No breach under this agreement shall be deemed waived or excused by either party unless such waiver or consent is in writing signed by the party granting such waiver or consent. The waiver by or consent of a party to a breach of any provision of this Agreement shall not operate or be construed as a waiver of or consent to any other or subsequent breach by such other party.

- This Agreement may not be assigned (including by operation of law or otherwise) by you without WILEY's prior written consent.

- Any fee required for this permission shall be non-refundable after thirty (30) days from receipt by the CCC.
- These terms and conditions together with CCC's Billing and Payment terms and conditions (which are incorporated herein) form the entire agreement between you and WILEY concerning this licensing transaction and (in the absence of fraud) supersedes all prior agreements and representations of the parties, oral or written. This Agreement may not be amended except in writing signed by both parties. This Agreement shall be binding upon and inure to the benefit of the parties' successors, legal representatives, and authorized assigns.
- In the event of any conflict between your obligations established by these terms and conditions and those established by CCC's Billing and Payment terms and conditions, these terms and conditions shall prevail.
- WILEY expressly reserves all rights not specifically granted in the combination of (i) the license details provided by you and accepted in the course of this licensing transaction, (ii) these terms and conditions and (iii) CCC's Billing and Payment terms and conditions.
- This Agreement will be void if the Type of Use, Format, Circulation, or Requestor Type was misrepresented during the licensing process.
- This Agreement shall be governed by and construed in accordance with the laws of the State of New York, USA, without regards to such state's conflict of law rules. Any legal action, suit or proceeding arising out of or relating to these Terms and Conditions or the breach thereof shall be instituted in a court of competent jurisdiction in New York County in the State of New York in the United States of America and each party hereby consents and submits to the personal jurisdiction of such court, waives any objection to venue in such court and consents to service of process by registered or certified mail, return receipt requested, at the last known address of such party.

WILEY OPEN ACCESS TERMS AND CONDITIONS

Wiley Publishes Open Access Articles in fully Open Access Journals and in Subscription journals offering Online Open. Although most of the fully Open Access journals publish open access articles under the terms of the Creative Commons Attribution (CC BY) License only, the subscription journals and a few of the Open Access Journals offer a choice of Creative Commons Licenses. The license type is clearly identified on the article.

The Creative Commons Attribution License

The Creative Commons Attribution License (CC-BY) allows users to copy, distribute and transmit an article, adapt the article and make commercial use of the article. The CC-BY license permits commercial and non-

Creative Commons Attribution Non-Commercial License

The Creative Commons Attribution Non-Commercial (CC-BY-NC)License permits use, distribution and reproduction in any medium, provided the original work is properly cited and is not used for commercial purposes.(see below)

Creative Commons Attribution-Non-Commercial-NoDerivs License

The Creative Commons Attribution Non-Commercial-NoDerivs License (CC-BY-NC-ND) permits use, distribution and reproduction in any medium, provided the original work is properly cited, is not used for commercial purposes and no modifications or adaptations are made. (see below)

Use by commercial "for-profit" organizations

Use of Wiley Open Access articles for commercial, promotional, or marketing purposes requires further explicit permission from Wiley and will be subject to a fee.

Further details can be found on Wiley Online Library
http://olabout.wiley.com/WileyCDA/Section/id-410895.html

Other Terms and Conditions:

v1.10 Last updated September 2015

Questions? customercare@copyright.com or +1-855-239-3415 (toll free in the US) or +1-978-646-2777.

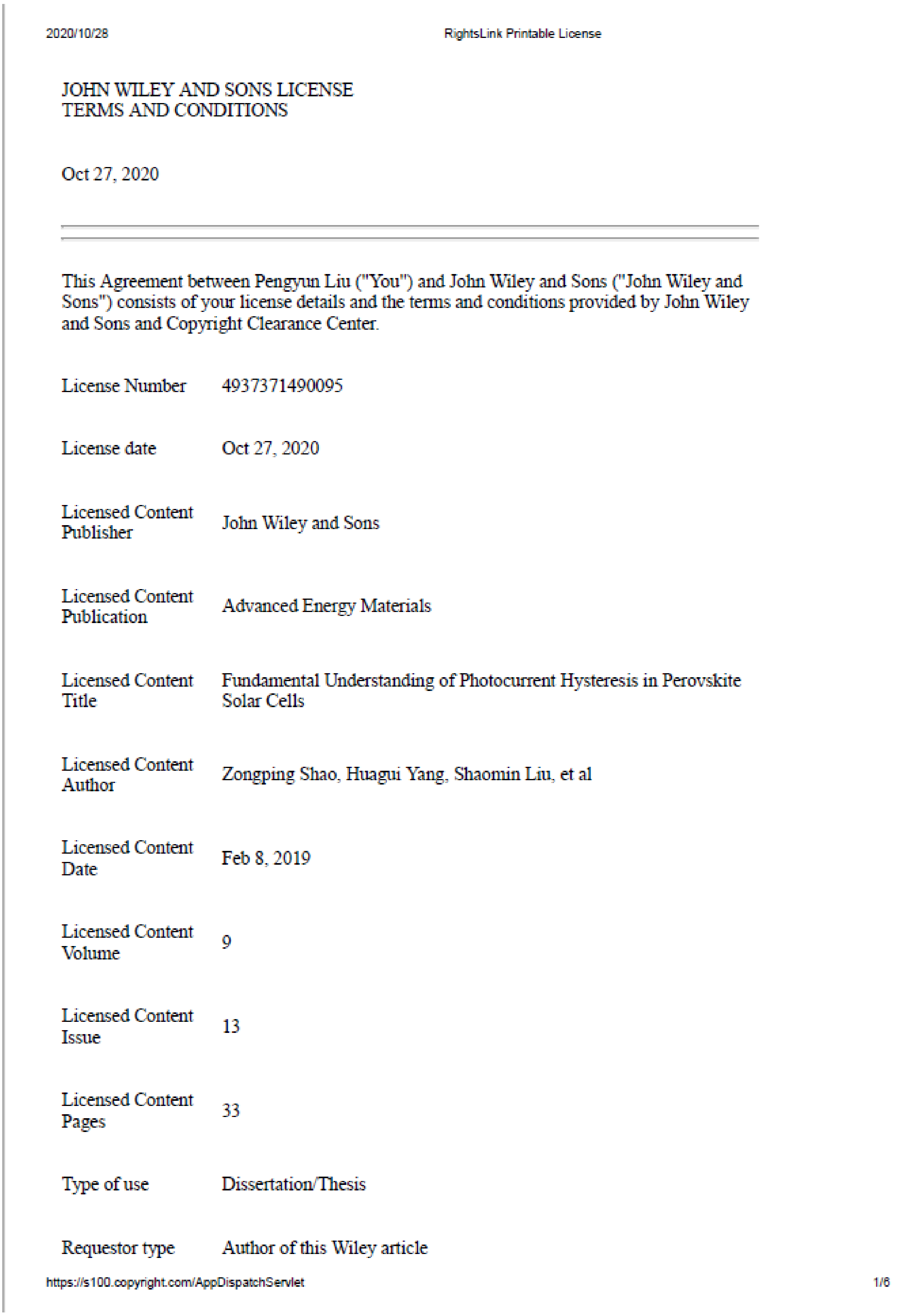

JOHN WILEY AND SONS LICENSE
TERMS AND CONDITIONS

Oct 27, 2020

This Agreement between Pengyun Liu ("You") and John Wiley and Sons ("John Wiley and Sons") consists of your license details and the terms and conditions provided by John Wiley and Sons and Copyright Clearance Center.

License Number	4937371490095
License date	Oct 27, 2020
Licensed Content Publisher	John Wiley and Sons
Licensed Content Publication	Advanced Energy Materials
Licensed Content Title	Fundamental Understanding of Photocurrent Hysteresis in Perovskite Solar Cells
Licensed Content Author	Zongping Shao, Huagui Yang, Shaomin Liu, et al
Licensed Content Date	Feb 8, 2019
Licensed Content Volume	9
Licensed Content Issue	13
Licensed Content Pages	33
Type of use	Dissertation/Thesis
Requestor type	Author of this Wiley article

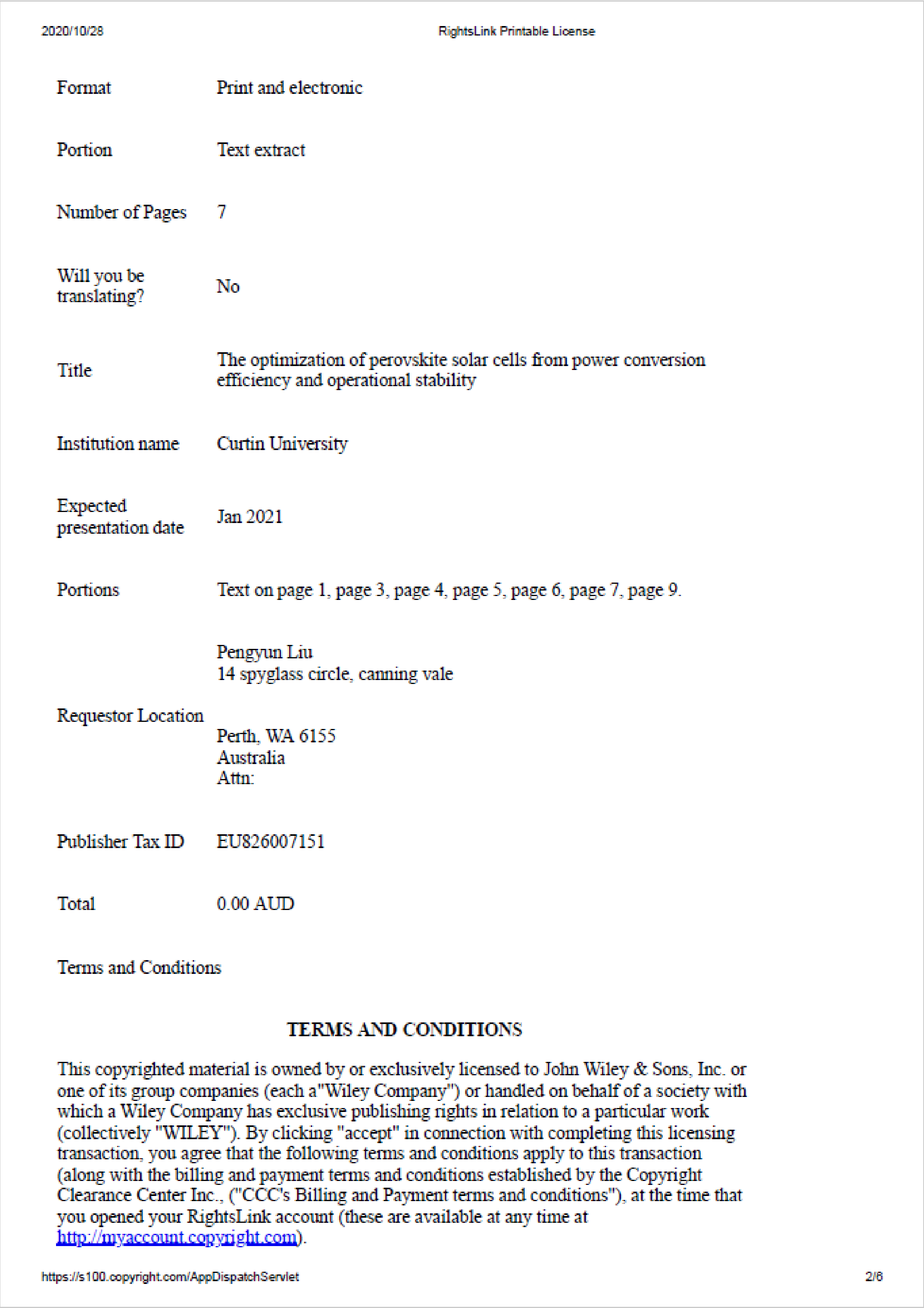

Format	Print and electronic
Portion	Text extract
Number of Pages	7
Will you be translating?	No
Title	The optimization of perovskite solar cells from power conversion efficiency and operational stability
Institution name	Curtin University
Expected presentation date	Jan 2021
Portions	Text on page 1, page 3, page 4, page 5, page 6, page 7, page 9.
Requestor Location	Pengyun Liu 14 spyglass circle, canning vale Perth, WA 6155 Australia Attn:
Publisher Tax ID	EU826007151
Total	0.00 AUD

Terms and Conditions

TERMS AND CONDITIONS

This copyrighted material is owned by or exclusively licensed to John Wiley & Sons, Inc. or one of its group companies (each a"Wiley Company") or handled on behalf of a society with which a Wiley Company has exclusive publishing rights in relation to a particular work (collectively "WILEY"). By clicking "accept" in connection with completing this licensing transaction, you agree that the following terms and conditions apply to this transaction (along with the billing and payment terms and conditions established by the Copyright Clearance Center Inc., ("CCC's Billing and Payment terms and conditions"), at the time that you opened your RightsLink account (these are available at any time at http://myaccount.copyright.com).

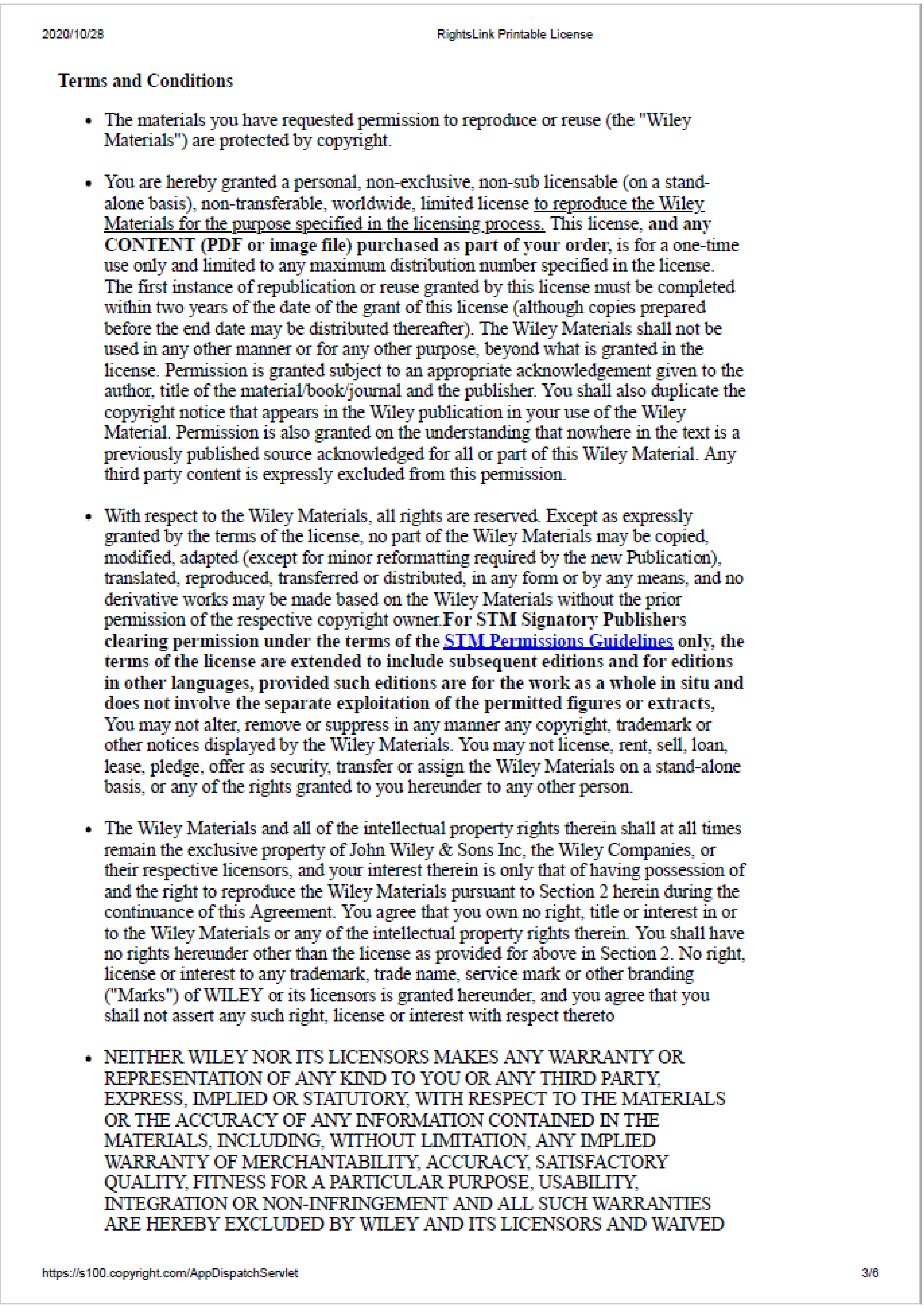

Terms and Conditions

- The materials you have requested permission to reproduce or reuse (the "Wiley Materials") are protected by copyright.

- You are hereby granted a personal, non-exclusive, non-sub licensable (on a stand-alone basis), non-transferable, worldwide, limited license to reproduce the Wiley Materials for the purpose specified in the licensing process. This license, **and any CONTENT (PDF or image file) purchased as part of your order**, is for a one-time use only and limited to any maximum distribution number specified in the license. The first instance of republication or reuse granted by this license must be completed within two years of the date of the grant of this license (although copies prepared before the end date may be distributed thereafter). The Wiley Materials shall not be used in any other manner or for any other purpose, beyond what is granted in the license. Permission is granted subject to an appropriate acknowledgement given to the author, title of the material/book/journal and the publisher. You shall also duplicate the copyright notice that appears in the Wiley publication in your use of the Wiley Material. Permission is also granted on the understanding that nowhere in the text is a previously published source acknowledged for all or part of this Wiley Material. Any third party content is expressly excluded from this permission.

- With respect to the Wiley Materials, all rights are reserved. Except as expressly granted by the terms of the license, no part of the Wiley Materials may be copied, modified, adapted (except for minor reformatting required by the new Publication), translated, reproduced, transferred or distributed, in any form or by any means, and no derivative works may be made based on the Wiley Materials without the prior permission of the respective copyright owner.**For STM Signatory Publishers clearing permission under the terms of the STM Permissions Guidelines only, the terms of the license are extended to include subsequent editions and for editions in other languages, provided such editions are for the work as a whole in situ and does not involve the separate exploitation of the permitted figures or extracts,** You may not alter, remove or suppress in any manner any copyright, trademark or other notices displayed by the Wiley Materials. You may not license, rent, sell, loan, lease, pledge, offer as security, transfer or assign the Wiley Materials on a stand-alone basis, or any of the rights granted to you hereunder to any other person.

- The Wiley Materials and all of the intellectual property rights therein shall at all times remain the exclusive property of John Wiley & Sons Inc, the Wiley Companies, or their respective licensors, and your interest therein is only that of having possession of and the right to reproduce the Wiley Materials pursuant to Section 2 herein during the continuance of this Agreement. You agree that you own no right, title or interest in or to the Wiley Materials or any of the intellectual property rights therein. You shall have no rights hereunder other than the license as provided for above in Section 2. No right, license or interest to any trademark, trade name, service mark or other branding ("Marks") of WILEY or its licensors is granted hereunder, and you agree that you shall not assert any such right, license or interest with respect thereto

- NEITHER WILEY NOR ITS LICENSORS MAKES ANY WARRANTY OR REPRESENTATION OF ANY KIND TO YOU OR ANY THIRD PARTY, EXPRESS, IMPLIED OR STATUTORY, WITH RESPECT TO THE MATERIALS OR THE ACCURACY OF ANY INFORMATION CONTAINED IN THE MATERIALS, INCLUDING, WITHOUT LIMITATION, ANY IMPLIED WARRANTY OF MERCHANTABILITY, ACCURACY, SATISFACTORY QUALITY, FITNESS FOR A PARTICULAR PURPOSE, USABILITY, INTEGRATION OR NON-INFRINGEMENT AND ALL SUCH WARRANTIES ARE HEREBY EXCLUDED BY WILEY AND ITS LICENSORS AND WAIVED

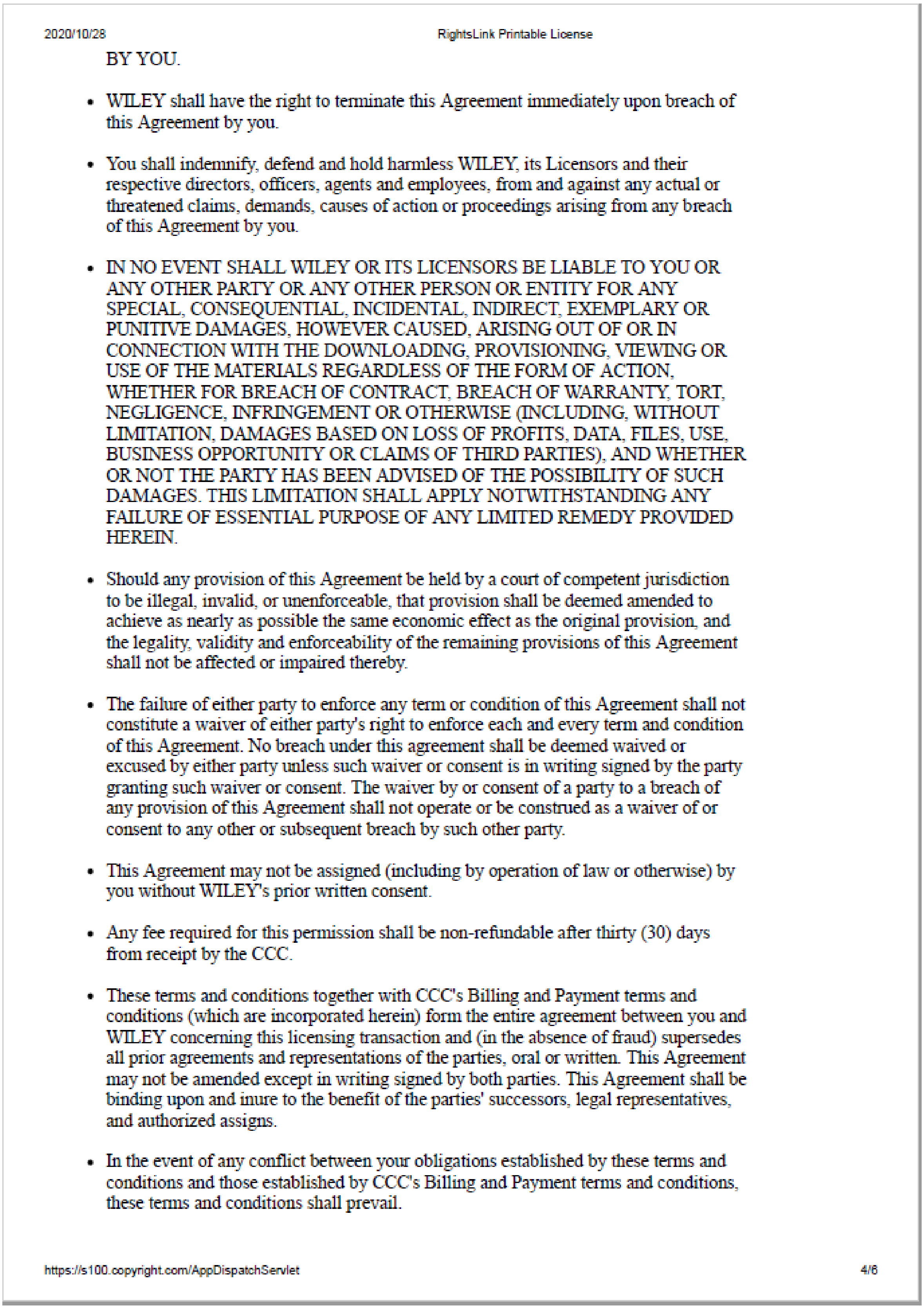

2020/10/28 RightsLink Printable License

BY YOU.

- WILEY shall have the right to terminate this Agreement immediately upon breach of this Agreement by you.

- You shall indemnify, defend and hold harmless WILEY, its Licensors and their respective directors, officers, agents and employees, from and against any actual or threatened claims, demands, causes of action or proceedings arising from any breach of this Agreement by you.

- IN NO EVENT SHALL WILEY OR ITS LICENSORS BE LIABLE TO YOU OR ANY OTHER PARTY OR ANY OTHER PERSON OR ENTITY FOR ANY SPECIAL, CONSEQUENTIAL, INCIDENTAL, INDIRECT, EXEMPLARY OR PUNITIVE DAMAGES, HOWEVER CAUSED, ARISING OUT OF OR IN CONNECTION WITH THE DOWNLOADING, PROVISIONING, VIEWING OR USE OF THE MATERIALS REGARDLESS OF THE FORM OF ACTION, WHETHER FOR BREACH OF CONTRACT, BREACH OF WARRANTY, TORT, NEGLIGENCE, INFRINGEMENT OR OTHERWISE (INCLUDING, WITHOUT LIMITATION, DAMAGES BASED ON LOSS OF PROFITS, DATA, FILES, USE, BUSINESS OPPORTUNITY OR CLAIMS OF THIRD PARTIES), AND WHETHER OR NOT THE PARTY HAS BEEN ADVISED OF THE POSSIBILITY OF SUCH DAMAGES. THIS LIMITATION SHALL APPLY NOTWITHSTANDING ANY FAILURE OF ESSENTIAL PURPOSE OF ANY LIMITED REMEDY PROVIDED HEREIN.

- Should any provision of this Agreement be held by a court of competent jurisdiction to be illegal, invalid, or unenforceable, that provision shall be deemed amended to achieve as nearly as possible the same economic effect as the original provision, and the legality, validity and enforceability of the remaining provisions of this Agreement shall not be affected or impaired thereby.

- The failure of either party to enforce any term or condition of this Agreement shall not constitute a waiver of either party's right to enforce each and every term and condition of this Agreement. No breach under this agreement shall be deemed waived or excused by either party unless such waiver or consent is in writing signed by the party granting such waiver or consent. The waiver by or consent of a party to a breach of any provision of this Agreement shall not operate or be construed as a waiver of or consent to any other or subsequent breach by such other party.

- This Agreement may not be assigned (including by operation of law or otherwise) by you without WILEY's prior written consent.

- Any fee required for this permission shall be non-refundable after thirty (30) days from receipt by the CCC.

- These terms and conditions together with CCC's Billing and Payment terms and conditions (which are incorporated herein) form the entire agreement between you and WILEY concerning this licensing transaction and (in the absence of fraud) supersedes all prior agreements and representations of the parties, oral or written. This Agreement may not be amended except in writing signed by both parties. This Agreement shall be binding upon and inure to the benefit of the parties' successors, legal representatives, and authorized assigns.

- In the event of any conflict between your obligations established by these terms and conditions and those established by CCC's Billing and Payment terms and conditions, these terms and conditions shall prevail.

https://s100.copyright.com/AppDispatchServlet 4/6

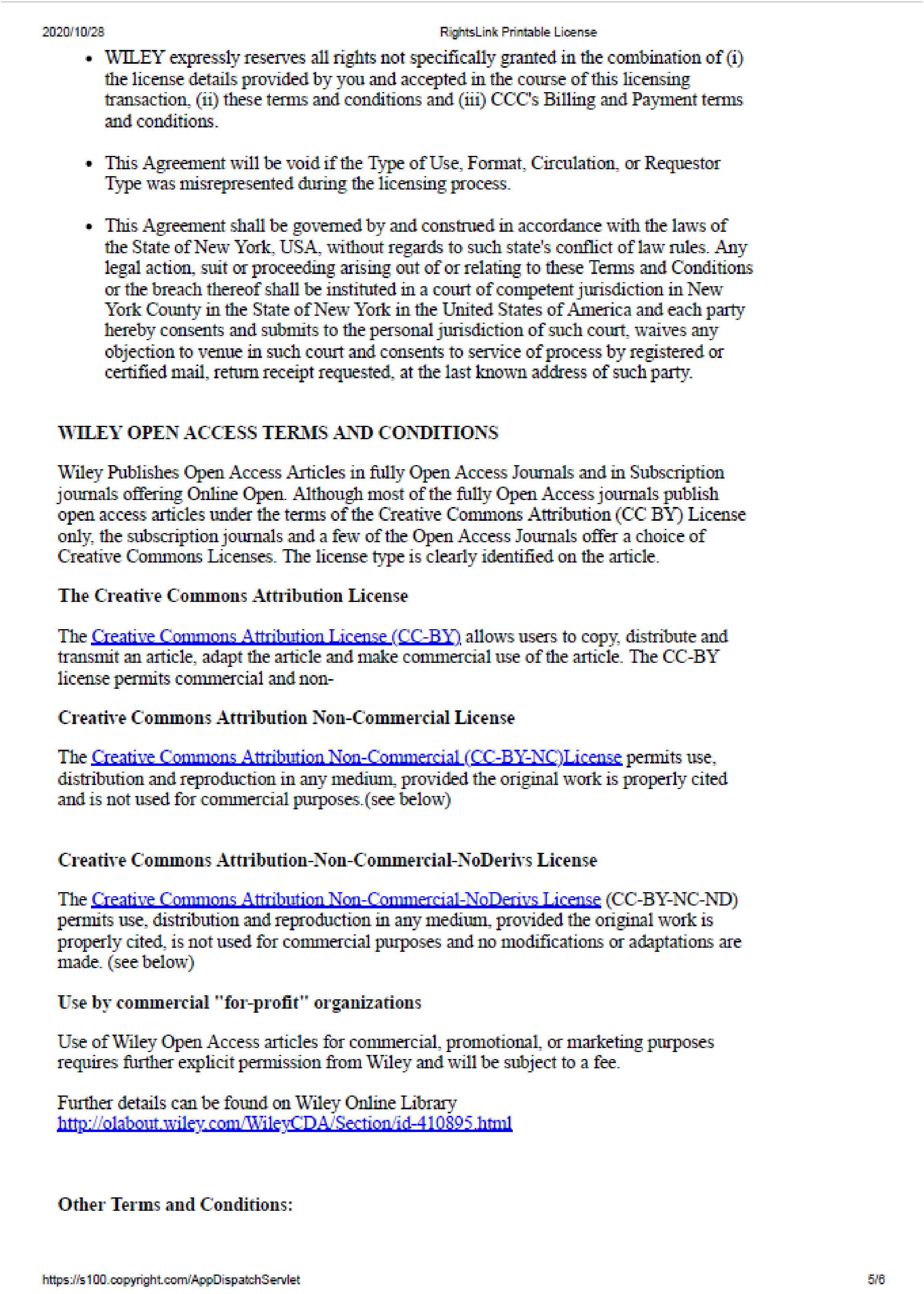

- WILEY expressly reserves all rights not specifically granted in the combination of (i) the license details provided by you and accepted in the course of this licensing transaction, (ii) these terms and conditions and (iii) CCC's Billing and Payment terms and conditions.

- This Agreement will be void if the Type of Use, Format, Circulation, or Requestor Type was misrepresented during the licensing process.

- This Agreement shall be governed by and construed in accordance with the laws of the State of New York, USA, without regards to such state's conflict of law rules. Any legal action, suit or proceeding arising out of or relating to these Terms and Conditions or the breach thereof shall be instituted in a court of competent jurisdiction in New York County in the State of New York in the United States of America and each party hereby consents and submits to the personal jurisdiction of such court, waives any objection to venue in such court and consents to service of process by registered or certified mail, return receipt requested, at the last known address of such party.

WILEY OPEN ACCESS TERMS AND CONDITIONS

Wiley Publishes Open Access Articles in fully Open Access Journals and in Subscription journals offering Online Open. Although most of the fully Open Access journals publish open access articles under the terms of the Creative Commons Attribution (CC BY) License only, the subscription journals and a few of the Open Access Journals offer a choice of Creative Commons Licenses. The license type is clearly identified on the article.

The Creative Commons Attribution License

The Creative Commons Attribution License (CC-BY) allows users to copy, distribute and transmit an article, adapt the article and make commercial use of the article. The CC-BY license permits commercial and non-

Creative Commons Attribution Non-Commercial License

The Creative Commons Attribution Non-Commercial (CC-BY-NC)License permits use, distribution and reproduction in any medium, provided the original work is properly cited and is not used for commercial purposes.(see below)

Creative Commons Attribution-Non-Commercial-NoDerivs License

The Creative Commons Attribution Non-Commercial-NoDerivs License (CC-BY-NC-ND) permits use, distribution and reproduction in any medium, provided the original work is properly cited, is not used for commercial purposes and no modifications or adaptations are made. (see below)

Use by commercial "for-profit" organizations

Use of Wiley Open Access articles for commercial, promotional, or marketing purposes requires further explicit permission from Wiley and will be subject to a fee.

Further details can be found on Wiley Online Library
http://olabout.wiley.com/WileyCDA/Section/id-410895.html

Other Terms and Conditions:

v1.10 Last updated September 2015

Questions? customercare@copyright.com or +1-855-239-3415 (toll free in the US) or +1-978-646-2777.

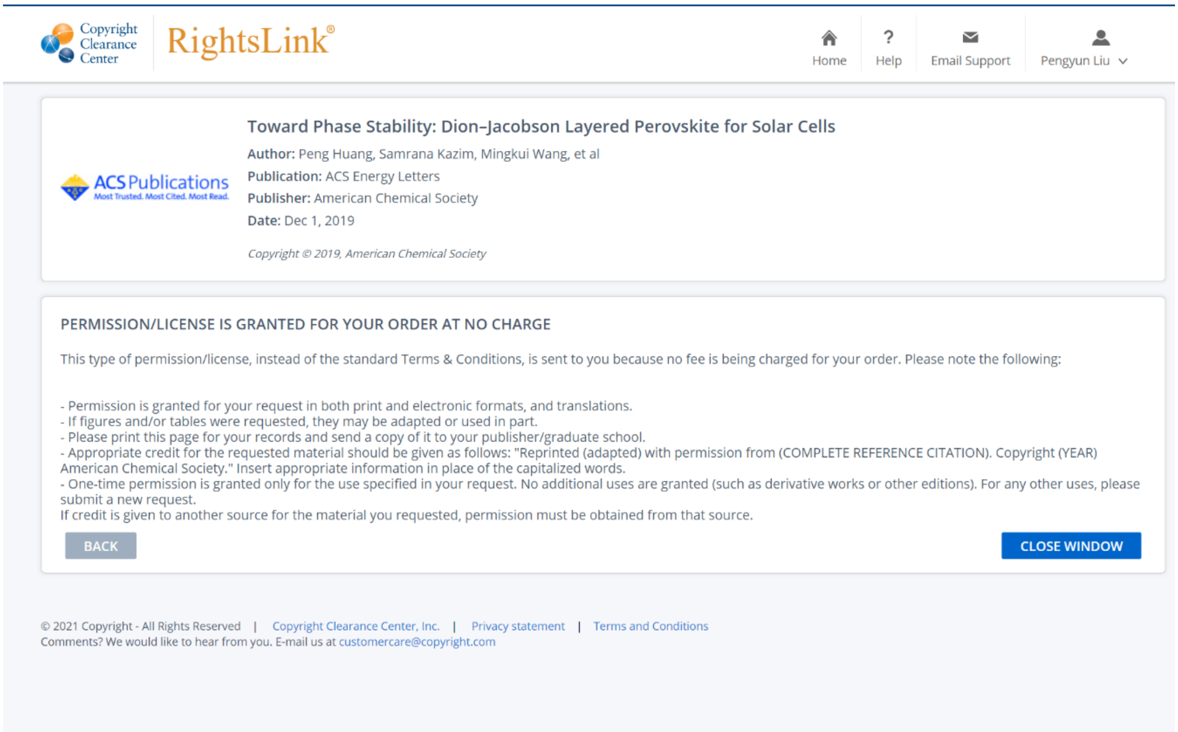

Toward Phase Stability: Dion–Jacobson Layered Perovskite for Solar Cells

Author: Peng Huang, Samrana Kazim, Mingkui Wang, et al

Publication: ACS Energy Letters

Publisher: American Chemical Society

Date: Dec 1, 2019

Copyright © 2019, American Chemical Society

PERMISSION/LICENSE IS GRANTED FOR YOUR ORDER AT NO CHARGE

This type of permission/license, instead of the standard Terms & Conditions, is sent to you because no fee is being charged for your order. Please note the following:

- Permission is granted for your request in both print and electronic formats, and translations.
- If figures and/or tables were requested, they may be adapted or used in part.
- Please print this page for your records and send a copy of it to your publisher/graduate school.
- Appropriate credit for the requested material should be given as follows: "Reprinted (adapted) with permission from (COMPLETE REFERENCE CITATION). Copyright (YEAR) American Chemical Society." Insert appropriate information in place of the capitalized words.
- One-time permission is granted only for the use specified in your request. No additional uses are granted (such as derivative works or other editions). For any other uses, please submit a new request.

If credit is given to another source for the material you requested, permission must be obtained from that source.

© 2021 Copyright - All Rights Reserved | Copyright Clearance Center, Inc. | Privacy statement | Terms and Conditions
Comments? We would like to hear from you. E-mail us at customercare@copyright.com

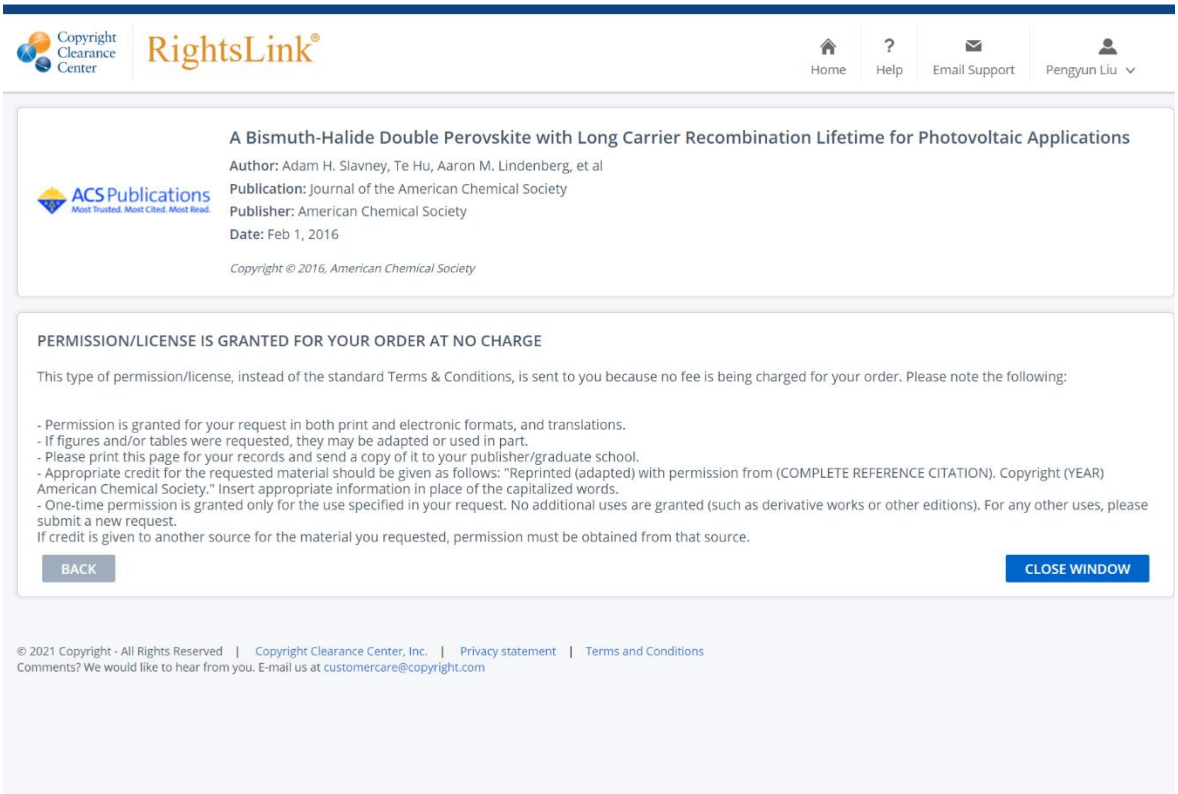

A Bismuth-Halide Double Perovskite with Long Carrier Recombination Lifetime for Photovoltaic Applications

Author: Adam H. Slavney, Te Hu, Aaron M. Lindenberg, et al

Publication: Journal of the American Chemical Society

Publisher: American Chemical Society

Date: Feb 1, 2016

Copyright © 2016, American Chemical Society

PERMISSION/LICENSE IS GRANTED FOR YOUR ORDER AT NO CHARGE

This type of permission/license, instead of the standard Terms & Conditions, is sent to you because no fee is being charged for your order. Please note the following:

- Permission is granted for your request in both print and electronic formats, and translations.
- If figures and/or tables were requested, they may be adapted or used in part.
- Please print this page for your records and send a copy of it to your publisher/graduate school.
- Appropriate credit for the requested material should be given as follows: "Reprinted (adapted) with permission from (COMPLETE REFERENCE CITATION). Copyright (YEAR) American Chemical Society." Insert appropriate information in place of the capitalized words.
- One-time permission is granted only for the use specified in your request. No additional uses are granted (such as derivative works or other editions). For any other uses, please submit a new request.

If credit is given to another source for the material you requested, permission must be obtained from that source.

© 2021 Copyright - All Rights Reserved | Copyright Clearance Center, Inc. | Privacy statement | Terms and Conditions
Comments? We would like to hear from you. E-mail us at customercare@copyright.com

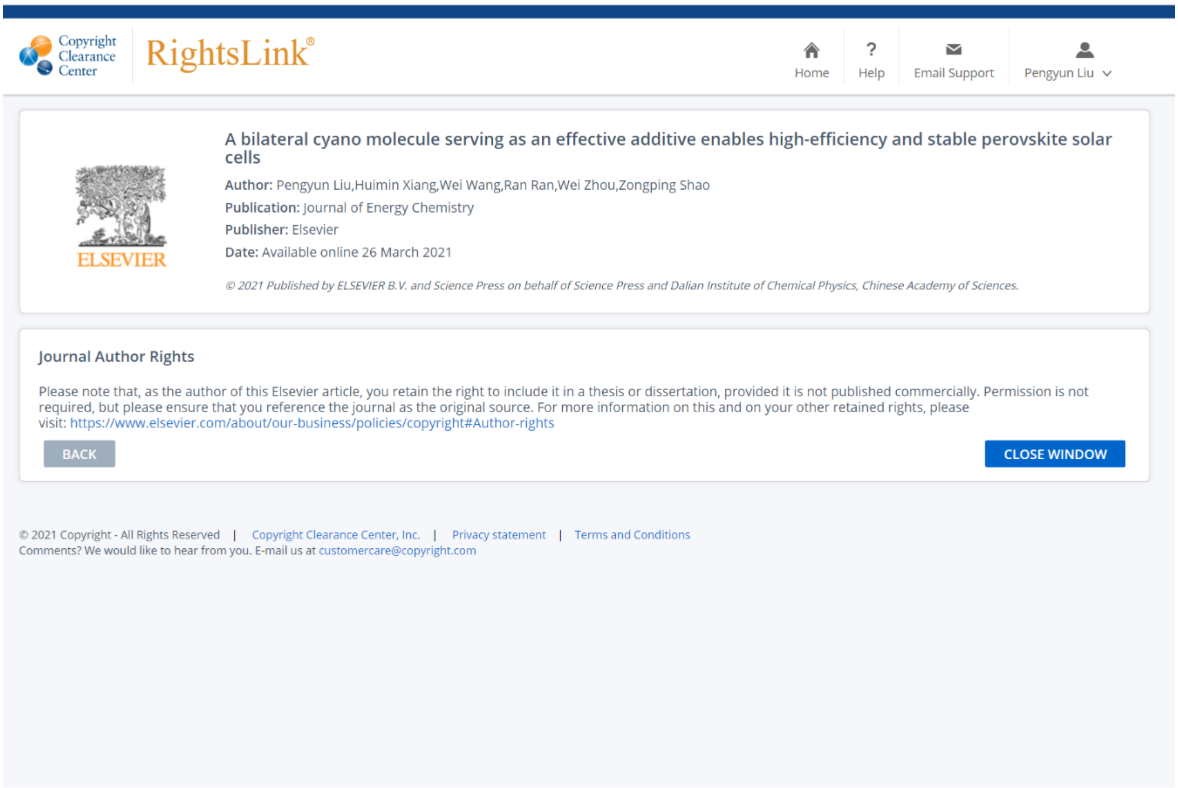

A bilateral cyano molecule serving as an effective additive enables high-efficiency and stable perovskite solar cells

Author: Pengyun Liu,Huimin Xiang,Wei Wang,Ran Ran,Wei Zhou,Zongping Shao
Publication: Journal of Energy Chemistry
Publisher: Elsevier
Date: Available online 26 March 2021

© 2021 Published by ELSEVIER B.V. and Science Press on behalf of Science Press and Dalian Institute of Chemical Physics, Chinese Academy of Sciences.

Journal Author Rights

Please note that, as the author of this Elsevier article, you retain the right to include it in a thesis or dissertation, provided it is not published commercially. Permission is not required, but please ensure that you reference the journal as the original source. For more information on this and on your other retained rights, please visit: https://www.elsevier.com/about/our-business/policies/copyright#Author-rights

---

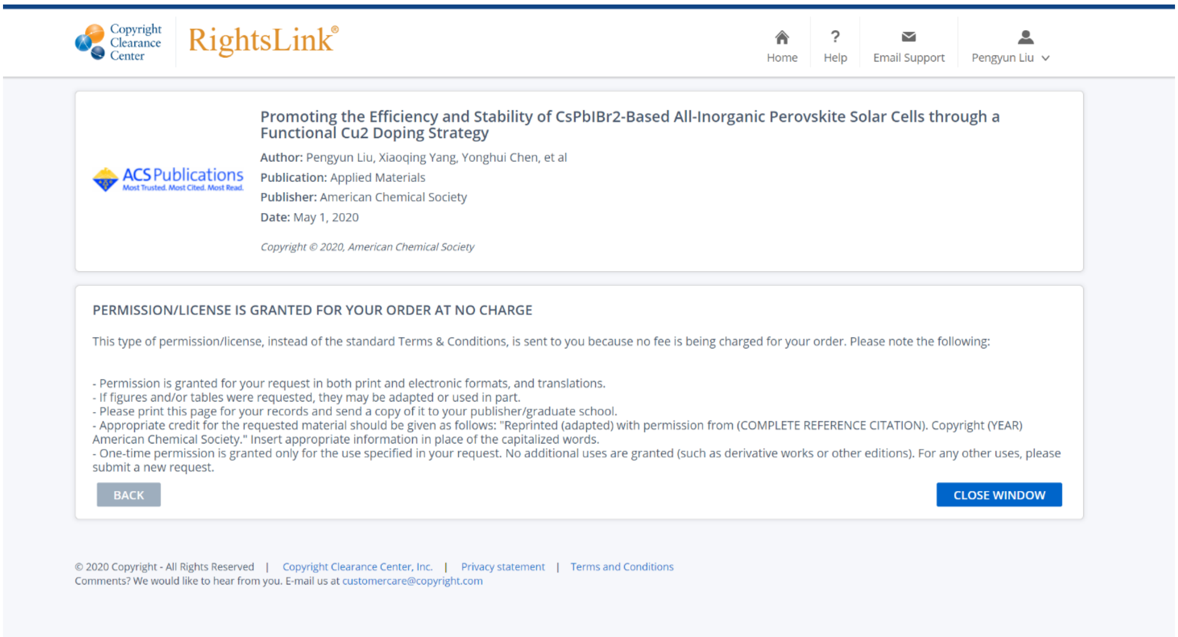

Promoting the Efficiency and Stability of CsPbIBr2-Based All-Inorganic Perovskite Solar Cells through a Functional Cu2 Doping Strategy

Author: Pengyun Liu, Xiaoqing Yang, Yonghui Chen, et al
Publication: Applied Materials
Publisher: American Chemical Society
Date: May 1, 2020

Copyright © 2020, American Chemical Society

PERMISSION/LICENSE IS GRANTED FOR YOUR ORDER AT NO CHARGE

This type of permission/license, instead of the standard Terms & Conditions, is sent to you because no fee is being charged for your order. Please note the following:

- Permission is granted for your request in both print and electronic formats, and translations.
- If figures and/or tables were requested, they may be adapted or used in part.
- Please print this page for your records and send a copy of it to your publisher/graduate school.
- Appropriate credit for the requested material should be given as follows: "Reprinted (adapted) with permission from (COMPLETE REFERENCE CITATION). Copyright (YEAR) American Chemical Society." Insert appropriate information in place of the capitalized words.
- One-time permission is granted only for the use specified in your request. No additional uses are granted (such as derivative works or other editions). For any other uses, please submit a new request.

Co-author Attribution Statement

Chapter 3 is reprinted (adapted) from the below publication. The coauthor attribution statement for this paper is given in the following table.

Publication detail:

Pengyun Liu, Huimin Xiang, Wei Wang, Ran Ran, Wei Zhou, Zongping Shao, A bilateral cyano molecule serving as an effective additive enables high-efficiency and stable perovskite solar cells. J. Energy Chem. 2021, DOI: 10.1016/j.jechem.2021.03.024

Co-author	**Conception and design**	**Methodology and data acquisition**	**Data processing and analysis**	**Interpretation and discussion**	**Manuscript writing, revision and finalization**	**Final Approval**
Huimin Xiang		×		×		×
	I acknowledge that these represent my contribution to the above result output.				Signed. [redacted]	
Wei Wang				×	×	×
	I acknowledge that these represent my contribution to the above result output.				Signed. [redacted]	
Ran Ran				×	×	×
	I acknowledge that these represent my contribution to the above result output.				Signed. [redacted]	
Wei Zhou				×	×	×
	I acknowledge that these represent my contribution to the above result output.				Signed. [redacted]	
Zongping Shao	×			×	×	×
	I acknowledge that these represent my contribution to the above result output.				Signed. [redacted]	

Chapter 4 is reprinted (adapted) from a manuscript which is being submitted. The coauthor attribution statement for this paper is given in the following table.

Manuscript detail:

Pengyun Liu, Yonghui Chen, Xiaoqing Yang, Wei Wang, Ran Ran, Wei Zhou, Zongping Shao, Benefitting from synergistic effect of anion and cation in antimony acetate for stable $CH_3NH_3PbI_3$-based perovskite solar cell with efficiency beyond 21%. (Under consideration)

Co-author attribution statement:

Co-author	**Conception and design**	**Methodology and data acquisition**	**Data processing and analysis**	**Interpretation and discussion**	**Manuscript writing, revision and finalization**	**Final Approval**
Yonghui Chen		×		×		×
	I acknowledge that these represent my contribution to the above result output.				Signed. [redacted]	
Xiaoqing Yang		×		×		×
	I acknowledge that these represent my contribution to the above result output.				Signed. [redacted]	
Huimin Xiang		×		×		×
	I acknowledge that these represent my contribution to the above result output.				Signed. [redacted]	
Wei Wang	×			×	×	×
	I acknowledge that these represent my contribution to the above result output.				Signed. [redacted]	
Ran Ran				×	×	×
	I acknowledge that these represent my contribution to the above result output.				Signed. [redacted]	
Wei Zhou				×	×	×
	I acknowledge that these represent my contribution to the above result output.				Signed. [redacted]	
Zongping Shao	×			×	×	×
	I acknowledge that these represent my contribution to the above result output.				Signed. [redacted]	

Chapter 5 is reprinted (adapted) from the below publication. The coauthor attribution statement for this paper is given in the following table.

Publication detail:

Pengyun Liu, Xiaoqing Yang, Yonghui Chen, Huimin Xiang, Wei Wang, Ran Ran, Wei Zhou, Zongping Shao, Promoting the efficiency and stability of CsPbIBr$_2$-based all-inorganic perovskite solar cells through a functional Cu^{2+} doping strategy. ACS Appl. Mater. Interfaces, 2020, 12, 23984–23994

Co-author attribution statement:

Co-author	**Conception and design**	**Methodology and data acquisition**	**Data processing and analysis**	**Interpretation and discussion**	**Manuscript writing, revision and finalization**	**Final Approval**
Xiaoqing Yang		×		×		×
	I acknowledge that these represent my contribution to the above result output.				Signed. [redacted]	
Yonghui Chen		×		×		×
	I acknowledge that these represent my contribution to the above result output.				Signed. [redacted]	
Huimin Xiang		×		×		×
	I acknowledge that these represent my contribution to the above result output.				Signed. [redacted]	
Wei Wang				×	×	×
	I acknowledge that these represent my contribution to the above result output.				Signed. [redacted]	
Ran Ran				×	×	×
	I acknowledge that these represent my contribution to the above result output.				Signed. [redacted]	
Wei Zhou				×	×	×
	I acknowledge that these represent my contribution to the above result output.				Signed. [redacted]	
Zongping Shao	×			×	×	×
	I acknowledge that these represent my contribution to the above result output.				Signed. [redacted]	